THE UNIVERSITY
of EDINBURGH

This thesis has been submitted in fulfilment of the requirements for a postgraduate degree (e.g. PhD, MPhil, DClinPsychol) at the University of Edinburgh. Please note the following terms and conditions of use:

This work is protected by copyright and other intellectual property rights, which are retained by the thesis author, unless otherwise stated.
A copy can be downloaded for personal non-commercial research or study, without prior permission or charge.
This thesis cannot be reproduced or quoted extensively from without first obtaining permission in writing from the author.
The content must not be changed in any way or sold commercially in any format or medium without the formal permission of the author.
When referring to this work, full bibliographic details including the author, title, awarding institution and date of the thesis must be given.

Early Characterisation of Neurodegeneration with High-Resolution Magnetic Resonance Elastography

Lucy V Hiscox
College of Medicine and Veterinary Medicine

THE UNIVERSITY
of EDINBURGH

A thesis submitted for the degree of
Doctor of Philosophy
June 2018

Declaration of Originality

I hereby declare that the research in this thesis, including journal publications and the thesis itself, was composed and originated entirely by myself, except where specifically stated otherwise, and has not been submitted for any other degree or professional qualification.

(Lucy V. Hiscox)

Abstract

This thesis contributes to recent interest within medical imaging regarding the development and clinical application of magnetic resonance elastography (MRE) to the human brain. MRE is a non-invasive phase-contrast MRI technique for measurement of brain mechanical properties *in vivo*, shown to reflect the composition and organisation of the complex tissue microstructure. MRE is a promising imaging biomarker for the early characterisation of neurodegeneration due to its exquisite sensitivity to variation among healthy and pathological tissue. Neurodegenerative diseases are debilitating conditions of the human nervous system for which there is currently no cure. Novel biomarkers are required to improve early detection, differential diagnosis and monitoring of disease progression, and could also ultimately improve our understanding of the pathophysiological mechanisms underlying degenerative processes. This thesis begins with a theoretical background of brain MRE and a description of the experimental considerations. A systematic review of the literature is then performed to summarise brain MRE quantitative measurements in healthy participants and to determine the success of MRE to characterise neurological disorders. This review further identified the most promising acquisition and analysis methods within the field. As such, subsequent visits to three brain MRE research centres, within the USA and Germany, enabled the acquisition of exemplar phantom and brain data to assist in discussions to refine an experimental protocol for installation at the Edinburgh Imaging Facility, QMRI (EIF-QMRI). Through collaborations with world-leading brain MRE centres, two high-resolution - yet fundamentally different - MRE pipelines were installed at the EIF-QMRI. Several optimisations were implemented to improve MRE image quality, while the clinical utility of MRE was enhanced by the novel development of a Graphical User Interface (GUI) for the optimised and automatic MRE-to-anatomical coregistration and generation of MRE derived output measures. The first experimental study was performed in 6 young and 6 older healthy adults to compare the results from the two MRE pipelines to investigate test-retest agreement of the whole brain and a brain structure of interest: the hippocampal formation. The MRE protocol shown to possess superior reproducibility was subsequently applied in a second experimental study of 12 young and 12 older cognitively healthy adults. Results include finding that the MRE imaging procedure is very well tolerated across the recruited population. Novel findings include significantly softer brains in older adults both across the global cerebrum and in the majority of subcortical grey matter structures including the pallidum, putamen, caudate, and thalamus. Changes in tissue stiffness likely reflect an alteration to the strength in the *composition* of the tissue network. All MRE effects persist after correcting for brain structure volume suggesting changes in volume alone were not reflective of the detected MRE age differences. Interestingly, no age-related differences to tissue stiffness were found for the amygdala or hippocampus. As for brain viscosity, no group differences were detected for either the brain globally or subcortical structures, suggesting a preservation of the *organisation* of the tissue network in older age. The third experiment performed in this thesis finds a direct structure-function relationship in older adults between hippocampal viscosity and episodic memory as measured with verbal-paired recall. The source of this association was located to the left hippocampus, thus complementing previous literature suggesting unilateral hippocampal specialisation. Additionally, a more significant relationship was found between left hippocampal viscosity and memory after a new procedure was developed to remove voxels containing cerebrospinal fluid from the MRE analysis. Collectively, these results support the transition of brain MRE into a clinically useful neuroimaging modality that could, in particular, be used in the early characterisation of memory specific disorders such as amnestic Mild Cognitive Impairment and Alzheimer's disease.

Lay Summary

Neurodegenerative disorders (ND) are an umbrella term for a range of conditions primarily affecting the neurons (i.e. nerve cells) in the human brain. Alzheimer's disease (AD) is the most common progressive ND, currently effecting 850,000 people in the UK with an annual cost to the economy of £26 billion. AD is characterised by increasing cognitive decline, typically involving memory, leading to substantial difficulties in activities of daily living. Currently there is no cure, with medication being used to alleviate some of the symptoms in mild-moderate cases and resulting in only modest and temporary effects. There is now evidence that the brain undergoes pathological changes up to 20 years before symptoms are noticeable. As a result, the diagnostic focus has increasingly shifted to the accurate detection of the earliest phase of the disease as this might enable early medical interventions that could slow the disease process. As such, the new diagnostic focus is on prevention rather than cure. Alternative methods are being sought to identify the earlier stages of disease and include the development of more sensitive forms of brain imaging. One such method is magnetic resonance elastography (MRE); an enhancement to traditional magnetic resonance imaging (MRI) that allows the stiffness (i.e. viscoelasticity) of biological tissue to be visualised and quantified. The properties measured by MRE have been shown to have a direct link with the health of biological tissue. MRE has had remarkable success in characterising the severity of diseases of the liver and has largely replaced liver biopsy in hospitals within the USA. The aim of this thesis was to investigate whether MRE could also be clinically useful to characterise the early stages of neurodegeneration. Recent advances in MRE methods now offer images with a high spatial resolution, thus enabling the study of small brain structures of interest including the hippocampus; a region well known for its role in memory. Two high-resolution techniques were installed in Edinburgh. Through scanning a small cohort of participants, one method was found to be more reliable than the other, which is important for any technique aiming to accurately monitor changes over time. In a larger group of subjects, the preferred method identified differences in brain viscoelasticity between young and healthy older adults across a range of brain structures. These finding was unrelated to differences in the size of each structure, which has traditionally been used to diagnose ND. Interestingly, no age-related differences were detected in the hippocampus, suggesting a preservation of the strength in the composition of the hippocampus in cognitively healthy older adults. Finally, hippocampal viscoelasticity was directly linked with performance on a memory test in older adults, whereas the size of the hippocampus was not associated with memory performance. In particular, assessment of left hippocampal viscoelasticity possessed a stronger relationship to memory recall, which may be linked to previous work suggesting that the left hippocampus is responsible for the recollection of verbal material. Overall, work presented in this thesis demonstrates that brain MRE provides unique information regarding brain tissue health and thus has potential for the characterisation of early pathological brain alterations. Work presented in this thesis, however, will need to be replicated in a larger group of participants to support these initial promising findings.

Acknowledgements

This thesis would not have been possible without the incredible support I have received from many sources. First, I wish to thank my supervisors for providing me with opportunities that I couldn't have imagined before embarking on this PhD. Thank you to Professors John Starr, Neil Roberts and Edwin van Beek. In particular, thank you to Neil, for invaluable insight, patience, and dedication to this work, which has allowed this thesis to become as comprehensive as possible.

When I first arrived in Edinburgh, Paul Kennedy, Eric Barnhill, and Lyam Hollis were instrumental in explaining the complexities that go hand in hand with Magnetic Resonance Elastography. As I near the end of my studies, I wish to thank the current members of our lab: Michael Perrins, Helen Marshall and Michel Simmons. A special thanks to Mike P for enduring some of the late nights at the QMRI with me nearing the completion of this thesis. I am also sure Mike too will acknowledge the Aroma coffee shop - a frequent source of strength to us both.

It has been a pleasure to work with all the radiographers at the Edinburgh Imaging Facility who have come and gone over the last 4 years, in particular special thanks goes to Annette Cooper, Aimee Littlejohn, Barbara Allan, Rosie Speed, Mairi MacFarlane, and Ken Dolan. Not forgetting Irene McCulloch and Karen McCurdy who brighten up the QMRI basement, and Clair Young and Anne Grant who have helped me out too many times to mention. Calum Gray, Tom MacGillivray, and Giorgos Papanastasiou - many thanks for all your support in image analysis, and also to Julian Sparrow, without whom I wouldn't have had any data to analyse. Thanks also to Scott Semple, Lucy Kershaw, David Morris, and Gillian MacNaught. My second home at the ASDRC has been met with less frequent visits over the last couple of years, but it is always a pleasure to see other ASDRC members Ruth Sibbett, Katherine Walesby, Steph West, Denise Munro, and Tom Russ.

I also owe a huge debt of thanks to numerous external collaborators, in particular to Curtis Johnson and Matt McGarry. Curtis has provided endless insight into all aspects brain MRE, in addition to endless patience to my relentless questions, while Matt has been integral to a substantial chunk of the analysis performed throughout this thesis. I hope we can continue working together in the future. I have also had the pleasure of collaborating with many other exceptional researchers during my studies. Ingolf Sack, Sebastian Hirsch, and Florian Dittmann at Charité were particularly instrumental in assisting with introducing their version of brain MRE to Edinburgh. Their advice, insight and knowledge was always appreciated. I am also indebted to many others in the field of Magnetic Resonance Elastography including researchers at the Mayo Clinic, who provided access to the equipment required to perform this work. Thanks in particular goes to Arvin Arani, John Huston III, and Richard Ehman.

My family and friends have provided wonderful support throughout this process. I look forward to returning to a somewhat more normal life after the long days and even longer nights over the last few months aiming to bring this thesis to fruition. Special mention must go to Kelly Rocks. Kelly, you have always believed in me and I thank you for your support, spirit, and encouragement for me to take on the challenge in the first place! Huge thank yous must go to Grandma, my twin-sister Sophie and my Mum. I sincerely mean that I wouldn't have been able to complete this thesis without you. Your love and support mean the world to me. More than anything, I am sure they will be pleased that my student days are finally behind me.

Finally, I would like to dedicate this thesis to the loving memory of my dad, Robert Hiscox. Dad, I wish you were here to celebrate this achievement with me.

Contents

Abstract **iv**

Lay Summary **vi**

Acknowledgements **viii**

List of Figures **xvi**

List of Tables **xviii**

List of Abbreviations **xx**

List of Symbols **xxii**

1 Introduction **1**

1.1 Human Nervous System . . . 5
  1.1.1 *Cellular Components* . . . 5
  1.1.2 *Brain Anatomy* . . . 6
1.2 Neurodegeneration . . . 7
  1.2.1 *What are neurodegenerative diseases?* . . . 8
  1.2.2 *Treatments* . . . 9
  1.2.3 *Biomarkers* . . . 9
1.3 Neuroimaging . . . 10
  1.3.1 *Magnetic Resonance Imaging (MRI)* . . . 10
  1.3.2 *Magnetic resonance elastography (MRE)* . . . 13
  1.3.3 *MR Elastography of the Brain* . . . 13
1.4 Thesis Overview . . . 14
  1.4.1 *Objectives* . . . 14
  1.4.2 *Structure* . . . 16
References . . . 18

2 Brain MRE: Theoretical basis and experimental considerations **23**

2.1 Theoretical background . . . 25
  2.1.1 *Rheology* . . . 25
  2.1.2 *Linear Elasticity* . . . 26
  2.1.3 *Viscosity* . . . 28
  2.1.4 *Viscoelasticity* . . . 29
2.2 Measuring brain viscoelasticity . . . 32
  2.2.1 *Methods of actuation* . . . 32
  2.2.2 *Recording the MRE signal* . . . 34
  2.2.3 *MRE inversion* . . . 37
2.3 Determinants of brain stiffness . . . 43
  2.3.1 *Demyelination and inflammation* . . . 44
  2.3.2 *Neuronal network density* . . . 44
  2.3.3 *Beta-amyloid (Aβ) protein accumulation* . . . 44
2.4 Conclusions . . . 45
References . . . 46

3 Literature review on Brain Magnetic Resonance Elastography 51
3.1 Introduction 53
3.2 Methods 54
3.3 Results of literature review 55
3.3.1 *Studies identified* 55
3.4 Healthy Subjects 58
3.4.1 *MRE results for global brain tissue (GBT)* 58
3.4.2 *Grey and white matter results* 60
3.4.3 *Towards a Measure of Regional Neuroanatomy* 62
3.5 Clinical studies 64
3.5.1 *Focal diseases* 64
3.5.2 *Diffuse diseases* 67
3.6 Discussion 73
References 74

4 Establishing collaborations to refine protocol for Brain MRE in Edinburgh 79
4.1 Introduction 81
4.2 Methods 84
4.2.1 *Study of Phantom Object* 84
4.2.2 *Details of Phantom Data Acquisition and Analysis* 84
4.2.3 *Study of Human Subject* 88
4.2.4 *Details of Human Brain Data Acquisition and Analysis* 88
4.3 Results 90
4.3.1 *Phantom Results* 90
4.3.2 *Human Brain Results* 94
4.4 Discussion 96
4.4.1 *Limitations* 98
4.5 Conclusion 99
References 99

5 Installation, optimisation, and validation of Brain MRE at the Edinburgh Imaging Facility, QMRI 101
5.1 Introduction 103
5.2 SF-NLI protocol 104
5.2.1 *Acquisition* 104
5.2.2 *Analysis* 105
5.3 MF-MDEV protocol 109
5.3.1 *Acquisition* 109
5.3.2 *Analysis* 112
5.4 Image segmentation 115
5.5 GUI development 117
5.5.1 *Procedure* 117
5.5.2 *MeNA highlights* 120
5.6 Summary 120
References 120

6 An evaluation of the test re-test agreement of Brain MRE 123
6.1 Introduction 125
6.2 Materials and methods 128
6.2.1 *Subjects* 128
6.2.2 *MRI protocol* 128
6.2.3 *Anatomical segmentation and mask generation* 128

6.2.4 *MRE protocol* . . . 129
6.2.5 *Statistical analyses* . . . 131
6.3 Results . . . 132
6.3.1 *Test re-test agreement* . . . 132
6.3.2 *Inter-method reliability* . . . 135
6.3.3 *Biological sensitivity* . . . 136
6.4 Discussion . . . 139
6.4.1 *Limitations* . . . 142
6.5 Conclusion . . . 143
References . . . 144

7 Subcortical grey matter viscoelasticity in young and cognitively healthy older adults 147
7.1 Introduction . . . 149
7.2 Materials and methods . . . 152
7.2.1 *Subjects* . . . 152
7.2.2 *MRI scanning* . . . 153
7.2.3 *Anatomical segmentation and mask generation* . . . 153
7.2.4 *Volumetric analysis* . . . 154
7.2.5 *MRE analysis* . . . 154
7.2.6 *Assessment of subject comfort* . . . 155
7.2.7 *Statistical analyses* . . . 155
7.3 Results . . . 156
7.3.1 *MRE acceptability* . . . 156
7.3.2 *Volumetric MRI* . . . 157
7.3.3 *Shear stiffness* μ . . . 158
7.3.4 *Damping ratio* ξ . . . 161
7.4 Discussion . . . 161
7.5 Limitations . . . 165
7.6 Conclusions . . . 166
References . . . 166

8 The relationship between hippocampal viscoelasticity and memory performance 171
8.1 Introduction . . . 173
8.2 Materials and methods . . . 175
8.2.1 *Subjects* . . . 175
8.2.2 *Neuroimaging acquisition* . . . 176
8.2.3 *MRE inversion* . . . 176
8.2.4 *Hippocampal mask generation* . . . 176
8.2.5 *Volumetric analysis* . . . 177
8.2.6 *Neuropsychological assessments* . . . 177
8.2.7 *Statistical analyses* . . . 178
8.3 Results . . . 179
8.3.1 *Bilateral hippocampal measures* . . . 180
8.3.2 *Unilateral hippocampal measures* . . . 180
8.3.3 *Hippocampal MRE with and without voxels containing CSF* . . . 183
8.4 Discussion . . . 185
8.5 Conclusions . . . 189
References . . . 189

9 Discussion and future work 197
9.1 Overview of results . . . 199

9.2 Future work 202
9.2.1 *Strategies for Improving Imaging Acquisitions* 202
9.2.2 *Strategies for Improving Inversion Algorithms* 203
9.2.3 *Improving the precision of MRE measurements* 206
9.3 Conclusions 206
References 207

Publications **209**

Conference Proceedings **211**

Awards and Grants **212**

Appendix

I Appendix I **215**

II Appendix II **217**

III Appendix III **221**

List of Figures

1.1 (a) Schematic and, (b) histological representation of neuron anatomy showing cell body, dendrites, axon, nucleus and neuroglial cells (100X) 5

1.2 Schematic representation of the cerebrum highlighting the four main lobes of the brain, the cerebellum, and brainstem. 6

1.3 Schematic representation of the cerebral ventricles 7

1.4 (a) T_1-weighted; (b) T_2-weighted; and (c) fluid-attenuated inversion recovery (FLAIR) images have different contrasts that reveal specific information about various structures in the brain 11

1.5 Availability of MRE technology across the world. Source: Resoundant (MRE: connect) . 14

1.6 a-c) MRI and MRE data from 59-year-old female with meningioma: (a) axial T_2-weighted image demonstrating the tumour and associated oedema; (b) wave image shows longer wavelength throughout the tumour; (c) MRE elastogram shows the tumour to be substantially stiffer, whereas oedema is softer, in relation to unaffected tissue. (d-f) data from 39-year-old male with a glioma (grade IV): (d) T_2-weighted image showing the tumour mass; (e) wave image displays shorter wavelengths in the tumour; (f) MRE elastogram showing the tumour to be softer compared to unaffected brain tissue. 15

2.1 Illustration to show the nine stress components of the stress matrix acting upon a cube in three-dimensions. The diagonal components of the rank 2 stress tensor, σ_{ij}, are the normal strains whilst the non-diagonal components represent the shear strains. 27

2.2 (a) Pneumatic actuator design in which compressed air is transmitted through a plastic tube from an active driver, situated in the MRI control room, to a passive soft pillow-like device placed beneath the head (Resoundant, Mayo Clinic, Rochester, MN, USA); (b) photograph of the pillow-like driver within a MRI head-coil, taken at the Edinburgh Imaging Facility, QMRI. 33

2.4 Diagram of MRE sequence incorporating multishot, variable-density spiral readout gradients for generating high-resolution displacement data. Bipolar motion encoding gradients (dashed) are shown on each gradient axis, though are only applied one at a time. 37

2.5 Phase unwrapping and fast Fourier transform (FFT) are a pre-requisite for all MRE phase images: (a) stack of raw wrapped phase images capturing the wave at different phases of the vibration cycle; (b) phase images have been unwrapped using the Laplacian-Based Estimate (LBE) algorithm (available within PhaseTools software); (c) images are then temporally transformed. In the resulting frequency-resolved representation, the static offset is contained in the zero-frequency component, whereas the wave information falls into the first harmonic frequency image. The higher harmonic frequencies contain no information. 38

2.6 Schematic representation of subzone concept. The global problem domain is represented by Ω, with boundary Γ. The subzone domain is represented by Ωz, with boundary Γz. Boundaries are chosen arbitrarily, allowing for the global problem domain to be broken up into a number of smaller sub-domains for more efficient computation. 41

2.7 Correlation between stiffness and number of neurons in the murine brain; (a) a decrease in the number of neurons by middle cerebral artery occlusion (MCAO) correlates with a decrease in stiffness; (b) complementary to (a), the time course of stiffness in the hippocampal region in a Parkinson mouse model. MPTP was administered on day 20, causing a short-term increase in neuronal proliferation. The significant increase to brain stiffness on day 6 after injection followed by a decay to baseline values is correlated with the number of new neurons. 45

3.1 PRISMA flow diagram showing manuscript selection . . . 55
3.2 MRE results for healthy subjects - global brain tissue (GBT) . . . 59
3.3 MRE results for healthy subjects - grey and white matter . . . 61
3.4 MRE results for healthy subjects - lobar regions . . . 64

4.1 Stacked bar plot to display the composition of brain MRE publications according to research centre for the study of: (a) healthy participants and, (b) patients with neurological disorders. . . . 82
4.2 Summary of the experimental brain MRE protocols used throughout this chapter. . . . 83
4.3 Computer-aided-design (CAD) illustration showing the design of the CIRS phantom used in this study. . . . 85
4.4 (a) Position of the phantom in the scanner at UIUC, and (b) the adjoining Resoundant actuator; (c) the phantom positioned in the head-cradle at Charité, Berlin, which in turn is attached to the (d) non-magnetic piezoelectric driver, via a carbon fibre rod. . . 87
4.5 MRE data presented from each protocol for the CIRS phantom: (a) illustration of phantom; (b) high-resolution T_2-weighted structural image; Representative image slice of: (c) raw MRE magnitude; (d) Dietrich SNR, and (e) MRE elastogram. . . . 90
4.6 Recovered stiffness values (kPa) from each protocol, plotted against manufacturer specifications. . . . 92
4.7 Bland-Altman method, used to evaluate calculated stiffness of the phantom between *in vivo* MRE and the quasi-static measurement provided by the manufacturer. The 95% confidence limits of the bias are shown as two dashed lines, with the mean value of the differences shown as a solid line. Panel (a) shows SF-DI, (b) NLI, (c) MF-MDEV, and (d) MF-MDEV protocols. (a-c) show increased variance with increasing stiffness, whereas (d) shows the least bias between measurements. . . . 93
4.8 MRE data presented from each protocol for the same subject (LH) and similar slice: (a) 3D rendering of T_1-weighted MPRAGE highlighting the illustrated slice; (b) the aforementioned high-resolution T_1 axial slice; (c) MRE magnitude image; (d) Dietrich SNR, and (e) MRE stiffness map. . . . 95

5.1 Comparison of MRE data acquired of the same subject (LH) at UIUC and EIF-QMRI, with the 3D multi-slab multishot MRE sequence. Representative image slice of (a) raw T_2 MRE magnitude, (b) Dietrich method SNR; and (c) the resulting OSS-SNR distribution. . . . 106
5.2 Representative MRE images of the same subject (LH) acquired at UIUC and EIF-QMRI. Whole-brain shear stiffness, μ map in (a) axial, (b) sagittal, and (c) coronal orientation from non-linear inversion (NLI) of high-resolution MRE displacement data captured with the 3D multislab, multishot acquisition. . . . 108
5.3 Encoding sensitivity with 1 and 2 MEG cycles for a mechanical frequency of 50 Hz. . . . 111
5.4 Comparison of 50 Hz MRE data acquired of the same subject (LH) at Charité, Berlin and EIF-QMRI, with the spin-echo EPI MRE sequence. Representative image slice of: (a) raw T_2 MRE magnitude, (b) Dietrich method SNR; and (c) the resulting OSS-SNR distribution. . . . 113
5.5 Representative MRE images of the same subject (LH) acquired at Charité, Berlin and EIF-QMRI. Map of the magnitude of the complex shear modulus $|G^*|$ in (a) axial, (b) sagittal, and (c) coronal orientation from MDEV of multiple frequency MRE displacement data (i.e. 30, 40, 50 Hz) captured with a spin-echo EPI acquisition. . . . 114
5.6 `FREESURFER` output: (a) coronal, (b) sagittal, and (c) axial slice showing the T_1-weighted slice and the corresponding ‘aseg’ segmentations. The look-up table (LUT) (d) indicates the neuro-anatomical structure based on colour and number. . . . 116
5.7 Overview of the `FSL` coregistration pipeline. . . . 118
5.8 MeNA GUI for the SF-NLI pipeline . . . 119

6.1 MRE-derived values for Cp and Hp measured at two separate time points; (a) Ce stiffness results, measured as μ for NLI methods, and $|G^*|$ for MDEV methods; (b) relative viscous-to-elastic properties of Ce measured as ξ and ϕ, for NLI and MDEV protocols, respectively; (c) Hp stiffness results and, (d) Hp relative viscous-to-elastic measurements. Subjects 1-6 were young adults (mean age: 24 years), whereas subjects 7-12 were healthy older adults (mean age: 70 years). 133
6.2 Bland-Altman method, used to evaluate MRE cerebral stiffness and viscosity concordance between visits 1 and 2 for three brain MRE pipelines. The 95% confidence limits of the bias are shown as two dashed lines, with the mean value of the differences shown in purple. The figure suggests that the measured variance may increase as the stiffness parameter increases. 135
6.3 Bland-Altman method, used to evaluate MRE hippocampal stiffness and viscosity concordance between visits 1 and 2 for four brain MRE pipelines. The 95% confidence limits of the bias are shown as two dashed lines, with the mean value of the differences shown in purple. 137

7.1 Pie chart to show participant response to the MRE questionnaire; administered shortly after the imaging protocol. 157
7.2 Mean and standard deviation for (a) volume (cm^3), (b) shear stiffness, μ (kPa), and (c) damping ratio, ξ. N = 12 in each group. 159
7.3 Mean shear stiffness, μ properties of the cerebrum (Ce) for young and older adults, showing widespread softer brains in older age ($p < 0.001$) 160
7.4 Mean shear stiffness, μ properties of SGM structures (Ca, Caudate; Pa, Pallidum; Pu, Putamen; Th, Thalamus) for young and older adults, in standard MNI space 162

8.1 Bilateral hippocampal (HC) structural metrics of (a) shear stiffness, (b) damping ratio, and (c) volume, plotted against episodic memory task performance 181
8.2 Box and whisker plots depicting the values for hippocampal (a) shear stiffness, (b) damping ratio, and (c) volume, according to measurements obtained for the left and right hemisphere 182
8.3 Unilateral hippocampal (HC) damping ratio ξ plotted against episodic memory task performance; positive values indicate better task performance 183
8.4 Example images of left hippocampal damping ratio, ξ for one high scoring participant, and one low scoring participant 184
8.5 Three-dimensional rendering of hippocampal (HC) mask to illustrate the removal of voxels due to cerebrospinal fluid (CSF) 184

9.1 Comparison of results without (a) and with (b) nonlinear motion correction. 203
9.2 (a) T_1-weighted structural image transformed into MRE space to show anatomical structures in all three orthogonal orientations; (b) the default inversion used throughout this thesis, and (c) improved resolution with more conjugate gradient (CG) iterations per subzone iteration, lower total variation minimisation (TV) weight, and smaller spatial filter (SF) width. 205

List of Tables

2.1 Summary of MRE parameters 31
2.2 Determinants of brain stiffness 43

3.1 Twenty-four MRE studies which have investigated the mechanical properties of the human brain in healthy participants. 56
3.2 Seventeen MRE studies which have investigated the mechanical properties of the human brain in patient populations 57
3.3 MRE studies investigating GBT in healthy participants 58
3.4 MRE studies investigating GM and WM in healthy participants 60
3.5 List of MRE studies investigating ROIs in healthy participants 63
3.6 MRE results for GBM and NAWM 67
3.7 MRE results for GBT in MS patients and control participants 68
3.8 MRE results for GBT in patients with AD and FTD 69
3.9 MRE results for GBT in patients with NPH 71
3.10 MRE results for GBT in patients with PD, PSP and control participants 73

4.1 Imaging parameters used to scan the CIRS phantom 86
4.2 Summary of the MRI/MRE parameters used to study the same human subject 88
4.3 Phantom results from four different MRE protocols 91
4.4 Difference (%) between MRE values and manufacturer specifications 91
4.5 Stiffness values from four different MRE protocols 94

6.1 Mean MRE results for Ce and Hp from all protocols at two separate time points 132
6.2 Ce ICC results for visit 1 versus visit 2 134
6.3 Hp ICC results for visit 1 versus visit 2. 136
6.4 Mean Ce MRE results from all four experimental protocols 136
6.5 Mean Hp MRE results from all four experimental protocols 138
6.6 Mean MRE results for young and older participants according to protocol 138

7.1 Demographic data for subjects included in the ageing study. 152
7.2 Subjective assessment of MRE comfort by twenty-four volunteers. 156
7.3 Population statistics for MRI volumetry and MRE parameters 158

8.1 Demographic data for participants included in the cognitive study 179
8.2 Relationships between hippocampal viscoelasticity and volumetry and VPA recall score 180
8.3 Descriptive statistics for HC ξ and the relationship between HC ξ and VPA score depending on the exclusion/ inclusion of voxels containing cerebrospinal fluid 185

List of Abbreviations

AD	Alzheimer's disease
CSF	cerebrospinal fluid
DI	direct inversion
EM	episodic memory
EPI	echo-planar imaging
ESP	elastography software pipeline
FEM	finite-element model
GBT	global brain tissue
GM	grey matter
HF	hippocampal formation
IA	intrinsic activation
LFE	local frequency estimation
MDEV	multi-dual elasto-visco
MEG	motion encoding gradient
MCI	mild cognitive impairment
MRE	magnetic resonance elastography
MRI	magnetic resonance imaging
NAWM	normal appearing white matter
NLI	non-linear inversion
OSS-SNR	octahedral shear strain SNR
PET	positron emission tomography
PD	Parkinson's disease
ROI	regions of interest
SLIM	sample interval modulation
SNR	signal-to-noise ratio
VPA	verbal paired associates
WM	white matter
WMS	Wechsler memory scale

List of Symbols

Roman symbols

E	Young's modulus
G	shear modulus
G'	storage modulus
G''	loss modulus
G^*	complex shear modulus
$\lvert G^* \rvert$	magnitude of the complex shear modulus
K	bulk (compression) modulus
T	vibration period
TE	echo time
TR	repetition time
$\mathbf{u}$	displacement field

Greek symbols

α	spring-pot interpolation factor
γ	proton gyromagnetic ratio
ϵ	strain tensor
η	viscosity
κ	compressibility
λ	second Lamé parameter
μ	shear stiffness OR spring-pot shear modulus
υ	Poisson's ratio
ξ	damping ratio
ρ	material density
σ	stress tensor
Φ	error function in NLI
ϕ	phase angle of the complex shear modulus
ω	angular vibration frequency

Chapter 1

Introduction

Preface

This chapter begins by outlining the clinical research question and the thesis objectives. First, a brief description is given of the cellular components of the human nervous system, including an overview of basic brain anatomy. The concept and possible causes of neurodegeneration are explained, and examples provided of some of the more common forms of neurodegenerative diseases (ND). The lack of successful treatments for ND and the important role biomarkers have to play in assisting with the development of new therapies are explained. The strengths and limitations of current brain imaging modalities for detecting or predicting the progression of ND are highlighted, while the importance of the development of a new imaging contrast mechanism is emphasised. An emerging MRI based technique capable of measuring soft tissue mechanical properties, known as Magnetic Resonance Elastography (MRE) is introduced, while its success in diagnosing liver disease has led to recent interest in its application for characterising disorders of the brain. By the end of this chapter, the key clinical research question, the necessity of a new imaging biomarker, and the exciting opportunities that MRE affords, will have been described.

1.1 Human Nervous System

1.1.1 *Cellular Components*

The human brain contains approximately 100 billion neurons; the basic structural and functional unit of the central nervous system (CNS). Neurons, or nerve cells, are electrically excitable cells that are highly specialised for the receipt, integration, and transmission of information via rapid electrochemical impulses. A single neuron, which is between 5-120 μm in diameter, consists of various parts including the nucleus, dendrites, and myelinated axons, and may be connected to up to 10,000 other neurons. Figure 1.1 shows both a schematic representation of a neuron, and an image from the discipline of histology.

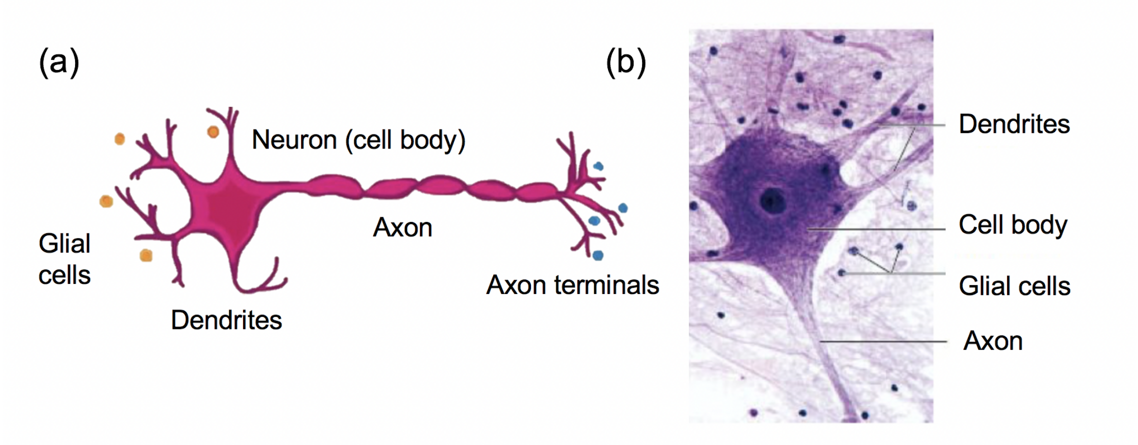

Figure 1.1: (a) Schematic and, (b) histological representation of neuron anatomy showing cell body, dendrites, axon, nucleus and neuroglial cells (100X). Source: Human Anatomy and Physiology [1].

Dendrites form extensions from the neuron to conduct electrical messages to the neuron cell body for the cell to function, whereas axons extend from the cell body to send signals to other neurons to release neurotransmitters at junctions known as synapses. There are believed to be as many as 1,000 trillion synaptic connections throughout the human brain. In addition to neurons, the nervous system contains a variety of support cells known collectively as glial, derived from the Greek word for "glue". Glia are ten times more common than neurons, and are responsible for maintaining homeostasis, forming myelin, and providing neuronal support and protection. The glial matrix, largely made up of astrocytes, oligodendrocytes, and microglia cells, also play an important role in the nutrition of neurons that are not connected to the blood circuit, and are part of the brain's immune response [2].

1.1.2 *Brain Anatomy*

The human brain can be divided into three main parts: the forebrain, midbrain and hindbrain. The forebrain is made up of the cerebrum and limbic system, the midbrain consists of the tectum and tegmentum, whereas the hindbrain contains the cerebellum, pons and medulla. The cerebrum forms the largest part of the human brain, divided into the frontal, parietal, occipital and temporal lobes, as shown in Figure 1.2. The cerebrum contains two hemispheres separated by a deep groove known as the longitudinal cerebral fissure, however, communication between hemispheres is enabled through the corpus callosum, located at the floor of the cerebral fissure [3].

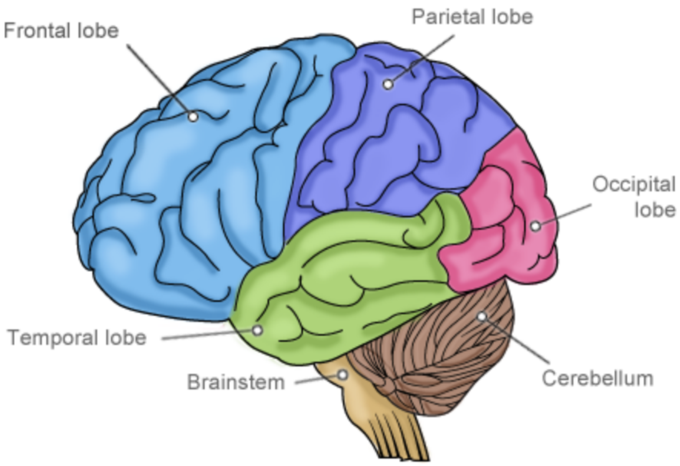

Figure 1.2: Schematic representation of the cerebrum highlighting the four main lobes of the brain, the cerebellum, and brainstem. Source: 2018 Physiotherapy @ Home [4].

The outer few millimetres of each hemisphere are known as the cerebral cortex which form both *gyri* (i.e. elevations) and *sulci* (i.e. depressions) and are associated with higher-order brain functions. The cerebral cortex is defined by the presence of neuronal cell bodies, dendrites, myelinated as well as unmyelinated axons, glial cells, including astroglia and oligodendrocytes, synapses, and capillaries. The cerebral cortex is known as *grey matter*, even though in living tissue it actually has a very light grey colour with yellowish or pinkish hues, which come from capillary blood vessels and neuronal cell bodies [5].

The majority of the cerebrum consists of white matter; white matter is distinguished from grey matter in that it contains relatively few cell bodies and is largely composed of bundles of long-range myelinated axons or *tracts* [3]. Myelin is a fatty white sheath wrapped around axons, hence the term *white matter*. Through its special construction, myelin accelerates the propagation of impulses along nerve fibres by up to 100 times. Long thought to be passive tissue, white matter has been found to modulate the distribution of action potentials, thus coordinating communication between different parts of the brain [6].

The entire CNS is suspended in cerebrospinal fluid (CSF), effectively embedding the brain into a fluid cushion. The CSF is a clear fluid manufactured in the ventricles, a cavernous system of four interconnected cavities. These are located in the centre of the two hemispheres (lateral ventricles), the diencephalon (third ventricle) and between the brainstem and the cerebellum (fourth ventricle). Apart from the role of mechanical protection of the brain, the CSF is also the recipient of brain metabolites and with that plays an important role in the maintenance of a constant extracellular environment. A further fluid component of the brain is the vascular system, which occupies 3-5% of the entire brain volume [7]. The location of the ventricular system within the cerebrum is illustrated in Figure 1.3.

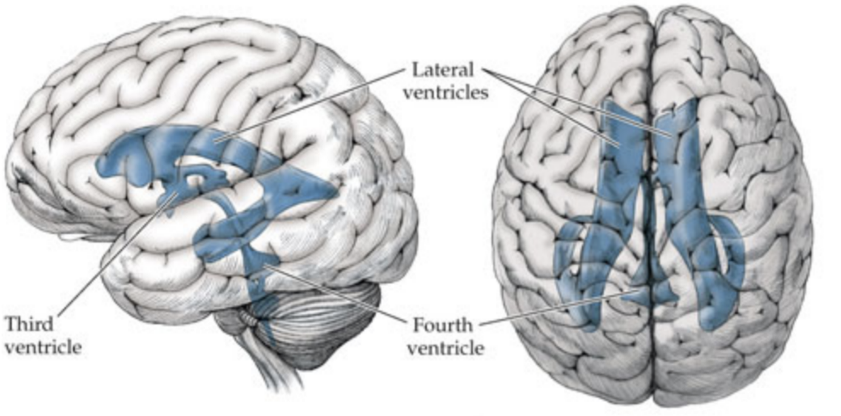

Figure 1.3: Schematic representation of the cerebral ventricles. Source: Sinauer Associates, Inc (2016) [8].

1.2 Neurodegeneration

The term neurodegeneration is composed of the prefix “neuro-,” which designates neurons, and “degeneration,” which refers to the process of losing structure or function and indicates the progressive and often irreversible loss of cells, and their synaptic function, within the CNS. Much of what is known about the causes of neurodegeneration have been learnt from examination of post-mortem tissue and studies of animal or tissue culture models. Suggested causes include toxic protein accumulation, and the inadequate degradation of inappropriately folded proteins [9], reduced mitochondrial energy production, resulting in toxic molecules that damage neurons [10,11], and viral infection or inflammatory processes, for which the influx of microglia, - the immune response cells - eventually damage neuron structure in attempting to remove virus-infected cells [12]. Furthermore, almost all neurodegenerative conditions are additionally marked by disruption of the glial matrix that leads to oligodendrocyte death and axonal demyelination. As a result of these processes, programmed cell death, known as apoptosis, results in self destruction of the neuron for the purpose of protecting other nearby neurons from toxic substances [13, 14]. A small proportion of neurodegenerative diseases are known to be caused purely by genetic mutations ($\sim$5%), however, the greatest risk factor for their development is increasing age [15]. Other risk factors may include gender, endocrine conditions, oxidative stress, vascular conditions, depression, head trauma, tumours, level of education, and environmental pollutants such as pesticides [16–18].

1.2.1 *What are neurodegenerative diseases?*

Neurodegenerative diseases are debilitating conditions of the CNS and cause problems with movement (i.e. ataxias), or cognitive functioning (i.e. dementias) and primarily affect older adults. Some forms, however, such as Creutzfeldt-Jakob disease, can affect younger individuals [19]. For decades, chronic disorders affecting the CNS have been classified into two major groups: neurodegenerative and neuroinflammatory diseases. However, typical degenerative disorders such as Alzheimer's disease (AD) and Parkinson's disease (PD) are demonstrably affected by inflammation, while classical neuroinflammatory diseases such as multiple sclerosis (MS) and amyotrophic lateral sclerosis (ALS) present aspects of neurodegeneration [20]. As such, typical neuroinflammatory disorders may now be broadly classified within the term neurodegeneration.

The number of neurodegenerative diseases is currently estimated to be several hundred, with diseases displaying disparate, but sometimes overlapping clinical presentation and aetiologies, rendering their practical classification quite challenging [21]. AD is the most common age-related neurodegenerative disease [22]. AD is characterised by increasing cognitive decline; most commonly involving memory, language and executive functioning, leading to substantial difficulties in activities of daily living. According to the Alzheimer's Society, as of 2015, there are an estimated 850,000 people in the UK living with AD with a cost to the economy of £26 billion per annum [23]. Age is the most significant risk factor with 1/6 of people over the age of 80 developing the condition. The hippocampus, a brain structure located within the medial temporal lobe and an area critical for learning and memory, is especially vulnerable to damage in Alzheimer's disease (AD) [24]. In Parkinson's disease, dopamine producing neurons concentrated within the substantia nigra of the midbrain progressively degenerate [25]. Dopamine is a chemical that relays messages between the substantia nigra and other parts of the brain to control smooth, coordinated muscle movements.

1.2.2 *Treatments*

In the face of great clinical need with the incidence of neurodegenerative diseases on the rise, there has been little success in developing effective treatments. Between 2002 and 2012, 413 clinical trials assessing 214 compounds to treat AD yielded just one new approval by the U.S. Food and Drug Administration; a success rate of 0.4% [26]. Even for those with a well-defined aetiology, such as Huntington's disease (HD), no treatment can meaningfully modify disease progression. Medication can only help alleviate symptoms and may help improve quality of life. For example, cholinesterase inhibitors can sometimes slow the progression of cognitive and functional symptoms in mild-moderate cases of AD, usually with only modest and temporary effects [27], and even after 40 years of clinical experience, levodopa remains the most effective method of managing the symptoms of PD [28].

The brain has an incredible capacity to overcome large deficits, which means that by the time clinical symptoms emerge, neuronal cell loss is extensive. In the case of AD, the brain can undergo pathological changes up to 20 years before a diagnosis is given [29]; the compensatory mechanisms of the brain are so great that there are no obvious outward behavioural symptoms for many years. Similarly, in the case of PD, up to 75% of the substantia nigra may undergo degeneration without any obvious symptoms; exceeding this threshold, however, leads to the appearance of the hallmark motor symptoms [30]. Unfortunately, the development of treatment that can repair the destruction that has occurred by the time the disease is detected, appears extremely unlikely at this time. Currently, many potential disease-modifying therapies are being developed and evaluated at the preclinical stage, and will lead to clinical trials in the near future for which biomarkers are urgently needed [31].

1.2.3 *Biomarkers*

A major goal of current clinical research into neurodegenerative diseases is to improve early detection of disease by characterising presymptomatic neuronal dysfunction. There is consensus that predicting disease development offers the best hope in accelerating the development of new therapeutic targets. As such, the diagnostic focus in neurology has shifted towards *prevention* rather than cure. A biomarker, short for biological marker, is objectively measured and evaluated as an indicator of normal biological processes, pathogenic processes or pharmacological responses to a therapeutic intervention [32] The sensitivity, specificity and ease-of-use are the most important factors that ultimately define the diagnostic utility of a biomarker. The ideal biomarker also needs to be reproducible, not subject to wide variation in the general population and unaffected by co-morbid factors [31].

Currently, a definitive diagnosis of AD is only available at *post-mortem*; however a combination of brain imaging, biochemistry and neuropsychological assessments can permit a *probable* AD diagnosis. In most instances, the lack of presymptomatic markers and knowledge about the true kinetics of cell demise precludes our ability to determine disease onset. Many different approaches are being undertaken to identify biomarkers within the disciplines of biochemistry, genetics, and radiology. This thesis focuses on the role of brain imaging and, in particular, a novel form of brain imaging that shows promise for assisting with these objectives and could even enrich our understanding of the possible causes of degeneration. Ultimately, however, it should not be forgotten that it seems likely that only a combined analysis of several biomarkers will define a patient-specific signature to diagnose early signs of neurodegeneration in the future to ensure excellent specificity and sensitivity.

1.3 Neuroimaging

The primary aim of a medical imaging modality is to ensure that there is sufficient contrast between healthy and pathological tissue to as to enable accurate diagnosis. Brain imaging provides a non-invasive assessment of brain structures [e.g. magnetic resonance imaging (MRI)/computed tomography (CT)], function [functional MRI (fMRI), positron emission tomography (PET), single positron emission computerized tomography (SPECT)], metabolites [magnetic resonance spectroscopy (MRS)] or perfusion [arterial spin labelling (ALS)] [31]. Magnetic resonance imaging (MRI) is the most common imaging modality for assessing neurodegenerative diseases since it is non-invasive, does not emit ionising radiation, and can provide many different and complementary contrast mechanisms with three-dimensional resolution.

1.3.1 *Magnetic Resonance Imaging (MRI)*

Magnetic resonance imaging (MRI) is a widespread medical imaging technique that has become an essential tool for the diagnosis of disorders of the central nervous system (CNS). MRI is based on the magnetisation properties of atomic nuclei and involves imaging of the proton; the positively charged spinning nucleus of hydrogen atoms that are abundant in tissues containing water and proteins. MRI employs a powerful, uniform, external magnetic field that causes protons in the body to absorb and emit radio frequency energy. Energy from an oscillating magnetic field temporarily is applied at the appropriate frequency [called the Larmor of resonance frequency (RF)], which excite protons causing them to emit a radiofrequency signal, moving them out of the equilibrium state. Magnetic field gradients then localise the signal in space, and the MRI receiver coils (i.e. sensors), are able to detect the energy released as the protons realign with the magnetic field. The time it takes for the protons to realign with the magnetic field (i.e. return to equilibrium state, or *relax*) is determined by the T_1 and T_2 relaxation times, which are dependent on the tissue environment and the chemical nature of the molecules.

Different MRI contrasts can be generated between tissues based on the relaxation properties of the hydrogen atoms. Figure 1.4 illustrates three different MRI contrasts including T_1-weighted, T_2-weighted, and fluid-attenuated inversion recovery (FLAIR) images. For most clinical studies, all three types of images may be used as they each contribute to the diagnosis of normal and abnormal structures. The degree of weighting depends on the selected pulse sequence, repetition time (TR), and echo time (TE). TR is the interval between repetitions of the pulse sequence, whereas TE is the interval between delivery of the RF excitation and the measurement of the magnetic resonance signal.

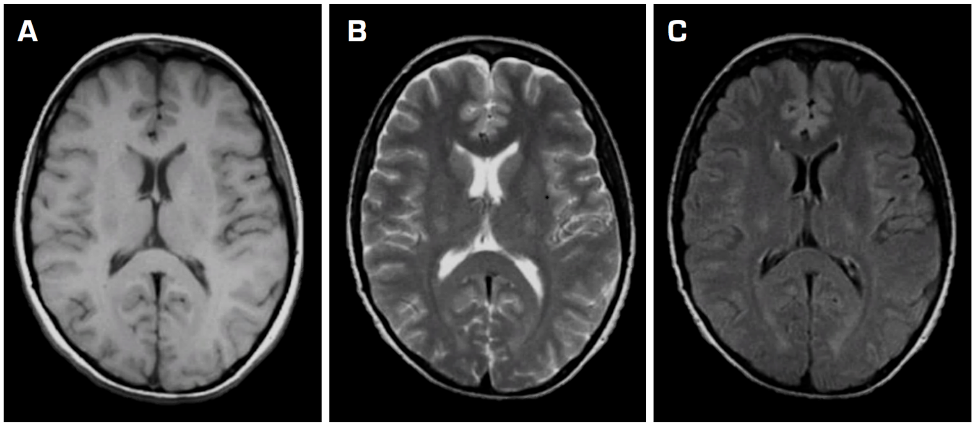

Figure 1.4: (a) T_1-weighted; (b)T_2-weighted; and (c) fluid-attenuated inversion recovery (FLAIR) images have different contrasts that reveal specific information about various structures in the brain.

While structural MRI, such as the image contrasts described previously, can be used to measure volumes of specific brain structures and thus quantify volume decline, atrophy can be subtle and hard to detect in the preclinical and early stages of neurodegenerative disorders. Furthermore, volume changes represent neuronal cell loss in which case pharmaceutical treatment is unlikely to be effective. Diffusion tensor imaging (DTI), a variant of conventional MRI, has become an increasingly prevalent and popular imaging modality for imaging the brain's white matter tracts. DTI has unparalleled sensitivity to water movements within tissue architecture and has been used to estimate white matter connectivity and microstructural tissue integrity [33]. However, DTI lacks specificity and researchers have stated that assumptions regarding white matter integrity should be made with extreme caution [34].

As a result, a new contrast mechanism may be needed to reliably evaluate microstructural tissue health to identify the specific processes causing clinical symptoms before the final, and what is considered irreversible, stages of neurodegeneration. One such property is the mechanical properties, stiffness, or viscoelasticity of tissue - terms that can be used synonymously - which through manual palpation has succeeded as a diagnostic tool throughout the history of medicine. The use of palpation can be traced back to the early physicians of ancient Egypt and to Traditional Chinese Medicine [35,36]. Even today, physicians routinely measure mechanical parameters by applying a strain to the tissue (by pushing it) to "measure" the resulting deformation through the sense of touch. For example, clinicians can differentiate between subcutaneous masses that are hard and more likely to be malignant and those that are soft and likely to be benign.

The success of diagnosing disease through palpation has no doubt been influential in the evolution of mechanobiology; an emerging field of science at the interface of biology and engineering. Mechanobiology focuses on how physical forces and changes in the mechanical properties of cells and tissues contribute to development, cell differentiation, physiology, and disease. Research now provides growing evidence of the importance of changes to cell mechanics or extracellular matrix structure tissue in the development of many diseases, including fibrosis and cancer [37]. Mechanical properties vary over a dynamic range much greater than MR relaxation time - the measurement of which provides the foundation for conventional structural images - with variations over 5 orders of magnitude among various physiological states of normal and pathologic tissues [38] A way to directly measure such properties, therefore, offers the prospect of an imaging technique with high sensitivity.

Developments within medical imaging have enabled the quantitative measurement of soft tissue mechanical properties [39]. The discipline of *Elastography* describes the use of imaging modalities such as ultrasound, optical coherence tomography and MRI to indirectly measure tissue mechanical properties. A mechanical stimulus of some kind must be used, as tissue mechanics cannot be measured directly, with modes of tissue excitation being either static, quasi-static, or dynamic in nature. The quasi-static methods measure strain resulting from macroscopic compression and attempt to compute elasticity based on a model of internal stress distribution [40], whereas dynamic elastography does not require such a model and is therefore applicable to structures such as the brain. Elastography with MRI, known as magnetic resonance elastography (MRE), has a distinct advantage over ultrasonic methods as it benefits from being both non-invasive and capable of generating images with a high spatial resolution.

1.3.2 *Magnetic resonance elastography (MRE)*

Magnetic resonance elastography (MRE) was first described by researchers from the Mayo Clinic through a seminal paper published in the journal *Science* in 1995 [41]. MRE is a non-invasive MRI-based technique that can directly map and quantify the mechanical properties, or stiffness, of biological tissue by imaging the propagation of applied acoustic waves. The advance which made MRE possible was the discovery of a way to include motion-encoding-gradients (MEGs) within a typical MRI sequence to capture multiple snapshots of the wave propagation. Original studies manually measured the wavelength in an image to estimate tissue stiffness [42, 43], before the subsequent development of automatic image processing techniques or mathematical inversion algorithms. A full summary of the MRE procedure, including details of data acquisition and data analysis, are provided in *Chapter 2*. An important milestone in the evolution of MRE was the demonstration that it can serve as a reliable, painless, and less-expensive alternative to liver biopsy for measuring the degree of liver fibrosis [44–46]. Importantly, MRE parameters have been corroborated with histological samples [45], and displays high diagnostic accuracy and inter-reader agreement [47]. Previously, conventional MRI had not been able to detect fibrosis as it does not change the anatomical appearance of the liver.

MRE became available as an FDA-approved upgrade for MRI scanners in 2009 and is now available on nearly any existing 1.5 T or 3 T systems from all major vendors (Siemens, GE Healthcare and Phillips). Between 2012 and 2016, more than 2,500 patients have undergone hepatic MRE exams at the Mayo Clinic, highlighting a successful laboratory to clinical translation. As of late 2017, MRE technology is available at over 800 Radiology and imaging centres across the world, as shown in Figure 1.5. Other organs to have been investigated with MRE include heart [48, 49], breast [50–52] skeletal muscle [53, 54], lungs [55, 56], kidney [57, 58], and prostate [59, 60], highlighting the capability of MRE to investigate a wide range of organs and associated pathologies.

1.3.3 *MRE of the Brain*

The next widely accepted clinical use of MRE is likely to be for preoperative surgical planning for patients with brain tumours and is already being used as part of the clinical work-up by neurosurgeons at the Mayo Clinic. Tumours of interest include meningioma, pituitary adenoma, and vestibular schwannoma [62, 63]. Prior knowledge of tumour consistency, including the tumour's intrinsic cohesiveness,

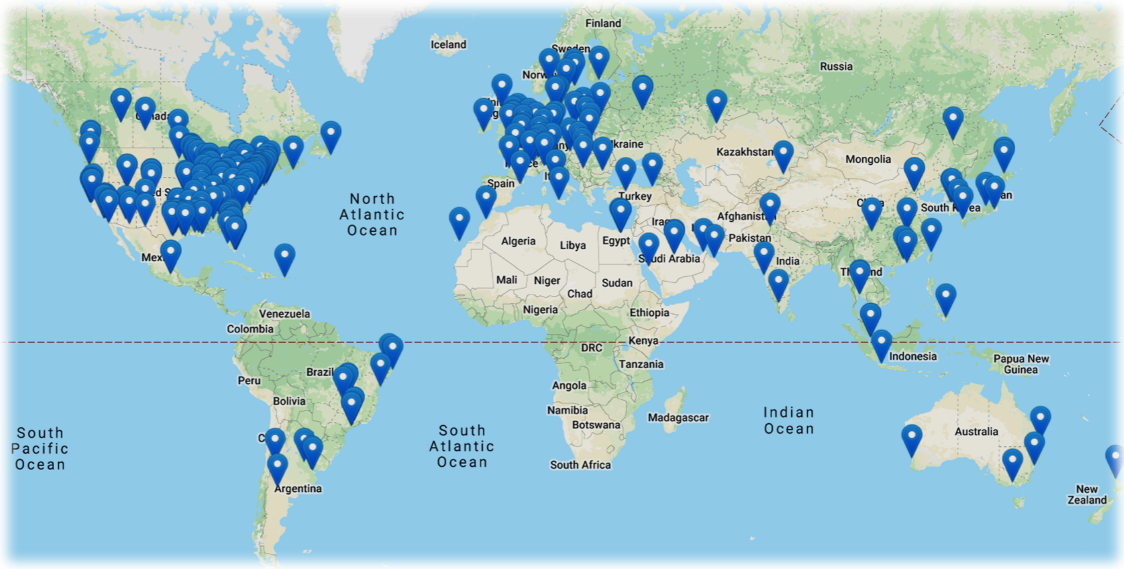
Finland
Iceland
Sweden
Russia
Ukraine
Kazakhstan
Mongolia
Spain
Turkey
North Atlantic Ocean
Algeria
Libya
Egypt
Pakistan
India
Indonesia
Mali
Niger
Chad
Sudan
Nigeria
Ethiopia
Venezuela
Colombia
DRC
Kenya
Tanzania
Papua New Guinea
Peru
Bolivia
Angola
Namibia
Botswana
Madagascar
Indian Ocean
Australia
South Pacific Ocean
South Atlantic Ocean
South Africa
Argentina
New Zealand

Figure 1.5: Availability of MRE technology across the world. Most of these centres have the technology to perform liver MRE which is increasingly becoming available for clinical use. Source: Resoundant (MRE: connect) [61]. Note: very few of these centres currently have the resources to perform brain MRE. At this time, approximately 5-10 research centres have published studies on brain MRE, including the Mayo Clinic in Minnesota, the University of Illinois at Urbana-Champaign, Charité – Universitätsmedizin Berlin, and the University of Edinburgh.

heterogeneity or infiltration into surrounding tissue, could assist surgeons in preoperative planning. The resection of stiff, fibrous tumours is typically more difficult and may require ultrasonic extraction which presents an increased risk to the patient. On the other hand, soft tumours are usually more easily removed with a minimally-invasive suction technique. Figure 1.6 illustrates two examples of a Grade I meningioma; the tumours are clearly on opposite ends of the mechanical spectrum despite the same histological characteristics underling the pathophysiological classification. Research groups are continuing to apply MRE to the diagnosis of other neurological conditions; a full summary is provided in *Chapter 3*.

1.4 Thesis Overview

1.4.1 *Objectives*

The primary objective of this thesis is to evaluate the clinical utility of MRE as an imaging biomarker for the early characterisation of neurodegeneration. MRE with a high-spatial resolution is sought to be able to more accurately investigate specific neuroanatomical regions of interest. This is first

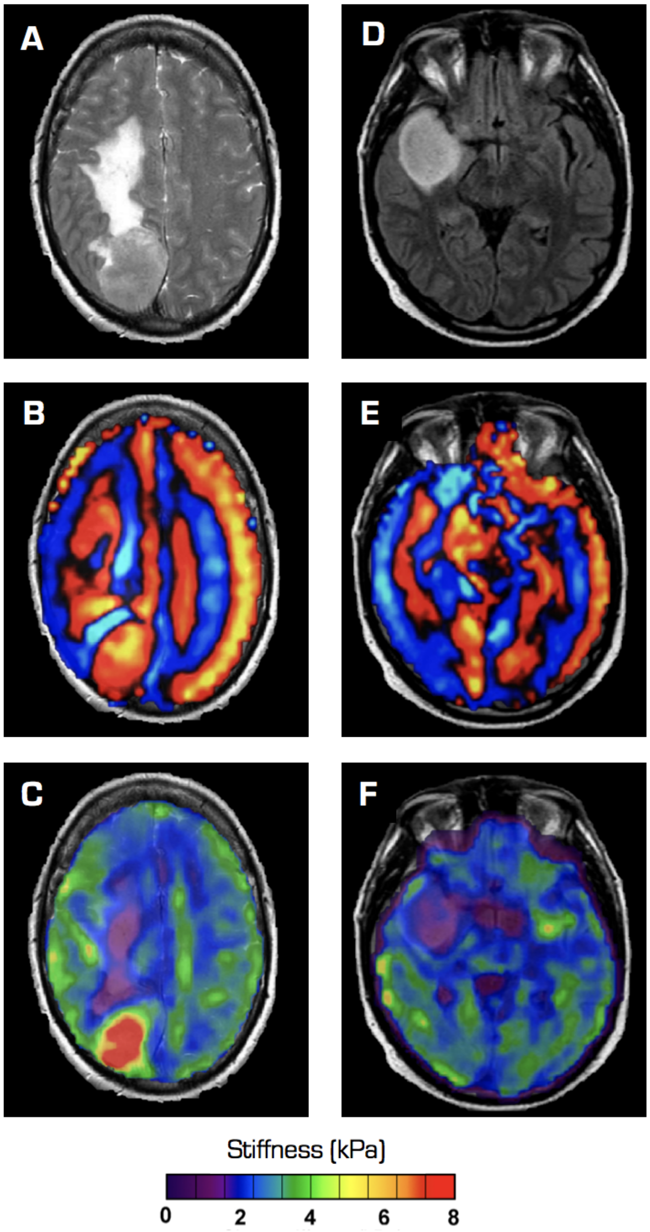

Figure 1.6: (a-e) MRI and MRE data from 59-year-old female with meningioma: (a) axial T_2*-weighted image demonstrating the tumour and associated oedema; (b) wave image shows longer wavelength throughout the tumour; (c) MRE elastogram shows the tumour to be substantially stiffer, whereas oedema is softer, in relation to unaffected tissue. (d-f) data from 39-year-old male with a glioma (grade IV): (d)* T_2*-weighted image showing the tumour mass; (e) wave image displays shorter wavelengths in the tumour; (f) MRE elastogram showing the tumour to be softer compared to unaffected brain tissue. Image adapted from Hiscox et al., 2016 [64] and used with permission.*

achieved by reviewing the experimental methods used across the literature with a particular focus on identifying approaches that provide images with a high-spatial resolution. A systematic review is then performed to evaluate results from studies that have investigated the mechanical properties of the brain in healthy participants, and to consider the success of MRE in characterising disease in patients with neurological disorders. Due to the wide range of reported methodologies, I discover widely different reports of brain stiffness in healthy participants despite the mathematical conversion of results to common MRE parameters. Importantly, there has been little to no cross-centre comparisons or validation studies. Consequently, I obtain both phantom and brain data from three leading brain MRE centres to perform a phantom validation study and to evaluate exemplar brain MRE images of the same subject. Collaborations are then established with the University of Illinois at Urbana-Champaign and Charité – Universitätsmedizin Berlin, to install two high-resolution brain MRE protocols at the Edinburgh Imaging Facility, QMRI. With the two high-resolution MRE protocols at my disposable, the reproducibility of each method is investigated. The optimal protocol is then utilised to investigate the mechanical properties of the brain in a larger sample of young and healthy older adults. Concurrently, the relationship between memory performance and hippocampal viscoelasticity is assessed in the older adult group.

1.4.2 *Structure*

The introduction chapter has introduced the relevant topics, the clinical research question, and the aims of this thesis.

In *Chapter 2*, I explain the theoretical basis of rheology and the experimental design to consider when performing a brain MRE investigation. Each phase of the experiment is described with prominence given to emerging techniques for performing high-resolution MRE. I also provide a summary of the biological correlates of MRE measures, as determined through the use of animal models of disease.

In *Chapter 3*, I perform a systematic review of the MRE literature to identify studies that have measured the mechanical properties of the human brain. From the data collected, results are mathematically converted to common parameters, to allow for a valid comparison, with values for global brain tissue (GBT), grey and white matter, and lobar regions (i.e. the frontal lobe), provided for healthy participants. In addition, data collected from clinical studies are summarised and linked to pathological manifestations.

In *Chapter 4*, MRE phantom and human brain data of the same volunteer (LH) are presented from three leading brain MRE research institutes. The CIRS phantom data is validated against the quasi-static measurements provided by the phantom manufacturer. The quality of human brain data is assessed visually and compared with published values reported in the literature.

Chapter 5 describes the installation and optimisation process of introducing two high resolution and widely published brain MRE protocols to the Edinburgh Imaging Facility, QMRI. The MRE images subsequently obtained in Edinburgh are compared with the images acquired at the associated research centres, as provided in *Chapter 4*. I also introduce a novel Graphical User Interface (GUI) MRE processing pipeline for the automatic coregistration and quantitative measurement of regions of interest (ROI).

In *Chapter 6*, I investigate the test re-test agreement of the two high-resolution brain MRE protocols whose installation had been described in *Chapter 5.* This study involves the recruitment and analysis of 6 young and 6 healthy older adult participants. Inter-method reliability, and biological sensitivity of each technique are also evaluated.

Chapter 7 applies the most reliable high-resolution MRE protocol in a cross-sectional study to investigate the effects of healthy ageing on brain mechanical properties. The global cerebrum and a range of subcortical grey matter structures are investigated in 12 young, and 12 cognitively healthy older adults. A particular emphasis is on whether MRE can provide novel information unrelated to volumetric information typically provided by conventional structural imaging.

In *Chapter 8* I investigate the possible structure-function relationship between hippocampal viscoelasticity and episodic memory performance in the older adult cohort.

Finally, I provide a summary of the work performed throughout this thesis in *Chapter 9.* I also suggest incorporating emerging MRE methodological developments that will further enhance spatial resolution, reliability and accuracy. I finish with the suggestion that this thesis provides the necessary framework for future validation investigations and that brain MRE should be expected to contribute to diagnostic neuroimaging in the future.

References

[1] Neuron anatomy from histology. *Human Anatomy and Physiology [ONLINE].*, Available at: http://mrsblackmonsscienceblackboard.weebly.com/anatomy.html [Accessed 5 June 2018].

[2] AV Gourine, V Kasymov, N Marina, F Tang, MF Figueiredo, S Lane, AG Teschemacher, KM Spyer, K Deisseroth, and S Kasparov. Astrocytes control breathing through pH-dependent release of ATP. *Science*, 329:571–5, 2010.

[3] H Blumenfeld. Neuroanatomy through clinical cases. *Sunderland, Mass: Sinauer Associates*, page 21, 2010.

[4] Lobar regions of the cerebrum. 2018 Physiotherapy @ Home. Physiotherapy at home [ONLINE]. Available at: http://www.physiotherapyathome.co.za/2016/09/19/understanding-the-brain/ [Accessed 5 June 2018].

[5] B Kolb and IQ Whishaw. Fundamentals of human neuropsychology. *Worth Publishers*, page 49, 2003.

[6] R Douglas Fields. White matter matters. *Sci Am*, 298:42–49, 2008.

[7] L Yiming, H Hongbin, Y Fan, J Aqeel, and Z Yong. The brain interstitial system: anatomy, modeling, in vivo measurement, and applications. *Prog Neurobiol*, 157:230–246, 2017.

[8] Cerebral ventricles of the adult brain. Sinauer Associates, Inc (2016), The Mind's machine 2e [ONLINE]. Available at: https://2e.mindsmachine.com/figures/02/02.17.html [Accessed 5 June 2018].

[9] AJ Thompson and CJ Barrow. Protein conformational misfolding and amyloid formation: characteristics of a new class of disorders that include alzheimer's and prion diseases. *Curr Med Chem*, 9:1751–1762, 2002.

[10] WG Tatton and CW Olanow. Apoptosis in neurodegenerative diseases: the role of mitochondria. *Biochim Biophys Acta*, 1410:195–213, 1999.

[11] RH Swerdlow. Mitochondrial DNA-related mitochondrial dysfunction in neurodegenerative diseases. *Arch Pathol Lab Med*, 126:271–280, 2002.

[12] S Hunot and EC Hirsch. Neuroinflammatory processes in Parkinson's disease. *Ann Neurol*, 53:58–60, 2003.

[13] PC Waldmeier and WG Tatton. Interrupting apoptosis in neurodegenerative disease: potential for effective therapy? *Drug Discov Today*, 9:210–218, 2004.

[14] MP Mattson. Apoptosis in neurodegenerative disorders. *Nat Rev Mol Cell Biol*, 1:120–129, 2000.

[15] T Niccoli and L Partridge. Ageing as a risk factor for disease. *Curr Biol*, 22:R741–R752, 2012.

[16] DA Butterfield. Amyloid beta-peptide (1-42)-induced oxidative stress and neurotoxicity: implications for neurodegeneration in Alzheimer's disease brain. A review. *Free Radic Res*, 36:1307–1313, 2002.

[17] RC Brown, AH Lockwood, and BR Sonawane. Neurodegenerative Diseases: An Overview of

Environmental Risk Factors. *Environ Health Perspect*, 113:1250–1256, 2005.

[18] M Chin-Chan, J Navarro-Yepes, and B Quintanilla-Vega. Environmental pollutants as risk factors for neurodegenerative disorders: Alzheimer and Parkinson diseases. *Front Cell Neurosci*, 9:124, 2015.

[19] L Letourneau-Guillon, R Wada, and W. Kucharczyk. Imaging of prion diseases. *J Magn Reson Imaging*, 35:998–1012, 2012.

[20] S Rossi, G Bernardi, and D Centonze. The endocannabinoid system in the inflammatory and neurodegenerative processes of multiple sclerosis and of amyotrophic lateral sclerosis. *Exp Neurol*, 224:92–102, 2010.

[21] S Przedborski, M Vila, and V Jackson-Lewis. Series Introduction: Neurodegeneration: What is it and where are we? *J Clin Investig*, 111:3–10, 2003.

[22] GJ Siegel, BW Agranoff, and Albers RW. Alzheimer's disease is the most common neurodegenerative disorder. Philadelphia: Lippincott-Raven, 1999.

[23] M Prince, M Knapp, M Guerchet, P McCrone, M Prina, A Comas-Herrera, R Wittenberg, B Adelaja, B Hu, D King, A Rehill, and D. Salimkumar. Dementia UK: Second edition - Overview. *Alzheimer's Society*, page 61, 2014.

[24] N Schuff, N Woerner, L Boreta, T Kornfield, L M Shaw, J Q Trojanowski, P M Thompson, C R Jack, M W Weiner, and the Alzheimer's; Disease Neuroimaging Initiative. MRI of hippocampal volume loss in early Alzheimer's disease in relation to ApoE genotype and biomarkers. *Brain*, 132:1067–1077, 2009.

[25] JO Rinne. Nigral degeneration in Parkinson's disease. *Mov Disord*, pages 31–5, 1993.

[26] JL Cummings, T Morstorf, and K Zhong. Alzheimer's disease drug-development pipeline: few candidates, frequent failures. *Alzheimer's Res Ther*, 6:37, 2014.

[27] R Howard, R McShane, J Lindesay, C Ritchie, A Baldwin, R Barber, A Burns, T Dening, D Findlay, C Holmes, A Hughes, R Jacoby, R Jones, R Jones, I McKeith, A Macharouthu, J O'Brien, P Passmore, B Sheehan, E Juszczak, C Katona, R Hills, M Knapp, C Ballard, R Brown, S Banerjee, C Onions, M Griffin, J Adams, R Gray, T Johnson, P Bentham, and P Phillips. Donepezil and Memantine for moderate-to-severe Alzheimer's disease. *N Engl J Med*, 366:893–903, 2012.

[28] DJ Brooks. Optimizing levodopa therapy for Parkinson's disease with levodopa/carbidopa/entacapone: implications from a clinical and patient perspective. *Neuropsychiatr Dis Treat*, 4:39–47, 2008.

[29] E Rodriguez-Vieitez, L Saint-Aubert, SF Carter, O Almkvist, K Farid, M Schöll, K Chiotis, S Thordardottir, C Graff, A Wall, B Långström, and A Nordberg. Diverging longitudinal changes in astrocytosis and amyloid PET in autosomal dominant Alzheimer's disease. *Brain*, 139:922–936, 2016.

[30] KGG Lloyd. CNS compensation to dopamine neuron loss in Parkinson's disease. *Adv Exp Med Biol*, 90:255–266, 1977.

[31] SMD Henley, GP Bates, and SJ Tabrizi. Biomarkers for neurodegenerative diseases. *Curr Opin Neurol*, 18:698–705, 2005.

[32] C Humpel. Identifying and validating biomarkers for Alzheimer's disease. *Trends Biotechnol*, 29:26–32, 2011.

[33] AL Alexander, JE Lee, M Lazar, and AS Field. Diffusion Tensor Imaging of the Brain. *Neurotherapeutics*, 4:316–329, 2007.

[34] JM Soares, P Marques, V Alves, and N Sousa. A hitchhiker's guide to diffusion tensor imaging. *Front Neurosci*, 7:31, 2013.

[35] D Berger. A brief history of medical diagnosis and the birth of the clinical laboratory. part 1–ancient times through the 19th century. *MLO Med Lab Obs*, 31:28–30, 1999.

[36] PNT Wells and H-D Liang. Medical ultrasound: imaging of soft tissue strain and elasticity. *J R Soc Interface*, 8:1521–1549, 2011.

[37] S Hirsch, J Braun, and I Sack. *Magnetic Resonance Elastography: Physical Background and Medical Applications*. Weinheim: Wiley-VCH, 2017.

[38] YK Mariappan, KJ Glaser, and RL Ehman. Magnetic resonance elastography: a review. *Clin Anat*, 23:497–511, 2010.

[39] J Ophir, SK Alam, B Garra, F Kallel, E Konofagou, T Krouskop, and T Varghese. Elastography: ultrasonic estimation and imaging of the elastic properties of tissues. *Proc Inst Mech Eng H*, 213:203–233, 1999.

[40] T Varghese. Quasi-Static Ultrasound Elastography. *Ultrasound Clin*, 4:323–338, 2009.

[41] R Muthupillai, DJ Lomas, PJ Rossman, JF Greenleaf, A Manduca, and RL Ehman. Magnetic resonance elastography by direct visualization of propagating acoustic strain waves. *Science*, 269:1854–1857, 1995.

[42] L Xu, Y Lin, ZN Xi, H Shen, and PY Gao. Magnetic resonance elastography of the human brain: a preliminary study. *Acta Radiol*, 48:112–115, 2007.

[43] L Xu, Y Lin, JC Han, ZN Xi, H Shen, and PY Gao. Magnetic resonance elastography of brain tumors: preliminary results. *Acta Radiol.*, 48:327–330, 2007.

[44] J Chen, M Yin, KJ Glaser, JA Talwalkar, and RL Ehman. MR Elastography of Liver Disease: State of the Art. *Appl Radiol*, 42:5–12, 2013.

[45] SK Venkatesh, M Yin, and RL Ehman. Magnetic Resonance Rlastography of Liver: Technique, Analysis, and Clinical Applications. *J Magn Reson Imaging*, 37:544–555, 2013.

[46] R Loomba, T Wolfson, B Ang, J Hooker, C Behling, M Peterson, M Valasek, G Lin, D Brenner, A Gamst, R Ehman, and C Sirlin. Magnetic resonance elastography predicts advanced fibrosis in patients with nonalcoholic fatty liver disease: a prospective study. *Hepatology*, 60:1920–1928, 2014.

[47] R Rustogi, J Horowitz, C Harmath, Y Wang, H Chalian, DR Ganger, ZE Chen, BD Bolster, S Shah, and FH Miller. Accuracy of MR Elastography and Anatomic MR Imaging Features in the Diagnosis of Severe Hepatic Fibrosis and Cirrhosis. *J Magn Reson Imaging*, 35:1356–1364, 2012.

[48] T Elgeti, M Beling, B Hamm, J Braun, and I Sack. Cardiac Magnetic Resonance Elastography: Toward the Diagnosis of Abnormal Myocardial Relaxation. *Invest Radiol*, 45:782–787, 2010.

[49] A Kolipaka, KP McGee, PA Araoz, KJ Glaser, A Manduca, AJ Romano, and RL Ehman. MR elastography as a method for the assessment of myocardial stiffness: comparison with an established pressure-volume model in a left ventricular model of the heart. *Magn Reson Med*, 62:135–140, 2009.

[50] R Sinkus, J Lorenzen, D Schrader, M Lorenzen, M Dargatz, and D Holz. High-resolution tensor MR elastography for breast tumour detection. *Phys Med Biol*, 45:1649–1664, 2000.

[51] R Sinkus, K Siegmann, T Xydeas, M Tanter, C Claussen, and M Fink. MR elastography of breast lesions: understanding the solid/liquid duality can improve the specificity of contrast-enhanced MR mammography. *Magn Reson Med*, 58:1135–1144, 2007.

[52] KC Siegmann, T Xydeas, R Sinkus, B Kraemer, U Vogel, and CD Claussen. Diagnostic value of MR elastography in addition to contrast-enhanced MR imaging of the breast-initial clinical results. *Eur Radiol*, 20:318–325, 2010.

[53] SF Bensamoun, SI Ringleb, Q Chen, RL Ehman, K An, and M Brennan. Thigh muscle stiffness assessed with magnetic resonance elastography in hyperthyroid patients before and after medical treatment. *J Magn Reson Imaging*, 26:708–713, 2007.

[54] Q Chen, J Basford, and K An. Ability of magnetic resonance elastography to assess taut bands. *Clin Biomech*, 23:623 – 629, 2008.

[55] YK Mariappan, KJ Glaser, DL Levin, R Vassallo, RD Hubmayr, C Mottram, RL Ehman, and KP McGee. Estimation of the absolute shear stiffness of human lung parenchyma using 1H spin echo, echo planar MR elastography. *J Magn Reson Imaging*, 40:1230–1237, 2014.

[56] BC Goss, KP McGee, EC Ehman, A Manduca, and RL Ehman. Magnetic resonance elastography of the lung: technical feasibility. *Magn Reson Med*, 56:1060–1066, 2006.

[57] SF Bensamoun, L Robert, GE Leclerc, L Debernard, and F Charleux. Stiffness imaging of the kidney and adjacent abdominal tissues measured simultaneously using magnetic resonance elastography. *Clin Imaging*, 35:284–287, 2011.

[58] K-J Streitberger, J Guo, H Tzschätzsch, S Hirsch, T Fischer, J Braun, and I. Sack. High-Resolution Mechanical Imaging of the Kidney. *J Biomech*, 47:639–644, 2014a.

[59] A Arani, M Da Rosa, E Ramsay, DB Plewes, MA Haider, and R Chopra. Incorporating endorectal MR elastography into multi-parametric MRI for prostate cancer imaging: Initial feasibility in volunteers. *J Magn Reson Imaging*, 38:1251–1260, 2013.

[60] M Brock, B Löppenberg, F Roghmann, A Pelzer, M Dickmann, W Becker, P Martin-Seidel, F Sommerer, L Schenk, RJ Palisaar, J Noldus, and C von Bodman. Impact of real-time elastography on magnetic resonance imaging/ultrasound fusion guided biopsy in patients with prior negative prostate biopsies. *J Urol*, 193:1191 – 1197, 2015.

[61] Worldwide availability of MRE technology. Resoundant (mre:connect). Retrieved from: https://www.resoundant.com/mre-connect.

[62] M Reiss-Zimmermann, K-J Streitberger, I Sack, J Braun, F Arlt, D Fritzsch, and KT Hoffmann. High Resolution Imaging of Viscoelastic Properties of Intracranial Tumours by Multi-Frequency Magnetic Resonance Elastography. *Clin Neuroradiol*, 25:371–380, 2014.

[63] M Simon, J Guo, S Papazoglou, H Scholand-Engler, C Erdmann, U Melchert, M Bonsanto,

J Braun, D Petersen, I Sack, and J Wuerfel. Non-invasive characterization of intracranial tumors by magnetic resonance elastography. *New J Phys*, 15:085024, 2013.

[64] LV Hiscox, CL Johnson, E Barnhill, MDJ McGarry, J III Huston, EJR van Beek, JM Starr, and N Roberts. Magnetic resonance elastography (MRE) of the human brain: technique, findings and clinical applications. *Phys Med Biol*, 61:401–437, 2016.

Chapter 2

Brain MRE: Theoretical basis and experimental considerations

Plan for the Chapter

The first part of this chapter describes the concept of rheology with a focus on defining mechanical models such as *linear-elasticity*, *viscosity*, and *viscoelasticity.* The second part of this chapter introduces specific experimental considerations for performing a brain MRE investigation, with prominence given to methods that can provide images with a high spatial resolution. Details are provided including the choice of actuator, selection of vibration frequency, MRI pulse sequence, image pre-processing options, and alternative forms of inversion for calculating tissue mechanical properties. The mathematical assumptions required for different inversion techniques are also provided. Finally, an overview of the biological correlates of MRE measurements are provided through experimental work in animal models of disease, which have been essential for providing the link between the mechanical signature and the underlying microstructural profile.

2.1 Theoretical background

2.1.1 *Rheology*

Rheology is the branch of physics that is defined as the study of the deformation and flow of matter. The measurement of rheological properties is applicable to all materials and formulations, where elasticity, viscosity and viscoelasticity can vary depending upon the external conditions applied including stress, strain, timescale and temperature.

Hooke's law, law of elasticity discovered by the English scientist Robert Hooke in 1660, states that for relatively small deformations of an object, the displacement or size of the deformation is directly proportional to the deforming force (i.e. stress). As a result, an idealised elastic solid whose response to deformation that is only a function of displacement is known as a Hookean solid. On the other hand, an idealised viscous fluid whose response to deformation is only a function of the *rate* of displacement is known as a Newtonian fluid. Hooke's law of elasticity or Newton's law of viscosity, however, lack the ability to describe realistic solids and fluids due to the complex structure of matter. Thus, rheology tends to characterise materials as a combination of these two properties (i.e. *viscoelasticity)*, in order to provide a more complete description of their behaviour. This next section further outlines the basic principles of rheology relevant to this thesis.

2.1.2 *Linear Elasticity*

Traditionally, solids have been described by Hooke's law. In one-dimension, this states that the strain (displacement) ϵ, undergone by a material is proportional to the stress (force) σ, that is placed upon it:

$$\sigma = C\epsilon \tag{2.1}$$

where C is a real-valued constant dependent on the material under investigation. The constant property of the material often depends on physical state variables, including the material microstructure or underlying molecular level. This equation implies that the material will always return to its original shape once the stress, or load, is removed, meaning all energy is restored to the material. This theory also implies that the final deformation has no dependence upon the *rate* at which the load is applied, and thus the concept of time is not considered. Elastic materials therefore show time-independent material behaviour, deform instantaneously when they are subjected to externally applied loads, and resume their original (unstressed) shapes almost instantly when the applied loads are removed. While these conditions can be approximated for some materials under certain conditions, they do not hold true in general; the strain in a solid medium cannot be described by a single constant.

The concept of stress and strain can be extended to three-dimensions (3D), which complicates the mathematics considerably. Here, the stress σ_{ij} and strain ϵ_{kl}, tensors are related to one another by the material stiffness tensor, C_{ijkl}, a rank-4 tensor (indicial notation):

$$\sigma_{ij} = C_{ijkl}\epsilon_{kl} \tag{2.2}$$

C is now a fourth order elasticity tensor mapping each of the nine terms to each for a total of 81 terms; a formation known as Generalised Hooke's Law. The nine stress components acting upon the stress matrix is illustrated in Figure 2.1.

The number of terms can be reduced by assuming that shear stresses on the solid are equal, i.e. the cube must not be experiencing body torque. These symmetries reduce the independent stresses to 36 independent material parameters [2]. Additionally, since the stress and strain tensors and the stiffness tensor contain symmetries, they are often writen as vectors and a matrix, respectively. As a result, the simplest form of Hooke's law, for an isotropic 3D solid, is often written in Voigt notation as:

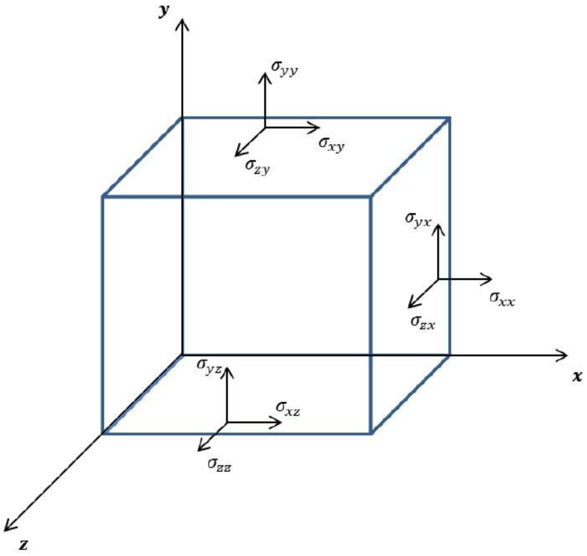

Figure 2.1: Illustration to show the nine stress components of the stress matrix acting upon a cube in three-dimensions. The diagonal components of the rank 2 stress tensor, σ_{ij}, are the normal strains whilst the non-diagonal components represent the shear strains. Source: Hollis et al., 2016 [1].

$$\begin{bmatrix}\sigma_{xx}\\ \sigma_{yy}\\ \sigma_{zz}\\ \sigma_{yz}\\ \sigma_{zx}\\ \sigma_{xy}\end{bmatrix} = \begin{bmatrix}C_{11} & C_{12} & C_{13} & C_{14} & C_{15} & C_{16}\\ C_{21} & C_{22} & C_{23} & C_{24} & C_{25} & C_{26}\\ C_{31} & C_{32} & C_{33} & C_{34} & C_{35} & C_{36}\\ C_{41} & C_{42} & C_{43} & C_{44} & C_{45} & C_{46}\\ C_{51} & C_{52} & C_{53} & C_{54} & C_{55} & C_{56}\\ C_{61} & C_{62} & C_{63} & C_{64} & C_{65} & C_{66}\end{bmatrix} \begin{bmatrix}\epsilon_{xx}\\ \epsilon_{yy}\\ \epsilon_{zz}\\ \epsilon_{yz}\\ \epsilon_{zx}\\ \epsilon_{xy}\end{bmatrix} \tag{2.3}$$

Where C is the stiffness matrix and $\sigma = C{\cdot}\epsilon$. Due to the inherent symmetries of σ, ϵ, and C, only 21 elastic coefficients are independent.

At this stage, material models such as isotropy, orthotropy, and transverse isotropy can be considered. For isotropic materials, which have the same physical properties in any direction - a common assumption made in brain MRE - C can be reduced to only two independent material constants, known as the Lamé parameters: λ and the shear modulus G. Since the strain tensor is dimensionless, the Lamé parameters are, like the stress tensor itself, measured in units of pressure. The shear modulus G is the proportionality constant between shear stress and shear strain and defined as the shear strain of a material along an axis when stressed perpendicular to that axis (i.e. magnitude of shear (off-diagonal) stresses). λ does not have a simple physical interpretation, it is defined to provide algebraic simplicity in the resulting elasticity equations. λ is related to the compressibility of the material, $\lambda \to \infty$ as a material approaches the incompressible limit. In other words, λ represents the relationship of the shear modulus to the bulk modulus K (i.e. the ratio of the pressure increase due to resulting decrease of a volume):

$$K = \lambda + \frac{2}{3}\mu \tag{2.4}$$

The isotropic assumption simplifies Eq. 2.2 to:

$$\sigma_{ij} = 2G\epsilon_{ij} + \lambda\delta_{ij}\epsilon_{kk} \tag{2.5}$$

where σ_{ij} is the strain tensor, ϵ_{ij} is the stress tensor and δ is the Kronecker delta. Of note, Hooke's law for isotropic materials, expressed by the linear relationship between stress and strain, is only valid for stresses up to a certain value, called the proportionality limit. Beyond the proportionality limit, nonlinearities set in.

2.1.3 *Viscosity*

Viscosity is the physical property that characterises the flow resistance of simple fluids; this resistance results from interactions between particles travelling at different velocities. In contrast to a linear elastic material, a viscous material does not return any of the energy stored during loading; all energy is lost once the load is removed. Newton's law of viscosity defines the simple linear relationship between the shear stress and shear rate of a fluid subjected to a mechanical stress. For a Newtonian fluid the shear rate, $\dot{\gamma}$, defined as the gradient of the velocity across the fluid layers, is directly proportional to the shear stress acting upon the solid over which the fluid is flowing:

$$\tau = \eta\dot{\gamma} \tag{2.6}$$

where τ is the viscous stress tensor and the viscosity of the fluid, η, is defined as the constant of proportionality. A Newtonian fluid requires that the viscosity remains constant, regardless of the force or rate of the shear stress. Examples of Newtonian fluids include water, organic solvents, and honey.

2.1.4 *Viscoelasticity*

Viscoelasticity is the property of materials that exhibit both elastic and viscous characteristics when undergoing deformation. Linear elasticity and viscosity offer descriptions in idealised situations that are often not representative of complex materials such as biological tissue. Instead, viscoelasticity combines these two concepts to provide a more accurate description of more complex material behaviour.

The most significant difference between viscoelastic and linear elastic models is that the strain the material is undergoing is not simply dependent upon the instantaneous stress placed upon it but additionally upon the stress history. As such, viscoelastic materials have several new properties that are not seen in linear elastic properties. First of all, if a constant stress is applied to the material, the strain will continue to increase through the phenomenon termed *creep*. Second, if a constant strain is maintained, the stress will decrease though *relaxation*. Finally, there will be a lag between the application of stress and the strain response through the process of *hysteresis*.

When considering dynamic MRE and the introduction of mechanical waves acting as the shear stress, the assumption of tissue viscoelasticity, and harmonic motion at angular frequency ω, the strain and stress oscillate with the same frequency but out of phase: From the time shift Δt and ω, the phase angle shift δ can be obtained. For an oscillating load this phase lag results in a dissipation of energy within the material and attenuation of propagating waves, such that stress and strain can be written as time-dependent sine functions:

$$\epsilon = \epsilon_0 sin(\omega t - \delta) \tag{2.7}$$

$$\sigma = \sigma_0 sin(\omega t) \tag{2.8}$$

where t is time, ω is the angular frequency, ϵ_0 and σ_0 represent the amplitudes of the strain and stress, respectively, and δ is defined as the phase lag between the oscillating stress and the strain response. Equation 2.7 can be redefined using a complex valued amplitude, $\epsilon_0^* = \epsilon_0' + i\epsilon_0''$, where i is the imaginary number equal to $\sqrt{-1}$.:

$$\epsilon(t) = \mathrm{Re}\{\epsilon_0^* e^{iwt})\} \tag{2.9}$$

where

$$\epsilon_0' = \epsilon_0 cos(\delta) \tag{2.10}$$

$$\epsilon_0'' = \epsilon_0 sin(\delta) \tag{2.11}$$

Simple trigonometric relations imply that:

$$|\epsilon^*{}_0| = ((\epsilon'{}_0{}^2 + (\epsilon''{}_0)^2)^{1/2} \tag{2.12}$$

$$\delta = tan^{-1}\left(\frac{\epsilon''{}_0}{\epsilon'{}_0}\right) \tag{2.13}$$

For viscoelastic materials, Eq. 2.5 can be rewritten using complex-valued Lamé parameters via the correspondence principle [3]. The correspondence principle states that the harmonic viscoelastic response can be calculated by converting the undamped elastic moduli to complex amplitudes and moduli:

$$\sigma^*_{ij} = 2G^*\epsilon^*_{ij} + \lambda^*\epsilon^*_{ij} \tag{2.14}$$

The real part of G^* describes energy storage, and is known as the storage modulus, G', and the imaginary part describes attenuation behaviour and is known as the loss modulus, G''.

This implies that the phase lag δ between the stress and the strain can also be defined in terms of the storage G' and loss G'' moduli:

$$\delta = tan^{-1}\left(\frac{G''}{G'}\right) \tag{2.15}$$

Shown in this equation, there is no phase lag δ in an elastic material as the imaginary component will be 0, whereas in a purely viscous material the phase lag is equal to $\pi/2$ radians.

The magnitude of the complex shear modulus $|G^*|$ is the ratio of the amplitudes of the stress to strain waves:

$$\begin{aligned} G^* &= \frac{\sigma_0}{\epsilon_0}(cos(\delta) + isin(\delta)) \\ \rightarrow |G^*| &= \frac{\sigma_0}{\epsilon_0} \end{aligned} \tag{2.16}$$

This also means that knowledge of $|G^*|$ allows for the determination of the storage G' and loss G'' moduli using the vector analysis and the phase angle shift δ, through the equations:

$$G' = |G^*|cos\,\delta \tag{2.17}$$

$$G'' = |G^*|sin\,\delta \tag{2.18}$$

The reason that a material with tan δ >1 shows more dampening is because the loss modulus G'' of the material is greater than the storage modulus G'. This suggests that the energy dissipating, viscous component of the complex modulus dominates the material behaviour. Brain MRE has reported variations of the complex shear modulus. Table 2.1 provides a summary of MRE parameters generally reported across the literature.

Table 2.1: Summary of MRE parameters

Symbol	Name	Description	Units
G'	Storage modulus	Real component of the complex shear modulus and a measure of the restoration of mechanical energy due to the elastic properties of the material. Related to the inherent mechanical rigidity of the tissue matrix, and has a strong frequency dependence.	**kPa**
G''	Loss modulus	Imaginary component of the complex shear modulus and a measure of the energy dissipated in tissue, represented by the wave attenuation, also has a strong frequency dependence; a greater loss in amplitude of a travelling wave indicating greater material viscosity [4, 5]	**kPa**
$\|G^*\|$	Complex shear modulus magnitude	A measure of the total response of tissue to harmonic vibration determined by $\|G^*\| = \sqrt{} G'^2 + G''^2$. Includes both elastic and viscous information and thus may relate to haptic distinction between stiff and soft materials, and is the parameter most similar to the information afforded by manual palpation [6].	**kPa**
μ	Shear stiffness	Another composite measure of the complex shear modulus $\mu = 2\ \|G^*\|^2/(G' + \|G^*\|)$. Determines the wavespeed in an attenuating material.	**kPa**
ϕ	Phase angle	A common measure of relative tissue viscosity, with a higher value indicating greater dissipative behaviour. ϕ is usually reported as a measure of relative viscosity as the measurement is not dependent on stiffness. $\phi = \arctan G''/G'$.	**rad**
ξ	Damping ratio	Similar in meaning to phase angle and related to complex shear modulus through $G''/2G'$. Term used in engineering and thus has a physical construct unlike ϕ.	**Unitless**

2.2 Measuring brain viscoelasticity

An MRE investigation involves a conventional MRI scanner, the modified pulse sequence incorporating motion-encoding gradients (MEG), and a source of harmonic motion to generate continuous shear waves in to the tissue of interest. The degree of tissue displacement is estimated to ultimately infer the inherent material property through the so-called *inverse* problem. In this chapter, a thorough description of the steps involved in performing a typical brain MRE investigation is provided, including an introduction to the types of vibration source, a description of how cyclic motion is encoded in MRI, and how the motion encoded wave images can be processed to measure tissue mechanical properties. Essentially, there are three key components to consider when performing an MRE investigation: (1) methods of actuation including frequency of vibration; (2) choice of MRE pulse sequence to record the MRE signal; and (3) choice of MRE inversion algorithm including assumed material model.

2.2.1 *Methods of actuation*

The first stage in an MRE experiment is the generation of a dynamic source of motion. Passive drivers are utilised to induce shear vibrations into the targeted tissue, causing shear deformation because of mode conversion and complex phenomena at boundaries and interfaces. External sources of motion have included electromagnetic [7,8], acousto-mechanical [9,10] pneumatic [11,12], and piezoelectric [13] devices, which transmit vibrations to the head via a passive driver such as a bite-bar, head cradle, or soft pillow. A soft mat has also been placed on the thorax to induce vibrations to the head indirectly [14]. The pneumatic design, which has gained recent popularity within the field, is illustrated in Figure 2.2. Each set-up causes the head to experience a gentle nodding motion on the order of microns (typically between 5 - 50 μm). The obvious limitation for all external actuation methods involves the need for extra hardware, which constrains the ease of which MRE can be installed at research and clinical centres. The concept of the additional equipment may also make participants feel claustrophobic, or they might be concerned about the vibration component in itself. As such, pilot studies have been performed to investigate whether brain MRE can be performed without external mechanical hardware. An MRE technique termed *intrinsic activation* (IA) has been developed to measure the low frequency motion generated by the natural pulsations of the brain's blood vessels [16, 17]. This approach uses a phase contrast MR angiography sequence to measure tissue displacements at multiple cardiac phases, where the arterial pulse wave passes through the branched arterial system from the circle of Willis to parenchymal arteries. Further work is needed to validate such a technique, although IA holds promise

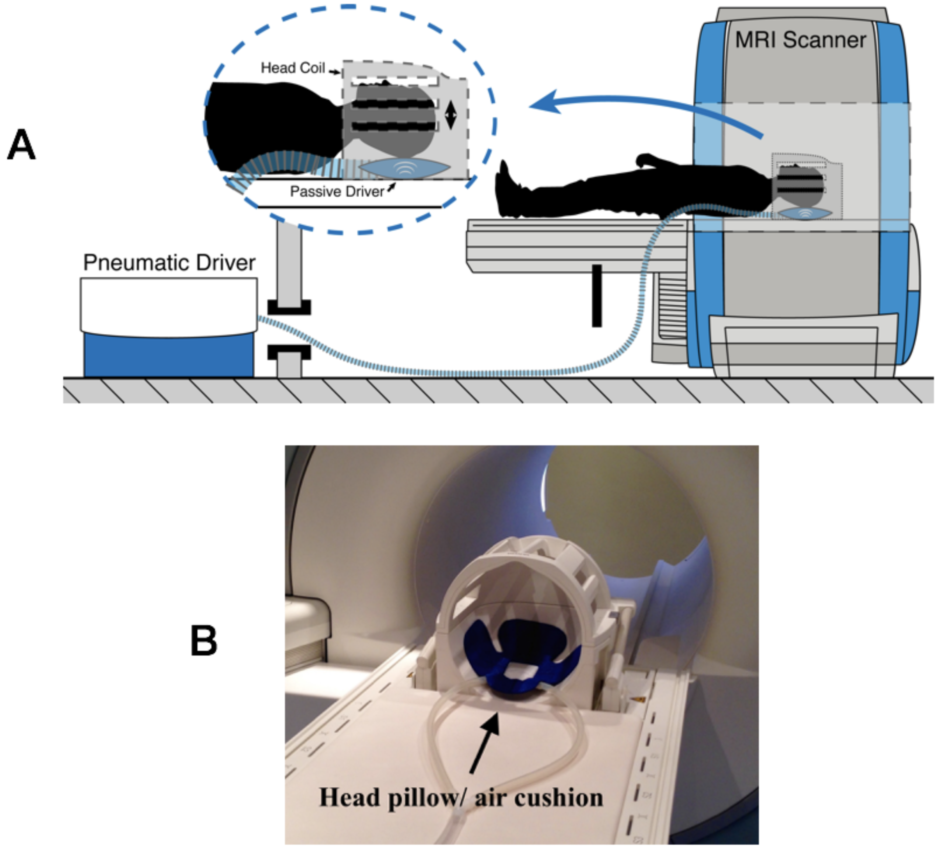

Figure 2.2: (a) Pneumatic actuator design in which compressed air is transmitted through a plastic tube from an active driver, situated in the MRI control room, to a passive soft pillow-like device placed beneath the head (Resoundant, Mayo Clinic, Rochester, MN, USA). Source: Klatt et al., 2015 [15]; (b) photograph of the pillow-like driver within a MRI head-coil, taken at the Edinburgh Imaging Facility, QMRI.

for the future in improving the clinical utility of brain MRE.

The frequency at which the brain tissue is vibrated typically ranges between 10-100 Hertz (Hz). The amplitudes of vibration at the prescribed frequencies are well within the safety margins permitted by the European Union whole-body vibration standard - designed to limit chronic occupational exposure [18]. Lower frequency waves attenuate less rapidly than higher frequency waves, enabling the analysis of deeper brain tissue. Frequencies below 10 Hz, however, will generate waves with too large a wavelength, resulting in the inability to sample the wave appropriately. On the other hand, high frequency waves with a shorter wavelength, can theoretically provide higher spatial resolution, however, frequencies above 100 Hz are generally not used due to discretisation errors [19] (i.e. where the wave cannot be sampled correctly), and for participant comfort. A standardised frequency has not been set across different research groups, largely due to the use of alternative MRE acquisition sequences and analysis protocols. However, the chosen frequency is selected by balancing the trade-off between depth of penetration, resolving power and noise levels. Generally speaking, the majority of brain MRE studies have used a frequency of 50 Hz - 60 Hz. However, within a limited frequency range (i.e. 10 - 100 Hz), brain mechanical properties have been shown to follow a power-law frequency dependence [20]. Some studies have therefore utilised a range of vibration frequencies to enable modelling of the frequency-dependent material properties, providing an opportunity to enhance tissue characterisation [21, 22]. Alternatively, data from multiple frequencies have been combined to improve image resolution [23, 24], more details of which are provided in *section 2.2.4*.

2.2.2 *Recording the MRE signal*

Conventional MRI applies a sequence of radiofrequency (RF) excitation pulses and phase and frequency encoding gradients to produce an image by encoding the spatial position of hydrogen nuclei (spins) in voxels within a tissue [25]. MRE further utilises the motion sensitivity of the spin phase of the protons. This sensitivity is a result of the high gyromagnetic ratio of protons which govern the scale of interaction of magnetic field gradients, as well as the position of a group of spins resonating at the same frequency (i.e. isochromat). The addition of a cyclic *motion-encoding gradient* (MEG) can be incorporated into nearly any MRI sequence between the excitation pulse and signal read-out to encode tissue oscillation into the signal phase. MEGs are typically trapezoidal, as opposed to sinusoidal, as they have previously been determined to provide more sensitivity to strain wave transmission [26].

In the presence of a magnetic field gradient, $\vec{G}_r(t)$, the application of the MEGs will encode the spins with trajectory, $\vec{r}(t)$, into the phase image, providing a single shot measure of the total amount of accrued phase ϕ.

$$\phi(\tau) = \gamma \int_0^{\tau} \vec{G}_r(t) \cdot \vec{r}(t)\, dt, \tag{2.19}$$

where γ is the gyromagnetic ratio characteristic of the nuclear isochromat under investigation. From the phase accumulation calculated at a single time point, it is possible to infer the amount of tissue displacement at each voxel; the phase of harmonically vibrating tissue is directly proportional to its displacement [27, 28].

Synchronisation of the externally applied motion with the MEG, is a critical step in the MRE acquisition process. Protons moving in synchronisation with the switching of the MEG, from one polarity to the other, will continually accumulate phase. Importantly, the MEG waveforms are always balanced, so that only moving spins experience phase accrual. In contrast, the effects of positive and negative gradient lobes on resting spins cancel each other out. Manipulation of the synchrony between the MEG and the external vibration can be created by the trigger pulse, causing a small delay, known as a phase offset θ. Four or eight phase offset images are usually sampled throughout the wave cycle, to capture the propagating wave over the vibration period. Two-dimensional (2D) MRE datasets are faster to require due to only one encoding direction being captured. However, accurate determination of tissue mechanical properties requires the capture of the full vector displacement field in three dimensions (3D) [29]. To capture the full wave field, the acquisition is repeated with the MEG in turn imposed along all three orthogonal directions, increasing the imaging time by a factor of three.

MEGs have been incorporated into sequences such as gradient-recalled (GR) [30, 31], and spin-echo (SE) Echo Planar Imaging (EPI) [8, 32, 33], multi-shot, variable density spiral [34, 35] and a 3D multi-slab multi-shot spiral acquisition [11]. Producing reliable estimates of brain mechanical properties relies on MRE sequences to obtain images with adequate resolution and signal-to-noise ratio (SNR). Low resolutions do not allow regional estimates of mechanical properties, whereas noise will warrant excessive filtering, limiting the ability to detect fine scale features. The most common sequence for brain MRE has been a single-shot spin-echo EPI sequence, which has an excellent temporal resolution, allowing the acquisition of entire images after a single excitation pulse [23]. The sequence begins by sending an external trigger pulse to the waveform generator to initiate mechanical vibrations. After an appropriate delay to allow for wave propagation into the region of interest, the imaging procedure occurs, comprising a sequence of 90° excitation pulse, MEG, 180° refocusing pulse and the full *k*-space readout in the typical EPI fashion, as shown in Figure 2.3. The main disadvantage of EPI, however, is that the entire range of phase encoding steps are acquired in one TR, thus leading to a long readout time. This renders EPI susceptible to B_0 inhomogeneities which inevitably lead to image artefacts - especially in regions adjacent to air-filled cavities, such as the parts of the brain surrounding the paranasal sinuses.

An advance in the acquisition of brain MRE data was achieved through the development of a multi-shot multi-slab spiral MRE sequence [11]. The so-called spiral sequence can capture MRE displacement data in a shorter scan time by using multiple 3D volumes, or slabs, that cover the entire brain. Previous brain MRE studies have either compromised imaging coverage to maintain an acceptable scan time or employed reduced spatial resolutions to obtain full-brain coverage. The reduced number of imaging volumes allows for the use of a short TR to maximise SNR efficiency, whereas spiral filling of *k-space*, which have the entire readout after the echo time, enables shorter echo

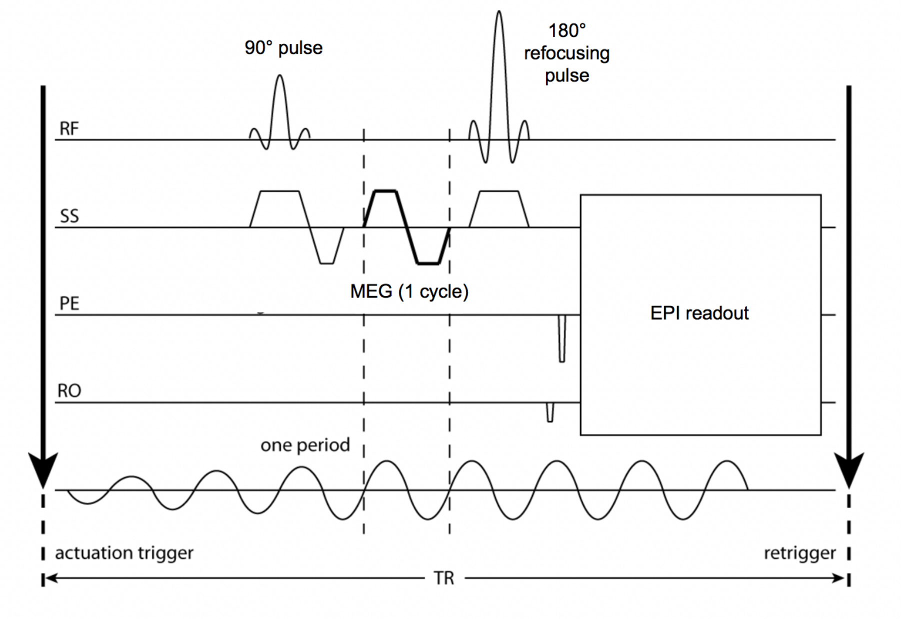

Figure 2.3: Diagram of a modified spin-echo EPI pulse sequence. Bipolar motion encoding gradients are shown on the slice-select (SS) axis. Two more acquisitions are required on the phase-encode (PE) and read-out (RO) axes so that full 3D information about the displacement vector field is recorded. In this example, only one MEG cycle is incorporated.

times resulting in less distortion from field inhomogeneities. MEGs are applied on either side of the refocusing pulse and before the in-plane spiral readout gradients. Following a second refocusing pulse, a low-resolution 3D navigator is acquired for motion-induced phase error correction. Correction for motion-induced phase errors has been shown to improve the quality of phase data with improved SNR and reduced slab-to-slab phase inconsistencies. The pulse sequence diagram is illustrated in Figure 2.4.

Once the time series has been acquired, the raw phase images undergo a number of processes prior to analysis, in order to remove unwanted noise contributions. The amplitude of vibration must be sufficient to produce waves deep within the brain [27]. However, too great an amplitude can create heavy *phase wrap*, particularly near the edges of the brain due to the phase of the wave shifting by more than 2π. Phase is bounded by the interval ($-\pi$, $+\pi$); if the original phase exceeds these limits, the measured phase will be wrapped back into this range, creating discontinuities in the data. These discontinuities can be eliminated using so-called phase unwrapping algorithms. Several unwrapping algorithms have been developed each with their own strengths and weaknesses relating to delivery of the exact solution, robustness to high noise, or full automation [36–38]. The tissue displacements encoded into the phase of the signal are then Fourier-transformed along the temporal axis to create

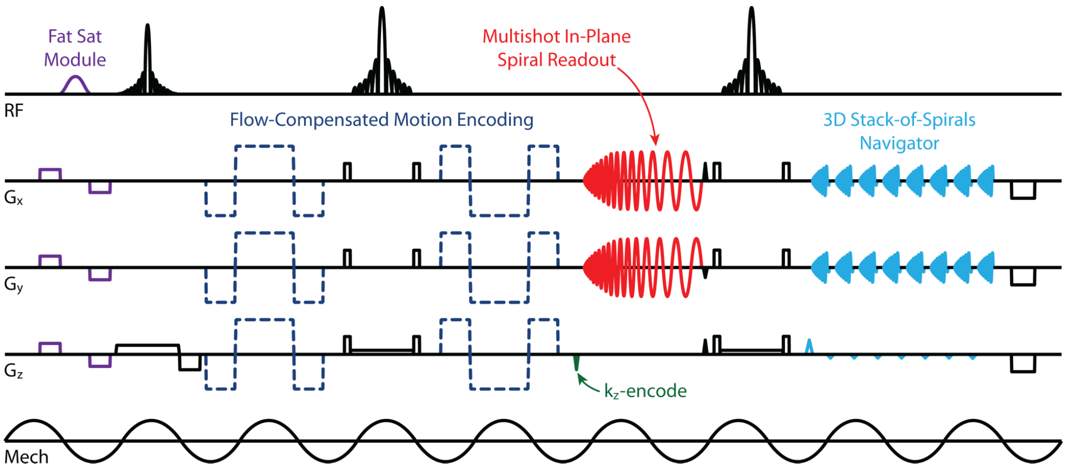
Fat Sat Module
Multishot In-Plane Spiral Readout
RF
Flow-Compensated Motion Encoding
3D Stack-of-Spirals Navigator
Gx
Gy
Gz
kz-encode
Mech

Figure 2.4: Diagram of MRE sequence incorporating multishot, variable-density spiral readout gradients for generating high-resolution displacement data. Bipolar motion encoding gradients (dashed) are shown on each gradient axis, though are only applied one at a time. Source: Johnson et al., 2014 [11].

a complex wave field in place of a time series. This procedure filters out noise and off-frequency behaviour, to isolate the harmonic motion of interest, see Figure 9.1. The tissue displacement data are then inverted through the equations of motion using an inversion algorithm, as described in the next section.

2.2.3 *MRE inversion*

Consider that the equation of conservation of linear momentum is:

$$\nabla \cdot \sigma = \rho \ddot{\mathbf{u}} \tag{2.20}$$

with ρ the density and u the displacement field. By substituting the isotropic stress-strain equation, as shown in Eq. 2.5, into this equation, provides the Navier-Cauchy equation. To do this, this equation needs to be rewritten in terms of displacements rather than stress and strain, to arrive at the displacement form of the Navier-Cauchy equation. If harmonic oscillations are considered, it can be assumed that $u(x,t) = \mathrm{Re}\{u^*(x)e^i\omega t\}$ and therefore use the harmonic form of the Navier-Cauchy equation, which governs motion in an isotropic, heterogeneous, viscoelastic solid:

$$-\rho\omega^2\mathbf{u}^* = \nabla \cdot (G^*(\nabla\mathbf{u}^* + \nabla\mathbf{u}^{*T}) + \nabla(\lambda^*\nabla \cdot \mathbf{u}^*) \tag{2.21}$$

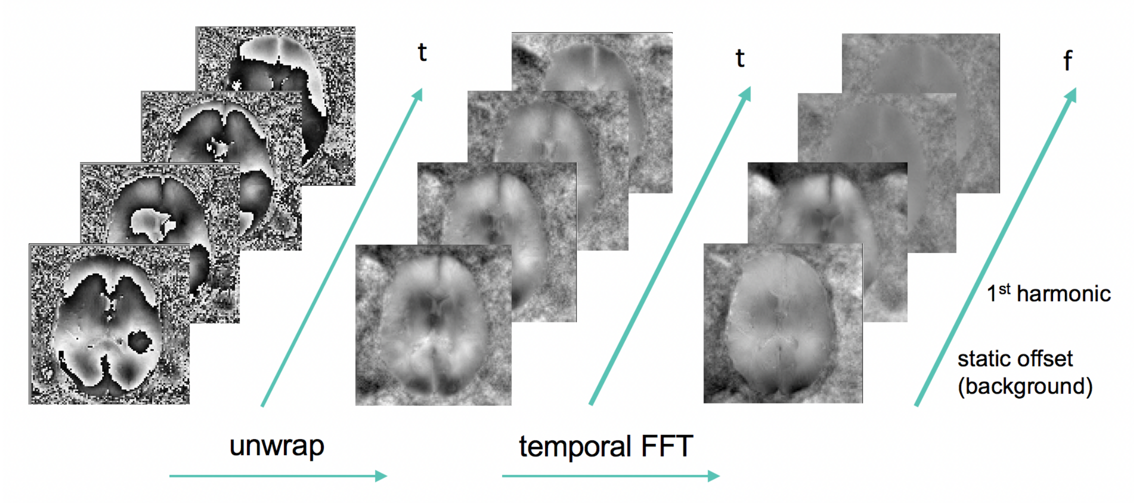

Figure 2.5: Phase unwrapping and fast Fourier transform (FFT) are a pre-requisite for all MRE phase images: (a) stack of raw wrapped phase images capturing the wave at different phases of the vibration cycle; (b) phase images have been unwrapped using the Laplacian-Based Estimate (LBE) algorithm (available within PhaseTools software [38]); (c) images are then temporally transformed. In the resulting frequency-resolved representation, the static offset is contained in the zero-frequency component, whereas the wave information falls into the first harmonic frequency image. The higher harmonic frequencies contain no information.

where G^* is the complex valued viscoelastic shear modulus, λ^* is the second Lamé parameter, ρ is the tissue density (~1000kg/m^3), $\boldsymbol{u}^*$ is the complex-valued amplitude of the harmonic vector displacement field, ∇ is the gradient operator, ^{T} represents tensor transposition, and ω the angular frequency, $\omega = 2\pi f$, where f is the applied mechanical frequency (Hz). Some groups solve this form of the equation, typically using finite-element based methods (FEM). The second Lamé parameter λ is approximately six orders of magnitude greater than G. Longitudinal waves travel at a high velocity (1540m/s) in soft tissue in the frequency range used in MRE, resulting in much longer wavelengths [39]. To solve this equation directly, a large value for λ is used with a stabilized incompressible finite element solution to model a nearly incompressible material - a reasonable assumption for the brain due to the large water content.

Another approach is to assume that the material is homogenous, treating G, λ, and ρ as locally constant, to arrive at the homogenous form of the equation for harmonic motion:

$$-\rho\omega^2\boldsymbol{u} = G\nabla^2\boldsymbol{u} + (\lambda + G)\nabla(\nabla \cdot \boldsymbol{u}) \tag{2.22}$$

For a nearly incompressible material, $\lambda \to \infty$ and $\nabla \cdot u \to 0$, which results in numerical issues for the second LHS term of equation 2.22 as $\infty \times 0$ is difficult to evaluate. High pass filtering techniques have been applied prior to inversion [27]. Alternatively, calculating the curl of the displacement field will also remove the compression terms. Other times, their contribution is simply ignored [27].

Once the bulk term has been removed, Eq 2.22 can be simplified to the Helmholtz-type equation:

$$-\rho\omega^2 \boldsymbol{u} = G\nabla^2 \boldsymbol{u} \tag{2.23}$$

This equation directly relates the measured displacements to the complex shear modulus G, by the angular frequency ω and the material density ρ, to allow direct algebraic inversion of shear wave data, (i.e. direct inversion).

These equations can be solved using techniques such as so-called direct inversion (DI - homogenous form - Eq. 2.23) and non-linear inversion (NLI - heterogeneous form Eq. 2.21). Additionally, further processing has been performed by utilising the DI equation across multiple frequencies to allow for viscoelastic modelling or multi-dual elasto-visco inversion (MDEV), as described in the next section.

Direct Inversion

Direct inversion (DI) calculates tissue mechanical properties by directly inserting the measured displacements into the appropriate wave equation governing the material, and was first introduced to MRE by Oliphant *et al.,* 2001 [2]. The constitutive equation of motion for an isotropic, homogeneous, viscoelastic material was found in Eq. 2.23. The central aspect of DI involves calculating the Laplacian, which requires estimating second order derivatives in space from the measured displacement data. This process is repeated for each displacement direction and used to solve G* using a least-squares approach, however the determination of spatial derivatives is particularly challenging in the presence of noise. The main drawback of a DI approach is the assumption that tissue mechanical properties are locally constant and contradicts what is known about brain anatomy; the brain is a heterogeneous structure whose different constituents likely have different non-linear, viscoelastic and anisotropic mechanical properties. Due to the violation of the heterogeneity assumption, values near interfaces are questionable, and heavy filtering is required to remove displacement contributions that do not fit the model of slowly varying material properties.

Non-linear inversion (NLI)

The alternative to direct inversion (DI) is the use of finite-element modelling (FEM) to perform so-called non-linear inversion (NLI). FEM is a numerical method of achieving approximate solutions to problems in solid mechanics using partial differential equations. FEM methods are known as the "forward problem", as prior knowledge of tissue geometry, boundary conditions, and mechanical properties are needed to initially build a model simulation [40,41]. NLI invokes a computational model of the mechanical motion of heterogeneous, isotropic, viscoelastic tissue (the forward problem - Eq. 2.16), and estimates a set of mechanical property parameters that best reproduces the measured displacements (the inverse problem) [40,42,43]. The process is repeated iteratively until the calculated displacements sufficiently match the measured displacements. Iterative methods use optimisation techniques, where an estimate of the unknown property distribution is iteratively updated, such that the displacements predicted by solution of the forward problem closely match the measured displacements.

More specifically, the optimisation problem is formulated in terms of minimizing an objective function (i.e. error function, Φ), which quantifies the difference between the measured displacements, ($\mathbf{u}_m$), and a set of displacements generated by a computational model of the system, ($\mathbf{u}_c$), with some estimate of the unknown material properties, ($\theta = [G',G'']$). Once the minimum of the error function Φ is reached and the computational model is the closest possible match to the measured data, the current estimate of Ω will be close to the true distribution, assuming that the forward model is a good match for the tissue's behaviour. The material property estimation is iteratively updated to minimize a mean-squared error cost function:

$$\Phi = \sum_{\Omega} ||\mathbf{u}_c(\theta) - \mathbf{u}_m||^2 \tag{2.24}$$

where the summation is over the physical domain of interest, Ω. The result of the reconstruction is a spatial map of the complex shear modulus G^*. Due to the enormous computational cost, minimization of Eq. 2.24 is reformatted in parallel as subzone subdomains of the full physical domain, Ω. The subzones are selected at random, properties are estimated on each subzone, and the results are reassembled in order to repeat with new zones until a global minimum is achieved allowing processing of the full-volume displacement data acquired. See Figure 2.6 for an illustration of the subzone concept.

The biggest limitation with NLI is that Gaussian smoothing is required to stabilise the inversion. This creates a large resel or effective resolution element, resulting in the loss of boundaries and interfaces. Further, NLI is computationally expensive with processing speed on the order of hours. This contrasts with direction inversion (DI) which can be performed within seconds. The ease of use and quick processing time partly explains the popularity of DI across the literature, as it would more readily allow brain MRE to fit within a typical clinical neuroimaging protocol.

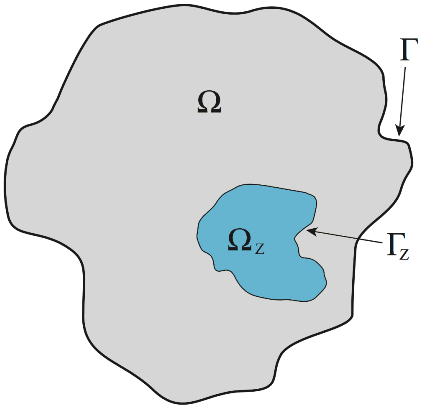

Figure 2.6: Schematic representation of subzone concept. The global problem domain is represented by Ω*, with boundary* Γ*. The subzone domain is represented by* Ωz*, with boundary* Γz*. Boundaries are chosen arbitrarily, allowing for the global problem domain to be broken up into a number of smaller sub-domains for more efficient computation. Source: McGarry et al., 2013a [44].*

Additional processing - Multi-frequency MRE

(i) Viscoelastic modelling

Mechanical properties derived from single wave frequency studies are a function of frequency, and therefore bound to specific experimental conditions. An alternative analysis technique has utilised the DI equation over multiple vibration frequencies in order to captures a wide spectrum of experimental results to improve the physical significance of MRE data [21, 22]. Multifrequency acquisitions have been acquired at, for example, 25, 37.5, 50 and 62.5 Hz, and the dispersion of waves across this frequency range are analysed for the ability to fit a prescribed rheological viscoelastic model. Viscoelastic models include the Maxwell model, Kelvin-Voigt model, and the Zener model, among others [45, 46]. The spring-dashpot parameter model has been determined to be the most suitable viscoelastic model for biological tissue, in which tissue is characterised by a hierarchical arrangement of elastic springs μ and viscous dashpots η [22]. While linear models do not show a power-law frequency dependence, shear moduli data can be fitted to a fractional spring-dashpot model:

$$G^* = \kappa(i \cdot 2\pi \cdot f)^\alpha \tag{2.25}$$

with $\kappa = \mu^{(1-\alpha)}\eta^\alpha$ yielding frequency independent elasticity μ, (not to be confused with shear stiffness, μ), frequency independent viscosity η and a tissue characterisation constant α. As μ and η

are co-dependent, η is assumed constant and assigned a value of 3.7 Pa - previously calculated as an approximate value of viscosity in human brain tissue [21]. Ultimately, two frequency-independent material parameters are reported. μ combines elasticity (stiffness) and viscosity (friction) in one parameter to describe the solid-fluid behaviour of the tissue, and is thus a measure of adhesion and soft tissue connectivity. The slope of the modulus dispersion is analysed to provide parameter α, which characterises the alignment of mechanical structure-building elements in the tissue. α is known as the *geometry* parameter due its correlation with the fractal dimension, indicating the sensitivity of α to material complexity [4]. As a side note, α is not comparable to the loss tangent ϕ, which in general is frequency dependent. However, in some complex and irregular materials, ϕ becomes less sensitive to frequency and thus $\phi = \alpha \times \pi/2$, may hold true [47]. In general, modelling may be able to improve the physical significance of MRE data, however, this approach does not readily fit into the framework of this thesis with the objective to acquire images with a high-spatial resolution.

(ii) Multi-frequency dual parameter elasto-visco inversion (MDEV)

Another alternative and innovative MRE analysis approach is to combine wave images from several actuation frequencies in one inversion [23]. Whereas the above mentioned modelling studies seek to determine the potential frequency dependence of tissue stiffness, MDEV is implicitly based on the assumption that the shear modulus is independent of the vibration frequency, i.e. $G^*=G^*(\mathbf{r})$ rather than $G^*(\mathbf{r},\omega)$.

The term dual, which forms part of the MDEV acronym, alludes to the fact that each parameter is retrieved from mutually independent calculation steps [48]. Making the usual assumptions such as homogeneity, linear viscoelasticity, and isotropy, both parameters provide just another representation of the storage and loss modulus usually parameterised in MRE. MDEV was created due to problems with single frequency schemes utilising direct inversion. Problems include inhomogeneous regions of interest due to standing wave nodes and attenuation; standing waves are characterised by nodes with zero displacement amplitude. In contrast, in MDEV inversion-based MRE, the information provided by frequency-resolved complex shear moduli is sacrificed for generating spatially highly resolved maps [49]. As a result, $|G^*|$ and ϕ refer to the amplitude and phase angle of the oscillatory response to a harmonic stress, respectively. In other words, the effective harmonic frequency of $|G^*|$ and ϕ is given by the mean of all vibration frequencies weighted by the wave amplitudes they produced. It is a true multifrequency inversion since the wave fields are first averaged over all components and frequencies before the division is performed [48]. For the mathematical calculation, the reader is referred to Streitberger *et al.,* 2014 [49]. Additionally, MDEV has been combined a new image processing pipeline known as the Elastography Software Pipeline (ESP) with the objective to preserve fine-scale image information [24]. One of the strengths of the analysis is the preservation of boundaries and interfaces due to regularisation in the wavelet domain using a complex dual-tree wavelet transform [50]; this approach does not force a window on the data and run the risk of losing useful information. ESP also applies a newly designed filter bank to extend the MDEV equations so that local directional spatial frequency information is used to weight the inversion at each voxel. MDEV and ESP, like single-frequency based DI, however, assumes local homogeneity, and thus the quantitative performance in heterogeneous tissue is expected to be limited.

2.3 *Determinants of brain stiffness*

The contributors to brain stiffness is an active field of research. Investigating the mechanical response of the mouse brain in disease models is a viable way to infer the relationship between MRE parameters and microstructural alterations, and promises to enhance the clinical utility of MRE. There is growing evidence that the following effects are relevant for brain mechanical parameters:

- demyelination of neurons
- inflammatory processes
- neuronal network density
- Aβ protein accumulation

Results are summarised in Table 2.2, and the studies which have performed these investigations are described in more detail below:

Table 2.2: Determinants of brain stiffness

Process	Population	Brain structure	Author(s)	Stiffness
Toxic demyelination	MS mice	Cerebrum	Schregel *et al.,* 2012 [51]	↓
Inflammation	EAE mice	Cerebrum	Riek *et al.,* 2012 [52]	↓
	EAE mice	Cerebellum	Millward *et al.,* 2015 [53]	↓
Reduced neuron density	MCAO mice	Cerebrum	Freimann *et al.,* 2013 [54]	↓
Neurogenesis	MPTP mice	Hippocampus	Klein *et al.,* 2014 [55]	↑
Amyloid (Aβ) plaques	APP23 mice	Hippocampus	Munder *et al.,* 2017 [56]	↑

2.3.1 *Demyelination and inflammation*

The first investigation into the biological correlates of MRE parameters was undertaken by Schregel *et al.,* 2012 [51] who induced reversible toxic demyelination in a mouse model of MS. Schregel *et al.,* 2012 demonstrated that stiffness decreases with both progressive demyelination and alterations in the structural integrity of the extracellular matrix. This work was supported by a follow up study by Riek *et al.,* 2012 [52] who performed MRE in a mouse model of experimental autoimmune encephalomyelitis (EAE). Higher levels of inflammation (perivascular T-cell infiltration) correlated with a decrease in stiffness in the cerebrum. Of note, EAE related decrease in brain stiffness was not correlated with demyelination but instead sensitive to the early inflammatory processes in the brain. In another EAS mouse model, Millward *et al.,* 2015 quantified macrophages and microglia cells in the cerebellum, and also found that increased levels of inflammation was associated with a reduction in tissue stiffness [53].

2.3.2 *Neuronal network density*

Two complementary MRE studies in mouse models suggest that brain stiffness correlates with the number of neurons. In a commonly used stroke model, Freimann *et al.,* 2013 demonstrated a clear correlation between brain tissue softening and reduced neuronal density after middle cerebral artery occlusion (MCAO) [54]. Neurons were counted histologically in both affected and contralateral hemispheres. Inducing neuronal loss with MCAO within one hemisphere was associated with a reduction in macroscopic brain stiffness, as shown in Figure 2.7 **A**. The second experiment employed a mouse model of Parkinsonism based on the administration of 1 methyl-4-phenyl-1,2,3,6-tetrahudropyidine hydrochloride (MPTP) to induce dopaminergic neurodegeneration and thus enhance neurogenesis [55]. Figure 2.7 **B** shows how enhanced proliferation of neurons in the hippocampus was associated with an increase in hippocampal stiffness. Taken together both studies shed light onto the important role of neurons as a supporting structure of the brain. Additionally, findings from single cell recordings suggest that neurons have higher stiffness than glial cells, which further supports the hypothesis that neurons establish the mechanical scaffold of the brain [57].

2.3.3 *Beta-amyloid (Aβ) protein accumulation*

In an established transgenic mouse model of AD, Munder *et al.,* 2017 reported a significant correlation between the stiffness of the hippocampus and the number of beta-amyloid (Aβ) cells in APP23 mice,

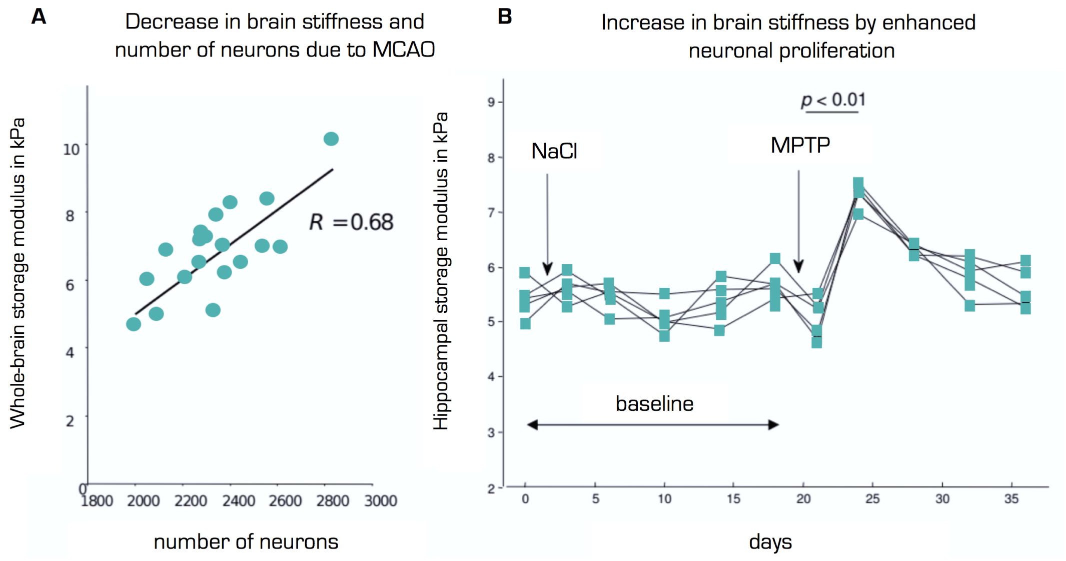

Figure 2.7: Correlation between the storage modulus G' and number of neurons in the murine brain; (a) a decrease in the number of neurons by middle cerebral artery occlusion (MCAO) correlates with a decline in G' [54]; (b) complementary to (a), the time course of G' in the hippocampal region in a Parkinson mouse model. MPTP was administered on day 20, causing a short-term increase in neuronal proliferation. The significant increase to G' on day 6 after injection followed by a decay to baseline values is correlated with the number of new neurons [55]. Graphs adapted from Hirsch et al., 2017 [48], and used with permission.

suggesting that the increased number of cells accumulating Aβ, may cause the rise in tissue stiffness [56]. Alternatively, the increase in hippocampal stiffness may be reflective of neurons undergoing apoptosis; it is expected that neurons undergoing programmed cell death, as a result of intracellular Aβ accumulation, will exhibit differing mechanical properties compared to healthy, fully functional neurons.

2.4 Conclusions

The brain has a large fluid component, resulting in a time lag between the stress and the resulting strain, which suggests that the brain is more accurately described by a viscoelastic model as opposed to an elastic model. Reported MRE output parameters for describing brain viscoelasticity are all derived from the complex shear modulus, and thus mathematically related to one another. The design of an MRE experiment includes considerations for the actuation, imaging and inversion components. In this chapter, many of the common elements of a brain MRE investigation have been outlined, which show how the acquisition and analysis pipelines can be wide-ranging. Finally, I describe how

MRE measurements can be related to biological events *in vivo*. In the next chapter, I will perform a systematic search of the literature to summarise results obtained to date concerning measurements for healthy participants. Due to the reporting of various forms of the complex shear modulus, all results will be mathematically converted to the same parameters of shear stiffness, μ and loss tangent, ϕ in order to provide a valid summary. I will also further consider the initial contribution brain MRE has had in characterising neurological disorders in clinical populations.

References

[1] L Hollis. Development of finite element analysis of magnetic resonance elastography to investigate its potential use in abdominal aortic aneurysms. *University of Edinburgh*, 2016.

[2] TE Oliphant, A Manduca, RL Ehman, and JF Greenleaf. Complex-valued stiffness reconstruction for magnetic resonance elastography by algebraic inversion of the differential equation. *Magn Reson Med*, 45:299–310, 2001.

[3] GH Paulino and ZH Jin. Correspondence principle in viscoelastic functionally graded materials. *J Appl Mech*, 68:129–132, 2000.

[4] J Guo, O Posnansky, S Hirsch, M Scheel, M Taupitz, J Braun, and I Sack. Fractal network dimension and viscoelastic powerlaw behavior: II. An experimental study of structure-mimicking phantoms by magnetic resonance elastography. *Phys Med Biol*, 57:4041–4053, 2012.

[5] O Posnansky, J Guo, S Hirsch, S Papazoglou, J Braun, and I Sack. Fractal network dimension and viscoelastic powerlaw behavior: I. A modeling approach based on a coarse-graining procedure combined with shear oscillatory rheometry. *Phys Med Biol*, 57:4023–4040, 2012.

[6] I Sack, K Johrens, J Wurfel, and J Braun. Structure-sensitive elastography: on the viscoelastic powerlaw behavior of in vivo human tissue in health and disease. *Soft Matter*, 9:5672–5680, 2013.

[7] L Xu, Y Lin, ZN Xi, H Shen, and PY Gao. Magnetic resonance elastography of the human brain: a preliminary study. *Acta Radiol*, 48:112–115, 2007.

[8] J Braun, J Guo, R Lützkendorf, J Stadler, S Papazoglou, S Hirsch, I Sack, and J Bernarding. High-resolution mechanical imaging of the human brain by three-dimensional multifrequency magnetic resonance elastography at 7T. *NeuroImage*, 90:308 − 314, 2014.

[9] I Sack, B Beierbach, U Hamhaber, D Klatt, and J Braun. Non-invasive measurement of brain viscoelasticity using magnetic resonance elastography. *NMR Biomed*, 21:265–271, 2008.

[10] A Lipp, R Trbojevic, F Paul, A Fehlner, S Hirsch, M Scheel, C Noack, J Braun, and I Sack. Cerebral magnetic resonance elastography in supranuclear palsy and idiopathic Parkinson's disease. *Neuroimage Clin*, 3:381–387, 2013.

[11] CL Johnson, JL Holtrop, MDJ McGarry, JB Weaver, KD Paulsen, JG Georgiadis, and BP Sutton. 3D multislab, multishot acquisition for fast, whole-brain MR elastography with high signal-to-noise efficiency. *Magn Reson Med*, 71:477–485, 2014.

[12] J Huston, MC Murphy, BF Boeve, N Fattahi, A Arani, KJ Glaser, A Manduca, DT Jones, and RL Ehman. Magnetic Resonance Elastography of Frontotemporal Dementia. *J Magn Reson Imaging*, 43:474–8, 2015.

[13] J Guo, S Hirsch, A Fehlner, S Papazoglou, M Scheel, J Braun, and I Sack. Towards an elastographic atlas of brain anatomy. *PLoS One*, 8:e71807, 2013.

[14] A Fehlner, S Papazoglou, M D McGarry, K D Paulsen, J Guo, K-J Streitberger, S Hirsch, J Braun, and I Sack. Cerebral multifrequency MR elastography by remote excitation of intracranial shear waves. *NMR Biomed*, 28:1426–1432, 2015.

[15] D Klatt, CL Johnson, and RL Magin. Simultaneous, multidirectional acquisition of displacement fields in magnetic resonance elastography of the in vivo human brain. *J Magn Reson Imaging*, 42:297–304, 2015.

[16] JB Weaver, AJ Pattison, MD McGarry, IM Perreard, JG Swienckowski, CJ Eskey, SS Lollis, and KD Paulsen. Brain mechanical property measurement using MRE with intrinsic activation. *Phys Med Biol*, 57:7275–7287, 2012.

[17] MDJ McGarry, CL Johnson, BP Sutton, JG Georgiadis, EEW Van Houten, AJ Pattison, JB Weaver, and KD Paulsen. Suitability of poroelastic and viscoelastic mechanical models for high and low frequency MR elastography. *Med Phys*, 42:947–957, 2015.

[18] EC Ehman, PJ Rossman, SA Kruse, AV Sahakian, and KJ Glaser. Vibration safety limits for magnetic resonance elastography. *Phys Med Biol*, 53:925–935, 2008.

[19] S Papazoglou, U Hamhaber, J Braun, and I Sack. Algebraic Helmholtz inversion in planar magnetic resonance elastography. *Phys Med Biol*, 53:3147–3158, 2008.

[20] TL Szabo and J Wu. A model for longitudinal and shear wave propagation in viscoelastic media. *J Acoust Soc Am*, 107:2437–2446, 2000.

[21] D Klatt, U Hamhaber, P Asbach, J Braun, and I Sack. Noninvasive assessment of the rheological behavior of human organs using multifrequency MR elastography: a study of brain and liver viscoelasticity. *Phys Med Biol*, 52:7281, 2007.

[22] I Sack, B Beierbach, J Wuerfel, D Klatt, U Hamhaber, S Papazoglou, P Martus, and J Braun. The impact of aging and gender on brain viscoelasticity. *NeuroImage*, 46:652–657, 2009.

[23] S Papazoglou, S Hirsch, J Braun, and I Sack. Multifrequency inversion in magnetic resonance elastography. *Phys Med Biol*, 57:2329–2346, 2012.

[24] E Barnhill, L Hollis, I Sack, J Braun, PR Hoskins, P Pankaj, C Brown, EJR van Beek, and N Roberts. Nonlinear multiscale regularisation in MR elastography: Towards fine feature mapping. *Med Image Anal*, 35:133–145, 2016.

[25] RR Edelman and S Warach. Magnetic Resonance Imaging. *N Engl J Med*, 328:708–716, 1993.

[26] T Dunn and S Majumdar. Comparison of motion encoding waveforms for magnetic resonance elastography at 3T. *Conf Proc IEEE Eng Med Biol Soc*, 7:7405–7408, 2005.

[27] A Manduca, TE Oliphant, MA Dresner, JL Mahowald, SA Kruse, E Amromin, JP Felmlee, JF Greenleaf, and RL Ehman. Magnetic resonance elastography: Non-invasive mapping of tissue elasticity. *Med Image Anal*, 5:237–254, 2001.

[28] YK Mariappan, KJ Glaser, and RL Ehman. Magnetic resonance elastography: a review. *Clin Anat*, 23:497–511, 2010.

[29] U Hamhaber, I Sack, S Papazoglou, J Rump, D Klatt, and J Braun. Three-dimensional analysis of shear wave propagation observed by in vivo magnetic resonance elastography of the brain. *Acta Biomater*, 3:127–137, 2007.

[30] L Xu, Y Lin, JC Han, ZN Xi, H Shen, and PY Gao. Magnetic resonance elastography of brain tumors: preliminary results. *Acta Radiol.*, 48:327–330, 2007.

[31] SA Kruse, GH Rose, KJ Glaser, A Manduca, JP Felmlee, CR Jack Jr, and RL Ehman. Magnetic resonance elastography of the brain. *NeuroImage*, 39:231–237, 2008.

[32] MC Murphy, 3rd J Huston, CR Jack Jr, KJ Glaser, A Manduca, JP Felmlee, and RL Ehman. Decreased brain stiffness in Alzheimer's disease determined by magnetic resonance elastography. *J Magn Reson Imaging*, 34:494–498, 2011.

[33] J Zhang, MA Green, R Sinkus, and LE Bilston. Viscoelastic Properties of Human Cerebellum using Magnetic Resonance Elastography. *J Biomech*, 44:1909–1913, 2011.

[34] CL Johnson, MDJ McGarry, EEW Van Houten, JB Weaver, KD Paulsen, BP Sutton, and JG Georgiadis. Magnetic resonance elastography of the brain using multishot spiral readouts with self-navigated motion correction. *Magn Reson Med*, 70:404–412, 2013a.

[35] CL Johnson, MDJ McGarry, AA Gharibans, JB Weaver, KD Paulsen, H Wang, WC Olivero, BP Sutton, and JG Georgiadis. Local mechanical properties of white matter structures in the human brain. *NeuroImage*, 79:145–152, 2013b.

[36] MA Schofield and Y Zhu. Fast phase unwrapping algorithm for interferometric applications. *Opt Lett*, 28:1194–1196, 2003.

[37] MA Herráez, DR Burton, MJ Lalor, and MA Gdeisat. Fast two-dimensional phase-unwrapping algorithm based on sorting by reliability following a noncontinuous path. *Appl Opt*, 41:7437–7444, 2002.

[38] E Barnhill, P Kennedy, CL Johnson, M Mada, and N Roberts. Real-time 4D phase unwrapping applied to magnetic resonance elastography. *Magn Reson Med*, 73:2321–2331, 2015.

[39] R Sinkus, J-L Daire, BE Van Beers, and V Vilgrain. Elasticity reconstruction: Beyond the assumption of local homogeneity. *C R Mecanique*, 338:474–479, 2010.

[40] EEW Van Houten, KD Paulsen, MI Miga, FE Kennedy, and JB Weaver. An overlapping subzone technique for MR-based elastic property reconstruction. *Magn Reson Med*, 42:779–786, 1999.

[41] MDJ McGarry, EEW Van Houten, CL Johnson, JG Georgiadis, BP Sutton, JB Weaver, and KD Paulsen. Multiresolution MR elastography using nonlinear inversion. *Med Phys*, 39:6388–6396, 2012.

[42] EEW Van Houten, MI Miga, JB Weaver, FE Kennedy, and KD Paulsen. Three-dimensional subzone-based reconstruction algorithm for MR elastography. *Magn Reson Med*, 45:827–837, 2001.

[43] EEW Van Houten, DvR Viviers, MDJ McGarry, PR Perrinez, II Perreard, JB Weaver, and KD Paulsen. Subzone based magnetic resonance elastography using a Rayleigh damped material

model. *Med Phys*, 38:1993–2004, 2011.

[44] MDJ McGarry. Improvement and Evaluation of Nonlinear Inversion MR Elastography. *Dartmouth College*, 2013a.

[45] H Schiessel, R Metzler, A Blumen, and TF Nonnenmacher. Generalized viscoelastic models: their fractional equations with solutions. *J Phys A Math Gen*, 28:6567, 1995.

[46] P Asbach, D Klatt, U Hamhaber, J Braun, R Somasundaram, B Hamm, and I Sack. Assessment of liver viscoelasticity using multifrequency MR elastography. *Magn Reson Med*, 60:373–379, 2008.

[47] K Urayama, T Kawamura, and S Kohjiya. Structure-mechanical property correlations of model siloxane elastomers with controlled network topology. *Polymer*, 50:347–356, 2009.

[48] S Hirsch, J Braun, and I Sack. *Magnetic Resonance Elastography: Physical Background and Medical Applications*. Weinheim: Wiley-VCH, 2017.

[49] K-J Streitberger, M Reiss-Zimmermann, FB Freimann, S Bayerl, J Guo, F Arlt, J Wuerfel, J Braun, K-T Hoffmann, and I Sack. High-Resolution Mechanical Imaging of Glioblastoma by Multifrequency Magnetic Resonance Elastography. *PLoS One*, 9:e110588, 2014b.

[50] IW Selesnick, RG Baraniuk, and NC Kingsbury. The dual-tree complex wavelet transform. *IEEE Signal Process Mag*, 22:123–151, 2005.

[51] K Schregel, E Wuerfel née Tysiak, P Garteiser, I Gemeinhardt, T Prozorovski, O Aktas, H Merz, D Petersen, J Wuerfel, and R Sinkus. Demyelination reduces brain parenchymal stiffness quantified in vivo by magnetic resonance elastography. *Proc Natl Acad Sci USA*, 109:6650–6655, 2012.

[52] K Riek, JM Millward, I Hamann, S Mueller, CF Pfueller, F Paul, J Braun, C Infante-Duarte, and I Sack. Magnetic resonance elastography reveals altered brain viscoelasticity in experimental autoimmune encephalomyelitis. *NeuroImage: Clin*, 1:81–90, 2012.

[53] JM Millward, J Guo, D Berndt, J Braun, I Sack, and C Infante-Duarte. Tissue structure and inflammatory processes shape viscoelastic properties of the mouse brain. *NMR Biomed*, 28:831–839, 2015.

[54] FB Freimann, S Muller, K Streitberger, J Guo, S Rot, A Ghori, P Vajkoczy, R Reiter, I Sack, and J Braun. MR elastography in a murine stroke model reveals correlation of macroscopic viscoelastic properties of the brain with neuronal density. *NMR Biomed*, 26:1534–1539, 2013.

[55] C Klein, EG Hain, J Braun, K Riek, S Mueller, B Steiner, and I Sack. Enhanced adult neurogenesis increases brain stiffness: in vivo magnetic resonance elastography in a mouse model of dopamine depletion. *PLoS One*, 9:e92582, 2014.

[56] T Munder, A Pfeffer, S Schreyer, J Guo, J Braun, I Sack, B Steiner, and C Klein. MR elastography detection of early viscoelastic response of the murine hippocampus to amyloid beta accumulation and neuronal cell loss due to Alzheimer's disease. *J Magn Reson Imaging*, 2017.

[57] Y Lu, K Franze, G Seifert, C Steinhäuser, F Kirchhoff, H Wolburg, J Guck, P Janmey, E Wei, J Käs, and A Reichenbach. Viscoelastic properties of individual glial cells and neurons in the CNS. *Proc Natl Acad Sci USA*, 103:17759–17764, 2006.

Chapter 3

Literature review on Brain Magnetic Resonance Elastography

Plan for the Chapter

Magnetic resonance elastography (MRE) of the liver has had success as a diagnostic marker, in part due to establishing cut-off values for the healthy liver and stages of fibrosis. The purpose of this chapter is to establish whether MRE quantitative measurements can be established for the brain in healthy participants. A systematic literature review is performed according to the Preferred Reporting Items for Systematic Reviews and Meta-Analyses (PRISMA) guidelines, to identify studies that have specifically utilised MRE to investigate the human brain. From the data identified from these studies, reference values for the mechanical properties of the brain will be provided in healthy participants for: 1) global brain tissue (GBT); 2) grey matter (GM) and white matter (WM), and 3) lobar regions (i.e. frontal lobe, temporal lobe, etc.). A further aim of this literature review is also to identify studies that have performed preliminary clinical investigations, and thus the extent to which MRE has revealed significant alterations to the brain in patients with neurological disorders is assessed and discussed in terms of known pathophysiology.

3.1 Introduction

An increasing body of research has now investigated the use of MRE to study the mechanical properties of the brain *in vivo*. As highlighted in the previous chapter, MRE research groups use different methods and report alternative MRE-derived variables, thus results must be standardised according to the same parameter to represent the same underlying mechanical response. Shear stiffness, μ, describes the resistance of a material to a harmonic shear stress at the given actuation frequency, and is related to the wavespeed in a viscoelastic material with density of 1000kg/m^3 [1,2]. The relationship between μ and the complex shear modulus $|G^*|$, was defined in *Chapter 2 - Table 2.1.* For studies that have reported spring-pot modelling parameters μ and α, shear stiffness, μ can be calculated from $|G^*|$ at any frequency (for the purpose of this review, 50 Hz is chosen). Results are converted to the shear stiffness, μ as opposed to $|G^*|$, as it provides the most data to summarise and review. Studies that typically report μ do not usually include values for G' and G'', rendering it impossible to calculate $|G^*|$. Furthermore, μ describes the effective *stiffness* in a viscoelastic material and is a concept more readily understood. Where possible, the loss tangent (G''/G') will also be calculated, with a great

---

This chapter contains material previously published, and is reprinted with permission. LV Hiscox, CL Johnson, E Barnhill, MDJ McGarry, J Huston III, EJR van Beek, JM Starr, N Roberts. Magnetic Resonance Elastography (MRE) of the Human Brain: Technique, Findings, and Clinical Applications. *Phys Med Bio*, **61**, R401-R437. The published version can be found in **Appendix I.**

angle indicating more dissipative (i.e. viscous) behaviour.

3.2 Methods

Search Strategy - All searches were performed on 9th August 2016. Search terms related to Magnetic Resonance Elastography (MRE) and the brain were included. Search filters included keyword, title and abstract information. Relevant publications were identified through searches of Medline (including work in progress from 1946 until 9th August 2016), Embase (1980 until 9th August 2016), and Web of Science (1900 until 9th August 2016). Articles with any combination of any of the MRE terms and any brain term were reviewed. The full search strategy can be found in **Appendix II.**

Data Extraction - A breakdown of the full review process is presented in Figure 3.1. A PRISMA (Preferred Reporting Items for Systematic Reviews and Meta-Analyses) Flow Diagram was used to report the number of records identified and summarise those included and excluded [3]. A total of 1101 articles were identified. After duplicates were removed, the titles and abstracts of 765 articles were screened for eligibility. 652 were excluded on review of title and/or abstract (for example MRE applied to other organs such as liver, to a murine model or phantom, or other MRI methods (excluding MRE) used to investigate the brain). One hundred and thirteen articles considered to be relevant were retrieved and assessed for agreement between two independent researchers, with the following inclusion and exclusion criteria:

Inclusion criteria - This review aimed to include all published studies that utilised MRE and reported the acquisition and analysis methods used to determine tissue mechanical properties of the human brain in healthy volunteers and/or patients with neurological disorders.

Exclusion criteria - (i) Unpublished studies, dissertations, theses, conference abstracts and poster presentations, (ii) editorials or comments in journals, (iii) MRE review articles, (iv) MRE applied to phantoms, (v) MRE applied to murine or other animal models, (vi) non-English articles, (vii) *ex-vivo* studies, (viii) engineering advancements in the technical design of MRE, (ix) MRE safety studies, (x) MRE applied to tissues/organs other than brain, (xi) studies with $n < 2$ subjects. Seventy-two studies were then excluded at this stage due to not being relevant to the research aims.

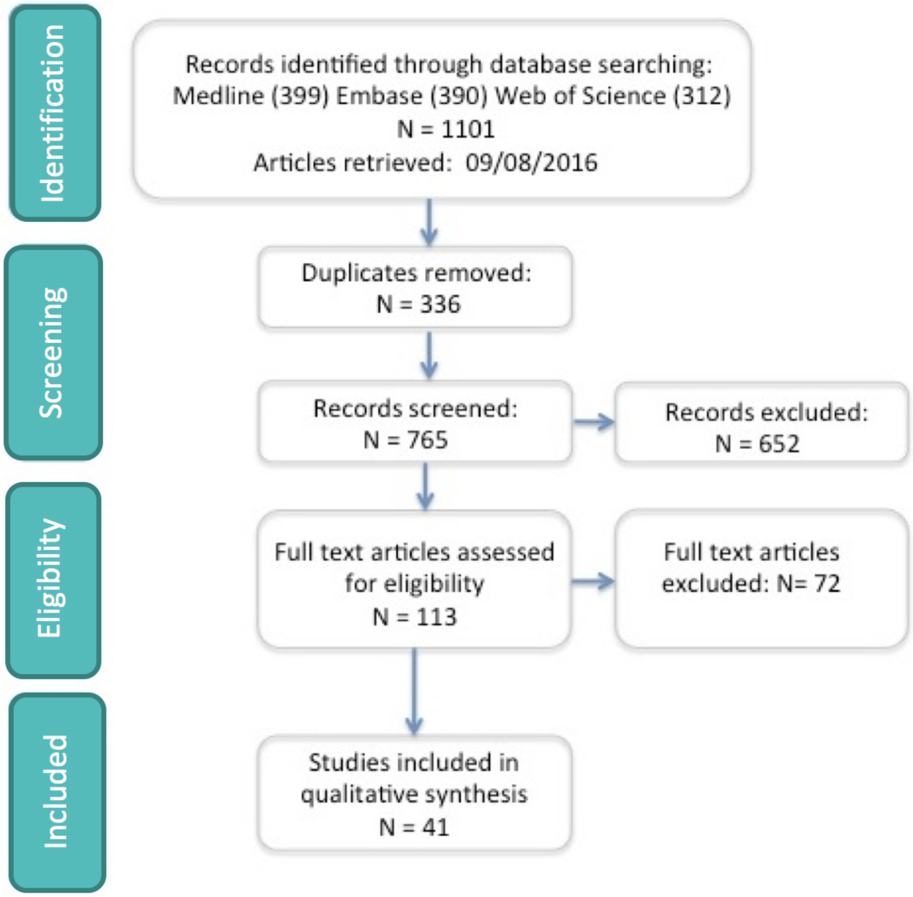
Identification
Records identified through database searching:
Medline (399) Embase (390) Web of Science (312)
N = 1101
Articles retrieved: 09/08/2016
Screening
Duplicates removed:
N = 336
Records screened:
N = 765
Records excluded:
N = 652
Eligibility
Full text articles assessed for eligibility
N = 113
Full text articles excluded: N= 72
Included
Studies included in qualitative synthesis
N = 41

Figure 3.1: PRISMA flow diagram showing manuscript selection

3.3 Results from literature review

3.3.1 *Studies identified*

Forty-one studies referring to MRE investigations performed in a total of 914 subjects met the inclusion criteria. The corresponding authors represented MRE research groups in four different countries: USA, Germany, Australia, and China. Twenty-four studies utilised MRE in the study of healthy participants, see Table 3.1, and seventeen studies investigated neurological disorders in patient populations, see Table 3.2. Ten of the seventeen clinical studies included a control group of healthy participants.

Table 3.1: Twenty-four MRE studies which have investigated the mechanical properties of the human brain in healthy participants.

Author	Brain structure	N	Age range
Klatt *et al.*, 2007 [4]	GBT	5	25-46
Sack *et al.*, 2008 [5]	GBT	6	34.5*
Sack *et al.*, 2009 [6]	GBT	55	18-88
Weaver *et al.*, 2012 [7]	GBT	6	22-55
Hatt *et al.* 2015 [8]	GBT	9	32.6*
Dittmann *et al.*, 2015 [9]	GBT	8	25-54
Sack *et al.*, 2011 [10]	GBT & inner, cortical, frontal, dorsal regions	66	18-72
Murphy *et al.*, 2013b [11]	GBT & frontal, occipital, parietal, temporal lobes, cerebellum, deep GM/WM	10	23-55
Arani *et al.*, 2015 [12]	GBT & frontal, occipital, parietal, temporal lobes, cerebellum, deep GM/WM	45	56-89
McCracken *et al.*, 2005 [13]	GM & WM	6	n/a
Xu *et al.*, 2007a [14]	GM & WM	3	28-32
Green *et al.*, 2008 [15]	GM & WM	5	23-61
Kruse *et al.*, 2008 [16]	GM & WM	25	23-79
Clayton *et al.*, 2012 [17]	GM & WM	6	19-42
Johnson *et al.*, 2013a [18]	GM & WM	3	24-52
Braun *et al.*, 2014 [19]	GM & WM	5	26-55
Zhang *et al.*, 2011 [20]	GM & WM & cerebellum	8	22-43
Johnson *et al.*, 2013b [21]	GM & WM, corpus callosum, corona radiata	6	24-52
Johnson *et al.*, 2014 [22]	GM & WM, brain stem, cerebellum	3	26-38
Romano *et al.*, 2012 [23]	Corticospinal tract	5	25-50
Guo *et al.*, 2013 [24]	WM, thalamus, corpus callosum genu, caudate nucleus	23	22-72
Fehlner *et al.*, 2015 [25]	Crus cerebri, capsula interna, pons	12	27-54
Johnson *et al.*, 2016 [2]	Amygdala, hippocampus, putamen, caudate, pallidum, thalamus	28	18-33
Schwarb *et al.*, 2016 [26]	Hippocampus, parahippocampal gyrus, entorhinal cortex	20	18-33

GBT= Global Brain Tissue, WM = White Matter, GM= Grey Matter

*Mean age of subjects.

Table 3.2: Seventeen MRE studies which have investigated the mechanical properties of the human brain in patient populations

Author	Disorder	Brain structure	Population	N	Age range
Xu *et al.*, 2007b [27]	Intracranial tumours (various)	GBT	Patients	6	16-63
Murphy *et al.*, 2013a [28]	Meningioma	TR	Patients	12	n/a
Simon *et al.*, 2013 [29]	Intracranical tumours (various)	TR, HRT	Patients	16	26-78
Reiss-Zimmermann *et al.*, 2014 [30]	Intracranical tumours (various)	TR, HRT	Patients	27	36-86
Streitberger *et al.*, 2014b [31]	Glioblastoma Multiforme	TR, HRT	Patients	22	64.5*
Hughes *et al.* 2015 [32]	Meningioma	TR	Patients	14	59*
Wuerfel *et al.* 2010 [33]	Multiple sclerosis (Relapse-Remitting)	GBT	Patients	45	21-51
			Controls	34	18-59
Murphy *et al.* 2011 [34]	Alzheimer's disease	GBT	Patients	7	76-94
			Controls	14	75-89
Streitberger *et al.*, 2010 [35]	Normal Pressure Hydrocephalus	GBT	Patients	20	69.1*
			Controls	25	62.1*
Freimann *et al.*, 2012 [36]	Normal Pressure Hydrocephalus (pre/post shunt)	GBT	Patients	20	51-85
Streitberger *et al.*, 2012 [37]	Multiple sclerosis (Chronic-Progressive)	GBT	Patients	23	51.5*
			Controls	38	48*
Lipp *et al.*, 2013 [38]	Parkinson's disease & Progressive Supra-nuclear Palsy	GBT, basal ganglia	PD Patients	18	63*
			PSP Patients	16	70*
			Controls	18	64*
Romano *et al.*, 2014 [39]	Amyotropic lateral sclerosis	Corticospinal tract	Patients	14	46-70
			Controls	14	45-69
Huston *et al.*, 2015 [40]	Fronto-temporal dementia	GBT, frontal, occipital, parietal temporal lobes, cerebellum, deep GM/WM, sensory/motor strip	Patients	5	53-65
			Controls	9	55-66
Fattahi *et al.*, 2015 [41]	Normal Pressure Hydrocephalus	GBT, frontal, occipital, parietal temporal lobes, cerebellum, deep GM/WM	Patients	10	67-79
			Controls	21	67-80
Fehlner *et al.*, 2016 [42]	Clinically Isolated Syndrome	GBT, WM	Patients	17	22-47
			Controls	33	18-53
Murphy *et al.*, 2016 [43]	Alzheimer's disease & Mild Cognitive Impairment (MCI)	GBT, frontal, occipital, parietal temporal lobes, cerebellum, deep GM/WM, sensory/motor, FPT	AD patients	8	n/a
			MCI patients	8	n/a
			CN + controls	16	n/a
			CN - controls	16	n/a

3.4 Brain MRE results in healthy subjects

3.4.1 *MRE results for global brain tissue (GBT)*

Table 3.3 shows mean MRE values for GBT in healthy subjects from 12 studies, and converted to μ (kPa) and ϕ (rad), where possible. Values for μ range between 0.62 - 2.99 kPa, with a mean value of 2.07 kPa ± 0.42 kPa at 50 Hz, see Figure 3.2 **A**. Lower stiffness values are apparent at lower frequencies, which can be attributed to the fact that biological tissue exhibits a frequency-dependent response [44]. To investigate the effect of frequency on μ, mean values from all studies was averaged at each frequency, and calculated from spring-pot studies at all four frequencies (25, 37.5, 50 and 62.5 Hz). A simple linear regression analysis was performed to determine the relationship between μ and actuation frequency for GBT in healthy participants. A significant regression equation was found (F(1, 4) = 15.31, $p = 0.02$, with an R^2 of 0.793. Participants' predicted μ is equal to 0.44 + 0.04 (frequency) (kPa) when frequency is measured in Hz, equating to an increase in brain stiffness of 0.4 kPa for each 10 Hz increase in frequency. Studies that employ alternative frequencies should bear this in mind when making comparisons with other research groups. I should, however, mention that subject age is also likely to contribute to variations to mechanical properties, as reported in a number of studies [6,10,12].

Table 3.3: MRE studies investigating GBT in healthy participants

Author	Inversion	f in Hz	μ (kPa)	ϕ (rad)
Dittmann *et al.,* 2015	MDEV	10, 15, 20	0.62 ± 0.08	0.09 ± 0.17
		10, 20, 30, 40, 50	1.38 ± 0.20	.24 ± 0.10
Hatt *et al.,* 2015	DI	30	1.03 ± 0.09	0.70 ± 0.21
Sack *et al.,* 2009	MF-SP	50	1.69 ± 0.26	0.38 ± 0.06
Wuerfel *et al.,* 2010*	MF-SP	50	1.82 ± 0.22	0.38 ± 0.08
Streitberger *et al.,* 2011*	MF-SP	50	2.30 ± 0.30	0.47 ± 0.12
Sack *et al.,* 2011	MF-SP	50	2.52 ± 0.32	0.47 ± 0.07
Lipp *et al.,* 2013*	DI	50	2.05 ± 0.19	0.26 ± 0.04
Murphy *et al.,* 2013b	DI	60	2.99 ± 0.02	n/a
Arani *et al.,* 2015	DI	60	2.59 ± 0.10	n/a
Huston *et al.,* 2015*	DI	60	2.76 ± 0.08	n/a
Fattahi *et al.,* 2015*	DI	60	2.55 ± 0.11	n/a
Murphy *et al.,* 2016*	DI	60	2.51 ± 0.09	n/a

Values show mean ± standard deviation (SD). *Control data from clinical studies. n/a = not available.

Calculation of ϕ for GBT was possible in six studies, where values range between 0.09rad - 0.70

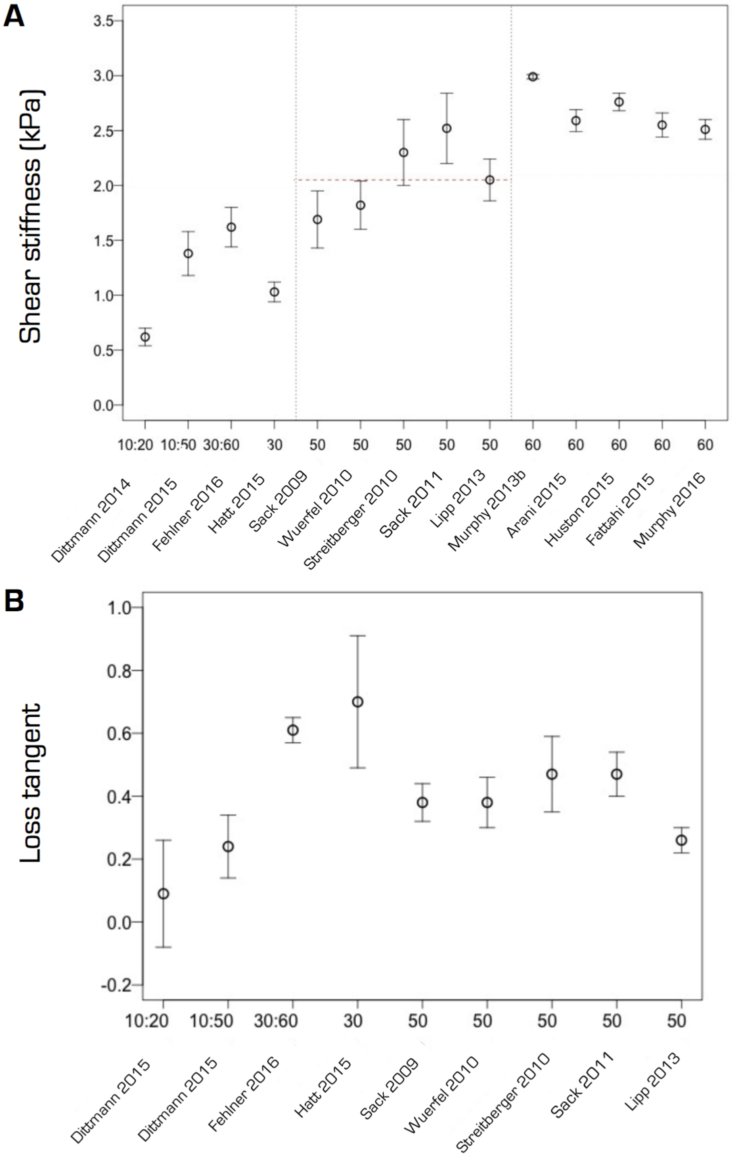

Figure 3.2: (a) shear stiffness, μ (kPa) and (b) loss tangent, ϕ (rad) of global brain tissue (GBT) in healthy participants. Values show mean and standard deviation (SD). First x-axis displays the actuation frequency f, secondary axis displays study reference.

rad with a mean value of 0.41 rad ± 0.06 rad at 50 Hz, see Figure 3.2 **B**. A wide disparity of values is evident, which may be attributed to variation in frequency and MRE methodology. For example, Dittmann *et al.,* 2015 [9] used low frequencies for MDEV inversion (10-20 Hz) and a revised calculation of ϕ to account for systemic noise bias and tissue heterogeneities, with the authors suggesting that previous values may have been overestimated [19, 45].

3.4.2 *Grey and white matter results*

MRE values for GM and WM for healthy participants were reported in 10 studies, however, quantitative data is only available for 8 of the 10 studies. Exclusion of two studies is due to one study providing a qualitative analysis of wave propagation [14], whereas data from only 1 subject is provided in the other [22]. Results are presented in Table 3.4.

Nine out of the 10 studies reported WM to be stiffer than GM, with 6 of these studies finding a statistically significant difference between the two types of tissue. This difference is interpreted to be due to the fact that WM primarily consists of tightly aligned myelinated highly orientated axons, whereas grey matter is largely composed of cell bodies, unmyelinated axons and neuroglia [46]. In contrast, one study reported that GM was stiffer than WM [15]. Potential explanations for this anomaly include the utilisation of a bite-bar actuator, which may not be effective at transmitting waves into the very centre of the brain, with low motion affecting SNR and resulting measurements. Interestingly, it has been suggested that cell body density has a larger impact on local tissue stiffness than cell stiffness itself [47]. The fact that MRE reports greater WM stiffness is not surprising due to the global measurement of an entire organ, where WM fibres are dense and compact. In contrast, GM has been found to be stiffer than WM on an individual cell level [48]. GM contains more (stiffer) neuronal cell bodies that WM, whereas WM is dominated by softer neuronal and glial cell processes; thus on alternative scales, mechanical properties of tissue may vary.

Table 3.4: MRE studies investigating GM and WM in healthy participants

Author	Approach	f in Hz	GM		WM	
			μ (kPa)	ϕ (rad)	μ (kPa)	ϕ (rad)
Braun *et al.,* 2014	MDEV	30, 40, 50, 60	0.98±0.25	0.95±0.03	1.16±0.29	1.03±0.04
Johnson *et al.,* 2013b	NLI	50	2.01±0.08	0.37±0.18	2.86±0.13	0.46±0.15
Johnson *et al.,* 2013a	NLI	50	2.41±0.19	0.48±0.17	3.30±0.35	0.52±0.20
Clayton *et al.,* 2012	LFE	60	3.77±0.50	0.50±0.27	4.16±0.17	0.54±0.08
McCracken *et al.,* 2005	DI	80	5.30±1.30	n/a	10.70±1.40	n/a
Zhang *et al.,* 2011	DI	80	2.72±0.22	0.44±0.14	2.85±0.36	0.47±0.28
Green *et al.,* 2008	DI	90	4.48±0.31	0.68±0.10	4.24±0.31	0.75±0.10
Kruse *et al.,* 2008	LFE	100	5.22±1.15	n/a	13.60±3.19	n/a

Values show mean ± standard deviation (SD). n/a = not available.

Values of μ for GM range between GM 0.98 kPa - 5.30 kPa, and for WM 1.16 kPa - 13.60 kPa, see Figure 3.3 **A**. At 50 Hz, mean GM stiffness is 2.29 kPa and WM stiffness is 3.21 kPa,

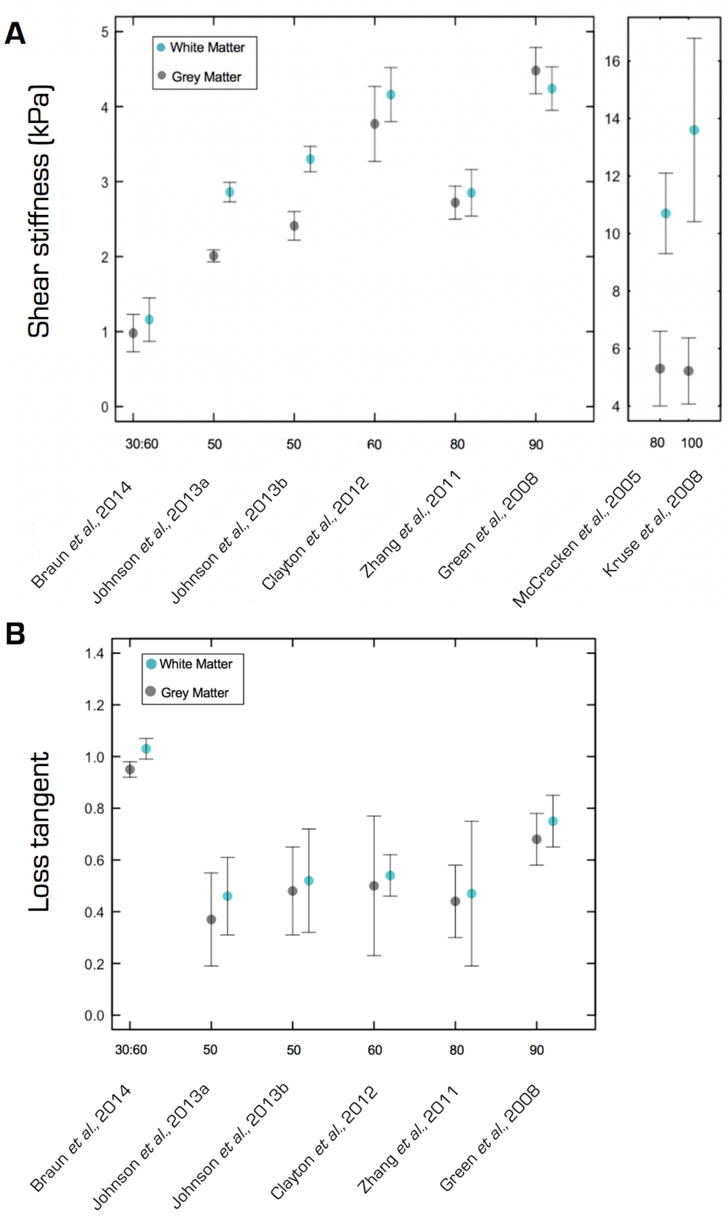

Figure 3.3: (a) shear stiffness, μ (kPa), and (b) loss tangent, ϕ (rad), of GM and WM in healthy participants, showing mean ± standard deviation (SD). First x-axis displays the actuation frequency f, secondary axis displays study reference.

equating to WM being approximately 40% stiffer than GM. Appreciably higher values were obtained by Kruse *et al.* 2008 compared to all other studies, even when taking into consideration the higher mechanical frequency of 100 Hz [16]. Stiffness of GM was 5.22 kPa and 13.60 kPa for WM. The higher measurements have been attributed to the 2D LFE inversion technique, which may not have been optimised to minimize through-plane wave propagation. Through-plane propagating waves can appear in 2D data as waves with longer wavelengths, thus overestimating tissue stiffness [34]. Furthermore, lower μ values are notable in a study by Braun *et al.,* 2014, who utilised multifrequency MRE and MDEV inversion [19]. Stiffness of GM was 0.98 kPa and 1.16 kPa for WM. Direct comparison of values with μ reported by other groups is not possible because of the inherent frequency averaging implied by MDEV inversion, and greater contribution of the lower frequency images due to naturally higher amplitudes [24]. This study also utilised an MRI scanner at 7 T. Field-strength *per se* is not expected to influence MRE measurements [49], however, higher image resolution may improve the ability to detect fine-scale features and thus measure different parts of the obtained wave profile.

Storage and loss moduli were provided for GM and WM in 6 out of the 10 studies, enabling the calculation of ϕ. WM was found to be more viscous than GM in all studies, see Figure 3.3 **B**. ϕ for GM range between 0.44 rad - 0.95 rad, and 0.47 rad - 1.03 rad for WM. Higher WM viscosity, relative to GM, indicates that the microstructure of WM has a highly complex structure and supports recent *in vitro* findings that measured both stress relaxation and relaxation times in both types of tissue [50]. In addition, higher WM viscosity is also consistent with the microstructural architecture of GM and WM, and found to reflect the network properties of WM found at the macromolecular level [51]. Particularly high values for ϕ are evident in Braun *et al.,* 2014, with 0.95 rad for GM and 1.03 rad for WM [19]. As previously mentioned, these values are likely to have been overestimated due to systemic noise bias; subsequent work has focused on the recalculation of ϕ* [9]. Nonetheless, the original parameter was reported as sensitive to a variety of pathological processes, as described in both Streitberger *et al.,* 2014b [31] and Reiss-Zimmermann *et al.,* 2014 [30], and detailed within the second part of this chapter.

3.4.3 *Towards a Measure of Regional Neuroanatomy*

More recently, brain MRE studies have reported values for specific neuroanatomical regions of interest (ROIs). Table 3.5 provides measurements from four studies which have investigated the four lobes of the brain (frontal, temporal, occipital, parietal), the sensory-motor region, deep GM/WM (defined as containing the thalamus, hypothalamus, subthalamus among other deep-brain structures), and the cerebellum.

Using the same DI analysis protocol at 60 Hz, all studies report highest μ in the deep GM/WM, see Figure 3.4. Conflicting evidence has been reported regarding whether the temporal [40, 43] or occipital [11] lobe displays the greatest stiffness out of the four anatomically distinct lobar regions. Whether lobar variation in stiffness is explained by fundamental brain architectural differences has not

Table 3.5: List of MRE studies investigating ROIs in healthy participants

Study Author	Murphy *et al.,* 2013b	Huston *et al.,* 2015	Arani *et al.,* 2015	Murphy *et al.,* 2016
N	10	9	45	32
Mean age	23-55	61	74	n/a
Frontal Lobe	3.15 ± 0.04	2.95 ± 0.10	2.70 ± 0.02	2.65 ± 0.15
Temporal Lobe	3.17 ± 0.04	3.00 ± 0.13	2.80 ± 0.02	2.69 ± 0.11
Occipital Lobe	3.21 ± 0.04	2.92 ± 0.09	2.80 ± 0.03	2.65 ± 0.13
Parietal Lobe	2.87 ± 0.03	2.70 ± 0.08	2.60 ± 0.02	2.42 ± 0.10
Deep GM/WM	3.41 ± 0.07	3.12 ± 0.33	3.00 ± 0.02	2.79 ± 0.25
Cerebellum	2.38 ± 0.03	2.36 ± 0.16	2.20 ± 0.02	2.15 ± 0.11
Sensory-motor	n/a	2.99 ± 0.18	2.80 ± 0.03	2.82 ± 0.29

Values show mean μ (kPa) ± standard deviation (SD). n/a = not available.

yet been determined, and is the subject of future investigations. In contrast, the cerebellum was found to be softer than any component of the cerebrum, supporting separate findings from Zhang *et al.* 201, who reported greater μ for cerebral WM (2.85 kPa ± 0.36), compared to cerebellar WM (2.31 kPa ± 0.36) [20]. This may be explained by the fact that the cerebellar surface is comprised of thin layers of tissue with finely spaced parallel grooves, thus displaying a finer microstructure compared to the broad irregular convolutions of the cerebral cortex. Finally, it is interesting to note that a consistent relationship between the values for each brain region was largely maintained across the three studies. Variation in results across studies may be attributed to the mean age of subjects lending support to studies that suggest increasing age may contribute to a loss of brain stiffness [6, 10, 12].

Mechanical properties of a number of neuroanatomical structures have been measured, and briefly summarised here. Using multifrequency MRE and MDEV inversion, [24] found decreasing $|G^*|$ values in the order of WM, corpus callosum genu, thalamus, and the head of the caudate nucleus. Johnson *et al.,* 2013b [21] used their multislab, multishot sequence with non-linear FEM, and found WM to be softer, as determined by G', than either the corpus callosum or the corona radiata, whereas the corpus callosum exhibited a higher stiffness and lower viscous damping, represented by G'', compared to the corona radiata. The development of a new remote driver was tested by Fehlner *et al.,* 2015, using MDEV between the frequency range 25-45 Hz [25]. An increase in $|G^*|$ was revealed within the CST in the cranial-caudal direction from the capsula interna (CI) to the crus cerebri (CC), whereas the pons was softer than both the CI and CC. The fibres in the superior region of the CST (CC) showed greater dissipative behaviour, as determined by ϕ, followed by the CI and pons, respectively. Finally, Johnson *et al.,* 2014 reported higher values for the storage modulus G' within the brainstem, compared to cerebral or cerebellar tissue [22].

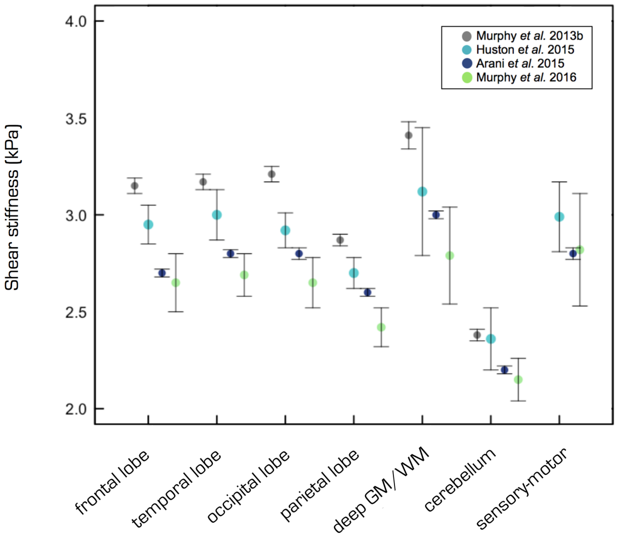

Figure 3.4: Regional shear stiffness, μ (kPa) values in healthy participants

3.5 Brain MRE Results from Clinical Studies

MRE has been used to investigate brain mechanical properties in a wide range of neurological disorders. These include focal intracranial tumours (ICT), as well as diffuse diseases such as Alzheimer's disease (AD) and multiple sclerosis (MS). In the previous section, output parameters for GBT, GM and WM were converted, where possible, to measures of shear stiffness, μ and loss tangent ϕ. In the following review of findings from clinical studies, the original MRE parameters will be maintained in order to report consistent changes according to the published findings. Although not directly comparable, shear stiffness μ, $|G^*|$ and spring-pot derived μ are all similar in meaning, referring to stiffness or cellular strength, whereas both ϕ and α relate the dissipative behaviour of tissue.

3.5.1 *Focal diseases*

MRE has been used as an investigative tool to study the mechanical properties of various intracranial tumours that span the full spectrum of gradings determined by the World Health Organization (WHO), such as meningioma and glioblastoma multiforme (GBM). MRE investigations into brain tumours can be generally grouped into two categories, (i) studies of the concordance between MRE results and *in vivo* surgical manual palpation, or (ii) studies of the sensitivity or specificity of MRE for the differential diagnosis of intracranial tumours.

(i) Concordance between MRE results and manual palpation

Knowledge of the consistency of brain tumours prior to surgical resection, could assist surgeons in preoperative planning, improving both patient care and work-flow optimisation. Differentiation of brain tumours from healthy tissue, during surgical resection is, for the most part, based on their differing mechanical properties, as discussed in the *Introduction*. Three studies have obtained MRE measurements in patients prior to surgery and have subsequently compared results with the surgeon's manual assessment, in order to assess the ability of MRE to accurately predict tumour stiffness, and hence procedural difficulty. The relationship between MRE results and brain palpation was first assessed by Xu *et al.,* 2007b in 6 patients with diverse tumour classifications [27]. A visual inspection of the wave propagation was correlated with the intraoperative assessment of tumour consistency determined by the neurosurgeon during the tumour resection. Blinded to the MRE results, the surgeon evaluated the tumour consistency as either soft (softer than white matter), intermediate (similar to white matter), or hard (stiffer than white matter). MRE was 100% accurate at predicting tumour stiffness as decided by the surgeon. Similarly, Murphy *et al.,* 2013a assessed 12 patients with Meningioma's, typically a benign lesion that arises from the meninges [28]. A quantitative analysis of tumour shear stiffness was used to determine statistical significance. Tumour stiffness determined with MRE significantly correlated with the surgeon's assessment, however an even greater correlation was found when the ratio of tumour stiffness to the surrounding brain tissue was measured ($p = 0.0032$). Furthermore, a higher resolution MRE protocol was developed and used to assess whether MRE could preoperatively detect intratumoural heterogeneity present within Meningioma's [32]. Data were obtained and analysed to measure heterogeneity for a ROI within the tumour mass. Intraoperative observations regarding softness or hardness were graded on a 5-point scale based on the degree of suction, ultrasonic aspiration, or scissors and cautery. In 15 patients, MRE measurements and intraoperative findings correlated in 67% of tumours ($p = 0.02$), with the correlation perhaps greater if highly vascular or smaller lesions had been excluded. Importantly, tumour stiffness measured by MRE outperformed predictions from conventional MRI using and T_2-weighted images [28]. MRI has previously found soft tumours to be hyperintense and less likely to be associated with oedema on T_2 images [52]. However, conventional MRI could only accurately predict the softest and hardest meningioma's prior to surgical resection, with little success determining the tumour consistency between the two extremes. It was suggested that future studies should aim to assess specific regions within the tumour mass to more accurately define intrinsic mechanical heterogeneity to enhance the potential utility of MRE as a pre-surgical tool. Measurement of tumour stiffness could also be normalised to surrounding brain tissue, as a result of intrasubject variability in presumably unaffected brain tissue [28].

(ii) MRE for the differential diagnosis of intracranial tumours

MRE has also been investigated as a technique to diagnose the type, grade and malignancy of tumours, as a possible alternative to routine biopsy procedures used for histological classification. Simon *et al.,* 2013 analysed a broad range of tumours in 16 patients, including those with meningioma, malignant glioma, anaplastic astrocytoma, and glioblastoma multiforme, among other tumour entities [29]. Using multifrequency MRE and MDEV inversion, malignant tumours presented with a loss of $|G^*|$, when compared to a selected contralateral region of normal appearing white matter (NAWM). Primary brain tumours of the highest malignancy (WHO IV) were more likely to yield soft tissue results, presenting between 33.6 - 52% softer than NAWM. In addition, the majority of tumours displayed a reduction in the loss tangent ϕ. A further pilot study which incorporated MDEV inversion, allowed for high-resolution imaging of the viscoelastic properties of a range of tumours in 27 patients [30]. Supporting findings from [29], high grade tumours (WHO Grade IV) were more likely to be softer, as determined by $|G^*|$, and less viscous than those identified as Grade I, II or III. Furthermore, meningioma tumours (Grade I), were on average much stiffer and displayed higher dissipative behaviour than other tumour entities. The same protocol was used to assess the mechanical properties of Glioblastoma Multiforme (GBM), a WHO Grade IV tumour [31]. Results from 22 subjects are provided in Table 3.6, for both tumour region and normal appearing white matter (NAWM). GBM was generally softer than healthy tissue, however, 23% of tumours were found to be stiffer than healthy tissue, supporting evidence of high intratumoural variability. There was a significant reduction in ϕ in all patients.

Investigations into the use of MRE as a technique for the differential diagnosis of brain tumours, suggest that more malignant tumours, determined by WHO classification, are

Table 3.6: MRE results for GBM and NAWM

	NAWM	GBM ROI	% difference	p value
$\|G^*\|$ (kPa)	1.54 ± 0.27	1.32 ± 0.26	-14.29%	<0.001
ϕ (rad)	0.58 ± 0.07	0.37 ± 0.08	-36.21%	<0.001

Values show mean ± standard deviation [31]. Key: GBM, glioblastoma multiforme; NAWM, normal appearing white matter.

more likely to be less stiff, as determined by $|G^*|$, and display a reduction in the loss tangent ϕ. While a uniform reduction in $|G^*|$ is interpreted as a weakening or softening of the mechanical rigidity of tissue, an alteration of the phase angle ϕ is interpreted as a more severe degradation of the tissue structure due to a change in the complexity of the tissue architecture [53]. In contrast, Meningioma tumours were the only tumour entity to display increased stiffness, $|G^*|$, and a highly cross-linked architecture ϕ. This may be attributed to the initial development of pathology in the meninges, which is comprised of a thick layer of dura mater, arachnoid mater, and pia mater, in addition to their propensity to calcify.

3.5.2 *Diffuse diseases*

(i) Multiple Sclerosis (MS)

MS is a demyelinating disease in which the insulating covers (myelin) of nerve cells in the brain and spinal cord become damaged, with symptoms determined by the location of lesions within white matter. Two studies have used multifrequency MRE and modelling to investigate whether MRE is sensitive to detect known microstructural alterations to the brain in MS. First, Wuerfel *et al.,* 2010 reported that patients with relapsing-remitting MS (MS-RR) displayed a 13% decrease in μ, ($p < 0.001$), with no significant changes to α [33]. Second, Streitberger *et al.,* 2012 found patients with primary or secondary chronic progressive MS (MS-CP), to exhibit a more pronounced reduction in μ (20%) in addition to a significant reduction in α (6%), both (p <0.001), as shown in Table 3.7 [37]. These studies show how disease severity can influence mechanical property measurements; in the early stages of MS (MS-RR), the strength of the brain is degraded, as indicated by μ, while the geometrical arrangement α remains intact.

To complement these findings, the underlying cellular and molecular mechanisms behind

Table 3.7: MRE results for GBT in MS patients and control participants

Subtype	MS-RR				MS-CP			
Author	Wuerfel *et al.,* 2010 [33]				Streitberger *et al.,* 2012 [37]			
	Patients	Controls	% difference	p value	Patients	Controls	% difference	p value
N	45	23	-	-	34	38	-	-
μ	1.87 ± 0.25	2.14 ± 0.31	-12.7%	$p < 0.001$	2.61 ± 0.48	3.28 ± 0.31	-20.5%	$p < 0.001$
α	0.27 ± 0.01	0.27 ± 0.01	0.3%	n.s.	0.28 ± 0.01	0.29 ± 0.01	-6.1%	$p < 0.001$

Values represent mean ± standard deviation (SD). % difference and p values refer to differences between groups of patients and healthy controls within the same study. Key: GBT, global brain tissue; MS-RR, multiple sclerosis (relapse-remitting); MS-CP, multiple sclerosis (chronic-progressive); n.s, non-significant.

these changes were examined in two mouse models of MS, as described in *Chapter* 2, which found an association between $|G^*|$ and progressive demyelination [54] and inflammation [55]. In the latter study, there was no significant change to the phase angle ϕ indicating that inflammation affects stiffness independently of alterations in tissue architecture - supporting human patient findings presented here from Wuerfel *et al.* 2010 [33]. On the other hand, patients with chronic MS (MS-CP), were found to exhibit even softer brains than patients with MS-RR, as determined by μ, as well as a less complex geometrical arrangement indicated by a significant loss to α. Deficits due to MS-CP are considered irreversible due to progressive neurodegeneration, and thus may explain the more drastic changes to the alignment of the tissue network, although to date, animal models of MS-CP have not been combined with MRE and histopathology. The need for standardisation across and within research groups becomes apparent when comparing the mechanical properties between MS-RR and MS-CP directly. Changes in the protocol between studies and in particular, the limits of bandpass filtering, have resulted in different base-line values for healthy control subjects. Nevertheless, the application of MRE to investigate patients with early or chronic MS, has shown how disease severity can differentially affect mechanical property measurements, thereby showing potential as a unique marker of disease progression.

(ii)Alzheimer's disease (AD)

AD is a progressive impairment of cognitive function, typically beginning with episodic memory, and is characterised pathologically by extracellular amyloid (Aβ) plaques and intracellular neuro-fibrillary tangles [56]. Murphy *et al.,* (2011) found that the stiffness of global brain tissue was decreased in patients with AD compared to age-matched healthy control subjects both with (HC+) and without (HC-) significant brain amyloid load, see Table 3.8. This is contradictory to what was initially hypothesised in AD patients, with the aggregation of stiff amyloid protein expected to lead to an increase in tissue stiffness. On reflection, this may be due to patients being in the later stages of disease, at which stage significant neurodegeneration is likely. Thus, MRE may be more sensitive to wide-spread cell death caused by the initial protein accumulation. More recently, Murphy *et al.,* 2016 measured the relationship between brain stiffness and severity of AD pathophysiology with 4 groups of subjects including HC-, HC+, MCI (mild cognitive impairment) and AD [43]. Using the regional MRE processing pipeline, as described in Murphy *et al.,* 2013b [11], brain stiffness decreased with increasing AD severity, as determined by existing imaging biomarkers such as hippocampal volume and Aβ load (PIB-SUVR). An optimised meta-region of interest including the frontal, parietal and temporal (FPT) lobes; regions known to be affected by the disease, outperformed all other regions for discriminating between AD patients and healthy control subjects. Interestingly, the relationship between brain stiffness and AD severity was non-linear and non-monotonic, suggesting that brain stiffness spikes at the onset of MCI, before falling to levels observed in AD during the later stages of MCI. This would appear to support the theory that the initial development of Aβ is associated with increased brain stiffness, before a decrease associated with wide-spread cell death and a loss of tissue integrity. Further investigations are warranted to corroborate that other aspects of the AD pathological cascade follow the same trajectory and to link MRE results with histological samples.

Table 3.8: MRE results for GBT in patients with AD and FTD

	N	Mean age	μ (kPa)	% difference	*p* value
Murphy *et al.,* 2011 [34]					
AD patients	7	85	2.20 ± 0.13	-	-
Healthy controls	14	81.5	2.37 ± 0.12	-7.20%	$p = 0.026$
Huston *et al.,* 2015 [40]					
bvFTD patients	5	60	2.59 ± 0.17	-	-
Healthy controls	9	61	2.76 ± 0.08	-6.50%	$p = 0.007$

Values show mean ± standard deviation (SD). % difference and *p* values refer to differences between groups of patients and healthy controls in the same study. Key: GBT, global brain tissue; AD, alzheimer's disease; FTD, fronto-temporal dementia.

(iii) Fronto-temporal dementia (FTD)

The behavioural-variant of FTD, (bvFTD), is characterized by prominent changes in personality, interpersonal relationships and conduct, and predominantly involves progressive neuronal loss in the frontal and/or temporal lobes. Specific regions of interest (ROIs) were investigated with MRE due to the well-known localised origin of pathology [40]. Using the regional MRE processing pipeline, described in Murphy *et al.,* 2013a [28], a specific pattern of brain softening was found in patients with bvFTD in comparison to age matched cognitively healthy participants. A 6.5% decrease was detected in global brain tissue, ($p < 0.01$), in addition to a 8.5% and 9% decrease in both the frontal lobe ($p < 0.001$), and temporal lobes ($p < 0.005$), respectively. No significant differences were found between groups for either the occipital or parietal lobes, deep grey/white matter, cerebellum or the sensory/motor region. This study shows how greater changes to the MRE-derived parameters are evident in regions (the frontal and temporal lobes), where neurodegeneration is known to originate [57]. The difference in brain stiffness between the AD and FTD healthy control subjects, as shown in Table 3.8, is likely due to subject age, with the AD control group approximately 20 years senior.

(iv) Normal Pressure Hydrocephalus (NPH)

NPH is a reversible neurological disorder that presents with a triad of clinical symptoms namely, an unusual gait, symptomatic dementia and urinary incontinence. Typical MRI findings are enlargement of the ventricles, while the onset has been attributed to transient intracranial pressure peaks, causing chronic mechanical stress on the ventricular wall. Streitberger *et al.,* 2010 were the first to study NPH patients with MRE, in order to elucidate whether mechanical changes to brain tissue may play a potential role in the aetiology of the disorder [35]. Assessment of a 2cm slab of brain tissue, centred through the ventricular region, found μ to be 25% lower in NPH patients, compared to healthy control participants. There was also a significant reduction in α, on the order of 10%, (both $p < 0.001$), see Table 3.9.

A surgical procedure to relieve some of the symptoms of NPH includes the placement of a ventriculoperitoneal (VP) shunt within the ventricles to drain excess cerebrospinal fluid (CSF). MRE was performed on NPH patients before and after shunt placement to determine the efficacy of treatment and assess mechanical alternations as a result of the intervention [36]. Prior to surgery, a reduction in both μ and α was found by 27% and 10%, respectively, compared to healthy control data taken from [35], (both $p < 0.001$).

Table 3.9: MRE results for GBT in patients with NPH

	N	μ	% difference	p value	α	% difference	p value
Streitberger *et al.* 201 [35]							
Healthy controls	25	2.84 ± 0.088	-	-	0.287 ± 0.002	-	-
NPH patients	20	2.27 ± 0.054	-25.1%	< 0.001	0.262 ± 0.002	-9.5%	< 0.001
Freimann *et al.* 2012 [36]							
NPH patients pre-shunt	20	2.24 ± 0.085	-26.8%	< 0.001	0.258 ± 0.003	-10%	< 0.001

Values show mean ± standard deviation (SD). % difference and p values refer to differences between both groups of patients and healthy controls. Key: GBT, global brain tissue; NPH, normal pressure hydrocephalus.

After the surgical procedure, patients did not exhibit any changes to μ, with data collected on average 3 months later. However, results for α normalised and returned within 3% of values found for healthy control subjects, ($p < 0.001$). The fact that μ remained unchanged supports the notion that spring-pot parameters represent two independent processes. Shunt placement was associated with reordering the geometry alignment of the mechanical scaffold of the brain, creating a more complex network, without influencing cellular strength or connectivity. More recently, Fattahi *et al.,* 2015 investigated specific regions of interest (ROIs) in the brain of NPH patients [41]. In contrast to findings from Streitberger *et al.,* 2010 and Freimann *et al.,* 2012, patients with NPH were found to exhibit an *increase* to the brain's shear stiffness, when compared to data collected from age-and-gender-matched controls [41]. An increase in stiffness was apparent in GBT (3.9%), occipital lobe (12%), parietal lobe (12.6%) and temporal lobe (2.6%). No significant differences were found in either the frontal lobe, cerebellum, or deep grey and white matter. An increase in brain stiffness may be caused by the dilation of the ventricles, leading to brain tissue compression. Resulting cellular alterations are likely to create a higher tissue-to-fluid ratio within the cerebrum. Importantly, the discrepancy in findings between studies has been attributed to the use of alternative protocols; however, it is possible that alternative brain regions will undergo disparate changes throughout the NPH process.

(v) Parkinson's disease (PD) and Progressive Supranuclear Palsy (PSP)

PD is characterised by death of dopaminergic neurons in the substantia nigra, which forms part of the basal ganglia, causing tremor, gait difficulty and rigidity. Patients with PSP also display a progressive deterioration in motor function, but pathology instead involves the widespread degeneration of specific axons, particularly in the brainstem, cerebral cortex and basal ganglia. PSP is frequently misdiagnosed as PD because of the shared clinical manifestations, and so MRE was used to elucidate possible alternative mechanical profiles to aid in differential diagnosis [38]. Both a 3D direct inversion approach of a volumetric slab of brain tissue, and 2D multi-frequency springpot analysis to model a single image slice, offered enhanced sensitivity to assess regional brain changes in addition to modelling the frequency-independent material properties. Results for GBT are given in Table 3.10, with no significant differences found between PD patients and healthy control participants. In PSP, however, all four parameters including $|G^*|$, ϕ, μ, and α, were reduced with μ in particular, undergoing the most statistically significant change, ($p < 0.001$). Regional analysis of the basal ganglia region in patients with PD detected a significant loss of $|G^*|$ and α in the lentiform nucleus by 6.9% and -7.4%, respectively, ($p < 0.05$), with PSP patients displaying even greater losses in all four assessed parameters. This study suggests that MRE may assist in differential diagnosis as results indicate that PD and PSP have distinct mechanical profiles. PD patients displayed significant changes to $|G^*|$ and α during an assessment of the basal ganglia; no significant changes were detected in GBT. PD pathology involves presynaptic accumulation of α-synuclein which starts focally and affects axonal integrity only later in the process of degeneration [58], and thus may explain why changes to GBT were not detected. In contrast, PSP patients displayed pronounced changes in $|G^*|$, ϕ, μ and α, both globally and in the basal ganglia. PSP typically involves an early loss of neuronal axons, which are essential in maintaining brain tissue integrity. This study highlights the importance of investigating a specific brain structure associated with a particular disorder as omission of the basal ganglia investigation would not have differentiated PD patients from healthy control participants.

(vi) Amyotrophic Lateral Sclerosis (ALS)

The corticospinal tract (CST) consists of nerve fibres that travel from the cerebral cortex and terminate in the spinal cord. Degeneration of the CST has been implicated in ALS, causing progressive and irreversible loss of motor function. Due to the highly anisotropic properties of these fibres, an innovative approach for measuring the mechanical properties of this structure combines the use of MRE with diffusion tensor imaging (DTI), and anisotropic equations of motion [23] - a technique termed Waveguide Elastography

Table 3.10: MRE results for GBT in patients with PD, PSP and control participants

Subtype		PD		PSP		
	Controls	Patients	% difference	Patients	% difference	p value
N	18	18	-	16	-	
$\|G^*\|$	1.97 ± 0.042	1.88 ± 0.061	n.s	1.68 ± 0.043	-10.6%	< 0.01
ϕ	0.26 ± 0.009	0.22 ± 0.016	n.s	0.17 ± 0.018	-34.6%	< 0.001
μ	2.79 ± 0.071	3.04 ± 0.191	n.s	1.98 ± 0.126	-28.8%	< 0.001
α	0.30 ± 0.002	0.30 ± 0.005	n.s	0.29 ± 0.003	-4.9%	< 0.01

Values represent mean and standard deviation (SD) [38]. % difference and p values refer to differences between both groups of patients and healthy controls. Key: GBT, global brain tissue; PD, Parkinson's disease; PSP, progressive supranuclear palsy.

(WGE). In particular, DTI was used to locate fibre pathways, before the application of spatial-spectral filtering to identify waves that are travelling in a specific direction relative to the fibre orientation. Clinically, this method has been used to assess the stiffness of the CST in 14 patients with ALS in comparison to 14 age-matched healthy controls [39]. Analysis of shear waves identified propagating parallel to the principal direction of nerve fibres in the CST, revealed a 5.3% decrease in the shear stiffness in the patient cohort, indicating a significant softening along this tract, ($p < 0.01$). This technique may prove to be valuable in the diagnosis of ALS, although further clinical trials are required. The combination of histological analyses with MRE measurements will be imperative in order to relate pathological cellular changes to MRE constants. Further, the use of WGE is unlikely to be useful for the assessment of tissue stiffness among other brain regions. WGE analysis is reliant on knowledge of the pathways along which the propagating waves will travel, however, most brain structures or regions do not possess anisotropic properties on the same scale as the CTS.

3.6 Discussion

In this chapter, I have reviewed the MRE literature to summarise data from studies that have utilised MRE to report mechanical property values for the human brain. Second, I have standardised MRE-derived variables reported for global brain tissue (GBT), grey matter (GM) and white matter (WM) in healthy volunteers, with values for specific brain lobar regions and structures also provided. Finally, I describe how MRE possesses the ability to detect changes to the brain in patients with a wide range of focal and diffuse neurological conditions.

As illustrated by this literature review, providing standardised baseline values for the healthy brain is very challenging. There is currently no consensus as to MRE values that may constitute a healthy normal brain, and as such, baseline values cannot be established. As a result, values provided for a clinical cohort will only be relevant to those who follow the same methodology. Whether brain MRE can provide *accurate* quantitative values for mechanical properties will be difficult to determine. Indentation methods can reliably record the stiffness of, for example, grey and white matter [50], but it remains an *ex vivo* technique that cannot predict the mechanical characteristics of living brain tissue *in situ*. On the other hand, accurate mechanical values *per se* may be less important than the determination of the most clinically sensitive and reliable protocol. More studies have been reporting repeatability figures, with promising results [2, 43]. Most repeatability measures, however, have been of a repeated measures design (i.e. scanning the same subject on the same day); there has been a distinct lack of test-retest agreement measures over a wide range of subjects scanned at two separate time points.

Initial clinical brain MRE studies show the promise of this technique as a novel biomarker, with values shown to differ between groups of healthy control participants and neurological patients. However, the majority of studies have reported values as global averages. Due to the recent enhancement in MRE methodology, it is now possible to investigate specific neuroanatomical regions of interest. The importance of such progress is demonstrated in the study into Parkinson's disease; differences between controls and patients would not have been detected if the basal ganglia region had not been investigated. The repeatability of the methods used, to my knowledge, have not been investigated, which is important considering the low-resolution acquisition sequence used in the study. As such, there is a specific need to acquire high-resolution images, to enable study of specific brain structures, which display high test-retest reliability across a wide range of subjects and at alternative time points. Future work in this thesis will aim to identify such an approach.

References

[1] A Manduca, TE Oliphant, MA Dresner, JL Mahowald, SA Kruse, E Amromin, JP Felmlee, JF Greenleaf, and RL Ehman. Magnetic resonance elastography: Non-invasive mapping of tissue elasticity. *Med Image Anal*, 5:237–254, 2001.

[2] CL Johnson, H Schwarb, MDJ McGarry, AT Anderson, GR Huesmann, BP Sutton, and NJ Cohen. Viscoelasticity of subcortical gray matter structures. *Hum Brain Mapp*, 2016.

[3] D Moher, A Liberati, J Tetzlaff, and DG Altman. Preferred reporting items for systematic reviews and meta-analyses: the PRISMA statement. *PLoS Med*, 6:e1000097, 2009.

[4] D Klatt, U Hamhaber, P Asbach, J Braun, and I Sack. Noninvasive assessment of the rheological behavior of human organs using multifrequency MR elastography: a study of brain and liver viscoelasticity. *Phys Med Biol*, 52:7281, 2007.

[5] I Sack, B Beierbach, U Hamhaber, D Klatt, and J Braun. Non-invasive measurement of brain viscoelasticity using magnetic resonance elastography. *NMR Biomed*, 21:265–271, 2008.

[6] I Sack, B Beierbach, J Wuerfel, D Klatt, U Hamhaber, S Papazoglou, P Martus, and J Braun. The impact of aging and gender on brain viscoelasticity. *NeuroImage*, 46:652–657, 2009.

[7] JB Weaver, AJ Pattison, MD McGarry, IM Perreard, JG Swienckowski, CJ Eskey, SS Lollis, and KD Paulsen. Brain mechanical property measurement using MRE with intrinsic activation. *Phys Med Biol*, 57:7275–7287, 2012.

[8] A Hatt, S Cheng, K Tan, R Sinkus, and LE Bilston. MR Elastography Can Be Used to Measure Brain Stiffness Changes as a Result of Altered Cranial Venous Drainage During Jugular Compression. *AJNR Am J Neuroradiol*, 36:1971–1977, 2015.

[9] F Dittmann, S Hirsch, H Tzschätzsch, J Guo, J Braun, and I Sack. In vivo wideband multifrequency MR elastography of the human brain and liver. *Magn Reson Med*, page doi: 10.1002/mrm.26006, 2015.

[10] I Sack, KJ Streitberger, D Krefting, F Paul, and J Braun. The Influence of Physiological Aging and Atrophy on Brain Viscoelastic Properties in Humans. *PLoS One*, 6:e23451, 2011.

[11] MC Murphy, J Huston 3rd, Jr CR Jack, KJ Glaser, ML Senjem, J Chen, A Manduca, JP Felmlee, and RL Ehman. Measuring the characteristic topography of brain stiffness with magnetic resonance elastography. *PLoS One*, 8:e81668, 2013b.

[12] A Arani, MC Murphy, KJ Glaser, A Manduca, DS Lake, SA Kruse, C Jack, RL Ehman, and J Huston 3rd. Measuring the effects of aging and sex on regional brain stiffness with MR elastography in healthy older adults. *NeuroImage*, 111:59 – 64, 2015.

[13] PJ McCracken, A Manduca, J Felmlee, and RL Ehman. Mechanical transient-based magnetic resonance elastography. *Magn Reson Med*, 53:628–639, 2005.

[14] L Xu, Y Lin, ZN Xi, H Shen, and PY Gao. Magnetic resonance elastography of the human brain: a preliminary study. *Acta Radiol*, 48:112–115, 2007.

[15] MA Green, LE Bilston, and R Sinkus. In vivo brain viscoelastic properties measured by magnetic resonance elastography. *NMR Biomed*, 21:755–764, 2008.

[16] SA Kruse, GH Rose, KJ Glaser, A Manduca, JP Felmlee, CR Jack Jr, and RL Ehman. Magnetic resonance elastography of the brain. *NeuroImage*, 39:231–237, 2008.

[17] EH Clayton, GM Genin, and PV Bayly. Transmission, attenuation and reflection of shear waves in the human brain. *J R Soc Interface*, 9:2899–2910, 2012.

[18] CL Johnson, MDJ McGarry, EEW Van Houten, JB Weaver, KD Paulsen, BP Sutton, and JG Georgiadis. Magnetic resonance elastography of the brain using multishot spiral readouts with self-navigated motion correction. *Magn Reson Med*, 70:404–412, 2013a.

[19] J Braun, J Guo, R Lützkendorf, J Stadler, S Papazoglou, S Hirsch, I Sack, and J Bernarding. High-resolution mechanical imaging of the human brain by three-dimensional multifrequency magnetic resonance elastography at 7T. *Neuroimage*, 90:308 – 314, 2014.

[20] J Zhang, MA Green, R Sinkus, and LE Bilston. Viscoelastic Properties of Human Cerebellum using Magnetic Resonance Elastography. *J Biomech*, 44:1909–1913, 2011.

[21] CL Johnson, MDJ McGarry, AA Gharibans, JB Weaver, KD Paulsen, H Wang, WC Olivero, BP Sutton, and JG Georgiadis. Local mechanical properties of white matter structures in the human brain. *NeuroImage*, 79:145–152, 2013b.

[22] CL Johnson, JL Holtrop, MDJ McGarry, JB Weaver, KD Paulsen, JG Georgiadis, and BP Sutton. 3D multislab, multishot acquisition for fast, whole-brain MR elastography with high signal-to-noise efficiency. *Magn Reson Med*, 71:477–485, 2014.

[23] A Romano, M Scheel, S Hirsch, J Braun, and I Sack. In vivo waveguide elastography of white matter tracts in the human brain. *Magn Reson Med*, 68:1410–1422, 2012.

[24] J Guo, S Hirsch, A Fehlner, S Papazoglou, M Scheel, J Braun, and I Sack. Towards an elastographic atlas of brain anatomy. *PLoS One*, 8:e71807, 2013.

[25] A Fehlner, S Papazoglou, M D McGarry, K D Paulsen, J Guo, K-J Streitberger, S Hirsch, J Braun, and I Sack. Cerebral multifrequency MR elastography by remote excitation of intracranial shear waves. *NMR Biomed*, 28:1426–1432, 2015.

[26] H Schwarb, CL Johnson, MDJ McGarry, and NJ Cohen. Medial temporal lobe viscoelasticity and relational memory performance. *NeuroImage*, 132:534–541, 2016.

[27] L Xu, Y Lin, JC Han, ZN Xi, H Shen, and PY Gao. Magnetic resonance elastography of brain tumors: preliminary results. *Acta Radiol.*, 48:327–330, 2007.

[28] MC Murphy, J Huston 3rd, KJ Glaser, A Manduca, FB Meyer, G Lanzino, JM Morris, JP Felmlee, and RL Ehman. Preoperative assessment of meningioma stiffness using magnetic resonance elastography. *J Neurosurg*, 118:643–648, 2013a.

[29] M Simon, J Guo, S Papazoglou, H Scholand-Engler, C Erdmann, U Melchert, M Bonsanto, J Braun, D Petersen, I Sack, and J Wuerfel. Non-invasive characterization of intracranial tumors by magnetic resonance elastography. *New J Phys*, 15:085024, 2013.

[30] M Reiss-Zimmermann, K-J Streitberger, I Sack, J Braun, F Arlt, D Fritzsch, and KT Hoffmann. High Resolution Imaging of Viscoelastic Properties of Intracranial Tumours by Multi-Frequency Magnetic Resonance Elastography. *Clin Neuroradiol*, 25:371–380, 2014.

[31] K-J Streitberger, M Reiss-Zimmermann, FB Freimann, S Bayerl, J Guo, F Arlt, J Wuerfel, J Braun, K-T Hoffmann, and I Sack. High-Resolution Mechanical Imaging of Glioblastoma by Multifrequency Magnetic Resonance Elastography. *PLoS One*, 9:e110588, 2014b.

[32] JD Hughes, N Fattahi, J Van Gompel, A Arani, G Lanzino, M Link, F Meyer, R Ehman, and J Huston 3rd. Higher Resolution Magnetic Resonance Elastography for the Evaluation of Intratumoral Heterogeneity in Meningiomas. *J Neurol Surg B*, 76:A139, 2015.

[33] J Wuerfel, F Paul, B Beierbach, U Hamhaber, D Klatt, S Papazoglou, F Zipp, P Martus, J Braun, and I Sack. MR-elastography reveals degradation of tissue integrity in multiple sclerosis. *NeuroImage*, 49:2520–2525, 2010.

[34] MC Murphy, 3rd J Huston, CR Jack Jr, KJ Glaser, A Manduca, JP Felmlee, and RL Ehman. Decreased brain stiffness in Alzheimer's disease determined by magnetic resonance elastography. *J Magn Reson Imaging*, 34:494–498, 2011.

[35] K-J Streitberger, E Wiener, J Hoffmann, FB Freimann, D Klatt, J Braun, K Lin, J McLaughlin, C Sprung, R Klingebiel, and I Sack. In vivo viscoelastic properties of the brain in normal pressure hydrocephalus. *NMR Biomed*, 24:385–392, 2010.

[36] FB Freimann, K Streitberger, D Klatt, K Lin, J McLaughlin, J Braun, C Sprung, and I Sack. Alteration of brain viscoelasticity after shunt treatment in normal pressure hydrocephalus. *Neuroradiology*, 54:189–196, 2012.

[37] K-J Streitberger, I Sack, D Krefting, C Pfuller, J Braun, F Paul, and J Wuerfel. Brain Viscoelasticity Alteration in Chronic-Progressive Multiple Sclerosis. *PLoS One*, 7:e29888, 2012.

[38] A Lipp, R Trbojevic, F Paul, A Fehlner, S Hirsch, M Scheel, C Noack, J Braun, and I Sack. Cerebral magnetic resonance elastography in supranuclear palsy and idiopathic Parkinson's disease. *Neuroimage Clin*, 3:381–387, 2013.

[39] A Romano, J Guo, T Prokscha, T Meyer, S Hirsch, J Braun, I Sack, and M Scheel. In vivo waveguide elastography: Effects of neurodegeneration in patients with amyotrophic lateral sclerosis. *Magn Reson Med*, 72:1755–1761, 2014.

[40] J Huston, MC Murphy, BF Boeve, N Fattahi, A Arani, KJ Glaser, A Manduca, DT Jones, and RL Ehman. Magnetic Resonance Elastography of Frontotemporal Dementia. *J Magn Reson Imaging*, 43:474–8, 2015.

[41] N Fattahi, A Arani, A Perry, F Meyer, A Manduca, K Glaser, M L Senjem, R L Ehman, and J Huston 3rd. MR Elastography Demonstrates Increased Brain Stiffness in Normal Pressure Hydrocephalus. *AJNR Am J Neuroradiol*, 37:ajnr.A4560v1–0, 2015.

[42] A Fehlner, JR Behrens, K-J Streitberger, S Papazoglou, J Braun, J Bellmann-Strobl, K Ruprecht, F Paul, J Wurfel, and I Sack. Higher-resolution MR elastography reveals early mechanical signatures of neuroinflammation in patients with clinically isolated syndrome. *J Magn Reson Imaging.*, 44:51–58, 2016.

[43] MC Murphy, DT Jones, CR Jack, KJ Glaser, ML Senjem, A Manduca, JP Felmlee, RE Carter, RL Ehman, and J Huston 3rd. Regional brain stiffness changes across the Alzheimer's disease spectrum. *NeuroImage: Clin*, 10:283–290, 2016.

[44] TL Szabo and J Wu. A model for longitudinal and shear wave propagation in viscoelastic media. *J Acoust Soc Am*, 107:2437–2446, 2000.

[45] J Guo, O Posnansky, S Hirsch, M Scheel, M Taupitz, J Braun, and I Sack. Fractal network dimension and viscoelastic powerlaw behavior: II. An experimental study of structure-mimicking phantoms by magnetic resonance elastography. *Phys Med Biol*, 57:4041–4053, 2012.

[46] MA Holland, KE Miller, and E Kuhl. Emerging brain morphologies from axonal elongation. *Ann Biomed Eng*, 43:1640–1653, 2015.

[47] DE Koser, E Moeendarbary, J Hanne, S Kuerten, and K Franze. CNS cell distribution and axon orientation determine local spinal cord mechanical properties. *Biophys J*, 108:2137–2147, 2015.

[48] Y Lu, K Franze, G Seifert, C Steinhäuser, F Kirchhoff, H Wolburg, J Guck, P Janmey, E Wei,

J Käs, and A Reichenbach. Viscoelastic properties of individual glial cells and neurons in the CNS. *Proc Natl Acad Sci USA*, 103:17759–17764, 2006.

[49] U Hamhaber, I Sack, S Papazoglou, J Rump, D Klatt, and J Braun. Three-dimensional analysis of shear wave propagation observed by in vivo magnetic resonance elastography of the brain. *Acta Biomater*, 3:127–137, 2007.

[50] S Budday, R Nay, R de Rooij, P Steinmann, T Wyrobek, TC Ovaert, and E Kuhl. Mechanical properties of gray and white matter brain tissue by indentation. *J Mech Behav Biomed Mater*, 46:318 – 330, 2015.

[51] G Franceschini, D Bigoni, P Regitnig, and GA Holzapfel. Brain tissue deforms similarly to filled elastomers and follows consolidation theory. *J Mech Phys Solids*, 54:2592–2620, 2006.

[52] JM Hoover, JM Morris, and FB Meyer. Use of preoperative magnetic resonance imaging T1 and T2 sequences to determine intraoperative meningioma consistency. *Surg Neurol Int*, 2:142, 2011.

[53] I Sack, K Johrens, J Wurfel, and J Braun. Structure-sensitive elastography: on the viscoelastic powerlaw behavior of in vivo human tissue in health and disease. *Soft Matter*, 9:5672–5680, 2013.

[54] K Schregel, E Wuerfel née Tysiak, P Garteiser, I Gemeinhardt, T Prozorovski, O Aktas, H Merz, D Petersen, J Wuerfel, and R Sinkus. Demyelination reduces brain parenchymal stiffness quantified in vivo by magnetic resonance elastography. *Proc Natl Acad Sci USA*, 109:6650–6655, 2012.

[55] K Riek, JM Millward, I Hamann, S Mueller, CF Pfueller, F Paul, J Braun, C Infante-Duarte, and I Sack. Magnetic resonance elastography reveals altered brain viscoelasticity in experimental autoimmune encephalomyelitis. *NeuroImage: Clin*, 1:81–90, 2012.

[56] G McKhann, D Drachman, M Folstein, R Katzman, D Price, and E M Stadlan. Clinical diagnosis of Alzheimer's disease: report of the NINCDS-ADRDA Work Group under the auspices of Department of Health and Human Services Task Force on Alzheimer's Disease. *Neurology*, 34:939–944, 1984.

[57] H Seelaar, J D Rohrer, Y A L Pijnenburg, N C Fox, and J C van Swieten. Clinical, genetic and pathological heterogeneity of frontotemporal dementia: a review. *J Neurol Neurosurg Psychiatry*, 82:476–486, 2011.

[58] WJ Schulz-Schaeffer. The synaptic pathology of alpha-synuclein aggregation in dementia with Lewy bodies, Parkinson's disease and Parkinson's disease dementia. *Acta Neuropathol*, 120:131–143, 2010.

Chapter 4

Establishing collaborations to refine protocol for Brain MRE in Edinburgh

Plan for the Chapter

This chapter has four specific objectives: (1) to identify the most widely used and highly published brain MRE protocols in both research and clinical use; (2) to consider methods of actuation most suitable for older participants or patient populations; (3) to obtain phantom MRE data using the aforementioned protocols for comparison with pre-determined quasi-static measurements; and (4) to obtain exemplar brain MRE images of the same subject. As a result of these objectives, the intention is to consolidate collaborations with the associated research centres to refine an experimental protocol for installation at the Edinburgh Imaging Facility, QMRI (EIF-QMRI).

4.1 Introduction

Chapter 3 consisted of a literature search to identify studies that had investigated and reported values for the mechanical properties of the human brain using MRE. Studies report methods using different modes of actuation, vibration frequencies, image resolutions, and inversion algorithms. This variability in methods has caused considerable variation of shear stiffness, μ (kPa) estimates for the cerebrum in healthy participants [1].

From the literature review, I note that a significant proportion of studies were performed at three centres, namely: (1) the Department of Radiology, Mayo Clinic, USA; (2) Beckman Institute, the University of Illinois at Urbana-Champaign, USA, and (3) Department of Radiology, Charité – Universitätsmedizin Berlin. For a breakdown of the relative contribution from each centre investigating the brain of heathy participants or patient populations, see Figure 4.1. The three aforementioned centres contributed 71% of publications that investigated the mechanical properties of the brain in healthy participants; it is worth mentioning that the other 29% was made up of contributions from five other centres. For investigations into clinical conditions, the three centres made up 88% of publications, whereas the other 12% was contributed by three other research groups.

Notably, these research centres employ fundamentally different methods from one another to study the human brain. For example, the Mayo Clinic have typically used a relatively low-resolution gradient-echo EPI sequence (3mm) at a single frequency of 60 Hz, and analyse the displacements by calculating the curl and performing a 3D direct inversion. The shear stiffness, μ (kPa) parameter is usually reported. From now on, this approach will be referred to as *single frequency DI* (SF-DI). In contrast, the University of Illinois at Urbana-Champaign (UIUC) have employed a novel high-resolution MRE spiral acquisition at 50 Hz in combination with a finite-element-based non-linear

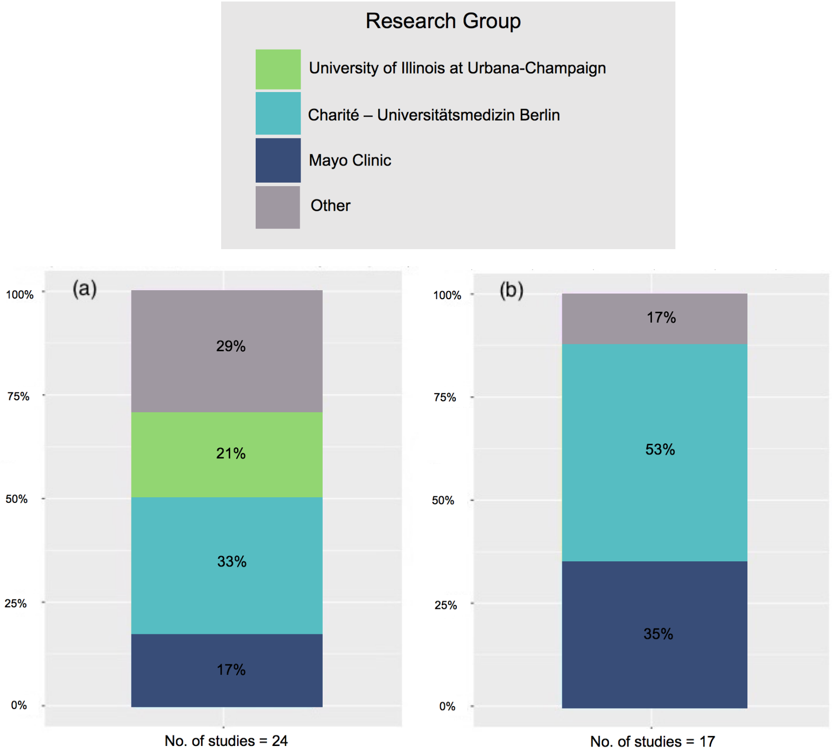

Figure 4.1: Stacked bar plot to display the composition of brain MRE publications according to research centre for the study of: (a) healthy participants and, (b) patients with neurological disorders.

inversion algorithm; now to be described as *single frequency NLI* (SF-NLI). UIUC have more recently begun to report two parameters of shear stiffness, μ (kPa), and damping ratio, ξ. Finally, the group at Charité – Universitätsmedizin Berlin typically acquire data at multiple frequencies using a fast single-shot spin-echo EPI sequence and have more recently used an inversion approach known as multi-dual elasto-visco inversion (MDEV) or the Elastography Software Pipeline (ESP), to produce maps of the magnitude of the complex shear modulus $|G^*|$ and its phase angle ϕ. These approaches will be referred to as *multi-frequency MDEV* (MF-MDEV) or *multi-frequency ESP* (MF-ESP). A summary of each protocol is illustrated in Figure 4.2.

In this chapter, I visited each of the three research centres to perform a phantom and human brain study of the same subject (LH). These visits also allowed an opportunity to assess common methods of actuation with patient comfort and operator convenience essential aspects to consider. Exemplar MRE phantom and brain images were then evaluated. To achieve this, I introduce a new SNR measure to MRE that utilises the inherent aspect of repeat acquisitions (i.e. phase offsets and motion encoding directions) to provide a more robust assessment of MRE raw image signal quality. SNR is a

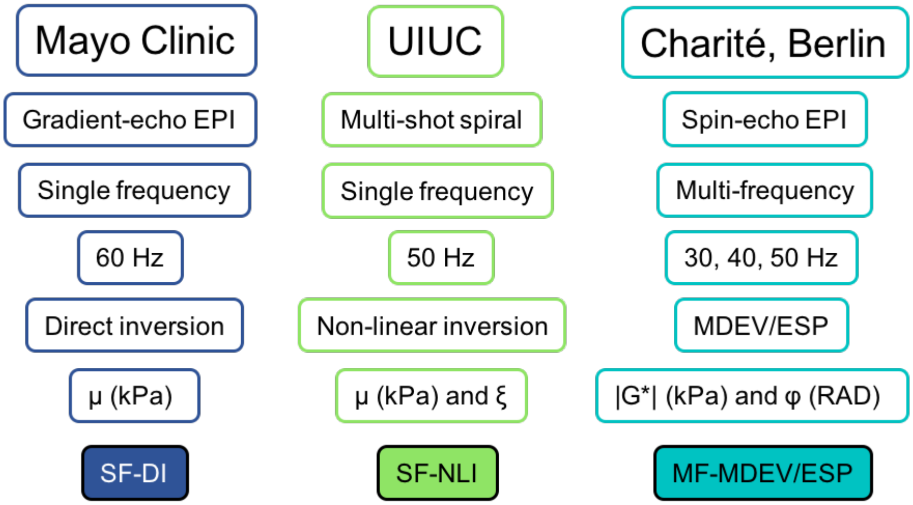
Mayo Clinic
Gradient-echo EPI
Single frequency
60 Hz
Direct inversion
μ (kPa)
SF-DI
UIUC
Multi-shot spiral
Single frequency
50 Hz
Non-linear inversion
μ (kPa) and ξ
SF-NLI
Charité, Berlin
Spin-echo EPI
Multi-frequency
30, 40, 50 Hz
MDEV/ESP
|G*| (kPa) and φ (RAD)
MF-MDEV/ESP

Figure 4.2: Summary of the experimental brain MRE protocols used throughout this chapter.

measure of how much true signal (e.g. reflecting actual anatomy) versus random superimposed signals (background noise). The most commonly used technique is based on the signal statistics in two separate regions of interest (ROIs) from a single image: one in the tissue of interest to determine the signal intensity, and one in the image background to measure the noise intensity. However, conventionally determined SNR, based on separate signal and noise regions in a single image, will in general not agree with the true SNR measured in images after the application of certain reconstruction filters, multi-channel reconstruction, or parallel imaging [2]. Since MRE provides repeat acquisitions in terms of phase offsets and motion encoding directions, SNR will be calculated using the so-called Dietrich method [2]:

$$SNR_{mult} = \frac{S_{mult}}{\sigma_{mult}} \tag{4.1}$$

where each voxel contains the SNR for that particular location. The 'signal' part of SNR$_{mult}$ for an ROI is the mean of the signal over time, whereas the ‘noise’ is represented by the mean standard deviation over time. Using this equation, the SNR of MRE magnitude images from each protocol will be calculated. The ability of each MRE elastogram to detect all targets (inclusions 1-4) and how closely the MRE phantom results match the quasi-static measurements provided by the phantom manufacturer will be compared. Further, the correlation between MRE results and quasi-static values for each of the stiffness targets and background (BG) will be evaluated. In addition, the similarity of the brain MRE elastograms will be assessed visually and the quantitative values compared with one another and to those found in the existing literature.

Previous brain MRE images in this thesis have been shown in a colour look up table (LUT) known as *aaasmo.* This is routinely used for liver MRE and shows stiffer tissue in red, and softer tissue in purple. However, this LUT does not have a continuous intensity gradient and therefore regions of stiffness may look exaggerated. To counteract these issues, I propose using a LUT known as *Parula*; the new default colour map used within MATLAB. *Parula* is red-green colour blind friendly, has a continuous intensity gradient (i.e. increases monotonically in lightness), and preserves scale when printing in greyscale. As a result, *Parula* will now be used throughout the rest of this thesis to visualise tissue stiffness.

4.2 Methods

4.2.1 *Study of Phantom Object*

The phantom used in this study was the CIRS elasticity QA model 049 phantom *Computerised Imaging Reference Systems Inc., Norfolk, Virginia, USA*. The phantom is marketed primarily for use in ultrasound elastography but was also designed such that it is MR-compatible, and has previously been used as a validation tool in MRE [3,4]. The phantom is constructed from a synthetic elastic substance, Zerdine and is a 135 x 95 x 190mm cuboid containing eight spherical inserts. Four of the inserts are at a depth of 15mm and are 10mm in diameter, whilst the other set, in a separate *yz*-plane, are at a depth of 35mm and of 20mm in diameter, see Figure 6.3. For this study, only the larger inserts of the phantom are investigated. The material properties were provided by the manufacturer as Young's moduli and were 8, 18, 48 and 80 kPa for the four inserts, and 23 kPa for the background. This equates to a shear modulus of 2.70, 6.0, 16.0, and 27 kPa, with a background of 7.70 kPa, as the Young's modulus and the shear modulus are related by a simple scale factor of 3: $E = 3\mu$. Due to factors such as pre-loading and a changing response to small strains [5, 6], quasi-static testing may produce different stiffness values to dynamic testing in the range of biological tissue. However, the stiffness values measured by MRE are expected to be in proportion to the manufacturer's reported values.

4.2.2 *Details of Phantom Data Acquisition and Analysis*

Prior to MRE imaging, a localised sequence was used to visualise the location of the inserts. Detailed imaging parameters for each protocol are provided in Table 4.1. To ensure consistency, the MRE

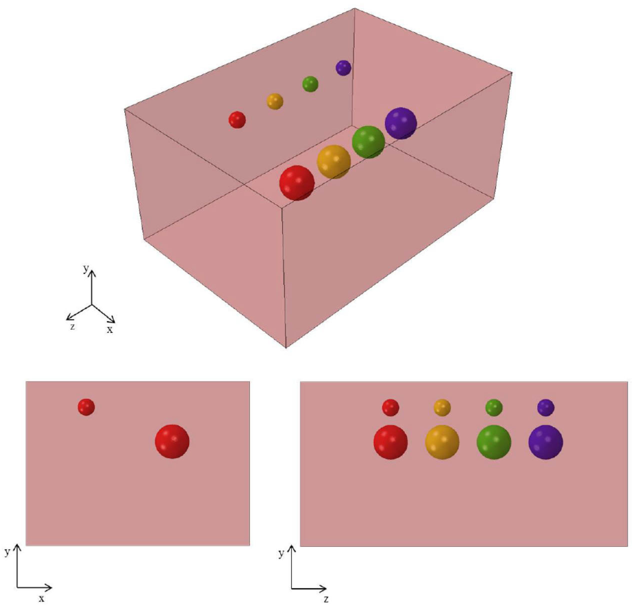

Figure 4.3: Computer-aided-design (CAD) illustration showing the design of the CIRS phantom used in this study. Image taken from Hollis et al., 2016 [7], and used with permission.

acquisition and analysis protocol typically used at each research centre to image the human brain was used to scan the phantom. The mechanical frequencies, however, were increased as 50-60 Hz, typically used for the human brain, would be too low to detect the stiffest inclusions. To obtain quantitative measures of Dietrich SNR and MRE for each insert, the ROI was first identified on the MRE magnitude image and manually traced using ImageJ [8]. Each ROI was then superimposed onto the SNR and MRE images. To quantify the background (BG) region, a large rectangular homogeneous region was selected below the location of the inserts.

(1) Single frequency DI (SF-DI)

Data acquisition

Data presented here represents a typical Mayo Clinic acquisition and analysis pipeline (collected at UIUC). A gradient-echo EPI sequence was used to capture MRE displacement data at a 3mm isotropic resolution. A MRE liver paddle was positioned underneath the phantom to cause displacements in the superior-inferior direction, as shown in Figure 4.4 **A**. Vibrations were generated at 100 Hz, with a vibration amplitude set to 30%, using the Resoundant actuator (Resoundant; Rochester, MN) as shown in Figure 4.4 **B**.

Table 4.1: Imaging parameters used to scan the CIRS phantom

Protocol	SF-DI	SF-NLI	MF-MDEV/ESP
MRI parameters			
Scanner	Siemens Trio	Siemens Trio	Siemens Trio
Field Strength	3T	3T	3T
Sequence type	GRE-EPI	Spiral	SE-EPI
TR (ms)	3997	180	4330
TE (ms)	60.8	75/135	83
Matrix size	128 x 128	150 x 150	100 x 100
Flip angle (degree)	90	90	90
Bandwidth (Hz)	250000	3922	1724
Isotropic voxel size	$3mm^3$	$1.6mm^3$	$2mm^3$
No. of slices	36	60	60
MRE parameters			
Mechanical Frequency (Hz)	100	100	70, 80, 90, 100
Phase encode	R>>L	N/A	R>>L
Phase offsets	8	4	8

Data analysis

Phase images were processed using *MRE-Lab*, an in-house software programme developed at the Mayo Clinic. A direct inversion algorithm, with curl application, produced a map of shear stiffness, μ.

(2) Single frequency NLI (SF-NLI)

Data acquisition

MR data were acquired at UIUC using a Siemens 3T Trio system (Siemens, Medical Solutions; Erlangen, Germany). A 3D multislab, multishot spiral sequence was used to capture whole-brain MRE displacement data at a 1.6mm isotropic resolution [9]. Vibrations were generated at 100 Hz by the liver paddle in combination with the Resoundant actuator (Resoundant; Rochester, MN).

Data analysis

Nonlinear inversion (NLI) [10], was used to determine the magnitude of the complex shear modulus $|G^*|$, from which the shear stiffness $\mu = 2|G^*|^2/\ (G' + |G^*|)$ was computed. Iteration structure was set to [1,0,0,1], [2,0,0,2], [3,0,0,2] and spatial filtering weight was originally set to at .0030 and finished at .0015. (Note: spatial filtering (SF) has a stabil-

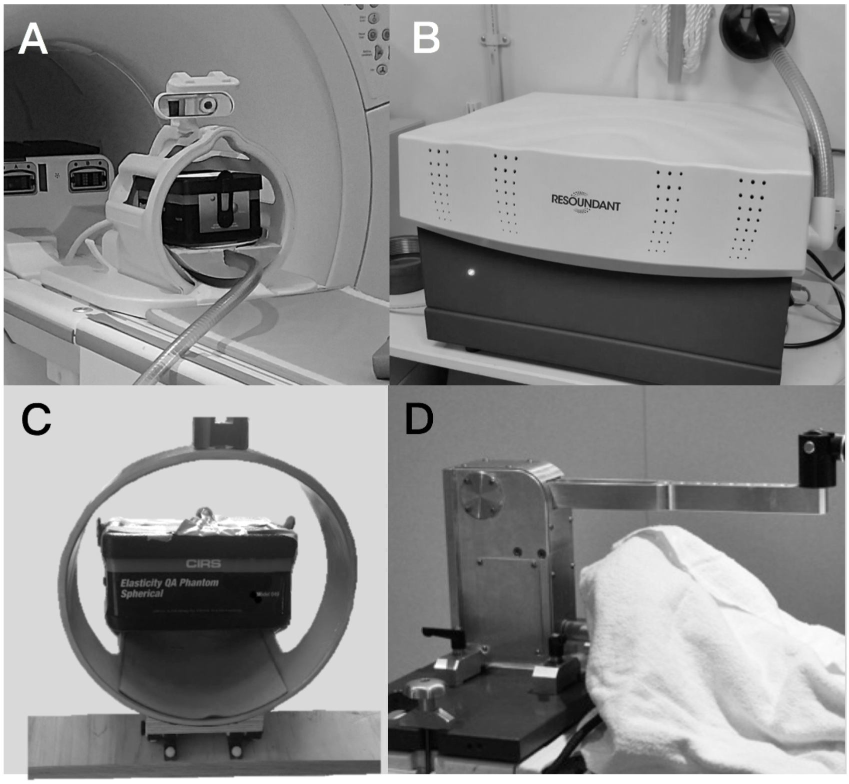

Figure 4.4: (a) Position of the phantom in the scanner at UIUC, and (b) the adjoining Resoundant actuator; (c) the phantom positioned in the head-cradle at Charité, Berlin, which in turn is attached to the (d) non-magnetic piezoelectric driver, via a carbon fibre rod.

ising effect on MRE measures; higher SF assists in early iterations when the algorithm is far from a solution).

(3) Multi-frequency MDEV/ESP (MF-MDEV/ESP)

Data acquisition

MR data were acquired at Charité, Berlin using a Siemens 3T Trio system (Siemens, Medical Solutions; Erlangen, Germany). A single-shot EPI was used to capture 60 slices at a 2mm isotropic resolution. Vibrations were generated at 70, 80, 90 and 100 Hz by a head-cradle attached to a carbon fibre rod and piezoelectric system as shown in Figures 4.4 **C** and **D**.

Data analysis

Multi-dual visco-elasto (MDEV) inversion [11], and the Elastography Software Pipeline (ESP) [12], were used to produce maps of the magnitude of the complex shear modulus $|G^*|$. As for typical MDEV processing, a 2D low-pass filter, based on 2D Fourier transform, and Butterworth Kernel with a 50 m^{-1} threshold, were applied to all three components of the wave field. ESP performed a 2D analysis with a denoise method of 1 and interpolation set to zero.

4.2.3 *Study of Human Subject*

The same participant was scanned at each research centre within 8 months (age 27; female; no known neurological disorder). Detailed imaging parameters for each protocol are provided in Table 4.2.

Table 4.2: Summary of the MRI/MRE parameters used to study the same human subject

Protocol	SF-DI	SF-NLI	MF-MDEV/ESP
MRI parameters			
Scanner	SIGNA Excite, GE	Siemens Trio	Siemens Trio
Field Strength	3T	3T	3T
Sequence type	GRE-EPI	Spiral	SE-EPI
TR (ms)	4320	180	4330
TE (ms)	69.1	75/135	83
Matrix size	128 x 128	150 x 150	100 x 100
Flip angle (degree)	90	90	90
Bandwidth (Hz)	3906	3922	1724
Coverage	Whole brain	Whole brain	Superior region
Isotropic voxel size	$3\mathrm{mm}^3$	$1.6\mathrm{mm}^3$	$2\mathrm{mm}^3$
No. of slices	48	60	20
MRE parameters			
Mechanical Frequency (Hz)	60	50	30, 40, 50
Phase encode	R>>L	N/A	R>>L
Phase offsets	8	4	8
MRE scan duration	6.47 minutes	12 mins	5 mins

4.2.4 *Details of Human Brain Data Acquisition and Analysis*

(1) Single frequency DI (SF-DI)

Data acquisition

MR data were acquired at the Mayo Clinic using a SIGMA Excite, GE 3T MRI scanner. A gradient-echo EPI sequence was used to capture whole-brain MRE displacement data at a 3mm isotropic resolution. Vibrations were generated at 60 Hz by the head-pillow using the Resoundant actuator (Resoundant; Rochester, MN).

Data analysis

Phase images were automatically processed on the scanner, using a direct inversion algorithm, to produce a map of shear stiffness, μ (kPa).

(2) Single frequency NLI (SF-NLI)

Data acquisition

MR data were acquired at UIUC using a Siemens 3T Trio system (Siemens, Medical Solutions; Erlangen, Germany). A 3D multislab, multishot spiral sequence was used to capture whole-brain MRE displacement data at a 1.6mm isotropic resolution [9]. Vibrations were generated at 50 Hz by the head-pillow using the Resoundant actuator (Resoundant; Rochester, MN).

Data analysis

Nonlinear inversion (NLI), was used to determine the magnitude of the complex shear modulus $|G^*|$, from which the shear stiffness, $\mu = 2|G^*|^2/\ (G' + |G^*|)$ was computed. Iteration structure was set to [1,0,0,1], [2,0,0,2], [3,0,0,2] and spatial filtering weight was originally set to at .0030 and finished at .0015. (Note: spatial filtering (SF) has a stabilising effect on MRE measures; higher SF assists in early iterations when the algorithm is far from a solution).

(3) Multi-frequency MDEV/ESP (MF-MDEV/ESP)

Data acquisition

MRE data were acquired at Charité, Berlin using a Siemens 3T Trio system (Siemens, Medical Solutions; Erlangen, Germany). A single-shot spin-echo EPI sequence was used to capture 20 slices of the superior region of the brain at a 2mm isotropic resolution. Three vibration frequencies of 30, 40 and 50 Hz were consecutively applied, as recently published by the Charité group [13]. MRE was performed utilising a head cradle actuator connected to a piezo-electrical vibration generator as detailed by Guo *et al.,* 2013 [14].

Data analysis

Multi-dual visco-elasto (MDEV) inversion [11], and the Elastography Software Pipeline (ESP) [12], were used to produce maps of the magnitude of the complex shear modulus

$|G^*|$. As with the phantom, a 2D low-pass filter, based on 2D Fourier transform, and Butterworth Kernel with a 50 m^{-1} threshold, were applied to all three components of the wave field. ESP performed a 3D analysis, with dtnoise *z-xy* set to 0.3 and interpolation x 4.

4.3 Results

4.3.1 *Phantom Results*

Example raw MRE magnitude images, Dietrich SNR maps and MRE elastograms from each protocol are provided in Figure 4.5.

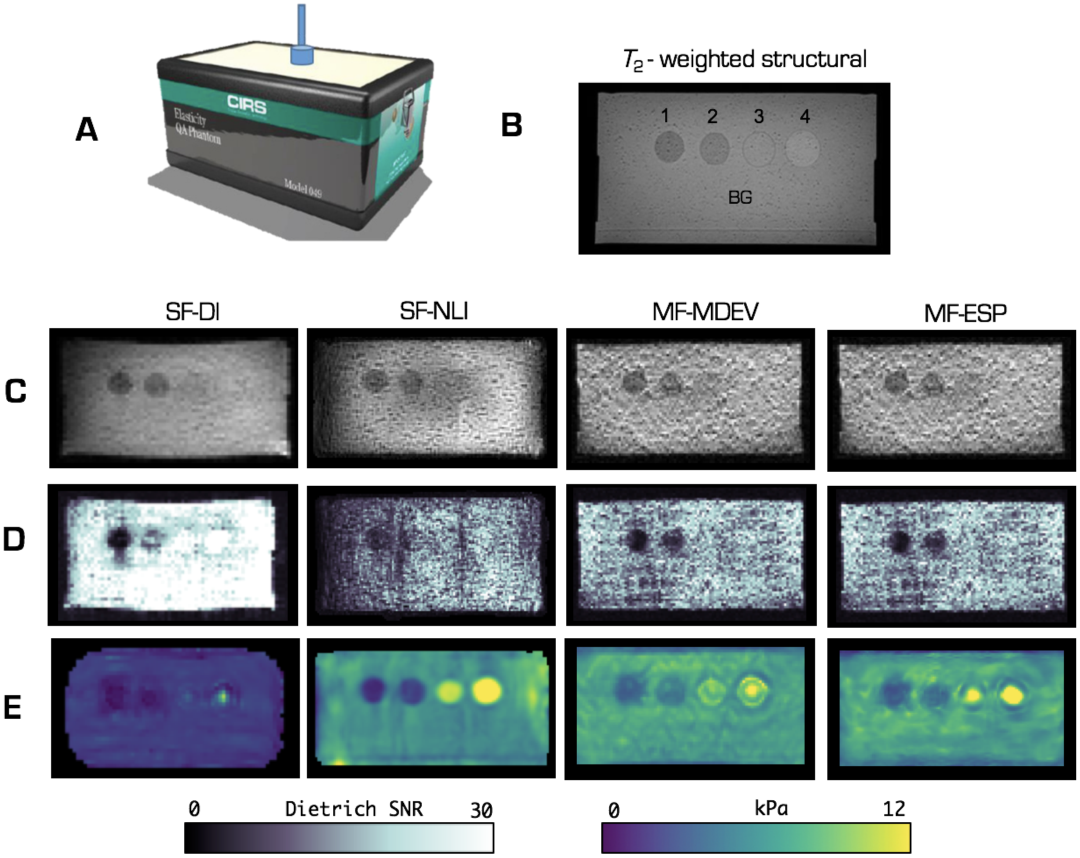
A
CIRS
Elasticity QA Phantom
Model 049
B
T_2 - weighted structural
1
2
3
4
BG
SF-DI
SF-NLI
MF-MDEV
MF-ESP
C
D
E
0
Dietrich SNR
30
0
kPa
12

Figure 4.5: MRE data presented from each protocol for the CIRS phantom: (a) illustration of phantom. Source: Honarvar et al., 2017 [15]; (b) high-resolution T_2-weighted structural image; Representative image slice of: (c) raw MRE magnitude; (d) Dietrich SNR, and (e) MRE elastogram. Abbreviations: SF-DI, single-frequency direct inversion; SF-NLI, single-frequency non-linear inversion; MF-MDEV, multi-frequency multi-dual elasto-visco inversion; MF-ESP, multi-frequency inversion using the elastography software pipeline.

As shown in Figure 4.5, greatest Dietrich SNR was provided by the use of the gradient-echo EPI sequence as part of the SF-DI protocol (28.52). This was to be expected due to the larger voxel size of 3mm. In contrast, SF-NLI resulted in the lowest SNR with signal drop out near the periphery (13.82). However, in terms of elastogram quality, the SF-DI protocol does not clearly define the four inserts, whereas SF-NLI produces exceptionally clear boundaries for all targets. MF-MDEV clearly defines all inserts, although a ringing artefact is particularly noticeable in Target 4. There are some minor distortions visible across the image slice for MF-ESP.

Table 4.3 provides quantitative MRE measurements from all four protocols. Mean differences (%) between each protocol and the quasi-static value for each target and background (BG) are provided in Table 4.4. To visualise the accuracy of the MRE protocols, a plot of the recovered values is provided against the manufacturer values in Figure 4.6. Bland-Altman plots were also used to assess the agreement between the 2 measures (e.g. the measured *in vivo* MRE stiffness versus the quasi-static measurements provided by the manufacturer), and are illustrated in Figure 4.7. The differences between the 2 measures are provided on the y-axis, and the average of the values are plotted on the x-axis.

Table 4.3: Phantom results from four different MRE protocols

	Target 1	Target 2	Target 3	Target 4	Background
Quasi-static	2.70	6.00	16.00	27.00	7.70
(1) SF-DI	0.86±0.44	1.03±0.37	2.51±0.42	3.51±2.21	2.15±0.21
(2) SF-NLI	1.41±0.13	2.38±0.18	10.86±0.18	15.80±0.57	5.93±0.33
(3) MF-MDEV	3.81±0.32	5.35±0.56	8.51±0.75	10.84±1.88	6.84±0.50
(4) MF-ESP	3.47±0.36	4.44±0.30	11.73±1.72	24.87±3.97	6.97±0.71

SF-DI and SF-NLI elastograms are presented as the shear stiffness, μ, whereas MF-MDEV and MF-ESP elastograms are presented as $|G^{*}|$.

Table 4.4: Difference (%) between MRE values and manufacturer specifications

	Target 1	Target 2	Target 3	Target 4	BG	Mean difference
(1) SF-DI	214%	483%	537%	669%	72%	395%
(2) SF-NLI	91%	152%	47%	71%	30%	78%
(3) MF-MDEV	29%	12%	88%	149%	13%	58%
(4) MF-ESP	22%	35%	36%	9%	10%	22%

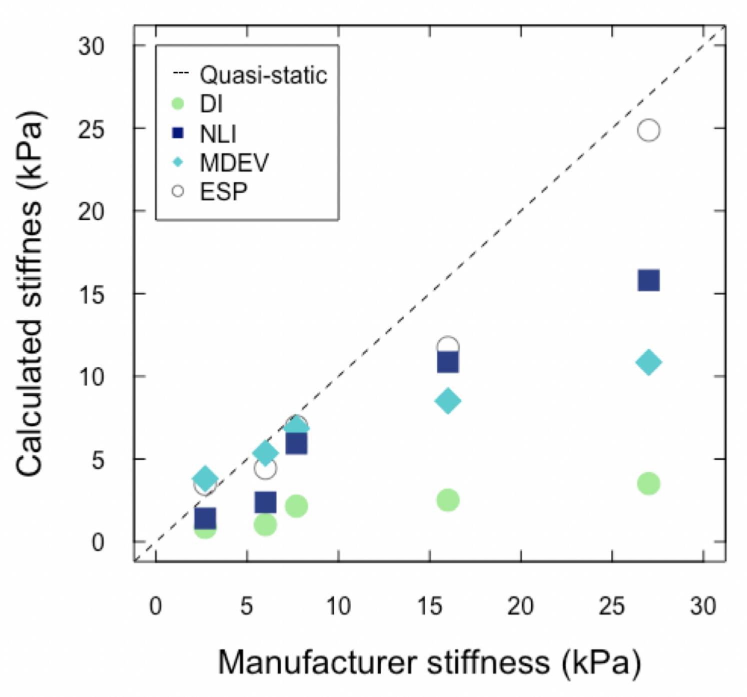

Figure 4.6: Recovered stiffness values (kPa) from each protocol, plotted against manufacturer specifications.

All protocols exhibited a very high and significant correlation coefficient with the quasi-static measurements (in the range of $R = 0.95$ - 0.99). Values generated by MF-ESP had the most accurate results on average, with a mean bias of 1.84 kPa when compared to manufacturer values using the Bland-Altman method, as shown in Figure 4.7. The mean bias was 9.86 kPa for SF-DI, 4.60 kPa for SF-NLI, and 4.81 kPa for MF-MDEV. On average, the MF-ESP protocol scores best by reporting values that differ by only 22% from the quasi-static measurements. In contrast, the SF-DI protocol differs from the manufacturer specifications by nearly 400%. Largely evident, however, is that all are below the values reported by the manufacturer, particularly for the stiffest inclusion of 27 kPa (Target 4). This is likely to be due to the vibration frequencies chosen to image the phantom (≈100 Hz), and the need for the use of higher vibration frequencies.

Considering the measurements most closely resembling the stiffness of biological tissue (Target 1), MF-MDEV and MF-ESP, were most accurate with a mean difference of 29% and 22%, respectively. While both MDEV and ESP use the same inversion equations, they use entirely different filtering and phase unwrapping techniques. Lower values by MDEV can be ascribed to loss of low-frequency bandwidth from the inversion, whereas ESP inverts original displacements and uses a divergence-free-

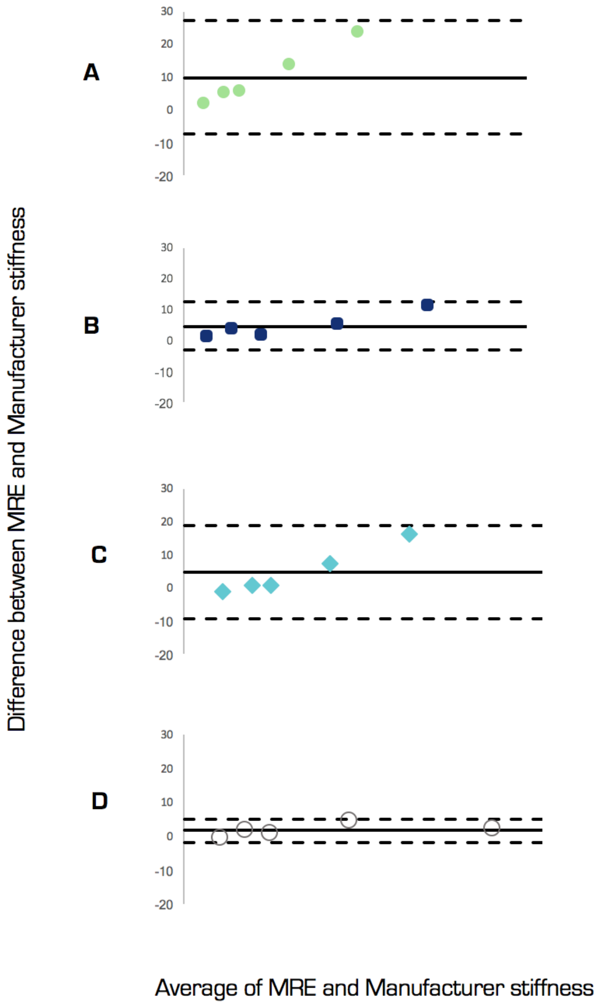

Figure 4.7: Bland-Altman method, used to evaluate calculated stiffness of the phantom between in vivo MRE and the quasi-static measurement provided by the manufacturer. The 95% confidence limits of the bias are shown as two dashed lines, with the mean value of the differences shown as a solid line. Panel (a) shows SF-DI, (b) NLI, (c) MF-MDEV, and (d) MF-MDEV protocols. (a-c) show increased variance with increasing stiffness, whereas (d) shows the least bias between measurements.

wavelet to remove bulk wave artefacts, to retain longer wavelengths resulting in the capability to measure the stiffest inclusion (Target 4) more accurately.

All four protocols provided a largely homogenous map for the background (BG) region. Methods using the local homogeneity assumption are expected to work well in areas where the elasticity is almost constant; the homogeneity assumption is not expected to deteriorate the inversion since the region is homogenous. SF-NLI does not use the local homogeneity assumption, and thus performance in regions of elasticity variation are expected to be superior, as illustrated.

4.3.2 *Human Brain Results*

Example raw MRE magnitude images, Dietrich SNR maps and MRE elastograms from each protocol are provided in Figure 4.8. Note that the edge profile of the SF-NLI elastogram is altered due to the data masking process required by the finite-element meshing process of NLI. The quantitative MRE results of the global cerebrum are provided in Table 4.5. Due to differences in brain coverage acquired across protocols, only the stiffness of the illustrated slice is measured and quantified, with the slices matched visually. SF-DI and SF-NLI elastograms are presented as the shear stiffness, μ, whereas MF-MDEV and MF-ESP elastograms are presented as $|G^*|$.

Table 4.5: Stiffness values from four different MRE protocols

Protocol	Stiffness (kPa)
(1) SF-DI	2.80 ± 0.64
(2) SF-NLI	3.29 ± 0.79
(3) MF-MDEV	2.05 ± 0.74
(4) MF-ESP	2.22 ± 1.12

Dietrich SNR was highest for the SF-DI protocol (64.52); as per the phantom images, this is to be expected due to the lower spatial resolution of 3mm voxels. The SNR for SF-NLI and MF-MDEV/ESP was 12.53 and 11.87, respectively. The magnitude images of the MF-MDEV/ESP protocols also display some distortion in the phase encoding dimension (R>>L). This is a result of the spin-echo EPI sequence utilised for the acquisition, and the inherent susceptibility of EPI to regions near air-filled cavities (a regional effect that is determined by the local magnetic susceptibility gradients). On initial visual inspection of the elastograms, there are few, if any, landmarks of correspondence. The ventricles are clearly defined on the MDEV and ESP elastograms, whereas there are patches of higher stiffness near the putamen on the SF-NLI elastogram. Of note, the resulting property map resolution from NLI has been estimated as approximately half that of the imaging resolution [16], as regularisation is needed to stabilise results in the presence of noise and model-data mismatch.

Overall, Figure 4.8 indicates that stiffness is highest for SF-NLI and lowest for MF-MDEV. Comparing the quantitative values generated for the global cerebrum, NLI was indeed highest at 3.29 kPa. As expected, this agrees with values reported published studies at UIUC. Johnson *et al.,* 2016 report a shear stiffness, μ value of 3.20 kPa in a sample of 21 healthy young adults. Second, SF-DI generates a value of 2.80 kPa which is similar to those reported by Huston *et al.* 2015 (2.76 kPa), and

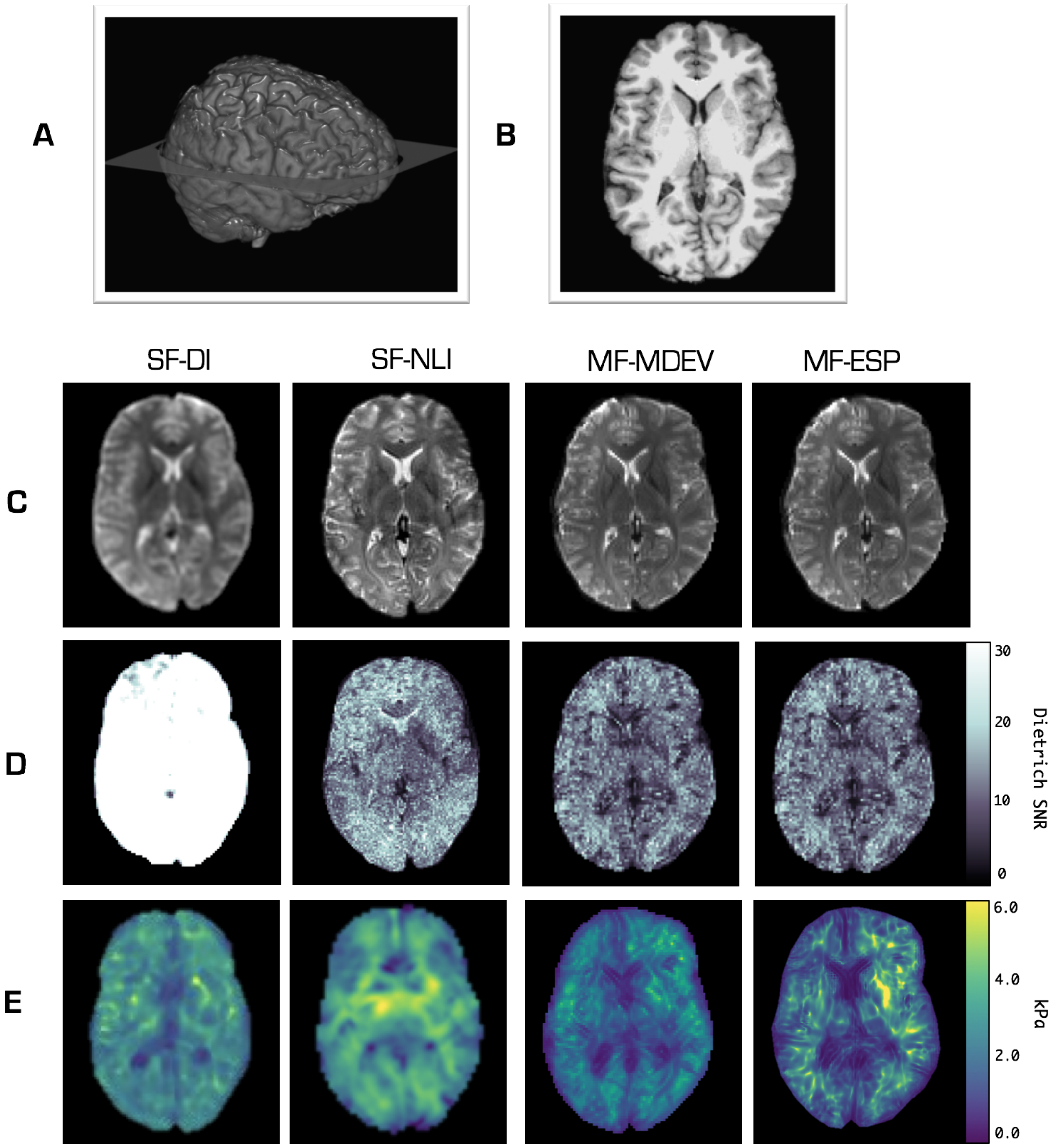

Figure 4.8: MRE data presented from each protocol for the same subject (LH) and similar slice: (a) 3D rendering of T_1-weighted MPRAGE highlighting the illustrated slice; (b) the aforementioned high-resolution T_1 axial slice; (c) MRE magnitude image; (d) Dietrich SNR, and (e) MRE stiffness map. Key: SF-DI, single-frequency direct inversion; SF-NLI, single-frequency non-linear inversion; MF-MDEV, multi-frequency multi-dual elasto-visco inversion; MF-ESP, multi-frequency inversion using the elastography software pipeline.

Murphy *et al.*, 2013 (2.99 kPa). MF-MDEV and MF-ESP report considerably lower brain stiffness estimates in comparison to those mentioned previously. This is to be expected as incorporating lower frequencies, with naturally higher wave amplitudes, have been shown to be more influential within inversion [17]. Low values are particular evident in cortical regions and may be caused by fluid-filled tissue heterogeneities such as sulci in the brain (thus reflecting edge-related biases). Nevertheless, MF-MDEV reported a value of 2.05 kPa at frequencies of 30, 40, 50 Hz which is within the range published by the Charité group. Dittmann *et al.,* 2015 reported a value of 1.56 kPa using 25, 30, 35 Hz and 2.18 kPa using 40, 45, 50 Hz [17].

Moreover, the MF-ESP protocol generates slightly higher values (8% higher) than MF-MDEV at 2.22 kPa. This is in agreement with Barnhill *et al.,* 2016, who reported ESP brain stiffness to be 16% higher than MDEV. ESP could potentially be extracting fine features and retaining a wider stiffness contrast, while removing noise and clutter from known MRE noise sources, thus explaining the higher regions of stiffness in the right hemisphere. Furthermore, values obtained from both MF-MDEV and MF-ESP images of the brain have been shown to correlate very well ($r = 0.85$), suggesting that both methods may deliver an accurate assessment of the relative viscoelastic properties of anatomical structures [12].

4.4 Discussion

This chapter had four objectives: (1) to identify the most widely used and highly published brain MRE protocols in both research and clinical use; (2) to consider methods of actuation most suitable for older participants or patient populations; (3) to obtain phantom MRE data using the aforementioned protocols for comparison with pre-determined quasi-static measurements, (4) to obtain exemplar brain MRE images of the same subject.

The literature review provided in *Chapter 3* allowed the identification of centres who contribute the majority of the research output on brain MRE, namely: Mayo Clinic, University of Illinois at Urbana-Champaign (UIUC), and Charité – Universitätsmedizin Berlin. Each protocol represents a fundamentally different approach to the same problem of deriving mechanical properties from displacement fields and can be broadly summarised into three categories: (a) single frequency direct inversion (SF-DI); (b) single frequency non-linear inversion (SF-NLI), and (c) multifrequency multi-dual elasto-visco inversion/elastography software pipeline (MF-MDEV/ESP).

The second objective of this chapter was to consider methods of actuation that would be both comfortable for older and patient populations and convenient for radiographer operators. Through personal experience of both the pneumatic Resoundant and associated head-pillow, and the piezoelectric device with the associated “head-rocker”, the former was determined to superior for comfort and convenience. Moreover, it is already in clinical use at the Mayo Clinic for preoperative assessment of tumour consistency and is soon to be designated as a FDA-approved product. On the other hand, a piezoelectric system and "head-rocker" actuator would need to be custom-made. Consequently, the Resoundant actuator system was commissioned on the MRI scanner at EIF-QMRI and the head-pillow driver was made available through an associated R&D Agreement with the Mayo Clinic. As such, all experiments performed throughout this thesis will use the Resoundant actuator to generate shear waves, and the head-pillow driver to transmit the shear waves into the brain, as illustrated in Figure 2.2 within *Chapter 2*.

For the phantom study, SF-NLI, MF-MDEV and MF-ESP all achieve good spatial accuracy of the four inserts. The SF-NLI protocol, in particular, clearly delineates each inclusion likely due to the use of the non-homogenous form of the Navier equation. However, another important factor in protocol selection is the processing time. MF-MDEV and MF-ESP are orders of magnitude faster than iterative methods (seconds on a desktop computer compared to hours on a specialised multi-processor cluster). Largely evident, however, is that all values are below the values reported by the manufacturer, particularly for the stiffest inclusion of 27 kPa (Target 4). This is likely to be due to the vibration frequencies chosen to image the phantom (≈100 Hz), and the need for the use of higher vibration frequencies. To illustrate this, we know that speed of sound changes in different media through the equation:

$$s = \frac{E}{p} \tag{4.2}$$

with s the wavespeed, E the elasticity of the material (Pa) and p the assumed density. As a result, the shear waves would travel though the stiffest inclusion of 27 kPa at 5.20m/s assuming a constant density of 1000kg/3. Further, the wavelength λ is associated with wavespeed s and vibration frequency f through $\lambda = \frac{s}{f}$. The wavespeed s of 5.20m/s at the 100 Hz actuation frequency, would therefore result in a shear wavelength of 5.2mm. The size of the inclusion is 20mm, demonstrating that only 4 wave lengths can be sampled within the target. Using the same calculation, I could determine that 200 Hz vibration frequency in a material of 27 kPa would provide shear waves of the order of 2.6mm, which instead allows nearly 8 waves to be sampled within the inclusion. In hindsight, frequencies within this range would have been needed to more accurately correspond to quasi-static measurements. Nevertheless, frequencies in this range would not be suitable for the study of the human brain, and of most interest, was whether MRE values were in proportion to the manufacturer's reported values. As for the human brain data, the images visually match those presented in the literature and the values are within the range of stiffness values published.

4.4.1 *Limitations*

Several limitations impede a thorough or complete comparison of protocols within the phantom study. First of all, it should be recognised that none of the phantom acquisition and analysis protocols were optimised for phantom imaging. Our aim was to instead run the standard brain MRE protocol from each centre in the phantom. This has greatly influenced the accuracy of the phantom results for the SF-DI pipeline. The SF-DI acquisition, typical of the Mayo Clinic, were instead collected from UIUC which uses a Siemens system and not a GE platform. Further, a typical Mayo Clinic protocol would perform edge adaptive processing, which has been shown to provide significant improvements in stiffness measurements for the 6 pixels adjacent to any boundary. Finally, to get accurate stiffness for a region of interest, (an inclusion in the case of the phantom), the ROI would usually be segmented from the T_1-weighted image with the application of mask edge adaptive operations and pixel erosions from each edge. Here, only a global stiffness map is provided without edge adaptive processing. As for the SF-NLI and MF-MDEV protocols, identical inversion parameters were used for the phantom as what would be typical for brain. MF-ESP, however, would usually use an interpolation factor (x4) for brain imaging, but interpolation was omitted for the phantom study due to the presence of significant artefacts.

Importantly, the brain acquisitions were entirely typical of the pipelines used at each research centre. This is confirmed by near identical values found from each protocol within the published literature. However, these results highlight the current discrepancies within brain MRE. Identical stiffness values for the same brain slice from the same subject would be expected. Another aspect of the acquisition that may also be contributing to these discrepancies is the direction of the primary source of motion. The principal direction of motion for MF-MDEV and MF-ESP is in the superior-inferior direction, whereas the primary source of motion in SF-NLI is in the anterior-posterior direction. MRE measurements have previously been shown to be direction-dependent, particularly in highly anisotropic regions such as white matter, and so this is another aspect of the study to take into consideration [18]. Nevertheless, this study has been useful in understanding the relative differences in MRE measurements that are apparent across the literature that simply arise because of the choice of MRE protocol.

4.5 Conclusion

All future work in this thesis will utilise the SF-NLI and MF-MDEV pipelines to generate high-resolution brain MRE elastograms. SF-NLI is chosen for its superior ability to clearly delineate each inclusion within the phantom and the inherent use of the non-homogenous form of the Navier equation. The brain is a highly heterogeneous organ and therefore it stands to reason that a heterogeneous model will be more spatially accurate, especially at tissue boundaries, where there are slowly varying material properties. MF-MDEV will also be used due to high accuracy for phantom measurements that closely match those expected for biological tissue. While MF-ESP was determined to be more accurate than MF-MDEV, there has been significantly less use of MF-ESP within the literature. MF-ESP holds promise for the future, but was omitted for use throughout this thesis, as significant developments are necessary to ensure stability. Furthermore, SF-NLI and MF-MDEV both offer a two-parameter approach, unlike SF-DI, which will increase sensitivity for meeting the thesis objectives. In the next chapter, both high-resolution pipelines are installed, optimised and validated at the EIF-QMRI through the collaborations established as a result of this study.

References

[1] LV Hiscox, CL Johnson, E Barnhill, MDJ McGarry, J III Huston, EJR van Beek, JM Starr, and N Roberts. Magnetic resonance elastography (MRE) of the human brain: technique, findings and clinical applications. *Phys Med Biol*, 61:401–437, 2016.

[2] O Dietrich, JG Raya, SB Reeder, MF Reiser, and SO Schoenberg. Measurement of signal-to-noise ratios in MR images: influence of multichannel coils, parallel imaging, and reconstruction filters. *J Magn Reson Imaging*, 26:375–385, 2007.

[3] M Honarvar, R Sahebjavaher, R Sinkus, R Rohling, and SE Salcudean. Curl-based finite element reconstruction of the shear modulus without assuming local homogeneity: Time harmonic case. *IEEE Trans Med Imaging*, 32:2189–2199, 2013.

[4] A Baghani, S Salcudean, M Honarvar, RS Sahebjavaher, R Rohling, and R Sinkus. Travelling wave expansion: a model fitting approach to the inverse problem of elasticity reconstruction. *IEEE Trans Med Imaging*, 30:1555–1565, 2011.

[5] VT Nayar, JD Weiland, CS Nelson, and AM Hodge. Elastic and viscoelastic characterization of agar. *J Mech Behav Biomed Mater*, 7:60–68, 2012.

[6] A Samani, J Bishop, C Luginbuhl, and DB Plewes. Measuring the elastic modulus of ex vivo small tissue samples. *Phys Med Biol*, 48:2183–2198, 2003.

[7] L Hollis. Development of finite element analysis of magnetic resonance elastography to investigate its potential use in abdominal aortic aneurysms. *University of Edinburgh*, 2016.

[8] ImageJ. Website: https://imagej.nih.gov/ij/.

[9] CL Johnson, JL Holtrop, MDJ McGarry, JB Weaver, KD Paulsen, JG Georgiadis, and BP Sutton. 3D multislab, multishot acquisition for fast, whole-brain MR elastography with high signal-to-noise efficiency. *Magn Reson Med*, 71:477–485, 2014.

[10] MDJ McGarry, EEW Van Houten, CL Johnson, JG Georgiadis, BP Sutton, JB Weaver, and KD Paulsen. Multiresolution MR elastography using nonlinear inversion. *Med Phys*, 39:6388–6396, 2012.

[11] K-J Streitberger, M Reiss-Zimmermann, FB Freimann, S Bayerl, J Guo, F Arlt, J Wuerfel, J Braun, K-T Hoffmann, and I Sack. High-Resolution Mechanical Imaging of Glioblastoma by Multifrequency Magnetic Resonance Elastography. *PLoS One*, 9:e110588, 2014b.

[12] E Barnhill, L Hollis, I Sack, J Braun, PR Hoskins, P Pankaj, C Brown, EJR van Beek, and N Roberts. Nonlinear multiscale regularisation in MR elastography: Towards fine feature mapping. *Med Image Anal*, 35:133–145, 2016.

[13] S Hetzer, P Birr, A Fehlner, S Hirsch, F Dittmann, E Barnhill, J Braun, and I Sack. Perfusion alters stiffness of deep gray matter. *J Cereb Blood Flow Metab*, page 271678X17691530, 2017.

[14] J Guo, S Hirsch, A Fehlner, S Papazoglou, M Scheel, J Braun, and I Sack. Towards an elastographic atlas of brain anatomy. *PLoS One*, 8:e71807, 2013.

[15] M Honarvar, RS Sahebjavaher, R Rohling, and SE Salcudean. A comparison of finite element-based inversion algorithms, local frequency estimation, and direct inversion approach used in MRE. *IEEE Trans Med Imaging*, 36:1686–1698, 2017.

[16] MDJ McGarry. Improvement and Evaluation of Nonlinear Inversion MR Elastography. *Dartmouth College*, 2013a.

[17] F Dittmann, S Hirsch, H Tzschätzsch, J Guo, J Braun, and I Sack. In vivo wideband multifrequency MR elastography of the human brain and liver. *Magn Reson Med*, doi: 10.1002/mrm.26006, 2015.

[18] AT Anderson, EEW Van Houten, MDJ McGarry, KD Paulsen, JL Holtrop, BP Sutton, JG Georgiadis, and CL Johnson. Observation of direction-dependent mechanical properties in the human brain with multi-excitation MR elastography. *J Mech Behav Biomed Mater*, 59:538–546, 2016.

Chapter 5

Installation, optimisation, and validation of Brain MRE at the Edinburgh Imaging Facility, QMRI

Plan for the Chapter

This chapter relates to my role in establishing state-of-the-art high-resolution brain MRE in Edinburgh. In particular, my contribution included: (a) establishing collaborations with leading brain MRE research institutes to obtain access to the required MRE pulse sequences and inversion algorithms; (b) the optimisation and validation of MRE pulse sequence design for implementation on the 3 T Siemens Verio MRI system in Edinburgh, and, (c) the novel development of a reliable and user-friendly graphical user-interface (GUI) to perform an automatic and optimised T_1-to MRE image coregistration and subsequent extraction of ROI quantitative measurements.

5.1 Introduction

In the previous chapter, a description was given of the collaborations that have been established with leading brain MRE research groups, and how during a visit to each laboratory, exemplar phantom and brain MRE images were obtained to assist in discussions and evaluations to establish the main experimental MRE protocol back at the Edinburgh Imaging facility, QMRI (EIF-QMRI).

The high-resolution MRE protocols introduced to Edinburgh represent two distinct and fundamentally different pipelines namely: (1) single frequency NLI (SF-NLI), and (2) multifrequency MDEV (MF-MDEV), associated with the University of Illinois at Urbana-Champaign and Charité, Berlin, respectively. Resolution is gained in the former from the multi-shot multi-slab spiral MRE acquisition sequence, whereas the multifrequency inversion scheme (i.e. MDEV) is the source of resolution in the latter. The reader is referred to *Chapter 2* to obtain further information regarding each aspect of the protocol. In this chapter, installation information is provided and, where possible, optimised for implementation on the 3 T Siemens Verio MRI system. Results are then validated against those previously obtained at the respective research institutes as shown in *Chapter 4*. The validation process is performed at both the acquisition and analysis stage. Dietrich-method SNR, as expressed in Eq. 4.1, and an octahedral shear strain signal-to-noise ratio (OSS-SNR), are used to assess the quality of the raw MRE data. OSS-SNR is a measure of the three-dimensional deformation [1], where values above 3 have been shown to be stable for inversion [2,3]. Visual correspondence and MRE quantitative values are used to assess the similarity of the processed MRE elastograms.

Later in the chapter, details of the T_1 image segmentation and MRE coregistration process is described. This is an essential component of each pipeline with regard to generation of reliable measures of specific neuro-anatomical regions of interest (ROIs). A user-friendly graphical user interface

(GUI) was developed and integrated in MATLAB, to perform an automated optimised T_1 to MRE coregistration and quantitative extraction of mechanical property measurements.

5.2 Single frequency with non-linear inversion (SF-NLI)

5.2.1 *Acquisition*

Multi-slab multishot spiral MRE

Whereas, the traditional MRI approach has been to divide the total imaging volume into thin slices, the 3D multi-slab multi-shot acquisition obtains whole brain coverage by dividing the total imaging volume into multi-slice slabs. In particular, the sequence used throughout this thesis employs ten slabs of eight 1.6mm thick slices; the number and size of slabs were specifically chosen with considerations of coverage for key brain structures. Imaging is repeated to encode motion each of the three gradient axes separately, with both positive and negative polarities, and at four time points spaced over a single vibration period. The acquisition can generate full vector field, complex displacement data at 1.6 x 1.6 x 1.6mm isotropic spatial resolution. Only four samples of the vibration are captured, as opposed to the typical eight of most MRE acquisitions, which halves the total acquisition time resulting in a total scan time of 12 minutes.

Installation:

Access to the 3D multi-slab multishot MRE sequence was obtained after a collaboration was established with Dr. Curtis Johnson at the University of Illinois at Urbana-Champaign (UIUC) - now based at the Mechanical Neuroimaging laboratory at the Department of Biomedical Engineering, University of Delaware. A successful Edinburgh NeuroResearcher's fund award provided additional finance to support the visit. The sequence was then shared with Edinburgh and installed on the 3 T Siemens Verio MRI system at EIF-QMRI. Image reconstruction of each dataset is performed offline using MATLAB on graphics processing units (GPUs). The *k*-space trajectory shifts for motion correction are incorporated, while the independently acquired sensitivity map performs a field inhomogeneity correction.

Optimisation:

Prior to running the spiral MRE acquisition, a 3D interactive shim and manual adjustments are implemented to homogenize the main magnetic field. While the magnetic fields produced by MRI scanners are specifically designed and manufactured to achieve fairly high levels of homogeneity, local supplemental magnetic fields (i.e. shim fields) are sometimes added to achieve the desired level of magnetic field homogeneity[a]. Further, the amplitude of vibration on the Resoundant system was set to 20%, which is within the range used by other centres; UIUC typically use 15% whereas the Mayo Clinic use 20%, although groups rarely report the vibration of amplitude in published work. I chose to implement an amplitude of 20% for the acquisition at EIF-QMRI as this is likely to increase the quality of displacement data (i.e. an increase to the OSS-SNR), whilst having a negligible effect on participant comfort.

Validation:

Multi-slab multi-shot data acquired at EIF-QMRI was then compared with the data acquired of the same subject (LH) at UIUC, as shown in Figure 5.1. Dietrich SNR was 12.53 and 9.51 for UIUC and EIF-QMRI, respectively. This is likely due to differing scanner models (i.e. Siemens Trio vs Siemens Verio), and the availability of MR head different coils. Higher number of channels will increase MR signal; therefore, it is expected that greater image quality will be obtained at UIUC with a 32-channel coil, compared with the 12-channel coil used at EIF-QMRI. OSS-SNR was 2.33 at UIUC and 8.11 at EIF-QMRI, corresponding to an improved OSS-SNR of over 110%. As the OSS-SNR was less than 3 at UIUC, this dataset is not stable for inversion, and supports the decision to use a slightly higher vibration amplitude at the EIF-QMRI. The UIUC acquisition, however, shows signs of subject movement which is also likely to affect the OSS-SNR distribution.

5.2.2 *Analysis*

Non-linear finite-element-based inversion (NLI)

Within the MRE literature, the high-resolution spiral acquisition has been paired with a non-linear finite-element-based inversion (NLI) algorithm. The NLI algorithm is coded in FORTRAN using parallelised programming with Message Passing Interface (MPI) and run on a distributed UNIX computing cluster with 64 processors. 100 iterations are run leading to a computer processing time of approximately 18 hours. The initial estimate for the real G' and imaginary G'' shear modulus is set to 3.30 kPa and 1.19 kPa, respectively, with density set to 1000kg/m^3. MATLAB files are returned to EIF-QMRI consisting of spatial maps of the complex shear modulus G^*.

---

[a] The shims are needed because of the residual field variations resulting from the magnet's manufacturing as well as alterations occurring by the presence of the subject to be imaged.

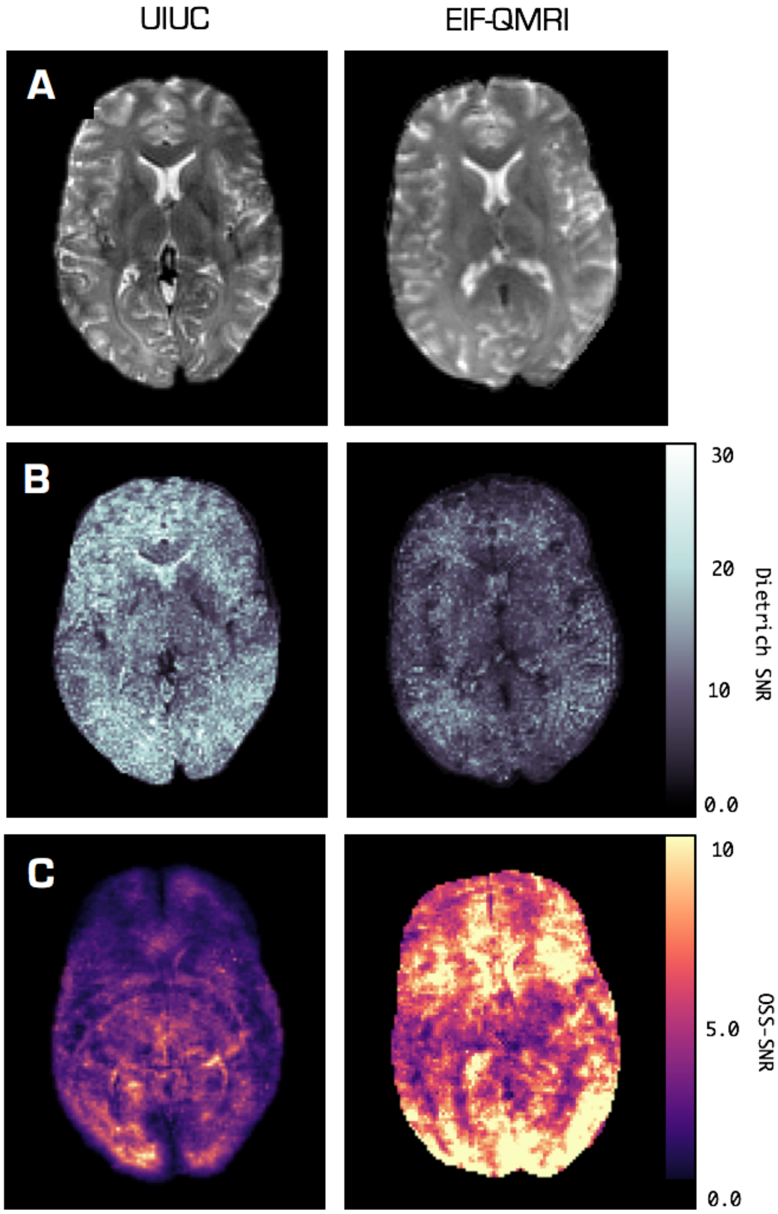

Figure 5.1: Comparison of MRE data acquired of the same subject (LH) at UIUC and EIF-QMRI, with the 3D multi-slab multishot MRE sequence. Representative image slice of (a) raw T_2 MRE magnitude, (b) Dietrich method SNR; and (c) the resulting OSS-SNR distribution. Differences in SNR are likely due to different scanner models (Siemens Trio vs Siemens Verio), and the availability of different MR head coils (32-channel vs. 12-channel). Higher OSS-SNR at EIF-QMRI is most likely due to selecting a higher vibration amplitude on the Resoundant actuator system. Increasing the % amplitude by 5% resulted in an improved OSS-SNR score of over 110%.

Installation:

A collaboration was established with Dr. Matthew McGarry, currently based at Thayer School of Engineering, Dartmouth College, Hanover, USA. Dr. McGarry has implemented several new aspects of the NLI algorithm including so-called subzone based multiresolution NLI [4]. Multiresolution NLI has the benefit of subsampling both parameters simultaneously to smooth and stabilize both estimates of the storage G' and loss G'' modulus - resulting in a more stable G''. As such, multi-slab, multishot displacement data were specifically formatted (i.e. generation of a binary mask and separation of the *x, y* and *z* components of motion), and sent to Dartmouth College for processing.

Optimisation:

Settings of the NLI algorithm (v7.34) used throughout this thesis are identical to those used in other brain MRE NLI publications [2, 3, 5, 6], and include subzone size of 25mm, spatial filter width of 1.5mm, with two conjugate gradient iterations per subzone. A high bulk modulus is used to provide a Poisson ratio close to 0.5.

Validation:

NLI was used to process the 1.6mm multi-slab multishot displacement data acquired at both UIUC and EIF-QMRI of the same subject (LH), as shown in Figure 5.2. Data was converted to shear stiffness μ to maintain consistent reporting. Whole brain μ was 2.81 kPa at UIUC and 2.90 kPa at EIF-QMRI. The EIF-QMRI elastogram appears to have better neuroanatomical agreement with the T_2-weighted image provided in Figure 5.1. The ventricles, in particular, are very well defined in the coronal view. The brainstem appears especially stiff in the UIUC elastogram which, however, is not apparent in the EIF-QMRI elastogram. This is most likely to be an artefact which could be attributed to subject motion, and therefore not a real feature. As previously mentioned, the OSS-SNR did not score above 3 to suggest the motion data was stable for inversion. As a result, quantitative stiffness values will not be reliable.

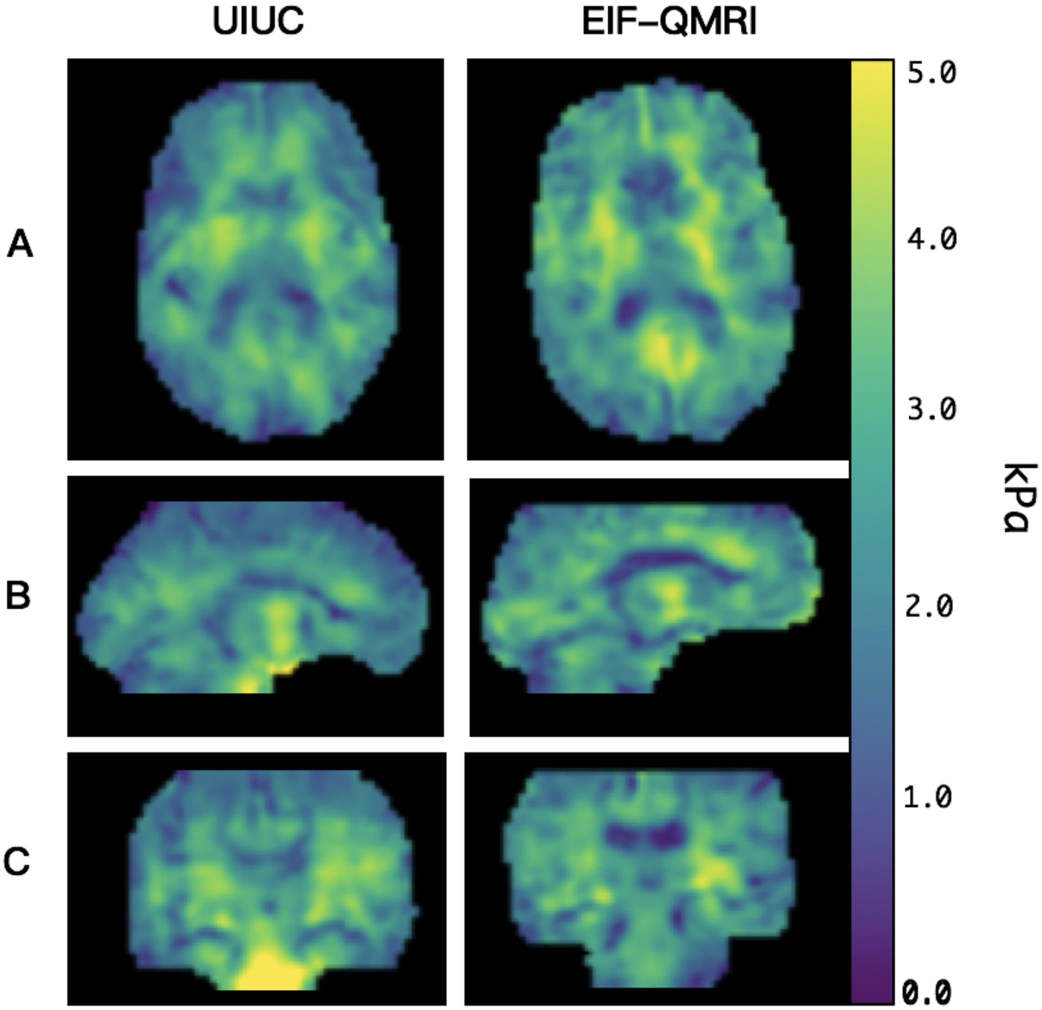

Figure 5.2: Representative MRE images of the same subject (LH) acquired at UIUC and EIF-QMRI. Whole-brain shear stiffness, μ map in (a) axial, (b) sagittal, and (c) coronal orientation from non-linear inversion (NLI) of high-resolution MRE displacement data captured with the 3D multislab, multishot acquisition. Note: UIUC motion data did not reach the threshold required for stable inversion as calculated with the OSS-SNR. As a result, the MRE elastograms are unlikely to be reliable. In particular, the stiff brain stem visualised in the coronal view is unlikely to be a "real" feature. Similar results for the brainstem have been reported previously [2], and the reliability of brainstem MRE results is currently under investigation.

5.3 Multi-frequency EPI with MDEV (MF-MDEV)

5.3.1 *Acquisition*

Spin-Echo Echo-Planar Imaging (EPI)

The acquisition sequence used as part of the MF-MDEV protocol is a Cartesian Spin-Echo Echo Planar Imaging (SE-EPI) sequence, with parallel imaging capabilities equipped with additional motion encoding gradients (MEGs) [7, 8]. To ensure the 3D displacement is captured, three sets of measurements are performed, each with the MEG incorporated along one of the three Cartesian axes, and 8 phase offsets are obtained to track the wave propagation in time.

Installation:

A modified spin-echo echo planar imaging (EPI) sequence was already available at EIF-QMRI from a previous PhD study investigating the mechanical properties of the musculoskeletal system [9].

Optimisation:

The selected mechanical frequencies to be used within the protocol at EIF-QMRI were 20, 30, 40, 50, and 60 Hz; within the range utilised in recent brain MRE publications from the Charité group [10–12]. In the next section, I perform four particular optimisations including: (1) choice of echo time (TE); (2) selection of optimal MEG frequencies; (3) preferred phase-encode direction; and (4) the addition of a whole-brain EPI for coregistration purposes.

(1) Choice of TE

Choice of TE is influential as a longer echo time allows for longer motion-encoding periods (i.e. an increase to the *max encoding time*)[b]. In general, longer motion-encoding periods with multiple MEG cycles offer superior motion sensitivity, as the sensitivity increases proportionally with the number of gradient pairs. The caveat being that a longer echo time (TE) invariably causes lower signal quality due to T_2 decay. For the EIF-QMRI protocol, a TE of 92 was selected as the brain has longer T_2 times compared to other tissues, enabling a longer encoding time and thus higher encoding efficiencies.

---

[b] The *max encoding time* refers to how much time is available to incorporate the MEG before the full k-space readout and can be found within the `special tab` on the scanner console.

(2) MEG frequency

Another important aspect of the acquisition is the selected MEG frequency for each mechanical frequency. Studies have previously matched the MEG frequency to the mechanical frequency, however, determination of the optimal MEG frequency can accomplish a higher encoding efficiency according to the principles of fractional motion encoding [13]. To assist with these calculations, a “plotSensitivity” MATLAB script, developed by Dr. Sebastian Hirsch - a member of the Charité MRE group, was used to ensure the highest encoding efficiency for the given TE. A demonstration for calculating the optimal MEG frequency for 50 Hz, is provided in Figure 5.3. The same calculation was then applied to determine the optimal MEG frequencies for the remaining mechanical frequencies.

(3) Phase encode (PE) direction

Susceptibility-induced distortions can be problematic in data acquired along the left-to-right (R>>L) PE orientation, causing the blurring of signal across the midline and hampering the natural symmetry of the left and right cerebral hemispheres. Data acquired in the anterior-to-posterior (A>>P) PE direction is more frequently applied in diffusion MRI [14], and therefore I propose using the A>>P PE direction in combination with this sequence, and within brain MRE in general.

(4) Acquisition of whole-brain EPI

Due to the multifrequency aspect of the MF-MDEV pipeline, a limited number of slices are acquired to enable a shorter acquisition time. A partial field-of-view acquisition, however, causes difficulties in the coregistration of the MRE elastogram to the structural T_1-weighted image (more information regarding the coregistration process is provided in *section 5.4*). As a result, I will acquire a full-brain EPI image, that contains identical parameters, including resolution and slice orientation, for the purpose of performing a multi-stage registration. This will enable: (1) a simple (3 degrees of freedom) registration between the partial-EPI with the full-brain EPI; (2) coregistration between the full brain EPI to T_1 space; and (3) the concatenation of the two steps to minimise resampling, thus enabling the partial-EPI to be transformed into T_1 space. A multi-stage registration has been shown to significantly improve coregistration accuracy.

Further imaging parameters are: 4590/92ms repetition/echo times; 240mm square field-of-view;

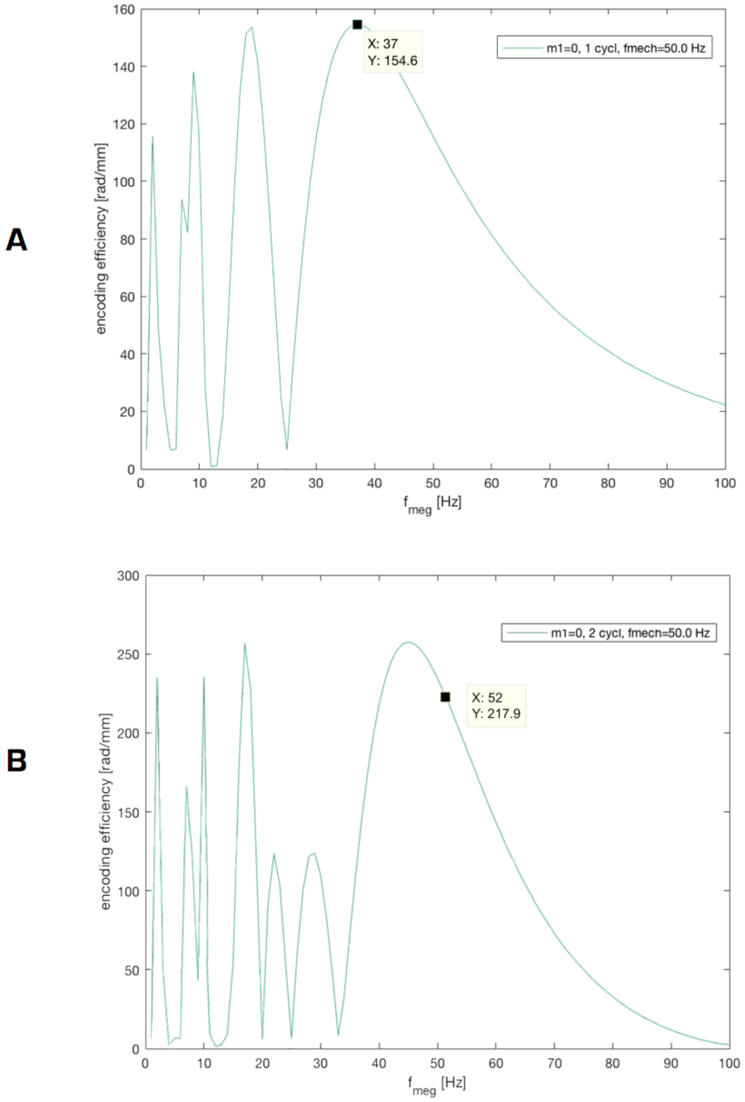

Figure 5.3: Encoding sensitivity with 1 and 2 MEG cycles for a mechanical frequency of 50Hz (TE:92 provides a max encoding time of 25.95 Hz): (a) one MEG cycle results in an optimal MEG frequency of 37 Hz and an encoding efficiency of 154.6 rad/mm; (b) two MEG cycles result in an optimal MEG frequency of 52 Hz and an encoding efficiency of 217.9 rad/mm. In this 50 Hz example, a MEG frequency of 52 would be selected allowing for two complete MEG cycles.

100 x 100 imaging matrix; twenty slices; MEG amplitude 35 mT/mm. The resulting imaging volume had a 2.3 x 2.3 x 2.3mm^3 isotropic voxel size, which was aligned approximately to the anterior commissure - posterior commissure (AC-PC) line to include the medial temporal lobe (MTL). The acquisition time for each frequency was 1.55 minutes.

Validation:

Spin-echo EPI MRE data acquired at the EIF-QMRI was then compared with the data acquired of the same subject (LH) at Charité, Berlin, as shown in Figure 5.4. Minor distortions are apparent in both T_2 magnitude images; the Charité acquisition in the R>>L direction, and EIF-QMRI in the A>>P direction, corresponding to the phase encode direction. Dietrich SNR at 50 Hz was 11.04 (Charité) and 14.49 (EIF-QMRI). Higher SNR in Edinburgh will be due to the larger voxel size (2.3mm as opposed to 2mm). OSS-SNR was 1.89 at Charité and 3.04 at EIF-QMRI. The vibration device used at Charité does not specify an exact vibration amplitude. In Edinburgh, the choice of vibration amplitude for each frequency, involved balancing the trade-off between sufficient motion seen in real-time on the scanner console, while limiting the presence of excessive phase wraps. In general, for mechanical frequencies from 20 - 60 Hz, the % amplitude was set between 15 - 40%.

5.3.2 *Analysis*

Multi-dual elasto-visco inversion (MDEV)

Within the MRE literature, the multi-frequency spin-echo EPI data has been paired with multi-dual elasto-visco (MDEV) inversion, or the Elastography Software Pipeline (ESP), as described in *Chapter 2*.

Installation:

The basic MDEV inversion code is freely available as a MATLAB script, and can be found at the Charité group's website: thhttp://elastography.de/support/

Optimisation:

The standard MDEV inversion code was used, as published in numerous studies [11, 15–17]. Interslice artefacts often hamper the full 3D direct inversion, as demonstrated in Hirsch *et al.* 2013 [18]. As a result, interslice phase inconsistencies were corrected by applying a low-pass filter along the slice dimension. Additionally, a 2D low-pass filter, based on 2D Fourier transform, and Butterworth Kernel with a 50 m^{-1} threshold, were applied to all three components of the wave field.

Validation:

Figure 5.5 displays the MRE elastograms obtained at both Charité and EIF-QMRI. The ad-

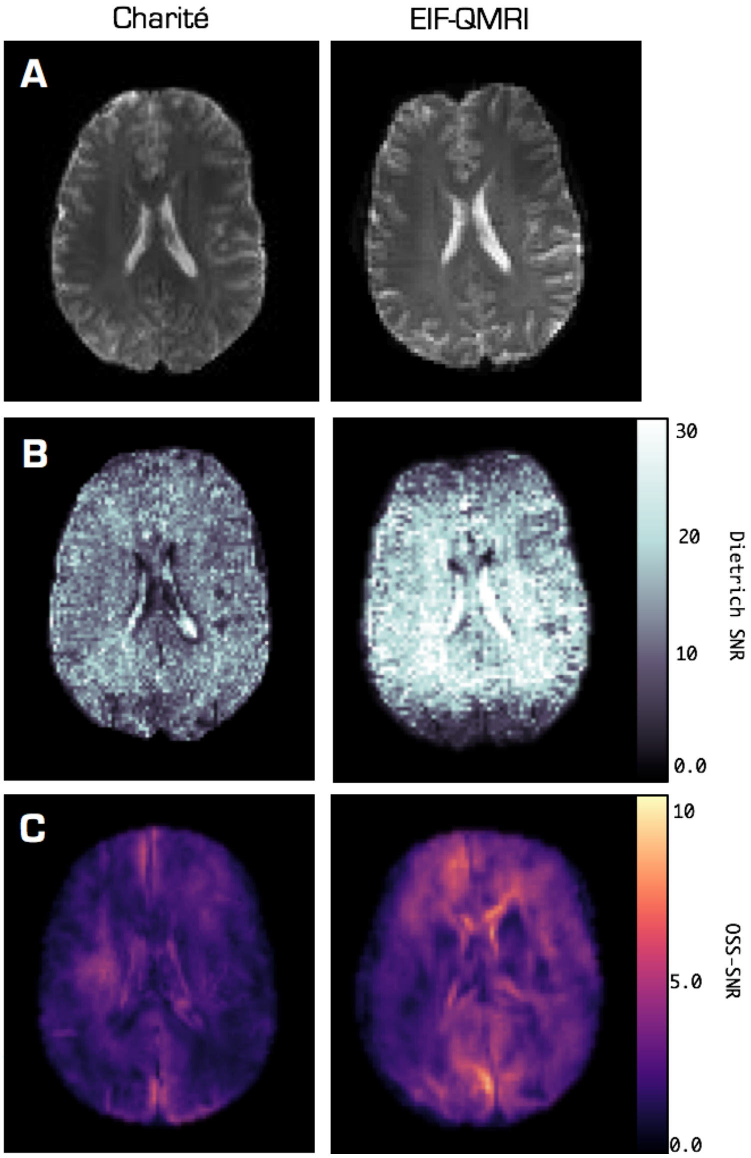

Figure 5.4: Comparison of 50 Hz MRE data acquired of the same subject (LH) at Charité, Berlin and EIF-QMRI, with the spin-echo EPI MRE sequence. Representative image slice of: (a) raw T_2 MRE magnitude, (b) Dietrich method SNR; and (c) the resulting OSS-SNR distribution. The Charité MRE magnitude image shows minor susceptibility-induced distortions along the left-to-right (R>>L) PE direction. In contrast, the EIF-QMRI magnitude image shows distortions in the anterior-to-posterior (A>>P) PE direction. I chose to change the phase encoding direction to minimise the blurring of signal across the midline that may hamper the natural anatomical symmetry of the left and right cerebral hemispheres. Dietrich method SNR is evidently higher for the EIF-QMRI acquisition due to the larger in-plane voxel size. The OSS-SNR maps in the final panel suggest that the Resoundant is providing greater motion, especially to the very centre of the brain, compared to the piezoelectric system.

ditional 20 Hz and 60 Hz acquisitions acquired at EIF-QMRI were omitted for this particular analysis to maintain a valid comparison. Both images are therefore a result of multifrequency MRE at 30, 40, and 50 Hz. $|G^*|$ at Charité yielded a global value of 2.01 kPa, and 2.30 kPa at EIF-QMRI. Visual comparison of both elastograms suggest excellent anatomical agreement as depicted by the arrows placed in Figure 5.5. The positioning of slices was slightly different at each research site, as can be seen from the images provided in the coronal and sagittal orientations.

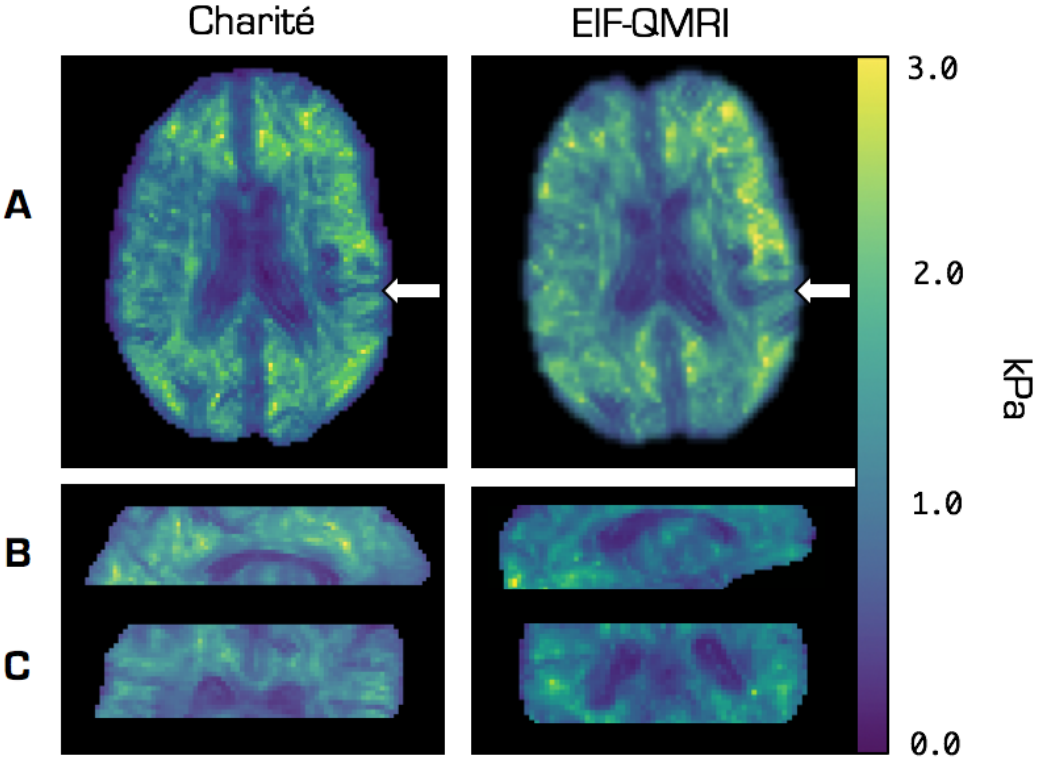

Figure 5.5: Representative MRE images of the same subject (LH) acquired at Charité, Berlin and EIF-QMRI. Map of the magnitude of the complex shear modulus $|G^*|$ in (a) axial, (b) sagittal, and (c) coronal orientation from MDEV of multiple frequency MRE displacement data (i.e. 30, 40, 50 Hz) captured with a spin-echo EPI acquisition. Similar features can be seen in both images, and there appears to be a number of asymmetries across the hemispheres. The right hemisphere (radiological convention) is also marked by several regions of stiff "hot-spots". It is important to note that the majority of brain MRE groups report asymmetries in their data. Also note that the slices are not symmetric themselves (i.e. not perfectly axial). The right lateral sulcus (arrowed) is present, but the left lateral sulcus isn't in plane.

5.4 Image segmentation and coregistration

The previous sections *(sections 5.2 and 5.3)* summarised the data acquisition and data analysis procedures to generate high-resolution elastograms for both of the SF-NLI and MF-MDEV pipelines. After installation, optimisation and validation of both protocols at the EIF-QMRI, the next important step is the generation of reliable quantitative MRE-derived values of regions of interest (ROIs), i.e. particular brain structures.

A number of different processes have been used to define ROIs, dividing into essentially two approaches, namely (i) manual boundary delineation of the ROI, and (ii) automatic segmentation of the ROI. Fortunately, for the brain there are a wealth of software programmes available to perform automatic segmentation. However, very few are open-source and able to generate numerous brain structures of interest. `FREESURFER` is one such software package that has also been found to show excellent reliability for subcortical regions in healthy older adults [19]. For this reason, in the present work, `FREESURFER` will be used to generate masks of brain structures of interest. As it is required to interpret the MRE results with reference to anatomical regions, coregistration will be performed to align the T_1-weighted image (and masks) to the MRE elastogram. As only a linear (affine) registration will be required, FMRIB's Linear Image Registration Tool (`FLIRT`) from the FMRIB Software Library (FSL) will be used. This particular processing pipeline that incorporates both `FREESURFER` and `FSL` is mostly identical to one used in previous work to segment and coregister ROI masks for MRE [3, 6]. While it was reported that there is variability in mask creation from both volume estimation during automatic segmentation and during registration, these differences contributed negligibly to the uncertainty of MRE measurements [3]. To maintain consistency with previously published work, I have adopted a similar (but not identical) pipeline. Both processes are described in more detail below.

Segmentation:

`FREESURFER` (Athinoula A. Martinos Center for Biomedical Imaging, Boston, USA), provides a suite of tools for the visualisation and analysis of human brain MRI data, which is open-source, documented, and free for download online [20]. Briefly, T_1-weighted images are input into `FREESURFER` through the recon-all pipeline (v. 5.3). The process automatically performs the following: skull stripping, automated Talairach transformation, segmentation of the subcortical white/grey matter structures, intensity normalization, automated topology correction, and registration to a spherical atlas. Manual corrections are sometimes necessary at any of the stages,

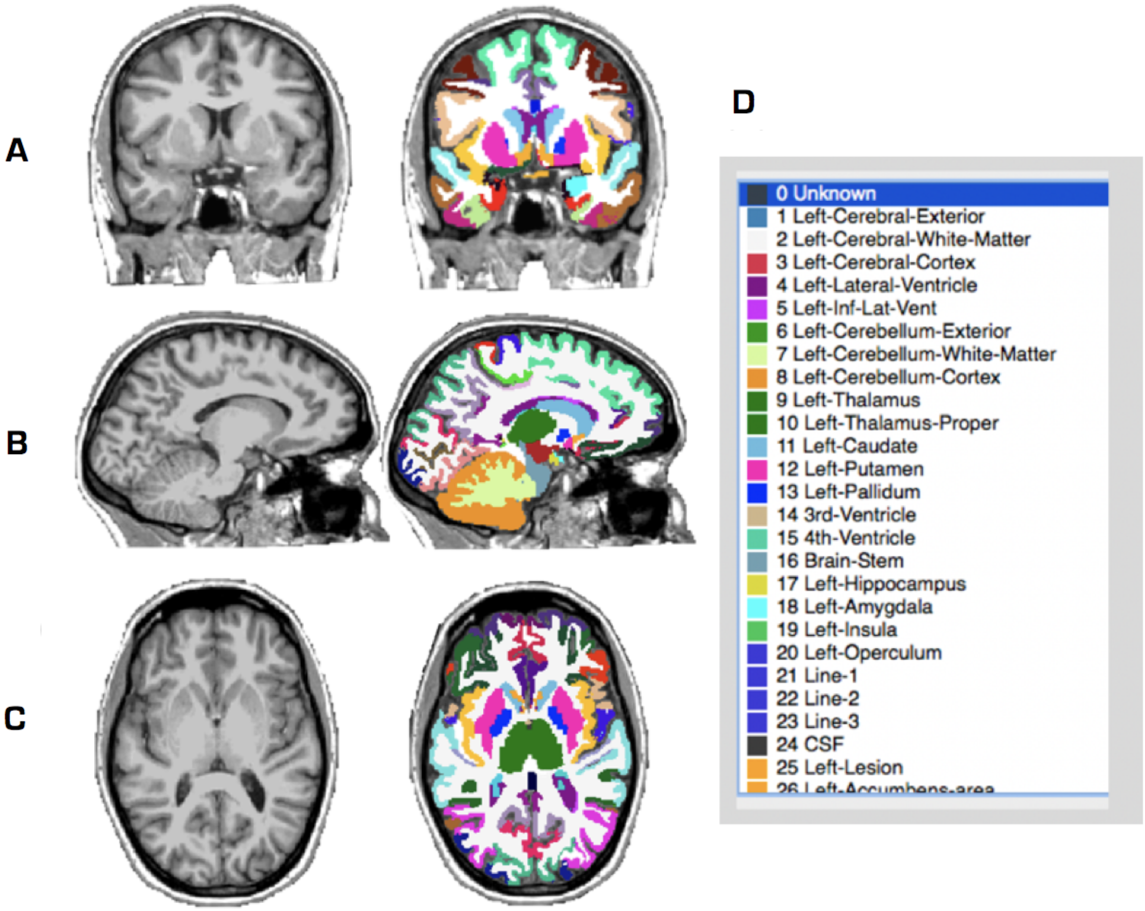

0 Unknown
1 Left-Cerebral-Exterior
2 Left-Cerebral-White-Matter
3 Left-Cerebral-Cortex
4 Left-Lateral-Ventricle
5 Left-Inf-Lat-Vent
6 Left-Cerebellum-Exterior
7 Left-Cerebellum-White-Matter
8 Left-Cerebellum-Cortex
9 Left-Thalamus
10 Left-Thalamus-Proper
11 Left-Caudate
12 Left-Putamen
13 Left-Pallidum
14 3rd-Ventricle
15 4th-Ventricle
16 Brain-Stem
17 Left-Hippocampus
18 Left-Amygdala
19 Left-Insula
20 Left-Operculum
21 Line-1
22 Line-2
23 Line-3
24 CSF
25 Left-Lesion
26 Left-Accumbens-area

Figure 5.6: `FREESURFER` output: (a) coronal, (b) sagittal, and (c) axial slice showing the T_1-weighted slice and the corresponding 'aseg' segmentations. The look-up table (LUT) (d) indicates the neuro-anatomical structure based on colour and number.

and are performed when appropriate. The `FREESURFER` output file *aseg.mgz* is of particular interest, as it contains the subcortical segmentation volumetric masks of approximately 40 brain structures[c].

Coregistration: Coregistration serves the purpose of accurately aligning anatomical information with the high-resolution MRE parameter maps. First of all, T_2-weighted magnitude MRE images are co-registered to the structural T_1-weighted MPRAGE using `FLIRT` - the linear registration tool within `FSL` [21]. A 12 parameter affine model is used, with tri-linear interpolation and a correlation ratio cost function. The registration is optimised by using weighting volumes specified using `-refweight`, `-inweight`, or both, and allows the cost function to have a different weighting at each voxel. This is useful for excluding areas of no interest (weight=0), or increasing the weighting around important structures such as the ventricles. Weighting of 1 was applied to the entire brain, whereas a weighting of 10 was applied to the lateral ventricles. Adding extra weighting to the ventricles may be especially important for coregistration accuracy in older subjects who are likely to have moderate atrophy and enlarged ventricles. Second, the *inverse* transform is calculated so that the T_1-weighted MRPAGE image can be transformed into MRE space. Most essential, is that use of this transform allows for the generated masks from `FREESURFER` to be transferred into MRE native space, to serve as ROIs for obtaining quantitative values. As MRE images contain quantitative information, it is preferential to keep MRE in its native space so as to not distort measures. `FREESURFER` ROI masks, however, are transformed using a nearest neighbour interpolation to preserve accurate boundaries. See Figure 5.7 for an illustration of the coregistration process.

---

[c] These include Cerebral White Matter, Cerebral Cortex, Lateral Ventricle, Inferior Lateral Ventricle, Cerebellum White Matter, Cerebellum Cortex, Thalamus, Caudate, Putamen, Pallidum, Hippocampus, Amygdala, Lesion, Accumbens area, Vessel, Third Ventricle, Fourth Ventricle, Brain Stem, Cerebrospinal Fluid, as illustrated in Figure 5.6.

5.5 Development of an automated coregistration GUI pipeline for ROI measurements

Prior to the present study a graphical user interface (GUI) did not exist to perform the automatic coregistration and generation of MRE-derived quantitative measures. It is important for research groups using brain MRE to develop a standardised method of calculating values, particularly of certain brain structures. This would also ensure consistency and reliability, and be of great use in a clinical environment. Consequently, a GUI was developed using *guide* within MATLAB known as `Mechanical Neuroanatomy (MeNA)`. Two separate GUIs were developed for the SF-NLI and MF-MDEV pipelines; this is because the latter requires a three part registration due to limited brain coverage in the z-direction.

5.5.1 *Procedure*

In this section, the use of the SF-NLI GUI procedure is described. Prior to running the GUI, `FREESURFER` data, the raw but reconstructed spiral data, and post-inversion MRE data should already be available[d]. After downloading the script files and setting the path to the `MeNA` folder, the

---

[d] Within the subject directory, output files from `FREESURFER` should be named “FREESURFER”, files containing the processed NLI data should be in a parent folder called “inv”, and the raw spiral should be in a folder called

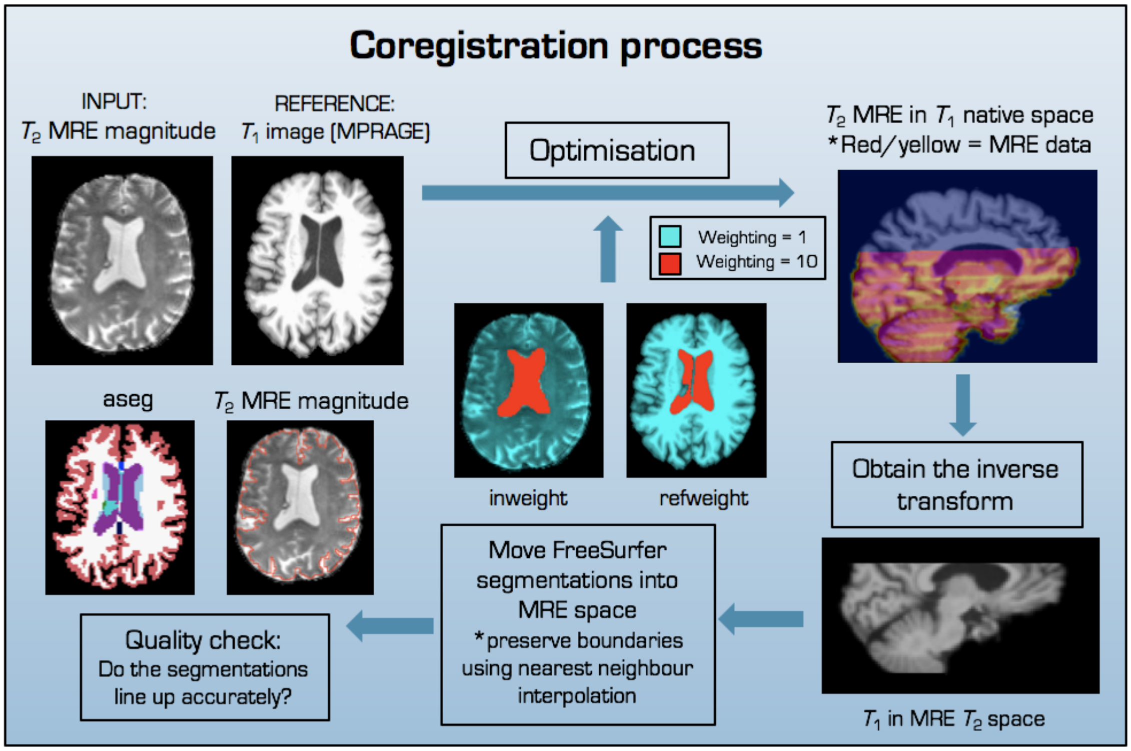
Coregistration process
INPUT:
T_2 MRE magnitude
REFERENCE:
T_1 image (MPRAGE)
Optimisation
T_2 MRE in T_1 native space
*Red/yellow = MRE data
🟦 Weighting = 1
🟥 Weighting = 10
inweight
refweight
aseg
T_2 MRE magnitude
Obtain the inverse transform
Move FreeSurfer segmentations into MRE space
*preserve boundaries using nearest neighbour interpolation
Quality check:
Do the segmentations line up accurately?
T_1 in MRE T_2 space

Figure 5.7: Overview of the `FSL` *coregistration pipeline. The MRE T_2-weighted images are first coregistered to the T_1-weighted MPRAGE using FLIRT. To optimise the registration, extra weighting is given to the lateral ventricles. Once this transform has been generated, the inverse transform is obtained to move the T_1-weighted MPRAGE into T_2-weighted MRE space. The inverse transform can then be used to transform the* `FREESURFER` *segmentations (i.e. aseg) into MRE space using a nearest neighbour interpolation for boundary preservation. Note: MRE elastograms are in the same space as the T_2-weighted MRE magnitude image.*

user simply needs to type `MeNA` into the command window within MATLAB, to access the GUI as shown in Figure 5.8.

(1) **Prepare files:** The first step in this process is the creation of a new folder called *CoReg_NLI*. `FREESURFER` data is converted from `FREESURFER` conformed space back to native anatomical space. Shear stiffness, μ and damping ratio ξ are calculated from the complex shear modulus $|G^*|$ and **NiFTI** image files are created for $|G^*|$, ϕ, μ and ξ. All data required for coregistration is then automatically transferred to the new folder *CoReg_NLI*[e].

"finished_recon".

[e] The **prepare files for SPR** button simply uses data processed with soft prior regularisation (SPR) and creates a *CoReg_NLI_SPR* folder instead.

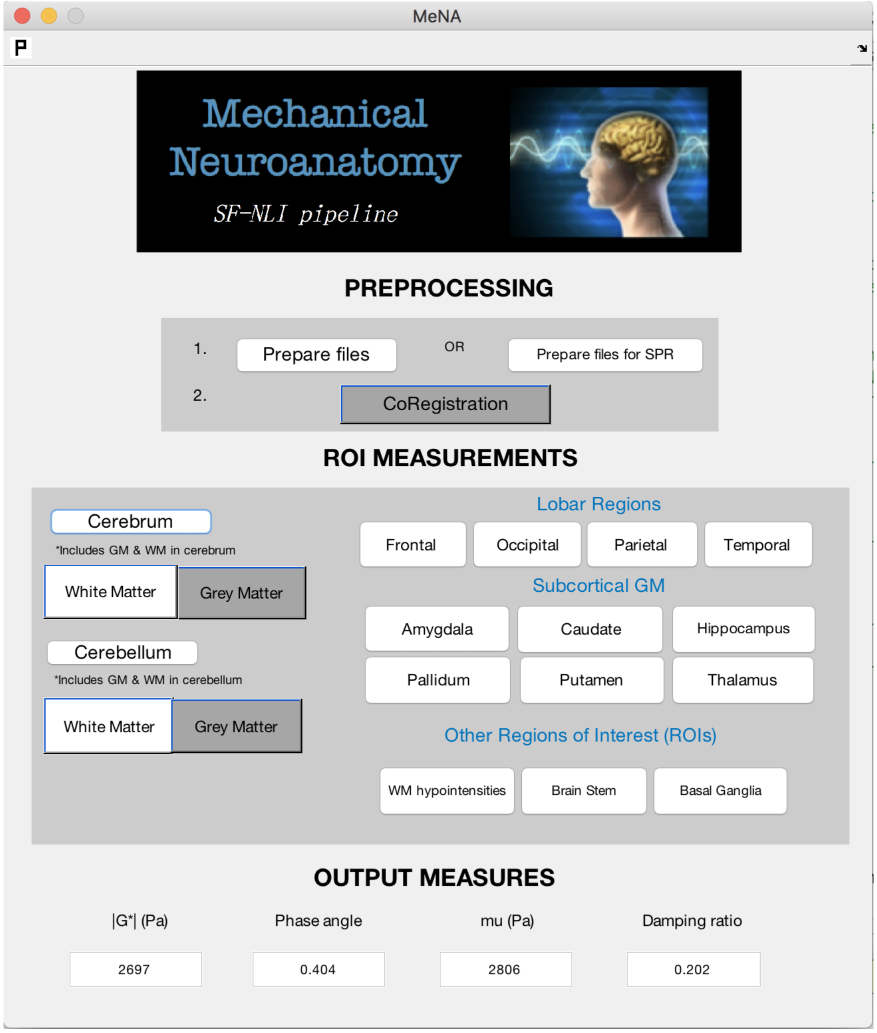
MeNA
Mechanical Neuroanatomy
SF-NLI pipeline
PREPROCESSING
1.
Prepare files
OR
Prepare files for SPR
2.
CoRegistration
ROI MEASUREMENTS
Cerebrum
*Includes GM & WM in cerebrum
White Matter
Grey Matter
Cerebellum
*Includes GM & WM in cerebellum
White Matter
Grey Matter
Lobar Regions
Frontal
Occipital
Parietal
Temporal
Subcortical GM
Amygdala
Caudate
Hippocampus
Pallidum
Putamen
Thalamus
Other Regions of Interest (ROIs)
WM hypointensities
Brain Stem
Basal Ganglia
OUTPUT MEASURES

|G*| (Pa)	Phase angle	mu (Pa)	Damping ratio
2697	0.404	2806	0.202

Figure 5.8: `Mechanical Neuroanatomy (MeNA)` *GUI for the SF-NLI pipeline.*

(2) Coregistration: This button performs the automatic and optimised coregistration as discussed in *section 5.4* and illustrated in Figure 5.7, and takes approximately 30 seconds. Once completed, `Freeview` within `FREESURFER` is opened automatically so the user can check coregistration accuracy.

(3) ROI measurements: Finally, the user can click any of the ROIs to automatically generate values for all four MRE-derived parameters for the selected brain structure[f]. Non-zero voxels in the (binary) mask are established and transferred to the $|G^*|$, ϕ, μ, and ξ images to obtain values only for that region. All masks are thresholded at a conservative value of 95%, as it is important to not include contamination from surrounding areas. Finally, values are presented and a new folder is created (i.e. the hippocampus) with the associated masks and measurements.

---

[f] A range of ROIs have been added to the GUI, but more can be easily added as the masks are generated depending on the numbers provided in the LUT as shown in Figure 5.6.

5.5.2 *MeNA highlights*

- Quick and easy to use.
- Reliable and consistent values.
- Optimal coregistration.
- Separate GUIs for SF-NLI and MF-MDEV pipelines.
- Values provided for four MRE parameters, i.e $|G^*|$, ϕ, μ, and ξ.

5.6 Summary

This chapter has focused on the installation, optimisation, and validation process for the introduction of two widely-published, high-resolution brain MRE protocols at the EIF-QMRI. Comparison of images acquired in Edinburgh with the respective research institutes show similar quality MRE elastograms. Furthermore, the image segmentation and coregistration process, used throughout this thesis, is described thoroughly to encourage researchers to use a similar approach for standardisation benefits. To aid this objective, I have developed an automated image coregistration and ROI measurement GUI (i.e. `MeNA`), to be user friendly and improve the measurements of local mechanical properties, which both enhance the clinical applicability of brain MRE. *Chapter 6* will focus on the repeatability of the quantitative measures generated in a small sample of both young and older subjects, across two separate time points, using the high-resolution schemes presented here. The test re-test agreement of each protocol has not been previously evaluated, while reliability is essential for the clinical adoption of any potential biomarker.

References

[1] MDJ McGarry, EEW Van Houten, PR Perrinez, AJ Pattison, JB Weaver, and KD Paulsen. An octahedral shear strain-based measure of SNR for 3D MR elastography. *Phys Med Biol*, 56:N153–64, 2011.

[2] CL Johnson, JL Holtrop, MDJ McGarry, JB Weaver, KD Paulsen, JG Georgiadis, and BP Sutton. 3D multislab, multishot acquisition for fast, whole-brain MR elastography with high signal-to-noise efficiency. *Magn Reson Med*, 71:477–485, 2014.

[3] CL Johnson, H Schwarb, MDJ McGarry, AT Anderson, GR Huesmann, BP Sutton, and NJ Cohen. Viscoelasticity of subcortical gray matter structures. *Hum Brain Mapp*, 2016.

[4] MDJ McGarry, EEW Van Houten, CL Johnson, JG Georgiadis, BP Sutton, JB Weaver, and KD Paulsen. Multiresolution MR elastography using nonlinear inversion. *Med Phys*, 39:6388–6396, 2012.

[5] H Schwarb, CL Johnson, MDJ McGarry, and NJ Cohen. Medial temporal lobe viscoelasticity and relational memory performance. *NeuroImage*, 132:534–541, 2016.

[6] H Schwarb, CL Johnson, AM Daugherty, CH Hillman, AF Kramer, NJ Cohen, and AK Barbey. Aerobic fitness, hippocampal viscoelasticity, and relational memory performance. *NeuroImage*, 153:179–188, 2017.

[7] D Klatt, U Hamhaber, P Asbach, J Braun, and I Sack. Noninvasive assessment of the rheological behavior of human organs using multifrequency MR elastography: a study of brain and liver viscoelasticity. *Phys Med Biol*, 52:7281, 2007.

[8] S Papazoglou, S Hirsch, J Braun, and I Sack. Multifrequency inversion in magnetic resonance elastography. *Phys Med Biol*, 57:2329–2346, 2012.

[9] P Kennedy. Magnetic resonance elastography studies of human skeletal muscle. *University of Edinburgh*, 2015.

[10] A Fehlner, S Papazoglou, M D McGarry, K D Paulsen, J Guo, K-J Streitberger, S Hirsch, J Braun, and I Sack. Cerebral multifrequency MR elastography by remote excitation of intracranial shear waves. *NMR Biomed*, 28:1426–1432, 2015.

[11] A Fehlner, JR Behrens, K-J Streitberger, S Papazoglou, J Braun, J Bellmann-Strobl, K Ruprecht, F Paul, J Wurfel, and I Sack. Higher-resolution MR elastography reveals early mechanical signatures of neuroinflammation in patients with clinically isolated syndrome. *J Magn Reson Imaging*, 44:51–58, 2016.

[12] S Hetzer, P Birr, A Fehlner, S Hirsch, F Dittmann, E Barnhill, J Braun, and I Sack. Perfusion alters stiffness of deep gray matter. *J Cereb Blood Flow Metab*, page 271678X17691530, 2017.

[13] J Rump, D Klatt, J Braun, C Warmuth, and I Sack. Fractional encoding of harmonic motions in MR elastography. *Magn Reson Med*, 57:388–395, 2007.

[14] M Kennis, SJH van Rooij, RS Kahn, E Geuze, and A Leemans. Choosing the polarity of the phase-encoding direction in diffusion MRI: Does it matter for group analysis? *NeuroImage: Clinical*, 11:539–547, 2016.

[15] K-J Streitberger, M Reiss-Zimmermann, FB Freimann, S Bayerl, J Guo, F Arlt, J Wuerfel, J Braun, K-T Hoffmann, and I Sack. High-Resolution Mechanical Imaging of Glioblastoma by Multifrequency Magnetic Resonance Elastography. *PLoS One*, 9:e110588, 2014b.

[16] J Braun, J Guo, R Lützkendorf, J Stadler, S Papazoglou, S Hirsch, I Sack, and J Bernarding. High-resolution mechanical imaging of the human brain by three-dimensional multifrequency magnetic resonance elastography at 7T. *NeuroImage*, 90:308 − 314, 2014.

[17] J Guo, S Hirsch, A Fehlner, S Papazoglou, M Scheel, J Braun, and I Sack. Towards an elastographic atlas of brain anatomy. *PLoS One*, 8:e71807, 2013.

[18] S Hirsch, D Klatt, F Freimann, M Scheel, J Braun, and I Sack. In vivo measurement of volumetric strain in the human brain induced by arterial pulsation and harmonic waves. *Magn Reson Med*, 70:671–683, 2013.

[19] F Liem, S Mérillat, L Bezzola, S Hirsiger, M Philipp, T Madhyastha, and L Jäncke. Reliability and statistical power analysis of cortical and subcortical FreeSurfer metrics in a large sample of healthy elderly. *NeuroImage*, 108:95–109, 2015.

[20] B Fischl, DH Salat, E Busa, M Albert, M Dieterich, C Haselgrove, A van der Kouwe, R Killiany, D Kennedy, S Klaveness, A Montillo, N Makris, B Rosen, and AM Dale. Whole brain segmentation: automated labeling of neuroanatomical structures in the human brain. *Neuron*, 33:341–355, 2002.

[21] M Jenkinson, CF Beckmann, TEJ Behrens, MW Woolrich, and SM Smith. FSL. *NeuroImage*, 62:782–790, 2012.

Chapter 6

An evaluation of the test re-test agreement of Brain MRE

Plan for the Chapter

This chapter contains a rigorous evaluation of the test-retest agreement of the two brain MRE protocols described in *Chapter 5*. The previous chapter focused on the installation and optimisation of both approaches at the Edinburgh Imaging Facility, QMRI, broadly categorised as single frequency non-linear inversion (SF-NLI) and multifrequency multi-dual elasto-visco inversion (MF-MDEV). This study will evaluate the test re-test agreement of each method in a sample of six younger (mean age: 24 years), and six older (mean age: 70 years) adult participants, scanned once over two separate time points within approximately 2-3 weeks. MRE measurements are provided for the global cerebrum (Ce), as well as a smaller brain structure of interest, i.e. the hippocampus (Hp). Secondary aims were to examine inter-method reliability, and the sensitivity of each protocol to ageing effects.

6.1 Introduction

Rapid improvements in magnetic resonance imaging (MRI) technology continue to provide new opportunities to deepen our understanding of brain structure and function in health and disease. Evaluation of neurodegenerative disease progression may be assisted by quantification of the brain's mechanical properties using magnetic resonance elastography (MRE). Through preliminary clinical investigations, as described in *Chapter 3*, brain MRE has displayed excellent potential as a diagnostic biomarker. Recent improvements in actuator design, imaging resolution, and inversion algorithms has only further enhanced the feasibility of using brain MRE as a clinical neuroimaging modality.

The construction of a new biomarker requires the examination of its psychometric properties. Any measurement tool is almost always prone to various sorts of error, causing the measured value to differ from the true value. Validity studies, therefore, are essential in order to examine whether the test can provide what is required (i.e. aiding diagnosis, predicting future patient outcomes, or serving as end points in randomised control trials). In other words, validity studies can assist in the calculation of whether the bandwidth of error is acceptable; a technique cannot be used to detect a change when its measurement error is larger that the change we want to be able to detect [1].

The successful transformation of liver MRE from lab to clinic is marked by numerous studies finding high agreement across raters and sessions [2], and small variability between imager manufacturers, field strengths, and pulse sequences [3]. As such, cut-off values have been established for liver fibrosis, with a shear stiffness μ value of below 2.5 kPa indicating normal liver tissue, values above 5 kPa indicating stage 4 fibrosis, with intermediary values accounting for stages 1-3. Of note, liver

MRE is overwhelmingly performed at 60 Hz vibration using a direct inversion algorithm. Images are then automatically generated and made available on the scanner console. For the brain, however, it has been more difficult to establish "normative" values of brain stiffness. This was highlighted in *Chapter 3*. Even when results for global brain tissue are standardised according to a mathematical common parameter, shear stiffness μ still deviates between 0.62 - 2.99 kPa for healthy normal subjects [4]. Values for white matter, in particular, have varied between 1.27 kPa and 13.60 kPa. There is clearly a wide disparity in values, which may be attributed to variation in frequency and MRE methodology. Whether brain MRE can provide accurate quantitative values for mechanical properties will be difficult to determine, as examining the mechanical characteristics of living brain tissue in situ has proved challenging. However, accurate mechanical values *per se*, may be less important than the determination of the most reliable and clinically sensitive protocol.

More studies have been reporting test re-test measurements, with promising results [5–8]. For example, Murphy *et al.* 2013b report that their MRE processing pipeline possesses a typical coefficient of variation (CV) of <1% for global brain stiffness, and <2% for regional lobe stiffness measurements in 10 young healthy subjects [7]. At a higher 1.6 mm spatial resolution, Johnson *et al.* 2016 report a test re-test repeated measures CV of 1–2% for global measures, and 3–7% for measures of subcortical grey matter structures [6]. However, brain MRE has so far lacked a test-retest agreement study assessing a range of subjects over two separate time points, while directly comparing performance of more than one MRE protocol.

In this chapter, the validity of two widely published protocols for generating brain mechanical property measurements are examined, to include single frequency non-linear inversion (SF-NLI) and multifrequency multi-dual elasto-visco inversion (MF-MDEV), as installed and optimised at the Edinburgh Imaging Facility, QMRI as described in *Chapter 5*. Additionally, the SF-NLI protocol was incorporated with soft prior regularisation (SF-NLI-SPR), whereas the multifrequency data were reanalysed with MDEV using a smaller band, or limited range (LR) of frequencies (MF-MDEV-LR), resulting in the availability of four experimental protocols. The SPR inversion scheme incorporates prior anatomical information to penalise heterogeneity in a ROI, thereby avoiding effects from neighbouring tissue or cerebrospinal fluid [9], with previous studies demonstrating improved sensitivity and less uncertainty (i.e. decreased coefficient of variation), of subcortical grey matter measurements [6]. A limited range of frequencies are also analysed with MDEV to assess whether this improves test-retest results. Previously, Dittman *et al.* 2015 suggested that the applied frequency range for brain MRE should be small to ensure that waves at different frequencies obey similar damping properties. This is because low frequencies cause values in the centre of the brain to be dominated by nearly undamped low-frequency waves [10]. More specifically, the present study will examine validity of each protocol for measurements of the global cerebrum (Ce) and the hippocampus (Hp). Results of Ce test re-test agreement can be compared with results obtained from other studies, as mentioned, whereas Hp is a particular brain structure of interest due its implication in Alzheimer's disease.

In order to understand the conducted analyses, it may be necessary to provide a description of the terms *agreement* and *reliability*. Across the literature, the distinction between both concepts remains anything but clear, and the term "repeatability" is commonly used for both agreement as well as reliability [11]. The first objective of this chapter is to assess test re-test *agreement* of each of the four brain MRE protocols. The term *agreement* is the capacity of a measurement tool applied twice on the same participants to provide strictly identical results. In this instance, we would expect the same brain MRE protocol, administered on different days, to provide identical values for each subject. It is acknowledged that in real conditions, perfect agreement is more of a theoretical concept than a reality, since there are many factors that are impossible to control for which can influence measurements. However, a perfect agreement should always be the objective because lowering expectations can only lead to unsatisfactory tools [11]. Test re-test agreement will be measured with the intraclass correlation efficient ICC (absolute agreement model), the coefficient of variation (CV) and Bland-Altman plots. An additional interest is to determine the *reliability* of measurements between protocols. *Reliability* refers to the ability of a test to replicate the same ordering between participants when measured twice; in this case, the two measurements correspond to results obtained by two different MRE protocols. We do not expect different protocols to provide identical quantitative values (i.e. show agreement), largely due to alterative actuation frequencies and MRE-derived output parameters, but it is essential that they are reliable (i.e. whether the stiffest brain measured using one method would also be the stiffest determined with another). Understandably, however, if agreement is found to be unacceptable, the reliability of the protocol is likely to be poor. Inter-method reliability will be measured using ICC, but with model type *consistency*. A further aim of this chapter is to establish whether one particular method is more sensitive at detecting mechanical differences between young and healthy older adults, as previously published using other brain MRE protocols [12–14].

6.2 Materials and methods

6.2.1 *Subjects*

Twelve apparently healthy participants were recruited from the Join Dementia Research (JDR) database; six were young adult participants (mean age: 23.8±3.5 years) and six were older participants (mean age: 69.5±1.8 years). Criteria for exclusion included: 1) history or current diagnosis of a psychiatric disorder, and 2) history of major head injury. Older participants were required to complete the Montreal Cognitive Assessment (MoCA) [15] and score within the normal range (>26/30) to rule out significant underlying memory problems. An equal number of female and male participants were recruited into each group to consider the known differences in brain viscoelasticity between men and women [12,14]. As in previous studies of MRI reliability, the interval between sessions included sources of variability that cannot be practically excluded such as instrument drift and subtle physiological changes, including hydration status or blood pressure [16]. The study was approved by the NHS Lothian ethics committee and all study participants gave written, informed consent prior to the examination.

6.2.2 *MRI protocol*

All volunteers underwent two MRI scanning sessions, with an average time of nineteen days between sessions (range = 6 - 31 days). MRI and MRE data were collected using a Siemens 3T Verio whole-body MRI scanner with a 12-channel head receive coil (Siemens Medical Solutions; Erlangen, Germany). The imaging protocol included high-resolution T_1-weighted and MRE series. T_1-weighted images were acquired using an MPRAGE sequence (magnetization-prepared rapid gradient echo; 1 x 1 x 1mm^3 voxel size; 2400/1000/2.97ms repetition/inversion/echo times).

6.2.3 *Anatomical segmentation and mask generation*

Masks of the hippocampus (Hp) were obtained via automatic segmentation of T_1-weighted images using `FREESURFER` v. 5.3 through the recon-all pipeline [17]. `FREESURFER` without user intervention (‘recon-all –i subjectid.mgz –all’) was run, since this is the mode of operation that would be used in an automated pipeline processing patient data. However, all segmentations were visually inspected for accuracy and manual corrections were made when necessary. An in-house graphical user interface (`MeNA`), was used to perform MRE to T_1 coregistration and extraction of quantitative measurements. Briefly, the T_2-weighted magnitude MRE images are co-registered to the structural

T_1-weighted MPRAGE using the `FLIRT` tool within `FSL` [18]. The inverse transform is calculated so that the generated Hp mask from `FREESURFER` can be transferred into MRE space, to serve as a mask for soft prior regularisation (SPR), and as a ROI for quantitative measurements.

6.2.4 *MRE protocol*

A pneumatic actuator (Resoundant; Rochester, MN, USA) was used to vibrate the brain through a soft pad placed below the occipital portion of the head. Two fundamentally different, and widely published, brain MRE protocols were employed: The first pairs a high-resolution single vibration frequency spiral acquisition [19], with a finite-element based non-linear inversion (SF-NLI) [20–22]. The second combines data from multiple vibration frequencies in one inversion, known as multi-dual elasto-visco inversion (MF-MDEV) [23,24]. Further details of each protocol are provided below:

MRE acquisition

SF-NLI: multi-slab multishot spiral acquisition:

The MRE acquisition employed a 3D multi-slab multishot spiral sequence to capture high-resolution displacement data, as previously described [19]. Imaging parameters included: 1800/75ms repetition/echo times; 240mm square field-of-view; 150 x 150 imaging matrix; and sixty 1.6mm thick slices acquired in ten overlapping slabs. The resulting imaging volume had a 1.6 x 1.6 x 1.6mm^3 isotropic voxel size with 96mm of coverage in the slab direction, which was aligned approximately to the anterior commissure - posterior commissure (AC-PC) line and included the medial temporal lobe (MTL). MRE acquisition time was 12 minutes.

MF-MDEV: spin-echo echo-planar imaging:

This acquisition involved the use of a single-shot spin-echo EPI sequence to acquire MRE images at five mechanical drive frequencies (20, 30, 40, 50 and 60 Hz) with eight acquisitions over one wave cycle. A 2.3mm isotropic resolution was achieved with 20 slices covering the MTL. Further imaging parameters were: 4590/92ms repetition/echo times; 240mm field-of-view, 100 x 100 imaging matrix, phase-encoding direction(A$\Rightarrow$P). MEG frequencies were optimised based on the principles of fractional encoding [25], and were as follows: MEG frequency (number of cycles): 22 (1), 26 (1), 30 (1), 52 (2), 54 (2). MRE acquisition time was 1.55 per frequency, resulting in a total MRE scan time of approximately 10 minutes.

MRE analysis

An octahedral shear strain-based SNR measure (OSS-SNR) was performed to ensure sufficient data quality for stable inversion [26]. Datasets with a OSS-SNR score <3, will be excluded from the final analysis due to low quality displacement SNR [26].

SF-NLI: Single frequency non-linear inversion (NLI):

Nonlinear inversion (NLI) was used to estimate brain viscoelasticity from MRE displacement data [20–22, 27]. NLI estimates the complex shear modulus, $G^* = G' + G''$, from which I determined the shear stiffness μ, and damping ratio, ξ, to maintain consistent reporting with published work.

SF-NLI-SPR: NLI with soft-prior regularisation (SPR):

Furthermore, NLI was combined with SPR [9] to estimate viscoelasticity from MRE displacement data, as recently utilised in a number of brain MRE studies [6, 28]. Both of the MRE displacement data and Hp masks in MRE space were input into the NLI algorithm with a weighting of $\alpha = 10^{-11}$. This weighting was chosen to balance homogeneity enforcement while ensuring convergence.

MF-MDEV: multi-dual elasto-visco inversion (MDEV)

Multifrequency data (20, 30, 40, 50, 60 Hz) was processed by a multifrequency MRE processing pipeline known as multifrequency dual elasto-visco inversion (MDEV), as outlined previously [24, 29]. MDEV inversion provides high-resolution maps of the magnitude of the complex shear modulus $|G^*|$ and phase angle ϕ. A 2D low-pass filter, based on 2D Fourier transform, and Butterworth Kernel with a 50 m^{-1} threshold, were applied to all three components of the wave field.

MF-MDEV-LR: MDEV with limited frequency range (LR)

The typical MDEV pipeline was used, but only the data from actuation frequencies of 30, 40 and 50 Hz were incorporated.

6.2.5 *Statistical analyses*

A well-established measure of agreement and reliability is the intra-class correlation coefficient (ICC) [30]. When measuring the agreement between pairs of observations, it represents the between-pair variance expressed as a proportion of the total variance of the observations (i.e., it is the proportion of the total variability in the observations that is due to the differences between pairs). It is suggested that ICC values less than 0.5 are indicative of poor reliability, values between 0.5 and 0.75 indicate moderate reliability, values between 0.75 and 0.9 indicate good reliability, and values greater than 0.90 indicate excellent reliability [31]. The coefficient of variation (CV), which expresses the standard deviation as a percent of the mean, was also computed. Since the CV is a dimensionless (unit-less) statistical measure, it can be validly used to compare the variability of data recorded in different units or magnitudes. Level of agreement was assessed using Bland-Altman plots [32]. To demonstrate agreement, it is mandatory to show that values measured on two successive occasions are equal at the individual level for each participant. All analyses were performed with SPSS software version 23.0.0 (SPSS Inc., Chicago, IL). The statistical methods used to meet the primary and secondary objectives, are summarised below.

1) Test re-test agreement: The test re-test agreement of μ and ξ obtained from SF-NLI, and $|G^*|$ and ϕ from MF-MDEV, involved the computation of the intra-class correlation coefficient (ICC), using a two-way mixed effects model (single measures) and type *absolute agreement* [33]. The coefficient of variation (CV), also known as % error, was calculated, whereas level of agreement was assessed using Bland-Altman plots, with mean differences specified.

2a) Inter-method reliability: Results from time point 1 and 2 were averaged to give an overall score for each protocol for each participant. Inter-method agreement was similarly assessed with the intra-class correlation coefficient (ICC), using a two-way mixed effects model (single measures), however the model was of type *consistency* [33]. Here, we are only interested in the relative ranking of scores rather on their exact value, and thus this particular model allows for values of variable magnitudes.

2b) Biological sensitivity: The averaged MRE results from time point 1 and 2 were also used to assess suspected age differences. An independent samples t-test was then used to assess MRE measurements between 6 young and 6 older subjects for all protocols and for both MRE parameters. Level of significance was set at $p < .05$.

6.3 Results

Brain MRE was successfully performed on all participants. For simplicity, μ and $|G^*|$ are referred to as *stiffness* parameters, and ξ and ϕ are known as *viscosity* parameters, with protocol abbreviations condensed to: NLI, NLI-SPR, MDEV and MDEV-LR. Table 6.1 contains the mean MRE measurements obtained at visits 1 and 2, from all four experimental protocols, for both Ce and Hp, and illustrated in Figure 6.1. Immediately obvious is the higher stiffness values obtained from NLI-based methods. This is expected due to MDEV incorporating lower frequencies within the averaged inversion. As for the viscosity parameter, MDEV based methods provide much higher values. Of note: $\phi = \arctan G''/G'$, whereas $\xi = G''/2G'$, meaning that ϕ values are approximately twice as large compared to those provided for ξ. However, results would still not be comparable, as can be seen from Table 6.1.

Table 6.1: Mean MRE results for Ce and Hp from all protocols at two separate time points

Protocol	**Stiffness (kPa)**		**Viscosity**	
	Visit 1	*Visit 2*	*Visit 1*	*Visit 2*
Cerebrum				
NLI	2.70±0.26	2.68±0.28	.259±.018	.261±.019
MDEV	1.97±0.24	1.95±0.19	.775±.033	.767±.027
MDEV-LR	1.94±0.22	1.92±0.21	.750±.023	.750±.024
Hippocampus				
NLI	2.74±0.32	2.65±0.34	.184±.037	.184±.030
NLI-SPR	2.72±0.32	2.61±0.34	.182±.038	.182±.031
MDEV	1.54±0.18	1.59±0.17	.778±.058	.777±.079
MDEV-LR	1.48±0.17	1.50±0.19	.760±.053	.757±.071

6.3.1 *Test re-test agreement*

First of all, the test-retest agreement of Ce using three experimental protocols was investigated. NLI-SPR results are not provided as SPR is typically used to promote homogeneity in small pre-defined regions (i.e. specific brain structures, or ROIs), and not the entire cerebral volume.

Cerebrum: Assessment of test re-test agreement for the stiffness parameter was *good* for the NLI (ICC: 0.89; CI: 0.67-0.97) and MDEV (ICC: 0.86; CI: 0.60-0.96) pipelines, and *excellent* for the MDEV-LR protocol (ICC: 0.90; CI: 0.71-0.97), see Table 6.2. Bland-Altman analysis revealed that the mean

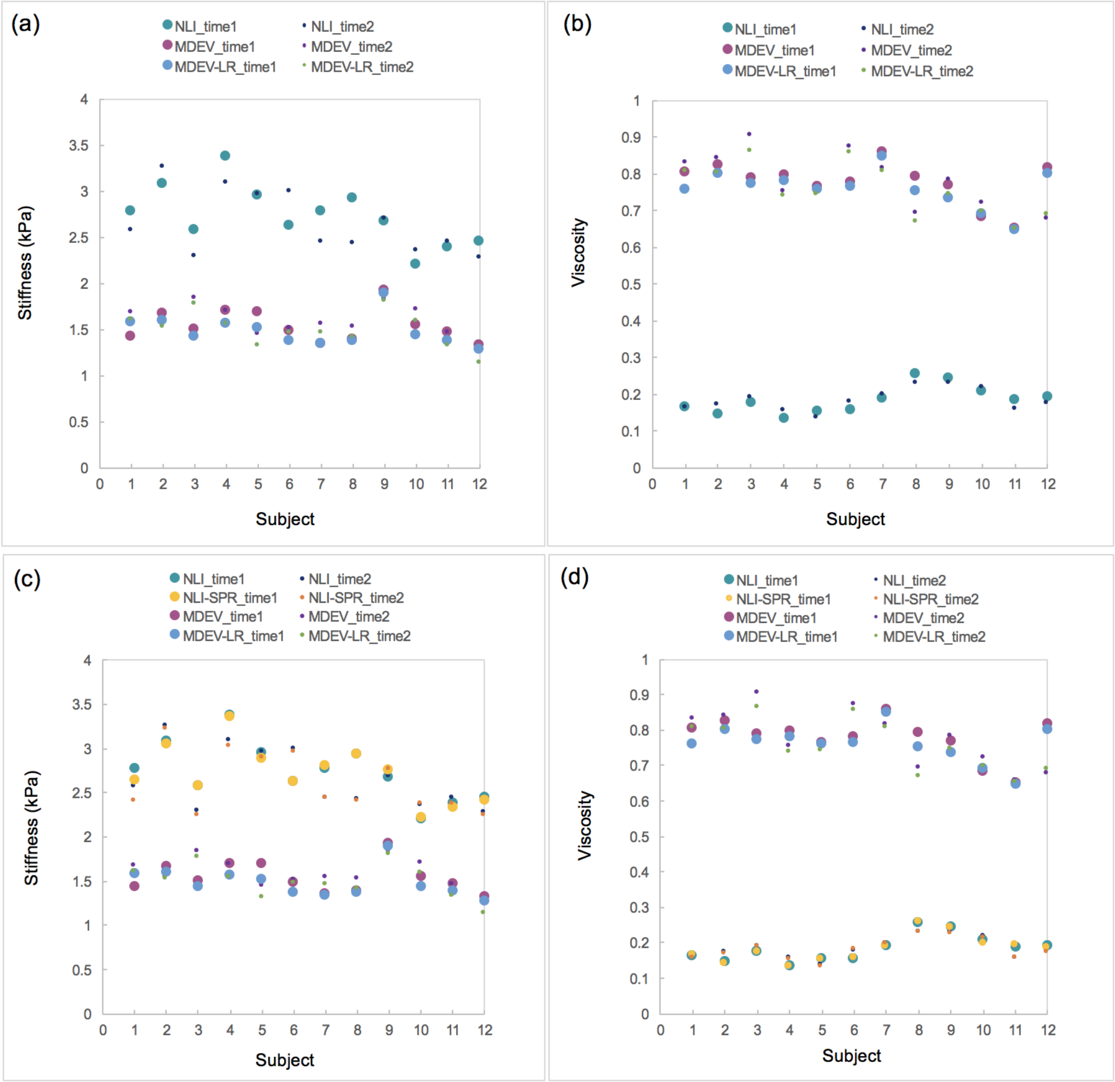

Figure 6.1: MRE-derived values for Cp and Hp measured at two separate time points; (a) Ce stiffness results, measured as μ for NLI methods, and $|G^*|$ for MDEV methods; (b) relative viscous-to-elastic properties of Ce measured as ξ and ϕ, for NLI and MDEV protocols, respectively; (c) Hp stiffness results and, (d) Hp relative viscous-to-elastic measurements. Subjects 1-6 were young adults (mean age: 24 years), whereas subjects 7-12 were healthy older adults (mean age: 70 years).

difference in stiffness for NLI, MDEV and MDEV-LR was 0.02 kPa (95% agreement limits: -0.23 - 0.28 kPa), 0.03 kPa (95% agreement limits: -0.20 - 0.25 kPa), and 0.02 kPa (95% agreement limits: -0.17 - 0.21 kPa), respectively. Mean within subject coefficient of variation (CV) was 2.54% for NLI, 3.32% for MDEV, and 2.80% for MDEV-LR.

For the viscosity parameters, test re-test agreement for NLI was *moderate* (ICC: 0.61; CI: 0.06-0.87), and *poor* for both MDEV (ICC: 0; CI: -0.65,0.52) and MDEV-LR (ICC: 0.37; CI:-0.28-0.77). Bland-Altman analysis revealed that the mean difference in viscosity for NLI, MDEV and MDEV-LR was -.001 kPa (95% agreement limits: -.035 - .032 kPa), .008 kPa (95% agreement limits: -.078 - .095 kPa), and .0001 kPa (95% agreement limits: -.053 - .053 kPa), respectively. Mean within subject coefficient of variation (CV) was 3.16% for NLI, 3.08% for MDEV, and 2.03% for MDEV-LR.

Table 6.2: Ce ICC results for visit 1 versus visit 2

Protocol	**Stiffness (kPa)**			**Viscosity**		
	ICC	**95% CI**	**Mean CV**	**ICC**	**95% CI**	**Mean CV**
NLI	0.89	(0.67, 0.97)	2.54%	0.61	(0.06, 0.87)	3.16%
MDEV	0.86	(0.60, 0.96)	3.32%	0	(-0.65, 0.52)	3.08%
MDEV-LR	0.90	(0.71, 0.97)	2.80%	0.37	(-0.28, 0.77)	2.03%

Hippocampus: Assessment of test re-test agreement for Hp stiffness was *moderate* for all four brain MRE protocols: NLI (ICC: 0.70; CI: 0.27-0.90), NLI-SPR (ICC: 0.68; CI: 0.22-0.89), MDEV (ICC: 0.51; CI: -0.05-0.83) and MDEV-LR (ICC: 0.68; CI: 0.19-0.90), as summarised in Table 6.3. Bland-Altman analysis revealed that the mean difference in stiffness for NLI, NLI-SPR, MDEV, and MDEV-LR was 0.09 kPa (95% agreement limits: -0.41 - 0.58 kPa), 0.11 kPa (95% agreement limits: -0.41 - 0.62 kPa), -0.05 kPa (95% agreement limits: -0.38 - 0.29 kPa), and -0.02 kPa (95% agreement limits: -0.31 - 0.27 kPa), respectively. Mean within subject coefficient of variation (CV) was 5.61% for NLI, 5.99% for NLI-SPR, 6.18% for MDEV and 5.36% for MDEV-LR.

For the viscosity parameters, test re-test agreement for Hp viscosity was *good* for NLI and NLI-SPR, (ICC: 0.84; CI: 0.54-0.95 and ICC: 0.81; CI: 0.45-0.94), respectively, *moderate* for MDEV-LR (ICC: 0.54; CI: -0.06-0.84) and *poor* for MDEV (ICC: 0.48; CI: -0.14-0.82). Bland-Altman analysis revealed that the mean difference in viscosity for NLI, NLI-SPR, MDEV and MDEV-LR was -.0001 kPa (95% agreement limits: -.039 - .039 kPa), .0008 kPa (95% agreement limits: -.042 - .044 kPa), .0013 kPa (95% agreement limits: -.140 - .143 kPa), and .0038 kPa (95% agreement limits: -.117 - .125 kPa), respectively. Mean within subject coefficient of variation (CV) was 6.90% for NLI, 7.84% for NLI-SPR, 4.76% for MDEV, and 4.17% for MDEV-LR.

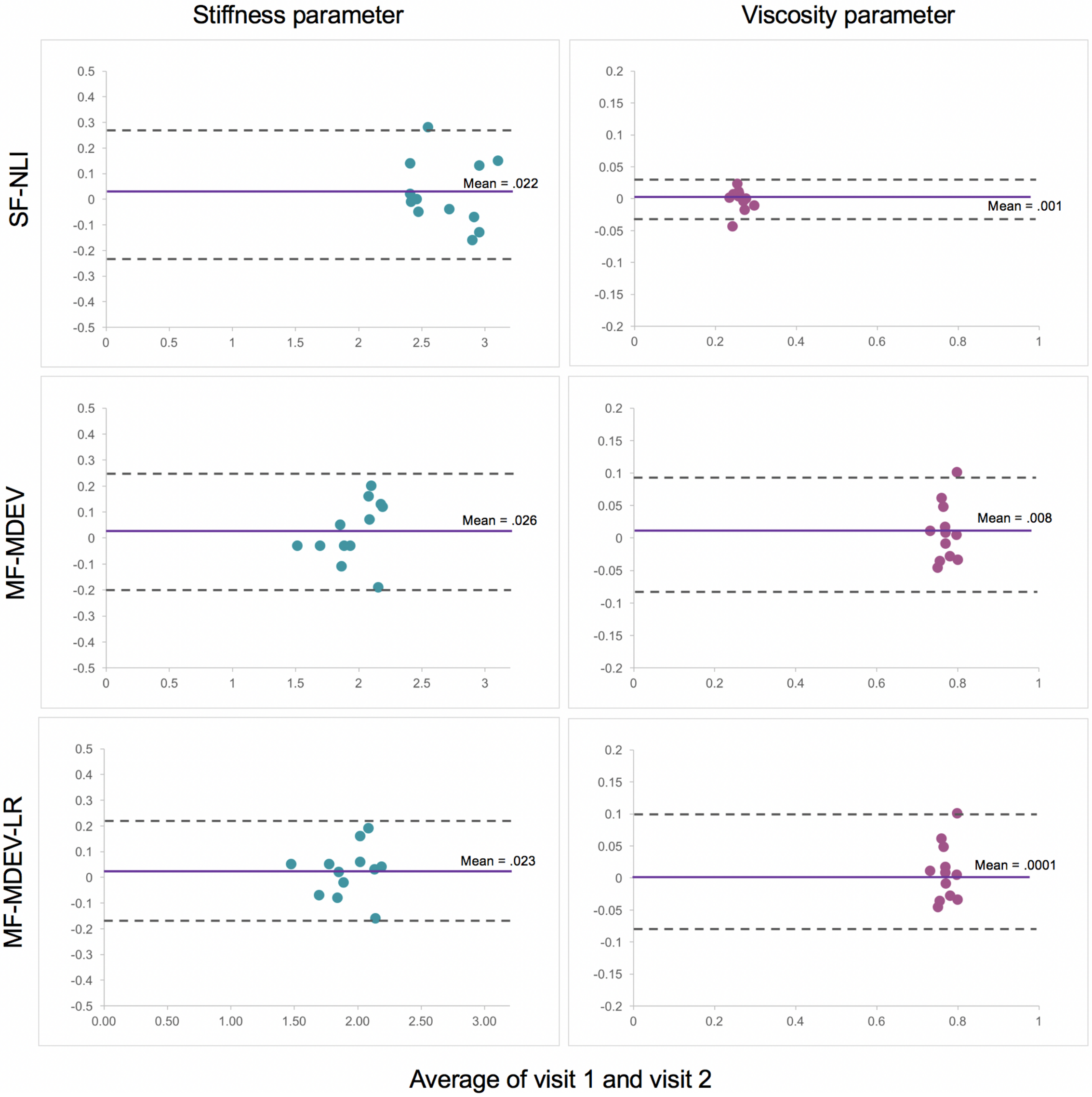

Figure 6.2: Bland-Altman method, used to evaluate MRE cerebral stiffness and viscosity concordance between visits 1 and 2 for three brain MRE pipelines. The 95% confidence limits of the bias are shown as two dashed lines, with the mean value of the differences shown in purple. The figure suggests that the measured variance may increase as the stiffness parameter increases.

6.3.2 *Inter-method reliability*

Reliability of Ce stiffness for NLI with MDEV, and NLI with MDEV-LR was *good* (ICC: 0.77; CI: 0.37-0.93) and ICC: 0.80; 0.43-0.94), respectively. *Excellent* reliability was found for Ce stiffness measures obtained by MDEV with MDEV-LR (ICC: 0.99; CI: 0.97-1). In contrast, very poor agreement was found for Ce viscosity between NLI with MDEV, and NLI with MDEV-LR (ICC: 0). *Good* reliability

Table 6.3: Hp ICC results for visit 1 versus visit 2.

Protocol	**Stiffness (kPa)**			**Viscosity**		
	ICC	**95% CI**	**Mean CV**	**ICC**	**95% CI**	**Mean CV**
NLI	0.70	(0.27, 0.90)	5.61%	0.84	(0.54, 0.95)	6.90%
NLI-SPR	0.68	(0.22, 0.89)	5.99%	0.81	(0.45, 0.94)	7.84%
MDEV	0.51	(-0.05, 0.83)	6.18%	0.48	(-0.14, 0.82)	4.76%
MDEV-LR	0.68	(0.19, 0.90)	5.36%	0.54	(-0.06, 0.84)	4.17%

was found between MDEV and MDEV-LF (ICC: 0.84; CI: 0.53-0.95), as shown in Table 6.4.

Table 6.4: Mean Ce MRE results from all four experimental protocols

	NLI	MDEV	MDEV-LR
NLI	-	**.77 (.37-.93)**	**.80 (.43-.94)**
MDEV	0 (-.73-.31)	-	**.99 (.97-.1)**
MDEV-LR	0 (-.72-.33)	.84 (.53-.95)	-

Note: stiffness parameters in **bold**. 95% confidence levels in parenthesis.

Table 6.5 illustrates inter-method Hp ICC results. *Excellent* reliability for Hp stiffness was found between NLI with NLI-SPR (ICC: 0.98; CI: 0.94-0.99), and MDEV with MDEV-LR (ICC: 0.94; CI: 0.82-0.98). *Poor* reliability was apparent between NLI with MDEV (ICC: 0.23, CI: 0.37-0.70), NLI with MDEV-LF (ICC: 0.21; CI: 0.39-0.68), NLI-SPR with MDEV (ICC: 0.29; CI: -0.31-0.73), and NLI-SPR with MDEV-LR (ICC: 0.26; CI: -0.35-0.71). For Hp viscosity, *excellent* reliability was found between NLI with NLI-SPR (ICC: 1; CI: 0.99-1), and MDEV with MDEV-LR (ICC: 0.98; CI: 0.92-0.99), whereas very *poor* reliability was found between NLI with MDEV, NLI with MDEV-LR, NLI-SPR with MDEV, and NLI-SPR with MDEV-LR (ICC: 0).

6.3.3 *Biological sensitivity*

Mean values for Ce and Hp was determined for each participant from both time point assessments. The mean stiffness and viscosity measurements for young and older subjects, categorised by protocol, are provided in Table 6.6. Independent-samples *t*-tests were performed to compare young and older

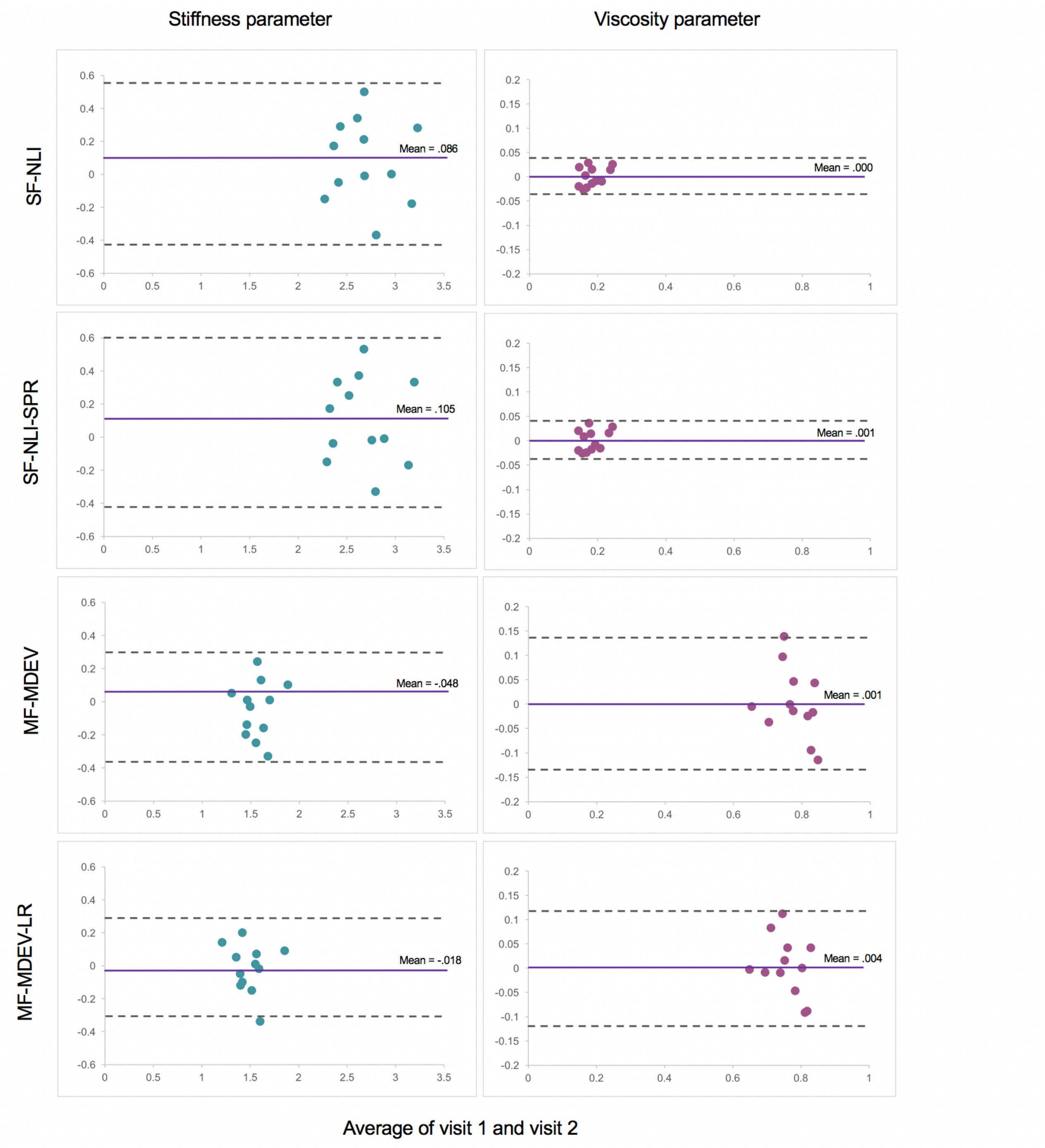

Figure 6.3: Bland-Altman method, used to evaluate MRE hippocampal stiffness and viscosity concordance between visits 1 and 2 for four brain MRE pipelines. The 95% confidence limits of the bias are shown as two dashed lines, with the mean value of the differences shown in purple.

Table 6.5: Mean Hp MRE results from all four experimental protocols

	NLI	NLI-SPR	MDEV	MDEV-LR
NLI	-	**.98 (.94-.99)**	**.23 (-.37-.70)**	**.21 (-.39-.68)**
NLI-SPR	1 (.99-1)	-	**.29 (-.31-.73)**	**.26 (-.35-.71)**
MDEV	0 (-.67-.41)	0 (-.68-.40)	-	**.94 (.82-.98)**
MDEV-LR	0 (-.71-.34)	0 (-.72-.33)	.98 (.92-.99)	-

Note: stiffness parameters in **bold**. 95% confidence levels in parenthesis.

participant MRE results for Ce and Hp for each protocol and both MRE parameters. There was a significant difference in Ce stiffness between age groups using all protocols: NLI: t=(10)=8.52, $p <$ .001; MDEV: t=(5.93)=5.03, p = .002 (equal variances not assumed); and MDEV-LR: t=(10)=5.06, p < .001. In contrast, none of the protocols detected a significant difference between age groups for the viscosity parameter: NLI: t=(10)= -1.93, p = .083; MDEV: t=(10)= .83, p = .426; and MDEV-LR: t=(10)=.371, p = .718.

Table 6.6: Mean MRE results for young and older participants according to protocol

Protocol	**Stiffness (kPa)**			**Viscosity**		
	Young	*Old*	*t-test*	*Young*	*Old*	*t-test*
Cerebrum						
NLI	2.93±0.12	2.45±0.05	p < .001	.252±.010	.269±.019	p = .083
MDEV	2.13±0.05	1.79±0.16	p = .002	.776±.021	.766±.021	p = .426
MDEV-LR	2.10±0.07	1.76±0.15	p < .001	.752±.021	.748±.019	p = .718
Hippocampus						
NLI	2.88±0.30	2.51±0.18	p = .026	.161±.014	.207±.029	p = .006
NLI-SPR	2.82±0.32	2.51±0.20	p = .067	.159±.015	.205±.028	p = .005
MDEV	1.60±0.08	1.53±0.20	p = .456	.811±.033	.744±.063	p = .042
MDEV-LR	1.53±0.08	1.46±0.22	p = .481	.789±.027	.728±.060	p = .051

Furthermore, there was a significant difference in Hp stiffness between age groups using NLI: t=(10)=2.62, p = .026; NLI-SPR was approaching significance: t=(10)= 2.06, p = .067; whereas MDEV: t=(10)=.776, p = .456; and MDEV-LR: t=(10)=.732, p = .481, reported no significant differences. NLI, NLI-SPR and MDEV protocols found a significant difference between age groups for Hp viscosity (t=(10)= -3.52, p = .006; t=(10)= -3.56, p = .005; t=(10)=2.34, p = .042), respectively, whereas MDEV-LF was approaching significance (t=(10)=2.21, p = .051).

6.4 Discussion

The primary objective of this study was to investigate the test re-test agreement of two fundamentally different high-resolution brain MRE protocols: so-called single-frequency non-linear inversion (NLI) and multifrequency multi-dual elasto-visco inversion (MDEV). The NLI based method was extended further to incorporate soft-prior regularisation (NLI-SPR), whereas multifrequency data were reanalysed with MDEV using a smaller bandwidth, or limited range of frequencies (MDEV-LR). Secondary objectives included an assessment of inter-method reliability, and an evaluation of biological sensitivity to suspected ageing effects.

The first aim involved an evaluation of the test re-test agreement of brain MRE for measuring the global cerebrum (Ce) and a smaller brain structure of interest, i.e. hippocampus (Hp). That is, the capacity of each of brain MRE protocol to provide strictly identical results at two separate time points. NLI, MDEV and MDEV-LR all exhibit *good* to *excellent* agreement for measuring Ce stiffness, with a coefficient of variation between 2.5-3.3%. NLI was found to exhibit *moderate* agreement for Ce viscosity, whereas MDEV methods show *poor* agreement. As for Hp, all protocols show *moderate* agreement for measuring Hp stiffness, with a coefficient of variation between 5.4-6.2%. For Hp viscosity, however, both NLI-based methods show *excellent* agreement whereas MDEV and MDEV-LR show *poor* and *moderate* agreement, respectively. A secondary aim of this study was to assess inter-method reliability (i.e. whether each MRE protocol could replicate the same ordering between subjects). A novel finding is that Ce stiffness measured with NLI and MDEV show *good* reliability, however *poor* reliability was found for Ce viscosity using the same protocols. Furthermore, neither NLI based pipeline with MDEV or MDEV-LR was reliable for Hp measurements. As expected, NLI based methods, and MDEV based methods both show *excellent* reliability with each other. The final objective was to assess whether any brain MRE protocol could detect mechanical differences between young and older adults, as previously reported. All protocols found a significant difference between age group for Ce stiffness, indicating lower Ce stiffness in older adults, whereas no age affect for Ce viscosity was found by any protocol. NLI was the only protocol to detect a difference in Hp stiffness between age groups, indicating that older adults may also possess a softer Hp. Finally, all protocols found a significant age related difference for Hp viscosity. Of interest, NLI-based methods suggest the Hp is more viscous in older age, whereas MDEV-based methods suggest Hp viscosity is actually higher in younger adults.

Previous studies investigating brain MRE reliability have not calculated the ICC; it has been more common to report the within-subject coefficient of variation (CV) as an estimate of the measurement uncertainty. Therefore, the CV results presented in this study will be compared to the CV results obtained previously. For example, this study reports a CV of between 2-3% for whole brain Ce stiffness. More specifically, NLI is 2.5%, MDEV is 3.3%, which decreases to 2.8% using a limited frequency range (MDEV-LR). These results are comparable to Sack *et al.,* 2009 who reported variations in Ce stiffness of 4.5% in a single image slice [12] and Murphy *et al.,* 2011 who reported a CV of 3.1% in whole-brain white matter [34]. More recently, Murphy *et al.,* 2015 reported CVs for global stiffness of less than 1%, in ten healthy volunteers, scanned three times each on the same day. However, intra-session variability is expected to be lower than inter-session variability, where there is likely to be a variety of uncontrolled confounds (i.e. scanner drift, biological effects). Additionally, Johnson *et al.* 2016 recently reported Ce stiffness CV of 1.4%, although this was a repeated measures analysis of one subject scanned 8 times on one day, where lower variation is inevitable. Johnson *et al.,* 2016 also report a CV of 2.1% for Ce viscosity. This study reports a slightly higher CV of 3.2% using the same protocol, whereas the use of MDEV-LR again improved the CV from 3.1% (MDEV) to 2.0%. In this instance, the importance of using additional validity measures is highlighted. While the CV is lower for MDEV based methods compared to NLI based methods, MDEV also show poor levels of agreement as shown by ICC measures, whereas in contrast, NLI shows acceptable levels of agreement.

Considering Hp, only one study has reported a reliability metric [6]. Johnson *et al.,* 2016 report a CV of 7.1% for Hp stiffness using NLI-SPR, whereas in this study it was 5.6% for NLI and 6.0% for NLI-SPR. Not only did the CV increase due to the addition of SPR, but the ICC also decreased from 0.70 to 0.68, and the mean difference of agreement increased from 0.09 kPa to 0.11 kPa. Additionally, the use of SPR also resulted in slightly poorer measures for Hp viscosity (i.e. ICC decreased from 0.84 to 0.81, and the CV increased from 6.90% to 7.84%). By applying SPR to heterogeneous regions such as the Hp, there is the possibility of further introducing modelling errors by attempting to enforce homogeneity where it is not appropriate [35]. However, the experimental literature supports its use [6,9,28,36], and in the very limited sample size analysed in this study, I acknowledge the possibility of measurement error. The use of a limited range of frequencies improved MDEV agreement, decreasing CV from 6.2% to 5.4% for Hp stiffness, and from 4.8% to 4.2% for Hp viscosity. In general, MDEV based methods show poorer agreement compared to NLI. Possible explanations for this include issues with coregistration accuracy due to the limited field of view acquisition and multi-stage registration process, as well as the selected slice positioning. Depending on the position of the slices, the entire Hp may not have been captured, which results in the possibility that different parts of the Hp may have been measured across the two time points.

To my knowledge, this study represents the first investigation into brain MRE inter-method reliability. Due to different experimental paradigms, it is not expected for alternative brain MRE protocols to provide identical quantitative values. However, an essential finding would be whether alternative protocols could replicate the same ordering of stiffness, or viscosity, between participants. In fact, this was found for measuring Ce stiffness using both NLI and MDEV-based methods. In particular, NLI with MDEV-LR show the highest levels of inter-method reliability with a ICC of 0.80. As discussed previously, higher test re-test agreement was seen for MDEV-LR over MDEV, and therefore it is not surprising that higher reliability with NLI is reported for MDEV-LR. Importantly, this finding suggests that the number of frequencies used for MDEV could be reduced to three, thereby nearly halving the MRE acquisition time. Another important finding from this study is demonstrating that the two NLI based methods, and the two MDEV methods, are highly reliable. While this might seem intuitive as the protocols exhibit many similar components, this finding has not been proven empirically. As such, previous studies that have used variations of these protocols can be assured that comparable results would be obtained regarding the respective position of each participant on the mechanical scale. Of concern is the results provided thus far for Ce viscosity. These results suggest that previous findings in animal models, patient studies, or investigations into cognition, regarding Ce viscosity, such as those performed by Streitberger *et al.,* 2014, Guo *et al.,* 2013, and Schwarb *et al.,* 2016, 2017 may have found entirely different results depending on the protocol of choice; the protocols did not agree on the relative differences between subjects.

These results also suggest that NLI may be more sensitive for detecting age-related mechanical differences between young and older adults. In this sample of six younger adults (mean age: 24 years), and older adults (mean age: 70 years), all protocols found a significant age affect that suggests that the brain softens in older age, supporting previous work from Arani *et al.,* 2015, Sack *et al.* 2009 and Sack *et al.,* 2011, who used entirely different MRE methods [12–14]. Furthermore, all protocols agree that there is no uniform age-related change to Ce viscosity - as reported by Sack *et al.,* 2011. However, NLI was the only method to find a significant difference in Hp stiffness ($p < .026$), suggesting the Hp also softens in older age. This is a novel finding that will require further investigation. Considering Hp viscosity, NLI and NLI-SPR found a strong significant age effect ($p = .006$ and $p = .005$), whereas MDEV and MDEV-LR report higher p values ($p = .042$, and $p = .051$), respectively. Interestingly, the NLI methods suggest that viscosity, or the dissipative behaviour or tissue, is greater in older adults, whereas the MDEV methods suggest the opposite (i.e. that viscosity is higher in younger adults).

NLI based methods have typically suggested that increased viscosity represents a reduction in tissue integrity, whereas MDEV methods have suggested that higher viscosity represent a more complex, and thus more healthy, tissue network. The biological correlates of the viscosity parameter is, therefore, currently open to interpretation. However, given the finding that MDEV and MDEV-LR possess poor levels of test-retest agreement, significant age effects should be approached with caution.

6.4.1 *Limitations*

A number of limitations are noted within this study. The first is the small sample size; larger numbers of participants may be able to more accurately determine the test re-test agreement, reliability, and biological sensitivity of each protocol. Furthermore, this study did not perform an intra-rater reliability analysis; a typical validity assessment for many MRI and MRE studies alike [37,38]. However, studies of liver MRE, for example, typically involve the researcher to manually select regions of interest, avoiding large vessels, and any areas affected by cardiac and vascular artefacts; a procedure which may be prone to individual error. This study, however, utilises a largely automated segmentation pipeline (i.e. `FREESURFER`) in addition to an optimised coregistration and automatic extraction of quantitative measurements using an in-house graphical user interface (`MeNA`) - see *Chapter 5*). Therefore, differences in intra-rater measurements are expected to be negligible, although this will need to be investigated in future studies.

Furthermore, while the spiral image acquisition and reconstruction used within the NLI protocol is designed to minimise residual field inhomogeneity distortions and motion-induced phase errors, the Hp region may still be particularly sensitive to artefacts, therefore, future strategies may further minimise the residual artefacts and improve Hp property measures [6]. As for the MDEV pipelines, while every effort was used to ensure an accurate coregistration between the Hp mask and MDEV-derived mechanical maps, the inherent image distortions caused by local susceptibility-induced Bo inhomogeneities from the EPI acquisition may hamper an optimal alignment. Future work could correct for EPI distortion as recently implemented with MRE [39], as it is well known that correction for EPI distortions can improve anatomical localisation, thereby also significantly increasing statistical power. Finally, recent work from the Charité group have used a recalculated version of the phase angle ϕ^* within MDEV to counteract the well-known overestimation of values due to high noise sensitivity [10]. The present study did not implement the revised calculation, and it stands to reason that the test-retest agreement of MDEV viscosity may be improved using ϕ^*, however, as yet, the relationship between the original and the recalculated parameter has not been established.

Finally, it needs to be mentioned that short term dynamics within the brain may have an influence on the measured stiffness. Parker *et al.,* 2017 recently theoretically demonstrated that measureable, time varying changes in brain stiffness are possible simply by accounting for vasodynamic or electrochemical changes in the state of any region of the brain, and suggest these should either be controlled for or elicited and measured as part of the experimental protocol [40]. Future studies could investigate this possible relationship by the use of different types of anaesthesia, or through specific mixes of oxygen and carbon dioxide, both of which have been to shown to have different effects on vasodilation [41]. The control of vasodynamic or electrochemical effects, therefore, could potentially improve the validity of MRE measurements by minimising within subject variability over time.

6.5 Conclusion

The analysis and results presented in this study demonstrate how NLI, MDEV, and MDEV-LR show comparably high levels of test-retest agreement for measurement of Ce stiffness. NLI was the only method to possess acceptable test re-test agreement for Ce viscosity. Analysis of a smaller region of interest (i.e. hippocampus) further demonstrates NLI and MDEV to show high levels of agreement for Hp stiffness, and that the use of a limited range of frequencies may improve test re-test agreement of MDEV. Again, agreement for NLI-based methods was much better than MDEV for Hp viscosity. Generally, the use of SPR was comparable to, or even slightly worse, than standard NLI. However, this may be attributed to the small sample size or measurement error, as I acknowledge that a wealth of literature supports its use. An important novel finding was the discovery that NLI and MDEV based approaches elicit high inter-method reliability in an assessment of Ce stiffness, however, future work will need to establish the reasons for poor inter-method reliability of the viscosity parameter. Finally, NLI generally appears to be marginally more sensitive to ageing effects, detecting a possible age-related change in Hp stiffness that was not apparent with other methods.

In summary, all future work in this thesis will utilise the NLI protocol due to generally superior test re-test agreement for both Ce and Hp stiffness and viscosity parameters, and its potentially increased sensitivity to ageing effects. SPR will also be incorporated based on the wealth of published experimental evidence that shows its use to stabilise measurements and improve reliability by decreasing the coefficient of variation. Furthermore, the spiral acquisition scheme, inherent to the NLI protocol, provides full brain coverage and as such, will allow for the study of a range of other brain structures of interest. In the next chapter, a larger scale study is conducted to assess the mechanical properties of the Ce and a range of subcortical grey matter structures (SGM) between young and cognitively healthy older adults; it stands to reason that alternative brain regions may be differentially affected by the ageing process. A particular focus will be on whether MRE can provide additional information unrelated to conventional volumetric imaging, typically used to measure the extent of age-related cerebral atrophy.

References

[1] G Guyatt, S Walter, and G Norman. Measuring change over time: assessing the usefulness of evaluative instruments. *J Chronic Dis*, 40:171–178, 1987.

[2] CDG Hines, TA Bley, MJ Lindstrom, and SB Reeder. Repeatability of Magnetic Resonance Elastography for Quantification of Hepatic Stiffness. *J Magn Reson Imaging*, 31:725–731, 2010.

[3] AT Trout, S Serai, AD Mahley, H Wang, Y Zhang, B Zhang, and JR Dillman. Liver stiffness measurements with MR Elastography: agreement and repeatability across imaging systems, field strengths, and pulse sequences. *Radiology*, 281:793–804, 2016.

[4] LV Hiscox, CL Johnson, E Barnhill, MDJ McGarry, J III Huston, EJR van Beek, JM Starr, and N Roberts. Magnetic resonance elastography (MRE) of the human brain: technique, findings and clinical applications. *Phys Med Biol*, 61:401–437, 2016.

[5] CL Johnson, MDJ McGarry, AA Gharibans, JB Weaver, KD Paulsen, H Wang, WC Olivero, BP Sutton, and JG Georgiadis. Local mechanical properties of white matter structures in the human brain. *NeuroImage*, 79:145–152, 2013b.

[6] CL Johnson, H Schwarb, MDJ McGarry, AT Anderson, GR Huesmann, BP Sutton, and NJ Cohen. Viscoelasticity of subcortical gray matter structures. *Hum Brain Mapp*, 2016.

[7] MC Murphy, J Huston 3rd, Jr CR Jack, KJ Glaser, ML Senjem, J Chen, A Manduca, JP Felmlee, and RL Ehman. Measuring the characteristic topography of brain stiffness with magnetic resonance elastography. *PLoS One*, 8:e81668, 2013b.

[8] AT Anderson, EEW Van Houten, MDJ McGarry, KD Paulsen, JL Holtrop, BP Sutton, JG Georgiadis, and CL Johnson. Observation of direction-dependent mechanical properties in the human brain with multi-excitation MR elastography. *J Mech Behav Biomed Mater*, 59:538–546, 2016.

[9] MDJ McGarry, CL Johnson, BP Sutton, EEW Van Houten, JG Georgiadis, JB Weaver, and KD Paulsen. Including spatial information in nonlinear inversion MR elastography using soft prior regularization. *IEEE Trans Med Imaging*, 32:1901–1909, 2013.

[10] F Dittmann, S Hirsch, H Tzschätzsch, J Guo, J Braun, and I Sack. In vivo wideband multifrequency MR elastography of the human brain and liver. *Magn Reson Med*, doi: 10.1002/mrm.26006, 2015.

[11] A Berchtold. Test–retest: Agreement or reliability? *Methodological Innovations*, 9:2059799116672875, 2016.

[12] I Sack, B Beierbach, J Wuerfel, D Klatt, U Hamhaber, S Papazoglou, P Martus, and J Braun. The impact of aging and gender on brain viscoelasticity. *NeuroImage*, 46:652–657, 2009.

[13] I Sack, KJ Streitberger, D Krefting, F Paul, and J Braun. The Influence of Physiological Aging and Atrophy on Brain Viscoelastic Properties in Humans. *PLoS One*, 6:e23451, 2011.

[14] A Arani, MC Murphy, KJ Glaser, A Manduca, DS Lake, SA Kruse, C Jack, RL Ehman, and J Huston 3rd. Measuring the effects of aging and sex on regional brain stiffness with MR elastography in healthy older adults. *NeuroImage*, 111:59 – 64, 2015.

[15] ZS Nasreddine, NA Phillips, V Bedirian, S Charbonneau, V Whitehead, I Collin, JL Cummings, and H Chertkow. The Montreal Cognitive Assessment, MoCA: a brief screening tool for mild cognitive impairment. *J Am Geriatr Soc*, 53:695–699, 2005.

[16] JS Wonderlick, DA Ziegler, P Hosseini-Varnamkhasti, JJ Locascio, A Bakkour, A van der Kouwe, C Triantafyllou, S Corkin, and BC Dickerson. Reliability of MRI-derived cortical and subcortical morphometric measures: Effects of pulse sequence, voxel geometry, and parallel imaging. *NeuroImage*, 44:1324–1333, 2009.

[17] B Fischl, DH Salat, E Busa, M Albert, M Dieterich, C Haselgrove, A van der Kouwe, R Killiany, D Kennedy, S Klaveness, A Montillo, N Makris, B Rosen, and AM Dale. Whole brain segmentation: automated labeling of neuroanatomical structures in the human brain. *Neuron*, 33:341–355, 2002.

[18] M Jenkinson, CF Beckmann, TEJ Behrens, MW Woolrich, and SM Smith. FSL. *NeuroImage*, 62:782–790, 2012.

[19] CL Johnson, JL Holtrop, MDJ McGarry, JB Weaver, KD Paulsen, JG Georgiadis, and BP Sutton. 3D multislab, multishot acquisition for fast, whole-brain MR elastography with high signal-to-noise efficiency. *Magn Reson Med*, 71:477–485, 2014.

[20] EEW Van Houten, KD Paulsen, MI Miga, FE Kennedy, and JB Weaver. An overlapping subzone technique for MR-based elastic property reconstruction. *Magn Reson Med*, 42:779–786, 1999.

[21] EEW Van Houten, DvR Viviers, MDJ McGarry, PR Perrinez, II Perreard, JB Weaver, and KD Paulsen. Subzone based magnetic resonance elastography using a Rayleigh damped material model. *Med Phys*, 38:1993–2004, 2011.

[22] MDJ McGarry, EEW Van Houten, CL Johnson, JG Georgiadis, BP Sutton, JB Weaver, and KD Paulsen. Multiresolution MR elastography using nonlinear inversion. *Med Phys*, 39:6388–6396, 2012.

[23] S Papazoglou, S Hirsch, J Braun, and I Sack. Multifrequency inversion in magnetic resonance elastography. *Phys Med Biol*, 57:2329–2346, 2012.

[24] K-J Streitberger, M Reiss-Zimmermann, FB Freimann, S Bayerl, J Guo, F Arlt, J Wuerfel, J Braun, K-T Hoffmann, and I Sack. High-Resolution Mechanical Imaging of Glioblastoma by Multifrequency Magnetic Resonance Elastography. *PLoS One*, 9:e110588, 2014b.

[25] J Rump, D Klatt, J Braun, C Warmuth, and I Sack. Fractional encoding of harmonic motions in MR elastography. *Magn Reson Med*, 57:388–395, 2007.

[26] MDJ McGarry, EEW Van Houten, PR Perrinez, AJ Pattison, JB Weaver, and KD Paulsen. An octahedral shear strain-based measure of SNR for 3D MR elastography. *Phys Med Biol*, 56:N153–64, 2011.

[27] EEW Van Houten, MI Miga, JB Weaver, FE Kennedy, and KD Paulsen. Three-dimensional

subzone-based reconstruction algorithm for MR elastography. *Magn Reson Med*, 45:827–837, 2001.

[28] H Schwarb, CL Johnson, AM Daugherty, CH Hillman, AF Kramer, NJ Cohen, and AK Barbey. Aerobic fitness, hippocampal viscoelasticity, and relational memory performance. *NeuroImage*, 153:179–188, 2017.

[29] J Guo, S Hirsch, A Fehlner, S Papazoglou, M Scheel, J Braun, and I Sack. Towards an elastographic atlas of brain anatomy. *PLoS One*, 8:e71807, 2013.

[30] PE Shrout and JL Fleiss. Intraclass correlations: uses in assessing rater reliability. *Psychol Bull*, 86:420–428, 1979.

[31] TK Koo and MY Li. A guideline of selecting and reporting intraclass correlation coefficients for reliability research. *J Chiropr Med*, 15:155–163, 2016.

[32] J Martin Bland and DG Altman. Statistical methods for assessing agreement between two methods of clinical measurement. *The Lancet*, 327:307–310, 1986.

[33] KO McGraw and SP Wong. Forming inferences about some intraclass correlation coefficients. *Psychological Methods*, 1:30–46, 1996.

[34] MC Murphy, 3rd J Huston, CR Jack Jr, KJ Glaser, A Manduca, JP Felmlee, and RL Ehman. Decreased brain stiffness in Alzheimer's disease determined by magnetic resonance elastography. *J Magn Reson Imaging*, 34:494–498, 2011.

[35] MDJ McGarry. Improvement and Evaluation of Nonlinear Inversion MR Elastography. *Dartmouth College*, 2013a.

[36] H Schwarb, CL Johnson, MDJ McGarry, and NJ Cohen. Medial temporal lobe viscoelasticity and relational memory performance. *NeuroImage*, 132:534–541, 2016.

[37] H An, Y Shi, Q Guo, and Y Liu. Test–retest reliability of 3D EPI MR elastography of the pancreas. *Clinical Radiology*, 71:1068.e7–1068.e12, 2016.

[38] SD Serai, NA Obuchowski, SK Venkatesh, CB Sirlin, FH Miller, E Ashton, PE Cole, and RL Ehman. Repeatability of MR Elastography of Liver: A Meta-Analysis. *Radiology*, doi: 10.1148/radiol.2017161398, 2017.

[39] A Fehlner, JR Behrens, K-J Streitberger, S Papazoglou, J Braun, J Bellmann-Strobl, K Ruprecht, F Paul, J Wurfel, and I Sack. Higher-resolution MR elastography reveals early mechanical signatures of neuroinflammation in patients with clinically isolated syndrome. *J Magn Reson Imaging*, 44:51–58, 2016.

[40] KJ Parker. Are rapid changes in brain elasticity possible? *Phys Med Biol*, 62:7425–7439, 2017.

[41] M Czosnyka, Z Czosnyka, S Momjian, and JD Pickard. Cerebrospinal fluid dynamics. *Physiol Meas*, 25:R51–76, 2004.

Chapter 7

Subcortical grey matter viscoelasticity in young and cognitively healthy older adults

Plan for the Chapter

A comprehensive investigation into the test re-test agreement of high-resolution brain MRE was provided in *Chapter 6*. The single-frequency non-linear inversion (SF-NLI) protocol was determined to display higher test re-test agreement, compared with multifrequency multi-dual elasto-visco inversion (MF-MDEV), when considering the global cerebrum (Ce) and a smaller brain structure of interest, i.e. the hippocampus (Hp). Furthermore, initial results from 6 young and 6 healthy older adults indicated that SF-NLI may also be more sensitive to potential ageing effects. Despite not finding overwhelming support for its use in the previous chapter, I will also incorporate soft-prior regularisation (SPR), due to the significant amount of support from published experimental work. As a result, in this chapter, I apply the SF-NLI-SPR protocol to evaluate global and regional MRE parameter differences in a larger cohort of 12 young (mean age: 25 years) and 12 healthy older adults (mean age: 69 years). The viscoelasticity of Ce and six regions of interest (ROIs) including the amygdala, hippocampus, caudate, pallidum, putamen, and thalamus, are investigated. Volumetric MRI is also measured, and used as a covariate, to determine whether MRE can provide additional information not related to traditional structural MRI. A further aim of this study is to establish baseline MRE values for both young, and healthy older participants, for a wide range of brain structures including the hippocampus; a brain structure of interest due to its implication in Alzheimer's disease.

7.1 Introduction

The use of medical imaging to identify and quantify brain tissue atrophy (i.e. neuronal cell loss) has been influential in aiding the prediction of onset and progression of many neurodegenerative disorders. Traditional diagnostic magnetic resonance imaging (MRI) is based on the radiologist grading of atrophy, often semi-quantitatively, through visual inspection of structural images, whereas research centres or centres involved in clinical trials, typically use manual, semi-automated or fully automated techniques to study volume changes of regions of interest. As an example, the European Medicines Agency has deemed low hippocampal volume an acceptable selection marker for clinical trials of people in the early stages of Alzheimer's disease [1].

Despite the apparent relationship between brain atrophy and clinical syndromes, the association

---

This chapter contains material previously published, and is reprinted with permission. LV Hiscox, CL Johnson, MDJ McGarry, M Perrins, A Littlejohn, EJR van Beek, N Roberts, JM Starr. High-resolution magnetic resonance elastography reveals differences in subcortical gray matter viscoelasticity between young and healthy older adults.*Neurobiol Aging*, **65**, 158-167. The published version can be found in **Appendix III.**

is not simple and linear; atrophy does not necessarily predict clinical symptoms or indeed their severity. Meta-analysis of results from 33 studies found a surprisingly weak positive relationship between hippocampal size and episodic memory ability in older adults, in addition to extreme variability among participants [2]. One possible reason for this weak relationship is that most age-associated behavioural impairments appear to result from region-specific changes in dendritic morphology, cellular connectivity, axonal integrity, gene expression, or other factors that ultimately alter the network dynamics of neural ensembles that support cognition [3, 4]. Accordingly, volumetric MRI is the most basic of neurobiological metrics; a gross proxy of tissue composition and integrity that is not specific to microstructural tissue characteristics. As a result, volumetric measurements are unlikely to characterise presymptomatic neuronal dysfunction, thus limiting the utility of volumetry as a clinical biomarker for the early detection of neurological disorders.

Prior to neurodegeneration, pathological processes, which cause a reduction to, for example, cellular connectivity, are reflected in the biophysical characteristics of brain tissue such as mechanical properties like stiffness and viscous energy dissipation. The mechanical properties of soft tissue may vary over a dynamic range much greater than other physical properties such as magnetic resonance relaxation time [5], and thus the ability to directly image properties such as tissue stiffness offers the prospect of an imaging technique with high sensitivity. Magnetic resonance elastography (MRE) is being actively developed to noninvasively measure the mechanical properties of the brain *in vivo*. MRE combines MRI with mechanical wave propagation and records harmonic displacements of soft tissue in MRI phase images using motion-sensitive magnetic field gradients, which are then inverted to estimate underlying viscoelasticity [6, 7]. Alterations in the mechanical properties of the brain, therefore, provide a unique contrast mechanism that appears to reflect the integrity of the underlying microstructure and health of brain tissue [8]. The sensitivity of MRE measures is confirmed by the observation of tissue softening in many neurological diseases [9–14], for a review, see Hiscox *et al.,* 2016 [15] or Murphy and Huston 2017 [16], with animal studies linking this softening to degree of myelin content [17–19], inflammation [20], and a reduction in neuronal density related to a decrease in neurogenesis [21, 22]. In general, tissue stiffness parameters likely reflect the composition of the tissue microstructure, whereas viscosity measures, including the phase angle and damping ratio, instead have been suggested to provide information regarding microstructural organization [8, 23].

Understanding normal mechanical changes in brain tissue with respect to healthy ageing is necessary before determining the efficacy of MRE for neurological disease diagnosis and therapy monitoring. Previous MRE studies into healthy ageing have assessed either the global cerebrum [24], parcellated slices [25], or lobar regional effects [26]. All studies reveal significant softening to the brain with increasing age, with brain softening occurring at a faster relative rate than brain volume loss with ageing [25]. In contrast, viscosity parameters remain constant suggesting a global preservation of the alignment of the tissue microstructure [24, 25]. However, no previous MRE studies into ageing have investigated specific neuroanatomical structures, including subcortical grey matter (SGM) ROIs such as the hippocampus. Lying deep within the medial temporal lobes, the hippocampal formation is one of the most studied neuronal systems in the brain due to its implication in memory-specific disorders such as AD and mild cognitive impairment. Rapid improvements of MRE imaging protocols have now transitioned MRE into a high-resolution technique, capable of acquiring whole-brain MRE displacement data at an isotropic resolution of 1.6 mm to enable the study of small brain structures [27]. Ageing effects have also never been studied with nonlinear inversion (NLI); formulated around a finite-element implementation of the full viscoelastic wave equation, NLI allows for local inhomogeneity and wave reflection effects [28, 29].

In this current cross-sectional exploratory study, I aim to use these methodological developments to assess the viscoelasticity of the cerebrum globally and 6 SGM matter structures (to include the amygdala [Am], hippocampus [Hp], caudate [Ca], pallidum [Pa], putamen [Pu], and thalamus [Th]), in both young and cognitively healthy older adults. First, I will assess the acceptability of the MRE examination by administering a questionnaire to all participants after the scanning procedure. Second, based on findings from previous work, I predict that the brain will be softer in older adults (i.e., show lower shear stiffness, μ), throughout the cerebrum and all SGM regions. Third, I predict that the global cerebrum will not differ between age groups in its relative viscous-to-elastic behaviour (i.e., damping ratio, ξ). It is currently unknown whether age-related differences for ξ will be detected in SGM regions, and thus the analysis is an exploratory one. Finally, I will take into consideration the volume of the cerebrum and each SGM region within the statistical analyses to investigate whether MRE results persist even once ROI volume has been accounted for. MRE results that remain significant after controlling for ROI volume would suggest that MRE parameters provide additive value over volumetric measures alone.

7.2 Materials and methods

7.2.1 *Subjects*

Thirty-one apparently healthy participants were recruited from the Join Dementia Research (JDR) database; thirteen were young adult participants aged between 18-30 years and eighteen were older participants aged between 65-75 years. Criteria for exclusion included history or current diagnosis of a severe medical, neurological, or psychiatric disorder, history of major head injury, and contraindications for undergoing MRI (such as claustrophobia or the presence of an implanted pacemaker). To ensure older participants, in particular, had no significant underlying memory problems, all were required to complete the Montreal Cognitive Assessment (MoCA) [30], and score within the normal range (>26/30). MRE data quality was measured by octahedral shear-strain based SNR (OSS-SNR) [31], (see *7.2.4 MRE analysis* section). Overall, one young adult was excluded due to OSS-SNR <3, and six older subjects were excluded from the analysis: three subjects had OSS-SNR <3, two subjects scored below the required level set for the MoCA, and one subject was excluded due to the presence of significant white matter abnormalities, as determined by a Consultant Radiologist. As a result, the final sample included 24 participants (12 young adults (mean age: 25.2±3.0 years) and 12 older adults (mean age: 69.4±2.5 years). An equal number of female and male participants were recruited into each group to consider the known differences in brain viscoelasticity between men and women [24, 26]. All subjects completed the Edinburgh Handedness Inventory (EHI) and National Adult Reading Test (NART), to measure handedness and IQ, respectively (see Table 7.1). The study was approved by the National Health Service (NHS) Lothian Research Ethics Committee (15/SS/0219) and all study participants gave written, informed consent before the examination.

Table 7.1: Demographic data for subjects included in the study.

	Young	Old
Number	12	12
Sex	6F/6M	6F/6M
Age	25.2 (19 - 30)	69.4 (66 - 73)
EHI	+0.88 (+0.7 - 1)	+0.86(+0.3 - 1)
MoCA	N/A	28.1 (26 - 30)
NART - Full scale IQ	114 (107 - 121)	123 (115 -128)

All values are mean values, with range in parenthesis.
Key: M, male; F, female; EHI, Edinburgh Handedness Inventory; MoCA, Montreal Cognitive Assessment; NART, National Adult Reading Test.

7.2.2 *MRI scanning*

MRI and MRE data were collected using a Siemens 3T Verio whole-body MRI scanner with a 12-channel head receive coil (Siemens Medical Solutions; Erlangen, Germany). The imaging protocol included high-resolution T_1-weighted and MRE series. T_1-weighted images were acquired using an MPRAGE sequence (magnetization-prepared rapid gradient echo; 1 x 1 x 1mm^3 voxel size; 2400/1000/2.97ms repetition/inversion/echo times). The MRE acquisition employed a 3D multi-slab multishot spiral sequence to capture high-resolution displacement data [27]. Imaging parameters included: 1800/75ms repetition/echo times; 240mm square field-of-view; 150 x 150 imaging matrix; and sixty 1.6mm thick slices acquired in ten overlapping slabs. The resulting imaging volume had a 1.6 x 1.6 x 1.6mm^3 isotropic voxel size with 96mm of coverage in the slab direction, which was aligned approximately to the anterior commissure - posterior commissure (AC-PC) line and included the medial temporal lobe. A pneumatic actuator (Resoundant; Rochester, MN, USA) was used to vibrate the brain at a single mechanical frequency of 50 Hz through a soft pad placed below the occipital portion of the head. The resulting tissue deformation was encoded using 26 mT/m motion-sensitive gradients embedded in the MRE sequence, which was repeated to capture motion along 3 separate axes with opposite gradient polarities and through 4 phase offsets to observe wave propagation in time. The total MRE acquisition time was approximately 12 minutes.

7.2.3 *Anatomical segmentation and mask generation*

SGM masks were obtained via automatic segmentation of the T_1-weighted images using FreeSurfer v. 5.3 through the recon-all pipeline [32]. This included skull stripping, automated Talairach transformation, segmentation of the subcortical white/grey matter structures, intensity normalization, automated topology correction, and registration to a spherical atlas. The pipeline generated six subcortical masks for the amygdala (Am), caudate (Ca), hippocampus (Hp), pallidum (Pa), putamen (Pu), and thalamus (Th). All segmentations were visually inspected for accuracy and manual corrections were made when necessary. The T_2-weighted magnitude MRE images were then co-registered to the structural T_1-weighted MPRAGE using FMRIB's Linear Image Registration Tool (FLIRT) within FMRIB Software Library (FSL) [33]. The inverse transform was calculated so that the generated SGM masks from FreeSurfer could be transferred into MRE space, to serve as masks for soft prior regularisation (SPR) (see *7.2.4 MRE analysis*), and as ROIs for obtaining quantitative values for each structure. This pipeline is similar to the one used in previous work to separate SGM masks for MRE with SPR; small differences within the pipeline are expected to contribute negligibly to the uncertainty of MRE measurements [34].

7.2.4 *Volumetric analysis*

The FreeSurfer pipeline generated subcortical volumes in cm^3 for all six ROIs. Estimated Total Intracranial Volume (eTIV) was used to normalize the volume of each ROI for head size using an automated atlas-based head-size normalisation pipeline [35]. Freesurfer output, BrainSegNotVent, was used as a measure of total cerebral volume. This ROI includes the sum of the volume of the structures identified in the aseg.mgz volume and the cerebellum, while excluding the brainstem, dura, ventricles (lateral, inferior lateral, 3rd, 4th, 5th), CSF, and choroid plexus.

7.2.5 *MRE analysis*

An octahedral shear strain-based SNR measure (OSS-SNR) was performed to ensure sufficient data quality for stable inversion [31]. Nonlinear inversion (NLI) [28, 36] was combined with SPR [37] to estimate viscoelasticity from MRE displacement data, as recently utilised in a number of brain MRE studies [34, 38]. The SPR inversion scheme incorporates prior anatomical information to penalize mechanical heterogeneity within an ROI and has previously been shown to improve MRE reproducibility measures [34]. Both the MRE displacement data and SGM structure masks in MRE space were input into the NLI algorithm with a weighting of $\alpha = 10^{-11}$. SPR weighting was chosen based on balancing the need to enforce homogeneity, while ensuring convergence. NLI estimates the complex shear modulus, $G^* = G' + G''$, from which I determined the shear stiffness μ, and damping ratio, ξ. Shear stiffness determines the wavelength in a viscoelastic solid [39], defined as $\mu = 2\ |G^*|^2/(G' + |G^*|)$, whereas damping ratio ξ is a dimensionless quantity describing the relative attenuation level in the material, defined by $\xi = G''/2G'$ [40], and is similar to the mechanical phase angle often reported in brain MRE [10, 41]. Higher ξ values mean that oscillations created by the shear waves attenuate more rapidly and would suggest that tissue exhibits more viscous fluid-like behaviour, as opposed to a more elastic-solid behaviour. A less densely connected solid phase, which allows more viscous and frictional losses as tissue constituents slide against each other, is indicative of a reduction in tissue integrity and is expected to relate to the microstructural organisation of tissue [8].

For illustration purposes only, I have co-registered each data set to the Montreal Neurological Institute (MNI152_ T1_1mm) template using Advanced Normalization Tools (ANTS) [42], to generate both young and old average MRE parameter templates.

7.2.6 *Assessment of subject comfort*

A questionnaire was administered to participants immediately after the scan, with participants asked to provide a score between 1:5 for each of the three questions presented. Question (1): Compared to a conventional MRI scan (where there is no vibration), what is your assessment of the discomfort caused by the vibrations required for MRE? Possible answers included: 1, severe discomfort; 2, moderate discomfort; 3, mild discomfort; 4, annoyance; 5, negligible. Question (2): How likely is it that you would take part in the same or a similar MRE study? Question (3): How likely is it that you would recommend this study to other potential participants? For questions (2) and (3), participants were asked to choose from the following options: 1, very unlikely; 2, unlikely; 3, not sure; 4, likely; 5, very likely.

7.2.7 *Statistical analyses*

All statistics reported are results obtained in MRE space for each individual. First, a two-way univariate general linear model (analysis of variance [ANOVA]) was used to examine the effect of age group and sex on cerebral (i.e., whole-brain ROI) MRE parameters μ and ξ. Separate ANOVAs were conducted for μ and ξ. Second, a two-way multivariate analysis of variance (MANOVA: Pillai's trace) was used to assess the effect of age group and sex on the combined ROIs including the Am, Ca, Hp, Pa, Pu, and Th. μ and ξ were analysed separately, and post hoc univariate analyses were summarised. A MANOVA was chosen because it effectively acts as a 'data reduction' (i.e. 'hypothesis reduction') method. It considers the individual outcomes as representing a single underlying trait as the primary hypothesis, but also allows one to look at post-hoc at univariate outcomes, which is reasonable to generate hypotheses for future research. As this is an exploratory study, the effect sizes - rather than p values, will provide more useful information. Finally, a univariate ANOVA was used to correct for structure volume, using volume as covariate and age and sex as fixed factors. This was to ensure that changes to MRE parameters were not simply reflecting changes to brain structure volumes. G* power 3.1 (http://www.gpower.hhu.de/en.html) was used to estimate available statistical power π. The calculations show that for a large effect size, of $f = 0.40$, [43], the power of ANOVA to detect an effect at $p = 0.05$ is $\pi = 0.46$. Therefore, we note that the MANOVA is substantially underpowered, resulting in an increased probability of a type II error (false negative). All analyses were performed using SPSS software version 24.0.0 (SPSS Inc., Chicago, IL).

7.3 Results

The average OSS-SNR of the brain MRE data was 5.41± 1.18 and 6.02 ± 1.67, for the young and older cohorts, respectively, indicating high-quality whole-brain displacement data that was stable to undergo inversion.

7.3.1 *MRE acceptability*

The MRE component within the scanning protocol was well tolerated, as indicated by the questionnaire scores provided in Table 7.2 and illustrated in Figure 7.1. Two subjects in the older group felt a moderate level of discomfort (grade 2) from the vibrations generated by the head-pillow, whereas two subjects in both the young and older groups felt a mild level of discomfort (grade 3). An independent samples *t*-test found that tolerance of the vibrations was not rated differently between age groups ($t(22)$=-.713; p = 0.484). Finally, 100% of all participants answered that they were likely to recommend that other potential participants take part in the study.

Table 7.2: Subjective assessment of MRE comfort by twenty-four volunteers.

Question	Young	Old
Q1. Vibration (1, severe discomfort; 5 negligible)	4.00 (0.60, 3-5)	3.75 (1.06, 2-5)
Q2. Would return (1, very unlikely; 5 very likely)	4.92 (0.29, 4-5)	4.58 (0.67, 3-5)
Q3. Recommend to others (1, very unlikely; 5 very likely)	4.83 (0.39, 4-5)	4.42 (0.51, 4-5)

Values in parentheses denote the standard deviation (SD) and the range.

Table 7.3 presents descriptive statistics (mean, standard deviation) for MRI volumetry results and MRE parameters (shear stiffness, μ and damping ratio, ξ), for young and older participants, with data illustrated in Figure 7.2. Bilateral values for all 3 parameters were reported as there were no significant left-right hemispheric differences in any ROI for either population ($p < 0.05$). Table 7.3 also includes the % difference between young and older participants, as well as ANOVA and MANOVA p values for the cerebrum and subcortical grey matter regions, respectively. A full summary of the statistical analyses and results are provided in the following sections.

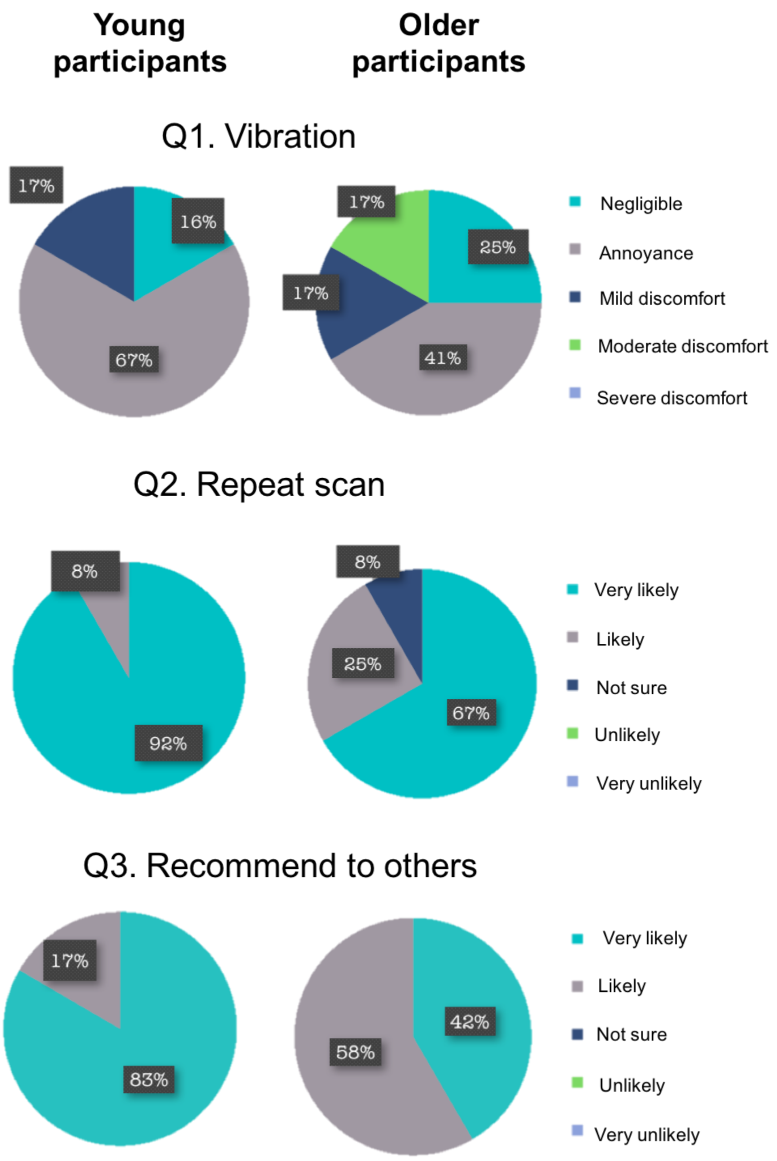

Figure 7.1: Pie chart to show participant response to the MRE questionnaire; administered shortly after the imaging protocol.

7.3.2 *Volumetric MRI*

Cerebrum (Ce): First, a two-way univariate general linear model (ANOVA) was performed to examine the effect of age group and sex on the cerebral volume. There was a statistically significant effect of age on cerebrum volume: [F(1,20) = 5.17, p = 0.034], indicating younger participants had larger brain volumes than older participants. There was also a significant effect of sex: [F(1,20) = 9.74, $p = 0.005$], indicating larger brain volume in males but no interaction between age and sex ($p = 0.713$).

Table 7.3: Population statistics for MRI volumetry and MRE parameters

	Ce	Am	Ca	Hp	Pa	Pu	Th
Volume (cm^3)							
Young	1161 ± 117	3.64 ± 0.37	7.39 ± 1.02	9.32 ± 0.62	2.88 ± 0.33	11.38 ± 1.16	16.15 ± 1.65
Older	1078 ± 89	3.11 ± 0.40	6.77 ± 0.75	8.23 ± 1.13	2.64 ± 0.29	9.28 ± 1.04	14.23 ± 1.44
% Difference	-3.85	-15.70	-8.76	-12.42	-8.70	-20.33	-12.64
ANOVA p value	0.034						
MANOVA (main effect)		0.006**	0.006**	0.006**	0.006**	0.006**	0.006**
MANOVA (post-hoc)		0.002**	0.063	0.011*	0.046*	0.001**	0.004**
μ (kPa)							
Young	2.95 ± 0.17	3.60 ± 0.30	2.92 ± 0.23	2.89 ± 0.32	3.59 ± 0.26	3.76 ± 0.15	3.35 ± 0.24
Older	2.70 ± 0.15	3.02 ± 0.42	2.21 ± 0.32	2.65 ± 0.39	3.04 ± 0.39	3.26 ± 0.23	2.76 ± 0.31
% Difference	-8.47	-16.11	-24.32	-8.30	-15.32	-13.30	-17.61
ANOVA p value	0.002**						
MANOVA (main effect)		< 0.001***	< 0.001***	< 0.001***	< 0.001***	< 0.001***	< 0.001***
MANOVA (post-hoc)		0.001**	< 0.001***	0.096	0.001**	< 0.001***	< 0.001***
ξ							
Young	0.254 ± 0.011	0.159 ± 0.022	0.254 ± 0.035	0.156 ± 0.012	0.211 ± 0.032	0.225 ± 0.014	0.195 ± 0.029
Older	0.260 ± 0.017	0.181 ± 0.025	0.236 ± 0.034	0.188 ± 0.032	0.192 ± 0.025	0.220 ± 0.016	0.205 ± 0.022
% Difference	+2.36	+13.84	-7.09	+20.51	-9.00	-2.22	+5.14
ANOVA p value	0.371						
MANOVA (main effect)		0.191	0.191	0.191	0.191	0.191	0.191
MANOVA (post-hoc)		0.045*	0.235	0.006**	0.130	0.371	0.355

Values represent mean ± standard deviation (SD).
Key: MRE, magnetic resonance elastography; MRI, magnetic resonance imaging; Am, amygdala; Ca, caudate; Hp, hippocampus; Pa, pallidum; Pu, putamen; Th, thalamus.

Subcortical grey matter regions of interest: Second, a two-way MANOVA was performed to assess the effects of age group and sex on volumetric MRI for all 6 SGM structures. There was a statistically significant effect of age [F(6,15) = 4.89, p = 0.006] and sex [F(6,15) = 3.10, $p = 0.035$] on the combined ROIs, with no interaction between age and sex, ($p = 0.966$). The univariate effects indicated significant age differences in volume for all individual SGM structures, except for Ca: Am ($p = 0.002$), Hp ($p = 0.011$), Pa ($p = 0.046$), Pu ($p < 0.001$), Th ($p = 0.004$), and Ca ($p = 0.063$). Significant sex differences in volume were found for Ca ($p = 0.008$), Pa ($p = 0.014$), Th ($p = 0.034$), whereas there were no differences in volume for Am ($p = 0.111$), Hp ($p = 0.518$), or Pu ($p = 0.103$).

7.3.3 *Shear stiffness* μ

Cerebrum (Ce): A two-way univariate general linear model (ANOVA) was performed to examine the effect of age group and sex on cerebral μ. There was a statistically significant effect of age on the stiffness of the Ce, [F(1, 20)=13.33, p= 0.002, partial η^2= 0.400], indicating younger participants had higher cerebral μ than older participants. There was no significant effect of sex (p= 0.651) or an interaction between age and sex (p= 0.849). Figure 7.3 shows 3 representative slices in Montreal Neurological Institute space of Ce stiffness for both young and older adults.

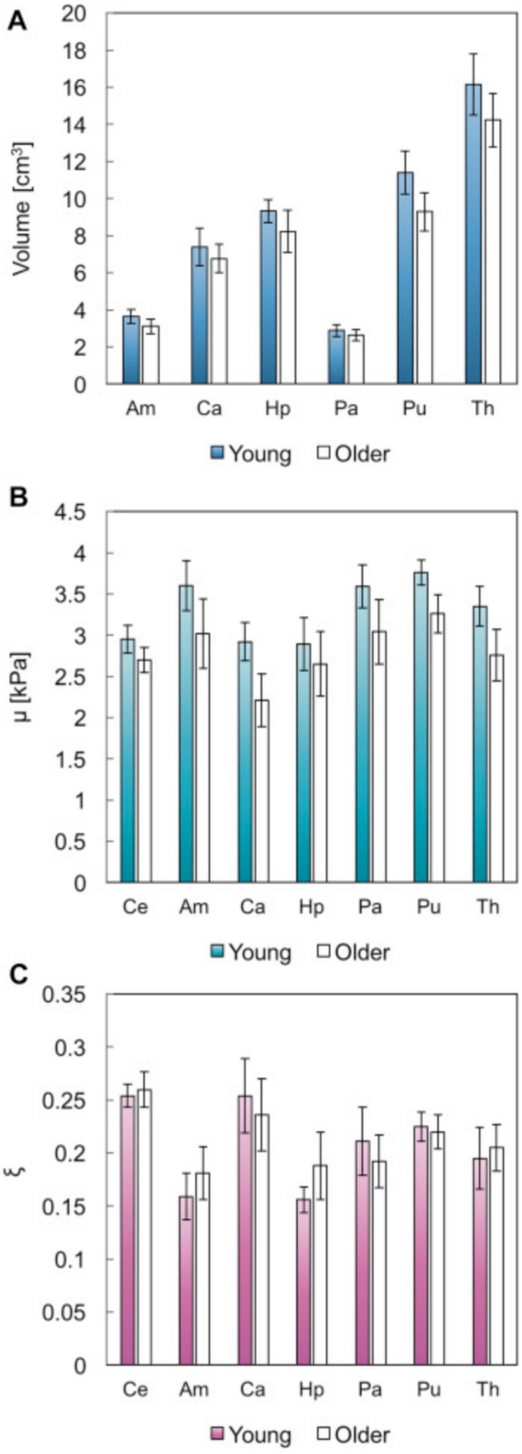

Figure 7.2: Mean and standard deviation for (a) volume (cm^3), (b) shear stiffness, μ (kPa), and (c) damping ratio, ξ. N = 12 in each group.

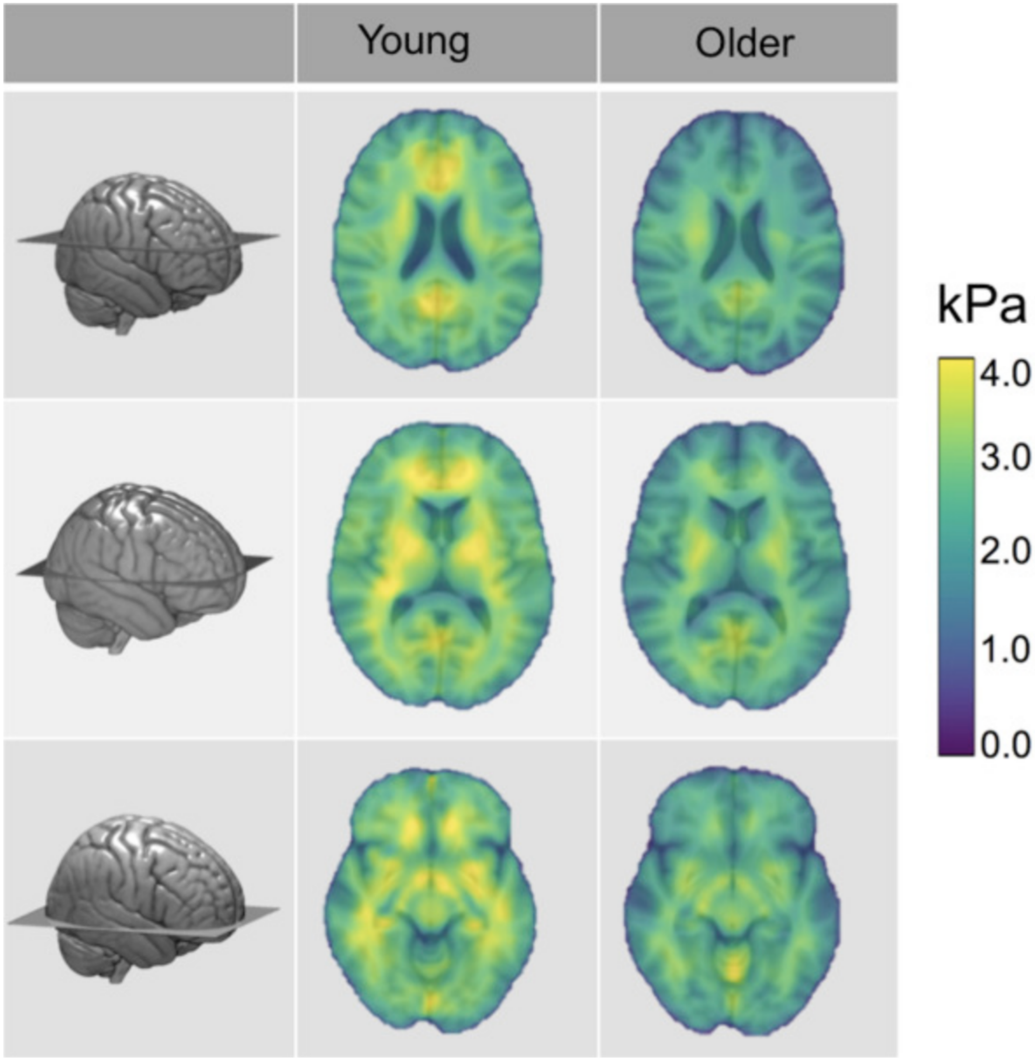

Figure 7.3: Mean shear stiffness, μ properties of the cerebrum (Ce) for young and older adults, showing widespread softer brains in older age ($p < 0.001$). MRE parameter maps have been transformed into standard MNI space, with anatomical information overlaid for illustration purposes. 3D rendering of the MNI template shows the location of the three representative slices. Abbreviation: MNI, Montreal Neurological Institute; MRE, magnetic resonance elastography.

Subcortical grey matter regions of interest: A two-way multivariate analysis of variance (MANOVA) was performed to assess the effects of age group and sex on μ for all six SGM structures. There was a statistically significant effect of age on the combined regions of interest (ROIs), [F(6,15) = 8.77, p<0.001, partial η^2= 0.778)], with no effect of sex (p= 0.382), or interaction between age and sex (p= 0.408). The univariate effects indicated significant age differences for all individual SGM structures:

Am (p= 0.001; partial η^2= 0.415), Ca (p<0.001; partial η^2= 0.649), Pa (p= 0.001; partial η^2= 0.437), Pu (p<0.001; partial η^2= 0.654), Th (p<0.001; partial η^2= 0.574), except for the Hp (p= 0.096).

Volume correction: Third, univariate analysis of variance (ANOVA) were used to correct μ for volume, using age and sex as fixed factors and volume as a covariate. Each ROI analysis was performed separately. μ of the Ce (p= 0.012; partial η^2= 0.291), Ca (p<0.001; partial η^2= 0.580), Pa (p= 0.002; partial η^2= 0.409), Pu (p= 0.003; partial η^2= 0.370), and Th (p= 0.003; partial η^2= 0.381) all remained significantly affected by age group after correcting for ROI volume size. Am was no longer significantly different between age groups once Am volume was used as a covariate (p= 0.102). Figure 7.4 shows mean young and older MRE parameter templates that remained significantly different between age groups after controlling for ROI volume size.

7.3.4 *Damping ratio* ξ

Cerebrum (Ce): Similarly, a univariate general linear model (ANOVA) was conducted to examine the effect of age group and sex on cerebral ξ. There was no significant effect of age (p = 0.371), or sex (p = 0.790) or an interaction between the two (p = 0.596).

Subcortical grey matter regions of interest: Two-way MANOVA was performed to assess the effects of age group and sex on ξ for all SGM structures. There was a non-significant effect of age group on the combined ROIs, [F(6,15) = 1.69, p = 0.191, partial η^2= 0.404], with no significant effect of sex (p = 0.827), or interaction between the two (p = 0.835). No volume correction or post hoc analyses were considered due to the non-significant omnibus result.

7.4 Discussion

This proof-of-concept investigation is the first to use a single-frequency, high-resolution, NLI MRE pipeline to assess the effect of healthy ageing on the viscoelastic properties of specific neuroanatomical structures *in vivo*.

First of all, I have demonstrated that the passive MRE driver, consisting of a soft pillow, is well tolerated, even in older adults aged 70 years and over. All participants also completed the study without interruption. These results provide the first quantitative measure that the MRE head pillow driver is acceptable to participants over a wide age range. This finding is essential when considering the potential clinical utility of MRE as a diagnostic tool. Second, these results indicate that there is

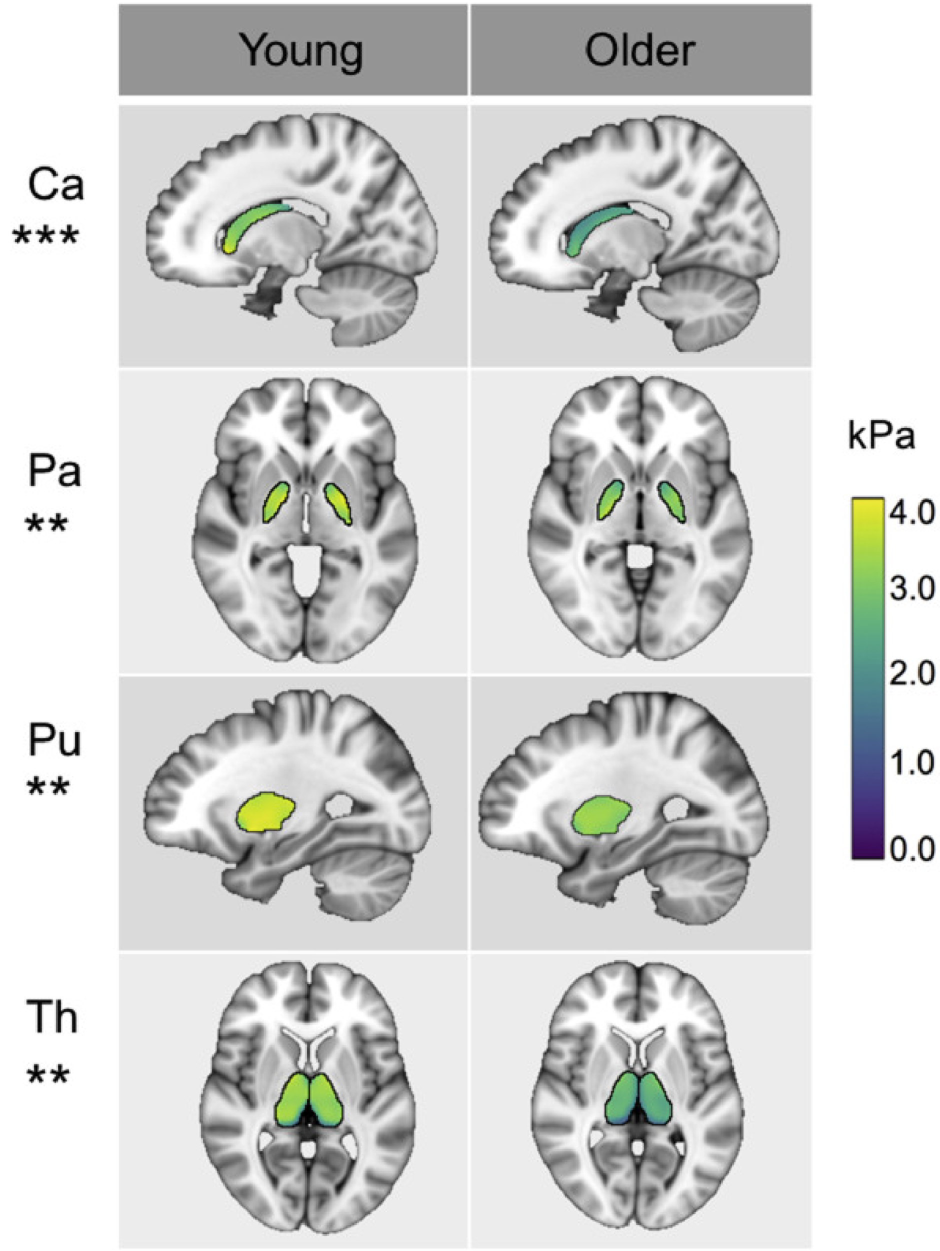

*Figure 7.4: Mean shear stiffness, μ properties of SGM structures (Ca, Caudate; Pa, Pallidum; Pu, Putamen; Th, Thalamus) for young and older adults, in standard MNI space. The stiffness of each of these brain structures remain significantly different between age groups after correcting for ROI volume, with all being softer in older adults. *** denotes $p < 0.001$ and ** denotes $p < 0.01$ significance levels. Abbreviation: SGM, subcortical grey matter; ROI, region of interest.*

significant softening to the global cerebrum, an area largely composed of white matter, and to most subcortical grey matter (SGM) structures as a result of increasing age. In older adults, the cerebrum (8%), caudate (24%), pallidum (15%), thalamus (18%), amygdala (16%), and putamen (13%) are all significantly softer compared to younger adults. The hippocampus was the only region of interest (ROI) to not exhibit a statistically significant difference in μ between age groups. Further, the stiffness of all the aforementioned ROIs, excluding the amygdala, were influenced by age group even after correcting these results to take into account ROI volume. Third, I have also demonstrated that there are no age-related differences in the damping ratio, ξ of the global cerebrum, suggesting no overall change in the relative viscous-to-elastic properties of the brain generally. Considering the volumetric MRI analysis independently, the size of the cerebrum and all SGM structures, except for the caudate, is statistically smaller in older adults, as expected.

These results complement previous MRE studies of cerebral ageing, which also found that the brain becomes softer with older age [24–26]. The results are not surprising given that numerous histopathological studies report that the brain undergoes microstructural and metabolic changes due to normal ageing [44–46], and that stiffness is reflective of degree of myelination and neuronal density [21, 22, 47]. This study, however, is the first to investigate microstructural differences in neuro-anatomical regions due to ageing. The benefits of this approach enable the investigation of specific brain structures and their associated cognitive functions. Previous work has found a significant correlation between relational memory and hippocampal damping ratio in young adults [23, 38], whereas more recently, a double dissociation was demonstrated between the orbitofrontal-fluid intelligence relationship and the hippocampal-relational memory relationship [48]. These findings provide new opportunities for future investigations to mechanically map the human brain with respect to ageing and cognition.

This work did not find a reduction in hippocampal μ in older adults in line with a decrease across other subcortical grey matter regions. However, the magnitude of the difference of the hippocampus between age groups (8.3%) is similar to that of the global cerebrum (8.5%), which did exhibit a statistically significant difference. Therefore, it is possible that this study was simply underpowered to detect age-related differences to hippocampal stiffness: see *section 7.2.7* for the post-hoc power calculation. Nonetheless, these results are in agreement with a force indentation study, which compared brain stiffness in healthy young-age to late-middle-age adult mice (human equivalent age of ∼20 years and ∼65 years, respectively), and found no age effect on hippocampal stiffness [47]. The finding reported in the present study may reflect the fact that only cognitively healthy participants were recruited; thus, the sample population may be more resilient to hippocampal microstructural alterations. This is especially relevant, given a recent study which found that hippocampal stiffness, determined using multifrequency MRE (MMRE), was lower in patients with AD when compared with healthy older adult controls [49]. Taken together, it can be speculated that the stiffness of the hippocampus may be maintained across the life span until the point of AD neurodegeneration, suggesting that MRE may be a promising non-invasive biomarker for early diagnosis. However, longitudinal investigations will be required to monitor the prodromal stages of disease for the purpose of evaluating whether changes to the mechanical properties of the hippocampus can predict the onset of dementia symptoms.

In both age groups, the putamen exhibited the highest μ, which complement findings from Hetzer *et al.,* 2017 who also found the putamen to be the stiffest deep grey matter region while investigating the amygdala, hippocampus, pallidum, thalamus, and nucleus accumbens [50]. Hetzer *et al.,* 2017 further analysed the perfusion pressure gradient, a measure of cerebral blood flow, and found the putamen to display the highest perfusion values, which in turn could predict its stiffness. The distinct mechano-vascular properties of the putamen, it was argued, could explain the well-known susceptibility of the ROI to haemorrhages. In the younger age group, the hippocampus was found to exhibit the lowest μ of all the SGM region, which agrees with previous MRE findings in young adults [34]. In contrast, the caudate was found to be the softest SGM structure in older adults, which agrees with Guo *et al.* 2013 who reported the caudate as being softer than white matter, the thalamus and, corpus callosum genu, in healthy adults aged between 22-72 years [41].

Considering the damping ratio ξ, no significant difference between age groups was found for the global cerebrum. These findings support the prediction that the brain globally will possess a similarly intact microstructure regardless of age. These results complement previous work by Sack *et al.,* 2009 and Sack *et al.,* 2011, which found the slope of the complex modulus dispersion (i.e. viscous power-law spring-pot exponent) to remain widely constant throughout the cerebrum with increasing age, which was attributed to an unaffected geometrical alignment of mechanically relevant structure elements [24, 25]. No significant age-related regional differences in ξ was found for the 6 selected subcortical grey matter regions of interest. Future region-specific studies with larger sample sizes may find age related differences in ξ, such as in the hippocampus. This suggestion is in part driven by the substantial % difference between young and older adults for hippocampal ξ reported in this study (21%), and the previous finding of a relationship between hippocampal ξ and relational memory in young adults [23, 38]. In addition, a recent murine study found that the viscous G'' properties of the hippocampus increase with age [47], which the authors suggest may be related to an increase in the number of mobile tissue components caused by age-related brain modifications.

7.5 Limitations

The main limitation of this study lies in the small number of participants. This renders the data to limited statistical power and thus an increased probability of a type II error (false negative). These results, therefore, should be interpreted with caution and replicated in a larger sample. The cross-sectional evidence presented here also cannot test causality between MRE measures and ageing, although the current work provides a necessary foundation for future investigations.

MRE inversion is a complex ill-posed problem and as such is under constant development. Due to difficulties in solving the MRE inverse problem, we should acknowledge that other geometrical factors could possibly influence the wave propagation and the quantitative outcomes. Older adults are known to have larger ventricles and a greater degree of CSF due to cerebral atrophy. While I have accounted for ROI volume within the statistical analyses and used conservative masks for the ROIs, it should be acknowledged that there may be atrophy within the ROI itself, thus altering the distribution of brain tissue and CSF. As CSF is an incompressible fluid, data model mismatch could cause issues for quantification, although the use of SPR should presumably limit the contribution of CSF-containing voxels. Another concern may be whether the analysis is biased toward the smaller SGM volumes in older adults, as reported in this study. However, previous NLI phantom reconstruction work has been shown to accurately identify changes in stiffness in regions as small as 1cm^3 [51]. Considering the smallest brain structure measured is the pallidum ($\sim 2.5\text{cm}^3$), it is unlikely that volume-related bias is related to the findings of age-related tissue softening.

Another limitation of this study is the inability to directly relate MRE-derived mechanical age differences to an underlying micro-structural profile. Most studies that have linked the integrity of tissue microstructure to MRE measurements have used a multiple-frequency acquisition [17, 20–22]. MMRE can capture a wide spectrum of experimental results, which are then modelled by a combined viscoelastic element called the spring pot model (a combination of the terms 'spring' and 'dashpot') [8]. Through these studies, MMRE has been shown to relate the measured dynamics of the complex shear modulus (i.e., powerlaw) to the fractal geometry of structures that build the mechanical scaffold of tissue: that is, changes to spring-pot parameters are associated with the material's complexity, which in turn have been associated with pathophysiological events. While it has been suggested that the powerlaw parameter can be determined from the complex shear modulus at a single frequency [52], further validation studies are required to investigate whether single-frequency MRE can capture the complex biophysical interactions at the microscopic level. In support of this data, I should mention that complementary age-related findings of brain tissue softening in lobar regions were reported using a single-frequency vibration of 60 Hz [26]. Nevertheless, the underlying neural substrates causing alterations to mechanical parameters at a single frequency are not fully understood. While tissue stiffness has correlated with neuronal density, demyelination, and levels of inflammation using MMRE, the specificity of this parameter needs further investigation. In addition, the biological correlates for the damping ratio, ξ are less well established, thus ξ currently remains an engineering term in which its relationship to underlying microstructural alterations can only be speculated.

7.6 Conclusions

In summary, this study is the first to investigate the influence of healthy ageing on the viscoelasticity of subcortical neuroanatomical structures *in vivo*. Novel findings are reported for which older adults displayed globally and regionally specific mechanical brain tissue differences when compared with younger adults. In older age, there is widespread softening (i.e., decrease in shear stiffness, μ) of the global cerebrum and in all subcortical grey matter structures investigated (amygdala, caudate, pallidum, putamen, and thalamus), except for the hippocampus. However, the stiffness of the amygdala was no longer influenced by age group once amygdala volume was used as a covariate. These results suggest that group differences in μ exist even when ROI volume is accounted for and that MRE has additive value over volume. In older age, the brain retains its relative viscous-to-elastic behaviour (i.e., damping ratio, ξ) both globally and regionally, suggesting a preservation of the organisation of the tissue network. These preliminary results suggest that MRE can characterise age-related differences to neural tissue not captured by volumetric imaging alone and motivate further investigation into the utility of viscoelastic parameters in patients within the clinical or preclinical stages of neurodegenerative disease.

References

[1] European Medicines Agency. Qualification opinion of low hippocampal volume (atrophy) by MRI for use in regulatory clinical trials - in pre-dementia stage of Alzheimer's disease. Technical report, 2011.

[2] C Van Petten. Relationship between hippocampal volume and memory ability in healthy individuals across the lifespan: review and meta-analysis. *Neuropsychologia*, 42:1394–1413, 2004.

[3] SN Burke and CA Barnes. Neural plasticity in the ageing brain. *Nat Rev Neurosci*, 7:30–40, 2006.

[4] DE Smith, PR Rapp, HM McKay, JA Roberts, and MH Tuszynski. Memory impairment in aged primates is associated with focal death of cortical neurons and atrophy of subcortical neurons. *J Neurosci*, 24:4373–4381, 2004.

[5] YK Mariappan, KJ Glaser, and RL Ehman. Magnetic resonance elastography: a review. *Clin Anat*, 23:497–511, 2010.

[6] R Muthupillai, DJ Lomas, PJ Rossman, JF Greenleaf, A Manduca, and RL Ehman. Magnetic resonance elastography by direct visualization of propagating acoustic strain waves. *Science*, 269:1854–1857, 1995.

[7] R Muthupillai and RL Ehman. Magnetic resonance elastography. *Nat Med*, 2:601–603, 1996.

[8] I Sack, K Johrens, J Wurfel, and J Braun. Structure-sensitive elastography: on the viscoelastic powerlaw behavior of in vivo human tissue in health and disease. *Soft Matter*, 9:5672–5680, 2013.

[9] J Huston, MC Murphy, BF Boeve, N Fattahi, A Arani, KJ Glaser, A Manduca, DT Jones, and RL Ehman. Magnetic Resonance Elastography of Frontotemporal Dementia. *J Magn Reson Imaging*, 43:474–8, 2015.

[10] A Lipp, R Trbojevic, F Paul, A Fehlner, S Hirsch, M Scheel, C Noack, J Braun, and I Sack. Cerebral magnetic resonance elastography in supranuclear palsy and idiopathic Parkinson's disease. *Neuroimage Clin*, 3:381–387, 2013.

[11] MC Murphy, 3rd J Huston, CR Jack Jr, KJ Glaser, A Manduca, JP Felmlee, and RL Ehman. Decreased brain stiffness in Alzheimer's disease determined by magnetic resonance elastography. *J Magn Reson Imaging*, 34:494–498, 2011.

[12] MC Murphy, DT Jones, CR Jack, KJ Glaser, ML Senjem, A Manduca, JP Felmlee, RE Carter, RL Ehman, and J Huston 3rd. Regional brain stiffness changes across the Alzheimer's disease spectrum. *NeuroImage: Clin*, 10:283–290, 2016.

[13] A Romano, J Guo, T Prokscha, T Meyer, S Hirsch, J Braun, I Sack, and M Scheel. In vivo waveguide elastography: Effects of neurodegeneration in patients with amyotrophic lateral sclerosis. *Magn Reson Med*, 72:1755–1761, 2014.

[14] K-J Streitberger, I Sack, D Krefting, C Pfuller, J Braun, F Paul, and J Wuerfel. Brain Viscoelasticity Alteration in Chronic-Progressive Multiple Sclerosis. *PLoS One*, 7:e29888, 2012.

[15] LV Hiscox, CL Johnson, E Barnhill, MDJ McGarry, J III Huston, EJR van Beek, JM Starr, and N Roberts. Magnetic resonance elastography (MRE) of the human brain: technique, findings and clinical applications. *Phys Med Biol*, 61:401–437, 2016.

[16] MC Murphy, J Huston 3rd, and RL Ehman. MR elastography of the brain and its application in neurological diseases. *NeuroImage*, https://doi.org/10.1016/j.neuroimage.2017.10.008, 2017.

[17] K Schregel, E Wuerfel née Tysiak, P Garteiser, I Gemeinhardt, T Prozorovski, O Aktas, H Merz, D Petersen, J Wuerfel, and R Sinkus. Demyelination reduces brain parenchymal stiffness quantified in vivo by magnetic resonance elastography. *Proc Natl Acad Sci USA*, 109:6650–6655, 2012.

[18] J Weickenmeier, R de Rooij, S Budday, P Steinmann, T C Ovaert, and E Kuhl. Brain stiffness increases with myelin content. *Acta Biomater*, 42:265–272, 2016.

[19] J Weickenmeier, R de Rooij, S Budday, TC Ovaert, and E Kuhl. The mechanical importance

of myelination in the central nervous system. *Journal of the Mechanical Behavior of Biomedical Materials*, http://dx.doi.org/10.1016/j.jmbbm.2017.04.017:, 2017.

[20] K Riek, JM Millward, I Hamann, S Mueller, CF Pfueller, F Paul, J Braun, C Infante-Duarte, and I Sack. Magnetic resonance elastography reveals altered brain viscoelasticity in experimental autoimmune encephalomyelitis. *NeuroImage: Clin*, 1:81–90, 2012.

[21] C Klein, EG Hain, J Braun, K Riek, S Mueller, B Steiner, and I Sack. Enhanced adult neurogenesis increases brain stiffness: in vivo magnetic resonance elastography in a mouse model of dopamine depletion. *PLoS One*, 9:e92582, 2014.

[22] FB Freimann, S Muller, K Streitberger, J Guo, S Rot, A Ghori, P Vajkoczy, R Reiter, I Sack, and J Braun. MR elastography in a murine stroke model reveals correlation of macroscopic viscoelastic properties of the brain with neuronal density. *NMR Biomed*, 26:1534–1539, 2013.

[23] H Schwarb, CL Johnson, MDJ McGarry, and NJ Cohen. Medial temporal lobe viscoelasticity and relational memory performance. *NeuroImage*, 132:534–541, 2016.

[24] I Sack, B Beierbach, J Wuerfel, D Klatt, U Hamhaber, S Papazoglou, P Martus, and J Braun. The impact of aging and gender on brain viscoelasticity. *NeuroImage*, 46:652–657, 2009.

[25] I Sack, KJ Streitberger, D Krefting, F Paul, and J Braun. The Influence of Physiological Aging and Atrophy on Brain Viscoelastic Properties in Humans. *PLoS One*, 6:e23451, 2011.

[26] A Arani, MC Murphy, KJ Glaser, A Manduca, DS Lake, SA Kruse, C Jack, RL Ehman, and J Huston 3rd. Measuring the effects of aging and sex on regional brain stiffness with MR elastography in healthy older adults. *NeuroImage*, 111:59 – 64, 2015.

[27] CL Johnson, JL Holtrop, MDJ McGarry, JB Weaver, KD Paulsen, JG Georgiadis, and BP Sutton. 3D multislab, multishot acquisition for fast, whole-brain MR elastography with high signal-to-noise efficiency. *Magn Reson Med*, 71:477–485, 2014.

[28] MDJ McGarry, EEW Van Houten, CL Johnson, JG Georgiadis, BP Sutton, JB Weaver, and KD Paulsen. Multiresolution MR elastography using nonlinear inversion. *Med Phys*, 39:6388–6396, 2012.

[29] J Testu, MDJ McGarry, F Dittmann, JB Weaver, KD Paulsen, I Sack, and EEW Van Houten. Viscoelastic power law parameters of in vivo human brain estimated by MR elastography. *J Mech Behav Biomed Mater*, 74:333–341, 2017.

[30] ZS Nasreddine, NA Phillips, V Bedirian, S Charbonneau, V Whitehead, I Collin, JL Cummings, and H Chertkow. The Montreal Cognitive Assessment, MoCA: a brief screening tool for mild cognitive impairment. *J Am Geriatr Soc*, 53:695–699, 2005.

[31] MDJ McGarry, EEW Van Houten, PR Perrinez, AJ Pattison, JB Weaver, and KD Paulsen. An octahedral shear strain-based measure of SNR for 3D MR elastography. *Phys Med Biol*, 56:N153–64, 2011.

[32] B Fischl, DH Salat, E Busa, M Albert, M Dieterich, C Haselgrove, A van der Kouwe, R Killiany, D Kennedy, S Klaveness, A Montillo, N Makris, B Rosen, and AM Dale. Whole brain segmentation: automated labeling of neuroanatomical structures in the human brain. *Neuron*, 33:341–355, 2002.

[33] M Jenkinson, CF Beckmann, TEJ Behrens, MW Woolrich, and SM Smith. FSL. *NeuroImage*,

62:782–790, 2012.

[34] CL Johnson, H Schwarb, MDJ McGarry, AT Anderson, GR Huesmann, BP Sutton, and NJ Cohen. Viscoelasticity of subcortical gray matter structures. *Hum Brain Mapp*, 2016.

[35] RL Buckner, D Head, J Parker, AF Fotenos, D Marcus, JC Morris, and AZ Snyder. A unified approach for morphometric and functional data analysis in young, old, and demented adults using automated atlas-based head size normalization: reliability and validation against manual measurement of total intracranial volume. *NeuroImage*, 23:724–738, 2004.

[36] EEW Van Houten, KD Paulsen, MI Miga, FE Kennedy, and JB Weaver. An overlapping subzone technique for MR-based elastic property reconstruction. *Magn Reson Med*, 42:779–786, 1999.

[37] MDJ McGarry, CL Johnson, BP Sutton, EEW Van Houten, JG Georgiadis, JB Weaver, and KD Paulsen. Including spatial information in nonlinear inversion MR elastography using soft prior regularization. *IEEE Trans Med Imaging*, 32:1901–1909, 2013.

[38] H Schwarb, CL Johnson, AM Daugherty, CH Hillman, AF Kramer, NJ Cohen, and AK Barbey. Aerobic fitness, hippocampal viscoelasticity, and relational memory performance. *NeuroImage*, 153:179–188, 2017.

[39] A Manduca, TE Oliphant, MA Dresner, JL Mahowald, SA Kruse, E Amromin, JP Felmlee, JF Greenleaf, and RL Ehman. Magnetic resonance elastography: Non-invasive mapping of tissue elasticity. *Med Image Anal*, 5:237–254, 2001.

[40] MDJ McGarry and EEW Van Houten. Use of a Rayleigh damping model in elastography. *Med Biol Eng Comput*, 46:759–766, 2008.

[41] J Guo, S Hirsch, A Fehlner, S Papazoglou, M Scheel, J Braun, and I Sack. Towards an elastographic atlas of brain anatomy. *PLoS One*, 8:e71807, 2013.

[42] BB Avants, NJ Tustison, G Song, PA Cook, A Klein, and JC Gee. A reproducible evaluation of ANTs similarity metric performance in brain image registration. *NeuroImage*, 54:2033–2044, 2011.

[43] J Cohen. *Statistical power analysis for the behavioural sciences.* New York: Academic Press., 1969.

[44] R Peters. Ageing and the brain. *J Postgrad Med*, 82:84–88, 2006.

[45] MF Callaghan, P Freund, B Draganski, E Anderson, M Cappelletti, R Chowdhury, J Diedrichsen, THB FitzGerald, P Smittenaar, G Helms, A Lutti, and N Weiskopf. Widespread age-related differences in the human brain microstructure revealed by quantitative magnetic resonance imaging. *Neurobiol Aging*, 35:1862–1872, 2014.

[46] VV Eylers, AA Maudsley, P Bronzlik, PR Dellani, H Lanfermann, and XQ Ding. Detection of normal aging effects on human brain metabolite concentrations and microstructure with whole brain mr spectroscopic imaging and quantitative mr imaging. *AJNR Am J Neuroradiol*, 37:447–454, 2016.

[47] T Munder, A Pfeffer, S Schreyer, J Guo, J Braun, I Sack, B Steiner, and C Klein. MR elastography detection of early viscoelastic response of the murine hippocampus to amyloid beta accumulation and neuronal cell loss due to Alzheimer's disease. *J Magn Reson Imaging*, 2017.

[48] CL Johnson, H Schwarb, HM Horecka, MDJ McGarry, CH Hillman, AF Kramer, NJ Cohen, and AK Barbey. Double dissociation of structure-function relationships in memory and fluid intelligence observed with magnetic resonance elastography. *NeuroImage*, 2018.

[49] LM Gerischer, A Fehlner, T Köbe, K Prehn, D Antonenko, U Grittner, J Braun, I Sack, and A Flöel. Combining viscoelasticity, diffusivity and volume of the hippocampus for the diagnosis of Alzheimer's disease based on magnetic resonance imaging. *NeuroImage: Clin*, https://doi.org/10.1016/j.nicl.2017.12.023, 2017.

[50] S Hetzer, P Birr, A Fehlner, S Hirsch, F Dittmann, E Barnhill, J Braun, and I Sack. Perfusion alters stiffness of deep gray matter. *J Cereb Blood Flow Metab*, page 271678X17691530, 2017.

[51] MDJ McGarry. Improvement and Evaluation of Nonlinear Inversion MR Elastography. *Dartmouth College*, 2013a.

[52] R Sinkus, K Siegmann, T Xydeas, M Tanter, C Claussen, and M Fink. MR elastography of breast lesions: understanding the solid/liquid duality can improve the specificity of contrast-enhanced MR mammography. *Magn Reson Med*, 58:1135–1144, 2007.

Chapter 8

The relationship between hippocampal viscoelasticity and memory performance

Plan for the Chapter

The previous chapter identified significant differences in the mechanical properties of the brain between young and healthy older adults. In particular, widespread softening to the brain and increased hippocampal relative viscosity were characteristics of the older adult group. Lying deep within the medial temporal lobe, the hippocampal formation is one of the most studied neuronal systems in the brain. Its particular role in memory has made the hippocampus a suitable candidate for neuroimaging studies aiming to characterise the early stages of memory specific disorders such as Alzheimer's disease (AD). In this chapter, I conduct an investigation into the possible structure-function relationship of MRE in combination with psychological testing. More specifically, I am interested in whether hippocampal MRE measures are associated with episodic memory, and whether this association outperforms that provided by hippocampal volumetry. For the first time, I isolate this investigation to the study of a sample of healthy older adults and consider the utility of mechanical asymmetry with regards to hemispheric lateralisation.

8.1 Introduction

Age-related cognitive decline affects an estimated 40% of an otherwise healthy population over the age of 60 and reduces both quality of life and independent living [1]. Episodic memory, which refers to the conscious recollection of a personal experience, is particularly sensitive to cerebral ageing [2], is more severely affected than other forms of memory [3], and often the first and most prominent neuropsychological domain altered by Alzheimer's disease (AD) [4, 5].

Episodic memory has long been recognised as being dependent on the function of an intact hippocampus (HC), a medial temporal lobe (MTL) structure essential for encoding and consolidating new memories [6–8]. To study this relationship, many researchers typically rely on structural magnetic resonance imaging (MRI) to investigate the association between hippocampal volume (i.e. macroscopic size) and neuropsychological assessments of memory performance [9]. The implicit link is that volume loss impairs function; however, measures of volume alone are not specific to the microstructural tissue alterations expected to impact memory function. As such, the conclusion from a large meta-analysis that the relationship between hippocampal size and episodic memory in normal ageing is weak is perhaps not surprising [10]. Instead, imaging techniques sensitive to the microscale characteristics of neural tissue are critically needed to better understand the origins of cognitive decline. Understanding how changes in hippocampal microstructure impacts cognition in the context of ageing may prove important for identifying critical neural underpinnings of the cognitive ageing process and intervention targets for combating cognitive decline.

Over the last several years, magnetic resonance elastography (MRE) [11] has emerged as a potentially useful clinical useful neuroimaging technique [12], due to its highly sensitive and unique contrast mechanism [13]. Unlike traditional magnetic resonance imaging (MRI), MRE provides a quantitative measurement of the mechanical properties (e.g. stiffness or viscosity) of the brain. Through recent advances in MRE technology, reliable *in vivo* measurements of brain viscoelasticity have been reported for individual brain structures and regions [14, 15]. Previous MRE investigations have found that brain viscoelasticity is affected by neuro-degeneration [16], intracranial tumours [17], including cerebral malignancies [18], and healthy ageing [19–21]. Evidence suggests that mechanical signals operate in tandem with biochemical cues to determine tissue characteristics [22], which suggests that brain viscoelasticity may provide novel information related to the underlying integrity of neural tissue microstructure [23]. Through animal models of disease, the mechanical properties from MRE have been directly linked to demyelination [24], and inflammation processes [25], as well as alterations in neuronal density [26, 27].

The high sensitivity of brain tissue viscoelasticity to underlying neural microstructure has also motivated the use of MRE for exploring brain-behaviour (i.e. structure-function) relationships within cognitive neuroscience. In particular, several studies have investigated MRE-derived hippocampal viscoelasticity and its relation to cognition [28–31]. Results revealed a strong correlation between the relative viscous-to-elastic behaviour (i.e. damping ratio, ξ) of the HC and episodic memory, whereas measures such as hippocampal volume, and metrics from diffusion tensor imaging (DTI) were not associated with memory performance [28]. This work was later replicated within a larger sample and further demonstrated that higher aerobic fitness was associated with hippocampal ξ, which is interpreted to have mediated the benefits of fitness on memory performance [29]. More recently, a significant double dissociation between the orbitofrontal cortex-fluid intelligence relationship and the hippocampal-relational memory relationship was observed, highlighting the potential of using MRE to map brain mechanical properties with regards to specific cognitive functions [31]. However, in these studies only healthy young adults were recruited; the impact of changes to hippocampal viscoelasticity in the context of age-related cognitive decline remains unexplored.

The present study sought to examine the relationship between hippocampal viscoelasticity and performance on a verbal paired associates task (VPA) in cognitively healthy older men and women. The VPA task involves learning the association between two pieces of information, with test materials presented as either semantically related or unrelated word pairs. This binding of information is thought to rely heavily on the hippocampal formation [32], and thus verbal paired associate learning tasks have become emblematic of hippocampal function. As lesion deficit and functional MRI (fMRI) studies have provided evidence for a material-specific lateralisation of function, with the dominant (usually the left) HC mediating verbal memory [33], and non-dominant (usually the right) HC mediating nonverbal or visual memory [34], I explored the potentially unique contributions of left and right HC viscoelasticity to VPA recall score. Additionally, as simulation experiments have demonstrated how atrophy, and the concomitant increase in cerebrospinal fluid (CSF), can produce a systematic bias in MRE-based stiffness measurements [14], I have developed and applied a novel image analysis procedure to remove CSF voxels from the MRE measurements that is compatible with the current protocol. This issue is of critical importance in the study of ageing, where on average, older adults are expected to have smaller brain volumes and higher levels of CSF [35].

Consistent with previous MRE studies of relational memory in young adults, I hypothesised that: (1) hippocampal viscoelasticity would show a significant correlation with memory performance in older adults - in particular, I predict that a relatively greater viscous to-elastic hippocampus (higher damping ratio, ξ), will be associated with poorer performance on the VPA recall task; (2) in a cohort of right handed participants, left hippocampal ξ would possess a stronger relationship with VPA score due to the verbal nature of the performance task; and (3) correction to take account of CSF in voxels within the HC could potentially increase the significance of any observed relationship with cognition.

8.2 Materials and methods

8.2.1 *Subjects*

The same older participants from the last chapter were included in this study. All subjects had been required to complete the Montreal Cognitive Assessment (MoCA) [36], and score above the normal range (>26/30). All participants were English native speakers, with no history of neurological or psychiatric episodes. No significant structural MRI abnormalities were reported by a consultant radiologist. The study met all criteria for approval from the National Health Service (NHS) Lothian Research Ethics Committee (15/SS/0219), and written informed consent was obtained from each participant prior to neuroimaging and neuropsychological assessment.

8.2.2 *Neuroimaging acquisition*

MRI scanning was performed using a Siemens 3T Verio whole-body MRI scanner with a 12- channel head receive coil (Siemens Medical Solutions; Erlangen, Germany). A high-resolution T_1-weighted MPRAGE (Magnetization-Prepared Rapid Gradient Echo) sequence was obtained consisting of the following parameters: 1 mm isotropic voxels; TE = 2.97 ms; TR = 2400 ms; FOV = 240 x 240; acquired in a sagittal orientation. To elicit brain tissue displacements for MRE, a pneumatic actuator (Resoundant; Rochester, MN, USA) was set to a single frequency of 50 Hz, where the vibrations were transferred to a soft pad placed below the occipital portion of the head. This particular actuator design has been found to be acceptable to participants over a wide age range [21]. The MRE acquisition employed a 3D multislab, multishot spiral sequence to capture high-resolution displacement data at an isotropic resolution of 1.6 mm, as previously described [37]. Following iterative image reconstruction and data processing, complex, full vector displacement fields were generated for mechanical property estimation.

8.2.3 *MRE inversion*

All octahedral shear strain-based SNR measures (OSS-SNR) were >3, determined to be stable for inversion [38]. Nonlinear inversion (NLI) [39–41] was combined with soft prior regularisation (SPR) of the HC to estimate the complex shear modulus ($G^* = G' + iG''$), from the full vector MRE displacement data by iteratively updating the property description to match the model to the measurements. SPR penalises heterogeneity within the region of interest (ROI), (see next section for HC mask generation), and thus reduces variability in measures potentially arising from partial volume effects or contamination from nearby regions of cerebrospinal fluid (CSF) due to the smoothing effect of the regularisation required to ensure stable inversion [42]. Maps of the complex shear modulus G^* were reformulated in MATLAB to provide quantitative maps of shear stiffness, $\mu = 2\ |G^*|^2/(G' + |G^*|)$, and damping ratio, $\xi = G''/2G'$.

8.2.4 *Hippocampal mask generation*

Hippocampal (HC) masks were obtained via automatic segmentation of the T_1-weighted images using FreeSurfer v.5.3 through the recon-all pipeline [43]. Segmentation quality was visually assessed, and manual adjustments were made when necessary. The MRE T_2-weighted magnitude images were then coregistered to the structural T_1-weighted MPRAGE using the FLIRT tool within FSL [44]. A 12-

parameter affine model was used with tri-linear interpolation and a correlation ratio cost function. The registration was optimised by using weighting volumes of the ventricles. The inverse of this transform was calculated to register the HC mask from the anatomical T_1 image into MRE space using nearest neighbour interpolation. A threshold of 95% was applied to the masks to reduce partial volume effects. To further remove any remaining voxels CSF, FAST (FMRIB's Automated Segmentation Tool), was used to extract CSF maps from the T_1-weighted image [45]. The output CSF map is a partial volume map containing intensity values representing the proportion of CSF within each voxel [from 0-100%]. The resulting CSF map from participants was then coregistered to their MRE data using the same inverse transform as previously described. The CSF maps were subsequently binarised at a 100% threshold and multiplied by the original masks to generate new smaller HC masks containing no voxels with CSF. The new HC masks were input into SPR with a weighting parameter of $\alpha = 10^{-11}$ within the NLI algorithm, as mentioned in the previous section.

8.2.5 *Volumetric analysis*

Automated labelling based on a spatial probabilistic atlas was performed to obtain bilateral HC volumes; Estimated Total Intracranial Volume (eTIV) was used to normalise HC volume for participant head size [46].

8.2.6 *Neuropsychological assessments*

The Montreal Cognitive Assessment (MoCA) is a widely used 30-point assessment administered in approximately 10 minutes to screen for global cognitive impairment [36]. All participants were required to score >26/30 on the MoCA to ensure normal cognitive function. The National Adult Reading Test (NART) was administered to measure full scale intelligence [47]. The NART can be used as a proxy for premorbid intelligence since it has been shown to remain impervious to mild-to-moderate memory decline [48]. All participants also completed the Edinburgh Handedness Inventory to measure handedness. Episodic memory was assessed by using the Verbal Paired Associates subtest (VPA) from the Wechsler Memory Scale-Revised (WMS-R) [49]. The VPA is one of the most widely used instruments for measuring explicit episodic memory [50]. In this study, only the immediate recall test scores are reported. Delayed recall data was collected, but participants performed at ceiling restricting inter-subject variability. This test involves the examiner reading eight word pairs to the participant across three study test trials. The VPA pairs can be divided into four "easy" pairs (semantically related) and four "hard" pairs (semantically unrelated). After each presentation of the list of eight pairs, the first word is given by the examiner and the participant is required to provide its associate. The maximum score from the three trials was 24.

8.2.7 *Statistical analyses*

All MRE data reported refer to results obtained in MRE native space for each participant. Due to significant skewness in the test of memory performance (i.e. the VPA), median absolute deviation (MAD) methods were used to detect statistical outliers [51,52]. A conservative criterion of 3 times the MAD was used for outlier detection [53]. One participant was excluded at this stage due to scoring below the MAD, suggesting a lack of engagement in the task, or an undiagnosed memory disorder with the score being within the range of that expected for a patient diagnosed with Alzheimer's disease [49]. MAD did not identify any significant outliers due to hippocampal viscoelastic measures. The analytic sample therefore included 11 older adults (mean age = 69.1 + 2.3 years, 6 female, 5 male).

Pearson partial correlation coefficients, r, were used to investigate how each HC MRE measure, μ and ξ, correlated with VPA performance, with age (years), sex, NART full-scale IQ, and HC volume used as covariates. Age and sex were used as control variables due to previous studies identifying a link between both variables and brain viscoelasticity [19,21]. Due to previous reports of associations between brain structure and intelligence [54], the NART full-scale IQ was used as a control variable. HC volume provided from FreeSurfer was also used as a covariate to ensure HC size did not account for the observed relationships between HC viscoelastic measures and VPA recall score. Volumetric measurements were derived from FreeSurfer, as opposed to the size of the HC masks, as this automatic procedure is routine for MRI studies of the hippocampus. Identical analyses were then performed on the right and left HC separately. For investigating the relationship between HC volume and VPA recall score, age (years), sex and NART full-scale IQ were used as control variables. Correlations were two-tailed with level of significance set at p <0.05. Statistical analyses were performed with SPSS software version 24.0.0 (SPSS Inc., Chicago, IL).

Statistical differences between correlations were determined using Steiger's Z test [55], which required the computation of a z-score based on the sample size and the correlation coefficients to be compared (r_{jk} and r_{jh}), along with the correlation of the unshared variable (r_{kh}). The correlation of the unshared variance is computed along with the appropriate covariates. By convention, z values greater than 1.96 are considered significant. Calculations were performed using a web utility provided by Lee *et al.,* 2013 [56].

8.3 Results

Descriptive statistics (mean, standard deviation, minimum/maximum values, and population coefficient of variation [CV]) for all study variables for the analytic sample of 11 subjects (6F/5M) are presented in Table 8.1. The mean OSS-SNR score indicates high quality MRE displacement data, and the mean NART full-scale IQ indicates that the sample was intellectually high functioning. All participants were right-handed as determined by the Edinburgh Handedness Inventory. Partial correlation coefficients, r, and associated p values between each HC structural measure and the observed relationship with VPA score are presented in Table 8.2.

Table 8.1: Demographic data for participants included in the study

	Mean	SD	Min/Max	CV
Demographics				
Age (years)	69.1	2.3	66/72	3.3%
NART full-scale IQ	123.4	4.25	115/128	3.4%
MoCA	28.3	1.73	26/30	6.1%
VPA Immediate Recall	20.7	1.95	17/24	9.4%
MRE measures				
OSS-SNR	5.79	1.54	4.19/8.37	26.5%
Stiffness μ [kPa]				
Bilateral HC μ	2.86	0.35	2.17/3.38	12.2%
Left HC μ	2.77	0.51	2.06/3.83	18.6%
Right HC μ	2.91	0.40	1.93/3.47	13.8%
Damping ratio ξ				
Bilateral HC ξ	0.176	0.039	0.118/0.243	22.5%
Left HC ξ	0.162	0.052	0.109/0.276	31.9%
Right HC ξ	0.186	0.038	0.126/0.249	20.3%
Volume [cm^3]				
Bilateral HC volume	8.20	1.17	6.94/10.46	14.3%
Left HC volume	4.02	0.66	3.17/5.16	16.5%
Right HC volume	4.17	0.52	3.61/5.29	12.7%

Abbreviations: MoCA, Montreal Cognitive Assessment; NART, National Adult Reading Test; VPA, verbal paired associates; OSS-SNR, octahedral shear strain signal-to-noise ratio; HC, hippocampus; CV, coefficient of variation.

Table 8.2: Relationships between hippocampal viscoelasticity and volumetry and VPA recall score

	HC stiffness [kPa]		HC damping ratio		HC volume [cm^3]	
	Correlation, r	p-value	Correlation, r	p-value	Correlation, r	p-value
Bilateral	-.01	0.98	-.88	0.008**	-.19	0.65
Left	.18	0.70	-.93	0.002**	-.19	0.65
Right	-.20	0.67	-.72	0.066	-.18	0.66

**denotes $p < 0.01$ significance level.

8.3.1 *Bilateral hippocampal measures*

There was no significant relationship between memory performance and bilateral HC stiffness (μ; r = -.01, p = 0.98), or bilateral HC volume (r = -.19, p = 0.65). However, bilateral HC ξ was significantly correlated with VPA score (r = -.88, p =0.008), as shown in Figure 8.1.

To demonstrate a single dissociation, a similar analysis to the above was performed to compare memory performance and viscoelastic measures for the caudate as a reference region [29]. The caudate is an optimal control region because it is not reported to be involved in episodic memory [57]. Caudate ξ was not significantly correlated with episodic memory performance (r=-.64, p=0.12). Furthermore, Steiger's z-test revealed that this correlation was significantly smaller than the correlation between HC ξ and episodic memory (z = 7.5, $p < 0.001$; r_{jk} = .64, r_{jh} = .88, r_{kh} = .94). To investigate whether regional specific analyses were warranted, I also performed the same analysis with the global cerebrum as a reference region. Cerebral ξ was not significantly correlated with episodic memory performance (r= -.13, p= 0.78), and this correlation was also significantly smaller than the correlation between HC ξ and episodic memory (z= 3.17, $p < 0.001$; r_{jk} = -.13, r_{jh} = .88, r_{kh} = .40).

8.3.2 *Unilateral hippocampal measures*

The individual contributions of left and right HC to the memory relationship were also investigated. Paired-samples t-tests revealed no significant differences between hemispheres for either viscoelastic MRE or volumetric MRI parameters: (μ [t (10) = -0.87, p = 0.40]; ξ [t (10) = -1.98, p = 0.08]; vol. [t (10) = -1.91, p = 0.09]), as shown in Figure 8.2.

Considering unilateral contributions to memory, analyses of unilateral HC ξ showed a stronger correlation between left HC ξ and VPA score (r = -.93, p = 0.002), whereas the correlation for right HC ξ was not significant (r = -.72, p = 0.07). Steiger's Z test revealed that the difference between the two correlations was statistically significant (z = 3.3, p = <0.001; r_{jk} = .93, r_{jh} = .72, r_{kh} =

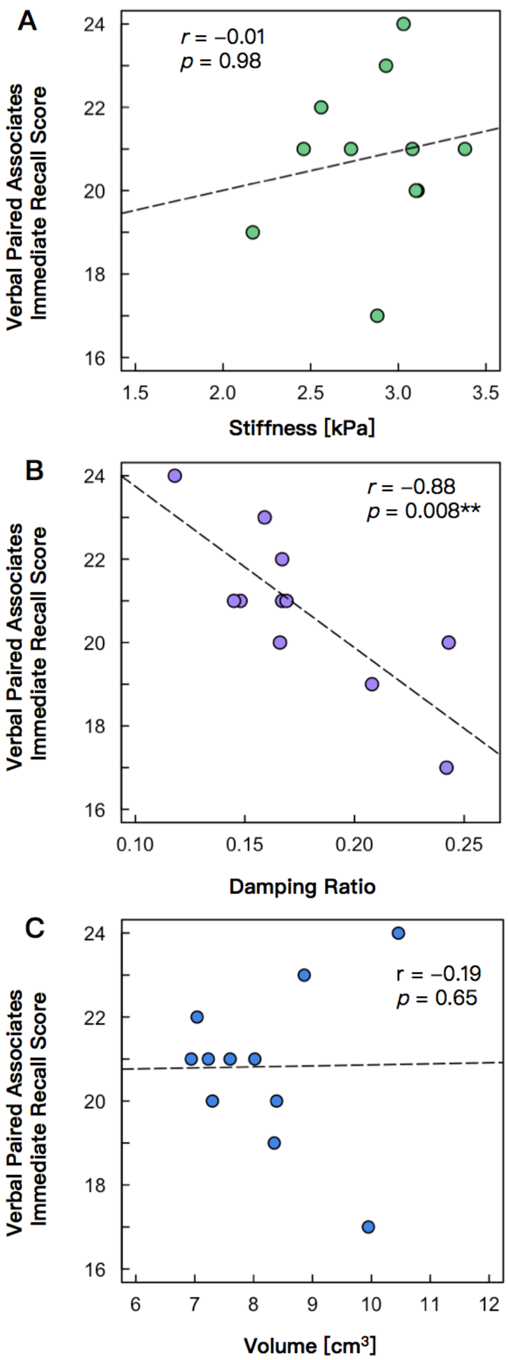

Figure 8.1: Bilateral hippocampal (HC) structural metrics of (a) shear stiffness, (b) damping ratio, and (c) volume, plotted against episodic memory task performance; positive values indicate better task performance. Pearson correlation coefficient, r, demonstrates a significant negative correlation for HC ξ suggesting that greater viscous energy dissipation in the hippocampus indicated by high ξ is correlated with poor performance in the individual's episodic memory assessment. Hippocampal stiffness and volume plotted against VPA task performance, demonstrate no significant relationship with recall score. MRE data were collected at a 50 Hz vibration frequency. Note that the trend lines do not consider the impact of covariates.

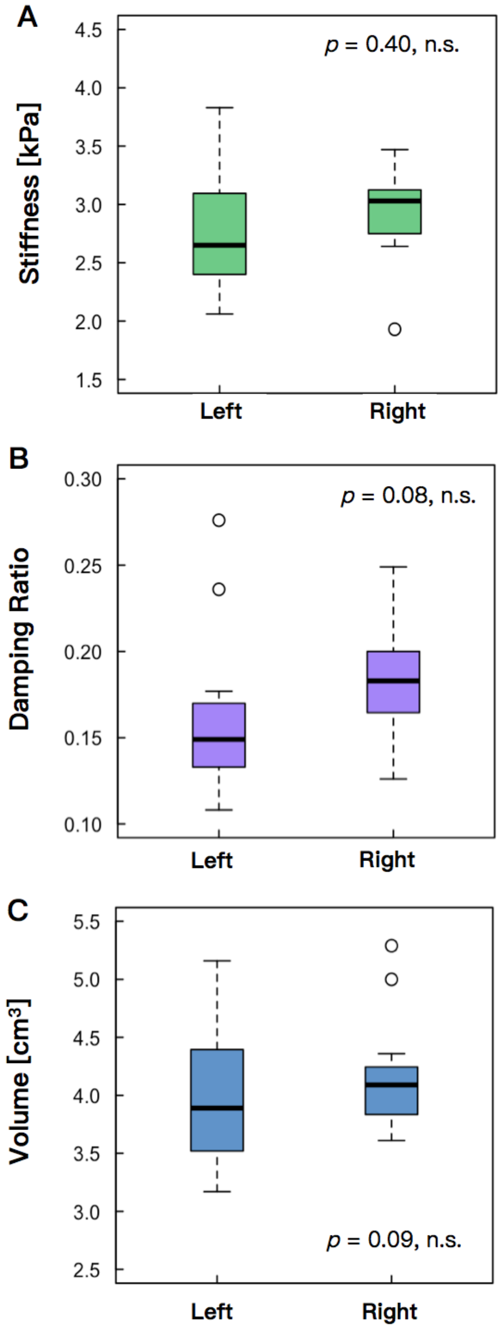

Figure 8.2: Box and whisker plots depicting the values for hippocampal (a) shear stiffness, (b) damping ratio, and (c) volume, according to measurements obtained for the left and right hemisphere. The central box represents values from the 25th to 75th percentiles and the middle line represents the median value. Whisker lines extend from minimum to maximum values, excluding outliers (which are displayed as separate points). Paired samples t tests reveal no significant left-right hemispheric differences in the hippocampus for any parameter ($p > 0.05$). MRE data were collected at a 50 Hz vibration frequency.

.88). Figure 8.3 illustrates the correlation for both left and right HC with VPA score, whereas Figure 8.4 provides example MRE images of the left HC for both a high and low performing participant. Analyses of left HC μ (r = .18, p = 0.70), and right HC μ (r = -.20, p = 0.67), yielded no significant correlation with VPA score. Neither did analyses of left and right HC volume reveal any significant correlation with VPA score (r = -.19, p = 0.65 and r = -.18, p = 0.66, respectively).

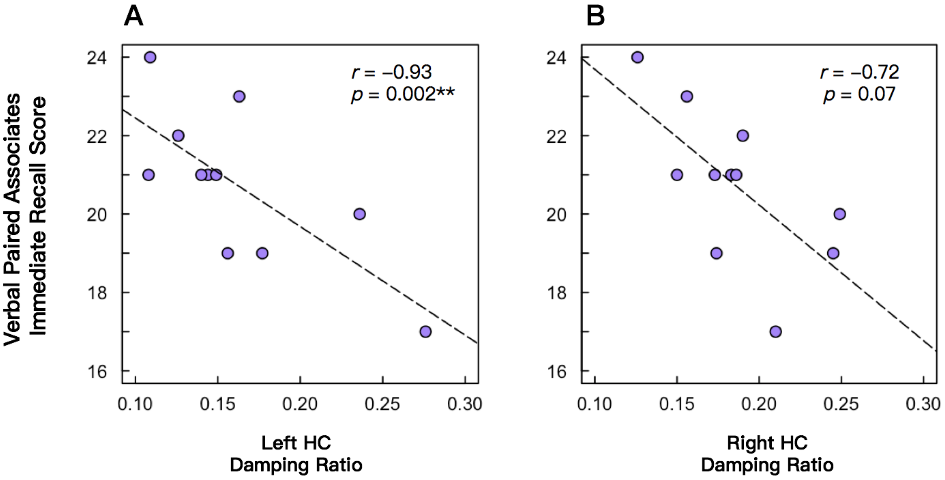

Figure 8.3: Unilateral (right and left) hippocampal (HC) damping ratio ξ plotted against episodic memory task performance; positive values indicate better task performance. Pearson correlation coefficient, r, demonstrates a significant negative correlation for (a) left HC ξ, suggesting that greater viscous energy dissipation in HC indicated by high ξ is correlated with poor performance in the individual's episodic memory assessment; (b) right HC ξ plotted against VPA task performance demonstrates no significant relationship with recall score. MRE data were collected at a 50 Hz vibration frequency. Note that the trend lines do not consider the impact of covariates.

8.3.3 *Hippocampal MRE with and without voxels containing CSF*

Finally, I sought to investigate whether retaining voxels containing cerebrospinal fluid (CSF) would have an effect on the statistical significance of the relationships between HC ξ and cognition. Whereas the mean size of the HC masks excluding CSF was 499 voxels (range: 291 – 863 voxels), the full HC masks, on average, contained 745 voxels (range: 555 – 1130 voxels). The procedure for removing CSF voxels, therefore, had removed approximately 34% (range: 22 - 48%) of voxels within the HC mask. There was no significant correlation between VPA score and HC mask size (without CSF: r = .38, p = 0.36; with CSF: r = .11, p = 0.80), or between HC ξ and HC mask size (without CSF: r = -.59, p = 0.13; with CSF: r = -.29, p = 0.49).

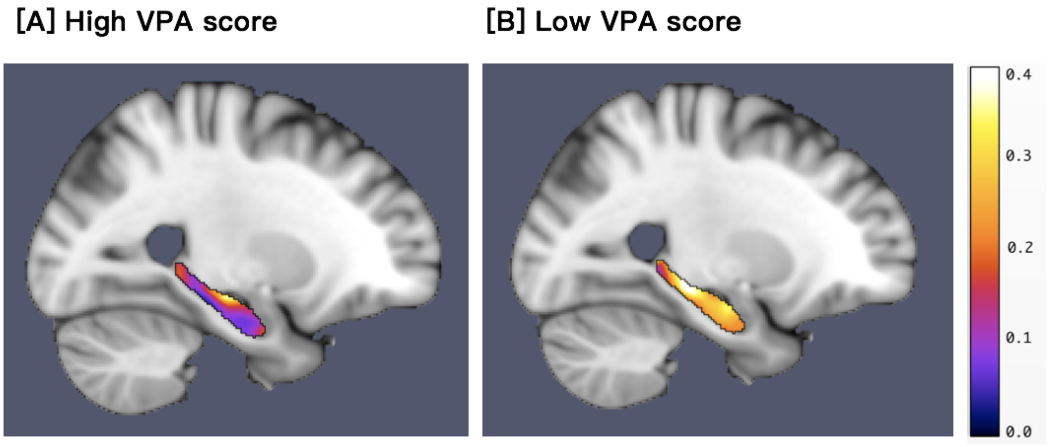

Figure 8.4: Example images of left HC damping ratio, ξ for two participants. Figure (a) shows ξ of a participant who achieved a high score on the VPA, indicating a more elastic HC, whereas (b) shows a participant who performed worse on the VPA, and displayed a more viscous HC. MRE information has been transformed to standard MNI-space for illustration purposes.

An illustration of an original HC mask and the same HC mask after CSF removal is provided in Figure 8.5. Mean values for HC ξ calculated using both procedures can be found in Table 8.3.

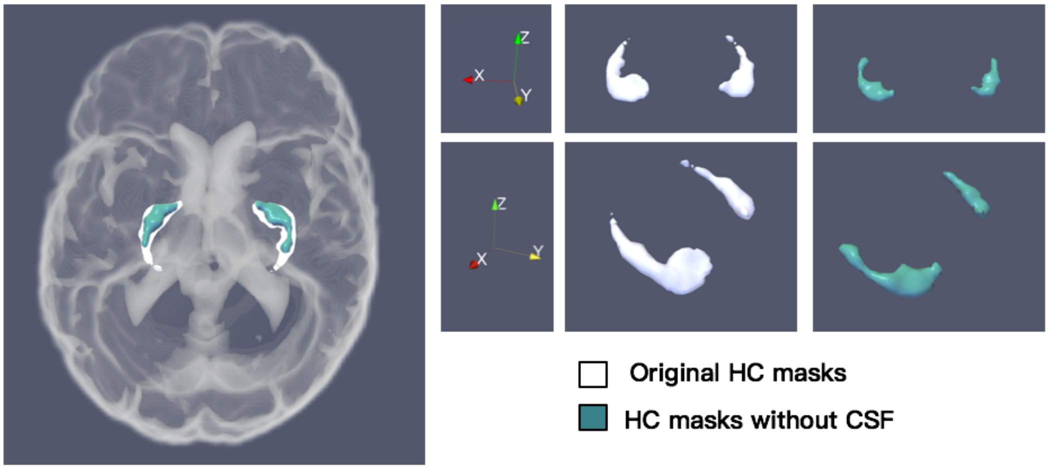

Figure 8.5: Three-dimensional rendering of hippocampal (HC) mask to illustrate the removal of voxels due to cerebrospinal fluid (CSF). In this example of one participant, 555 voxels were present in the original HC mask, as shown in white. After CSF removal, there were 291 voxels remaining, as shown in green. As a result, 48% of voxels were removed from the original mask.

Paired samples t-tests revealed significant differences in HC ξ depending on whether voxels

Table 8.3: Descriptive statistics for HC ξ and the relationship between HC ξ and VPA score depending on the exclusion/ inclusion of voxels containing cerebrospinal fluid

		Bilateral HC ξ	Left HC ξ	Right HC ξ
CSF excluded	Mean ± SD	0.176 ± 0.039	0.162 ± 0.052	0.186 ± 0.038
	Correlation, r, to VPA score	-.88	-.93	-.72
	p value	0.008**	0.002**	0.07
CSF included	Mean ± SD	0.184 ± 0.040	0.176 ± 0.052	0.190 ± 0.036
	Correlation, r, to VPA score	-.82	-.88	-.69
	p value	0.024*	0.010*	0.09
Group comparisons	t test (paired samples)	$p = 0.003$	$p = 0.003$	$p = 0.041$
	Z score	4.72	4.21	1.39
	p value	<0.001***	<0.001***	0.16

***denotes $p < 0.001$, ** denotes $p < 0.01$ and * denotes $p < 0.05$ significance levels.

containing CSF had been included or excluded in the HC measurements: bilaterally [t (10)=-3.83, p=0.003], the left hemisphere [t (10)= -3.87, p=0.003] and right hemisphere [t (10) = -2.34, p = 0.04]. All results show an increase to HC ξ when CSF voxels are included, as expected, indicating a more a viscous fluid as opposed to elastic solid. Additionally, the correlation between measurements from both procedures were highly significant, bilaterally (r =.99, $p < 0.001$), in the left hemisphere (r =.99, $p < 0.001$), and the right hemisphere (r =.99, $p < 0.001$).

The partial correlation coefficients, r, and associated p-values for each structural measure and the observed relationship with cognition are presented in Table 8.3. Streiger's z-test revealed significant differences between the correlations with memory performance depending on the presence, or absence, of CSF: bilaterally (z= 4.72, p = <0.001; r_{jk} = -.82, r_{jh} = -.88, r_{kh} = .99), and left hemisphere (z= 4.21, p = <0.001; r_{jk} = -.88, r_{jh} =. -.93, r_{kh} = .99), but not the right hemisphere (z= 1.39, p = 0.16; r_{jk} = -.69, r_{jh} = -.72, r_{kh} = .99), suggesting a stronger relationship between HC ξ and VPA score when voxels with CSF were excluded from the analysis.

8.4 Discussion

This preliminary investigation is the first to determine whether hippocampal (HC) viscoelasticity, measured *in vivo* using MRE, is associated with episodic memory performance in a group of healthy older adult participants. First, in a group of healthy older adults, I have demonstrated that the relative viscous-to-elastic behaviour (i.e. damping ratio, ξ) of HC is associated with explicit episodic memory, such that individuals with lower HC ξ performed better on the memory task. In contrast, neither HC volume nor HC stiffness were significantly associated with memory performance. Second, I have demonstrated that left HC ξ, as opposed to right HC ξ, possessed a stronger association with task performance. Finally, the conservative approach of excluding voxels that contain cerebrospinal fluid (CSF) was shown to improve the correlation with memory performance, when compared to the standard analysis used in previous publications.

The results presented here are consistent with previous work which has investigated the relationship between HC MRE and functional performance in healthy young adults [28,29,31]. The current study extends these findings by replicating this association in cognitively healthy older adults using a verbal-episodic memory task. However, it should be noted that in these previous studies, adjusted damping ratio, (ξ' = 1 - ξ) is reported, so that lower ξ' would instead be indicative of a reduction in tissue integrity. These studies, like the present study, also did not find HC stiffness or HC volume to account for individual differences in memory. While smaller hippocampal volumes, in general, tend to be associated with poorer memory performance, most studies that have investigated the relationship between size and memory has been in neurological patients, where smaller volumes are likely to be accompanied by other neuropathological features such as amyloid plaques and neurofibrillary tangles. In healthy ageing, however, there appears to be little evidence for the "bigger is better" hypothesis [10] - but see Erickson *et al.,* 2009 [58] and Erickson *et al.,* 2011 [59], with there being substantial overlap between hippocampal volume in healthy controls and patients with Alzheimer's disease [60], and a large range of hippocampal volumes in healthy adults [61, 62]. These results suggest that volume alone does not fully indicate hippocampal integrity, and smaller volumes may not necessarily signify deterioration. The large population variation found in this study for HC ξ (23%), compared with HC volume (14%), could suggest that MRE may be more sensitive for identifying the neural underpinnings of age-related cognitive decline within this older adult population.

All of the previous work highlighting the relationship between HC MRE and memory performance measured relational memory performance using a spatial reconstruction task. In the present study, participants were instead verbally presented with a list of word-pair items and after a very short delay were asked to provide the associate to a presented word. The current study took advantage of the VPA task from the WAIS-R, a standard neuropsychological measure of episodic memory. The VPA includes both an immediate and delayed test, though delayed recall measures were not considered in this report as performance was at ceiling limiting the utility of the statistical approach. While traditional views of hippocampal function often emphasise that the hippocampus is necessary only after a delay [e.g., Baddeley and Warrington, 1970 [63], and Smith and Milner, 1981 [34]], the relational memory theory of hippocampal function highlights the role of hippocampus in episodic binding across domains and delays [32, 64, 65]. Therefore, the data presented in this work is consistent with findings demonstrating a relationship between hippocampal structure and episodic memory with immediate recall only. Indeed, hippocampal amnestic patients show impairment on relational memory tasks even at very short delays [66, 67].

Unilateral HC MRE measurements have yet to be reported despite hemispheric asymmetries in the molecular and morphological characteristics of neuronal connections [68]; it has been suggested that unilateral specialisation may facilitate greater processing power by using the available neuronal circuitry more effectively. This study reports a 15% difference between left and right HC ξ, suggesting left HC exhibits greater relative elastic-to-viscous behaviour, and this will warrant further investigation. While no statistically significant left-right hemispheric differences were detected, increased statistical power with a larger number of subjects may detect mechanical hemispheric asymmetries in future studies.

The report of a stronger correlation of the left HC ξ to VPA recall score may be attributed to the role of the left HC in the storage of verbal material, as found in memory for immediate and delayed prose recall [69], free recall of word lists [33, 70], and narratives [71] as well as verbal memory, confrontation naming, and verbal conceptual ability [72]. In contrast, the right HC has been implicated in spatial and pictorial material, such as geometric faces and figures, not amenable to verbal processing [71, 73, 74], suggesting a functional hemispheric lateralisation of the right and left hippocampus [70, 75]. In this study, however, it is acknowledged that a single dissociation is not sufficient to demonstrate specificity for mapping cognitive function [76], and future MRE studies may identify more precisely the cognitive functions supported by right HC ξ.

Previous work that has investigated the MRE-cognition relationship has been performed in young, healthy participants where soft-prior regularisation (SPR) was deemed suitable to reduce partial volume effects and was shown to improve reliability and increase sensitivity of MRE measurements [15]. However, as normative ageing studies generally reveal a decrease in overall brain volume, and a concomitant increase in volume of CSF, it was deemed that in this population a more conservative approach was required to minimise potential systemic biased caused by CSF. Acknowledging the bias caused by atrophy, Murphy *et al.,* 2013b created an MRE processing pipeline, which utilised adaptive techniques to reduce edge artefacts due to the local homogeneity assumption required by direct inversion methods [14]. This work demonstrated that the edge-related bias can be eliminated by eroding the ROI by 1 voxel from the brain's surface. In the current study, a heterogeneous inversion protocol was used and a procedure was proposed that is specific for the removal of CSF present within the ROI itself. Removal of CSF from the HC masks prior to inversion is also likely to minimise the occurrence of quantitative errors due to data-model mismatch as a result of SPR enforcing CSF voxels to possess the same mechanical properties as solid tissue. In support of this procedure, this study has demonstrated that removal of CSF voxels influence HC ξ measures in the expected direction (i.e. lower ξ - indicating a more elastic solid due to the removal of fluid), remains highly correlated to the standard procedure, and statistically improves the association observed between HC ξ and memory performance.

The damping ratio, ξ dictates which component of the complex shear modulus is more dominant; a lower score thereby representing that the loss modulus, or imaginary component, is becoming increasingly influential in HC tissue behaviour. Accumulating neuroproteomic data demonstrates that hippocampal ageing involves common themes of dysregulated metabolism, increased oxidative stress, altered protein processing, and decreased synaptic function [77]. Taking these findings into consideration, one can speculate that age-related disorganised tissue components may manifest in the MRE signal by being more effective at absorbing strain energy. Alternatively, the mechanism behind alterations in hippocampal ξ have been speculated to potentially relate to neurogenesis [29, 78]; however, a recent study concluded that neurogenesis does not continue, or is extremely rare, in adult humans [79]. As such, research in animal models of disease will be necessary to allow full interpretation of the neurobiological basis of the MRE signal.

In the future it will be interesting to see if the findings of the present study are replicated and a number of refinements can be introduced. In particular, a limitation of the present study is the inability to rule out any covert neuropathology, even though reasonable effort was made to confirm participants were cognitively healthy. For example, a proportion of older adult participants may have an abnormal amyloid-beta (Aβ) burden, that would remain undetected with MRI, even though there is currently no consensus as to whether viscoelastic measures are sensitive to Aβ accumulation [16, 78]. Future studies could also employ a wider range of memory measures and include other imaging biomarkers such as the microstructural measures obtained from diffusion tensor imaging (DTI). DTI can probe the white matter pathways in the hippocampus and has previously revealed a loss of integrity with age [80], and a relationship between hippocampal mean diffusivity (MD) and verbal memory performance [81]. The combination of hippocampal MRE measures, MD from DTI and MR volumetry has recently been shown to improve the diagnostic accuracy of Alzheimer's disease (AD) [82]. Accordingly, it is conceivable to propose that a combination of imaging modalities that may include MRE could prove useful in the identification of healthy individuals at greatest risk for cognitive decline.

8.5 Conclusions

This is the first report of a significant structure-function relationship between hippocampal viscoelasticity and episodic memory performance in a sample of cognitively intact older adults. Consistent with previous studies of younger adults, greater relative viscous-to-elastic behaviour of the hippocampus (i.e. higher damping ratio, ξ), was associated with poorer performance on the verbal paired associates subtest, whereas hippocampal stiffness and hippocampal volume was not. Separate unilateral investigation of the left and right hippocampus found a stronger correlation for the left compared to the right hippocampus, which may be attributed to the verbal nature of the VPA task, thus supporting previous reports of hippocampal functional specialisation. Finally, this work demonstrates that the sensitivity of the MRE-cognition relationship may be improved by removing voxels containing CSF from the hippocampal mask prior to MRE inversion. Future research is now recommended to build upon these results in order to establish the causal nature between these variables and whether hippocampal MRE measures can predict future episodic memory decline. Ultimately, understanding how changes in hippocampal microstructure impacts cognition in the context of ageing may prove important for identifying intervention targets for combating cognitive ageing, and could suggest a possible role for MRE as an imaging biomarker for memory specific disorders such as Alzheimer's disease.

References

[1] GW Small. What we need to know about age related memory loss. *BMJ*, 324:1502–1505, 2002.

[2] K Kinugawa, S Schumm, M Pollina, M Depre, Ca Jungbluth, M Doulazmi, C Sebban, A Zlomuzica, R Pietrowsky, B Pause, J Mariani, and E Dere. Aging-related episodic memory decline: are emotions the key? *Front in Behav Neurosci*, 7:2, 2013.

[3] B Levine, E Svoboda, JF Hay, G Winocur, and M Moscovitch. Aging and autobiographical memory: dissociating episodic from semantic retrieval. *Psychol Aging*, 17:677–689, 2002.

[4] MS Albert, MB Moss, R Tanzi, and K Jones. Preclinical prediction of AD using neuropsychological tests. *J Int Neuropsychol Soc*, 7:631–639, 2001.

[5] MW Bondi, DP Salmon, D Galasko, RG Thomas, and LJ Thal. Neuropsychological function and apolipoprotein E genotype in the preclinical detection of Alzheimer's disease. *Psychol Aging*, 14:295–303, 1999.

[6] H Eichenbaum. Hippocampus: Cognitive Processes and Neural Representations that Underlie Declarative Memory. *Neuron*, 44:109–120, 2004.

[7] JP Aggleton and MW Brown. Episodic memory, amnesia, and the hippocampal-anterior thalamic axis. *Behav Brain Sci*, 22:425–444, 1999.

[8] F Vargha-Khadem, DG Gadian, KE Watkins, A Connelly, W Van Paesschen, and M Mishkin. Differential effects of early hippocampal pathology on episodic and semantic memory. *Science*, 277:376–380, 1997.

[9] KJ Ferguson, JM Wardlaw, and AMJ MacLullich. Quantitative and qualitative measures of hippocampal atrophy are not correlated in healthy older men. *J Neuroimaging*, 20:157–162.

[10] C Van Petten. Relationship between hippocampal volume and memory ability in healthy individuals across the lifespan: review and meta-analysis. *Neuropsychologia*, 42:1394–1413, 2004.

[11] R Muthupillai, DJ Lomas, PJ Rossman, JF Greenleaf, A Manduca, and RL Ehman. Magnetic resonance elastography by direct visualization of propagating acoustic strain waves. *Science*, 269:1854–1857, 1995.

[12] LV Hiscox, CL Johnson, E Barnhill, MDJ McGarry, J III Huston, EJR van Beek, JM Starr, and N Roberts. Magnetic resonance elastography (MRE) of the human brain: technique, findings and clinical applications. *Phys Med Biol*, 61:401–437, 2016.

[13] YK Mariappan, KJ Glaser, and RL Ehman. Magnetic resonance elastography: a review. *Clin Anat*, 23:497–511, 2010.

[14] MC Murphy, J Huston 3rd, Jr CR Jack, KJ Glaser, ML Senjem, J Chen, A Manduca, JP Felmlee, and RL Ehman. Measuring the characteristic topography of brain stiffness with magnetic resonance elastography. *PLoS One*, 8:e81668, 2013b.

[15] CL Johnson, H Schwarb, MDJ McGarry, AT Anderson, GR Huesmann, BP Sutton, and NJ Cohen. Viscoelasticity of subcortical gray matter structures. *Hum Brain Mapp*, 2016.

[16] MC Murphy, J Huston 3rd, and RL Ehman. MR elastography of the brain and its application in neurological diseases. *NeuroImage*, https://doi.org/10.1016/j.neuroimage.2017.10.008, 2017.

[17] JD Hughes, N Fattahi, J Van Gompel, A Arani, G Lanzino, M Link, F Meyer, R Ehman, and J Huston 3rd. Higher Resolution Magnetic Resonance Elastography for the Evaluation of Intratumoral Heterogeneity in Meningiomas. *J Neurol Surg B*, 76:A139, 2015.

[18] KM Pepin, RL Ehman, and KP McGee. Magnetic resonance elastography (MRE) in cancer: Technique, analysis, and applications. *Prog Nucl Magn Reson Spectrosc*, 90-91:32–48, 2015.

[19] I Sack, KJ Streitberger, D Krefting, F Paul, and J Braun. The Influence of Physiological Aging and Atrophy on Brain Viscoelastic Properties in Humans. *PLoS One*, 6:e23451, 2011.

[20] A Arani, MC Murphy, KJ Glaser, A Manduca, DS Lake, SA Kruse, C Jack, RL Ehman, and J Huston 3rd. Measuring the effects of aging and sex on regional brain stiffness with MR elastography in healthy older adults. *NeuroImage*, 111:59 – 64, 2015.

[21] LV Hiscox, CL Johnson, MDJ McGarry, M Perrins, A Littlejohn, EJR van Beek, N Roberts, and JM Starr. High-resolution magnetic resonance elastography reveals differences in subcortical gray matter viscoelasticity between young and healthy older adults. *Neurobiol Aging*, 65:158–167,

2018.

[22] S Chanet and AC Martin. Mechanical force sensing in tissues. *Prog Mol Biol Transl Sci*, 126:317–352, 2014.

[23] I Sack, K Johrens, J Wurfel, and J Braun. Structure-sensitive elastography: on the viscoelastic powerlaw behavior of in vivo human tissue in health and disease. *Soft Matter*, 9:5672–5680, 2013.

[24] K Schregel, E Wuerfel née Tysiak, P Garteiser, I Gemeinhardt, T Prozorovski, O Aktas, H Merz, D Petersen, J Wuerfel, and R Sinkus. Demyelination reduces brain parenchymal stiffness quantified in vivo by magnetic resonance elastography. *Proc Natl Acad Sci USA*, 109:6650–6655, 2012.

[25] K Riek, JM Millward, I Hamann, S Mueller, CF Pfueller, F Paul, J Braun, C Infante-Duarte, and I Sack. Magnetic resonance elastography reveals altered brain viscoelasticity in experimental autoimmune encephalomyelitis. *NeuroImage: Clin*, 1:81–90, 2012.

[26] FB Freimann, S Muller, K Streitberger, J Guo, S Rot, A Ghori, P Vajkoczy, R Reiter, I Sack, and J Braun. MR elastography in a murine stroke model reveals correlation of macroscopic viscoelastic properties of the brain with neuronal density. *NMR Biomed*, 26:1534–1539, 2013.

[27] C Klein, EG Hain, J Braun, K Riek, S Mueller, B Steiner, and I Sack. Enhanced adult neurogenesis increases brain stiffness: in vivo magnetic resonance elastography in a mouse model of dopamine depletion. *PLoS One*, 9:e92582, 2014.

[28] H Schwarb, CL Johnson, MDJ McGarry, and NJ Cohen. Medial temporal lobe viscoelasticity and relational memory performance. *NeuroImage*, 132:534–541, 2016.

[29] H Schwarb, CL Johnson, AM Daugherty, CH Hillman, AF Kramer, NJ Cohen, and AK Barbey. Aerobic fitness, hippocampal viscoelasticity, and relational memory performance. *NeuroImage*, 153:179–188, 2017.

[30] BM Sandroff, CL Johnson, and RW Motl. Exercise training effects on memory and hippocampal viscoelasticity in multiple sclerosis: a novel application of magnetic resonance elastography. *Neuroradiology*, 59:61–67, 2017.

[31] CL Johnson, H Schwarb, HM Horecka, MDJ McGarry, CH Hillman, AF Kramer, NJ Cohen, and AK Barbey. Double dissociation of structure-function relationships in memory and fluid intelligence observed with magnetic resonance elastography. *NeuroImage*, 2018.

[32] H Eichenbaum. The hippocampus and declarative memory: cognitive mechanisms and neural codes. *Behav Brain Res*, 127:199–207, 2001.

[33] V Frisk and B Milner. The role of the left hippocampal region in the acquisition and retention of story content. *Neuropsychologia*, 28:349–359, 1990.

[34] ML Smith and B Milner. The role of the right hippocampus in the recall of spatial location. *Neuropsychologia*, 19:781–793, 1981.

[35] Erber JT. Aging and older adulthood, third edition. Wiley-Blackwell, 2012.

[36] ZS Nasreddine, NA Phillips, V Bedirian, S Charbonneau, V Whitehead, I Collin, JL Cummings, and H Chertkow. The Montreal Cognitive Assessment, MoCA: a brief screening tool for mild cognitive impairment. *J Am Geriatr Soc*, 53:695–699, 2005.

[37] CL Johnson, JL Holtrop, MDJ McGarry, JB Weaver, KD Paulsen, JG Georgiadis, and BP Sutton. 3D multislab, multishot acquisition for fast, whole-brain MR elastography with high signal-to-noise efficiency. *Magn Reson Med*, 71:477–485, 2014.

[38] MDJ McGarry, EEW Van Houten, PR Perrinez, AJ Pattison, JB Weaver, and KD Paulsen. An octahedral shear strain-based measure of SNR for 3D MR elastography. *Phys Med Biol*, 56:N153–64, 2011.

[39] EEW Van Houten, KD Paulsen, MI Miga, FE Kennedy, and JB Weaver. An overlapping subzone technique for MR-based elastic property reconstruction. *Magn Reson Med*, 42:779–786, 1999.

[40] EEW Van Houten, MI Miga, JB Weaver, FE Kennedy, and KD Paulsen. Three-dimensional subzone-based reconstruction algorithm for MR elastography. *Magn Reson Med*, 45:827–837, 2001.

[41] MDJ McGarry, EEW Van Houten, CL Johnson, JG Georgiadis, BP Sutton, JB Weaver, and KD Paulsen. Multiresolution MR elastography using nonlinear inversion. *Med Phys*, 39:6388–6396, 2012.

[42] MDJ McGarry, CL Johnson, BP Sutton, EEW Van Houten, JG Georgiadis, JB Weaver, and KD Paulsen. Including spatial information in nonlinear inversion MR elastography using soft prior regularization. *IEEE Trans Med Imaging*, 32:1901–1909, 2013.

[43] B Fischl, DH Salat, E Busa, M Albert, M Dieterich, C Haselgrove, A van der Kouwe, R Killiany, D Kennedy, S Klaveness, A Montillo, N Makris, B Rosen, and AM Dale. Whole brain segmentation: automated labeling of neuroanatomical structures in the human brain. *Neuron*, 33:341–355, 2002.

[44] M Jenkinson, CF Beckmann, TEJ Behrens, MW Woolrich, and SM Smith. FSL. *NeuroImage*, 62:782–790, 2012.

[45] Y Zhang, M Brady, and S Smith. Segmentation of brain MR images through a hidden Markov random field model and the expectation-maximization algorithm. *IEEE Trans Med Imaging*, 20:45–57, Jan 2001.

[46] RL Buckner, D Head, J Parker, AF Fotenos, D Marcus, JC Morris, and AZ Snyder. A unified approach for morphometric and functional data analysis in young, old, and demented adults using automated atlas-based head size normalization: reliability and validation against manual measurement of total intracranial volume. *NeuroImage*, 23:724–738, 2004.

[47] HE Nelson and J Willison. The National Adult Reading Test (NART), second ed. Windsor, UK NFER-Nelson., 1991.

[48] B McGurn, JM Starr, JA Topfer, A Pattie, MC Whiteman, HA Lemmon, LJ Whalley, and IJ Deary. Pronunciation of irregular words is preserved in dementia, validating premorbid IQ estimation. *Neurology*, 62:1184–1186, 2004.

[49] DA Wechsler. Manual for the Wechsler Memory Scale-Revised. New York: Psychological Corporation, 1987.

[50] B Uttl, P Graf, and LK Richter. Verbal paired associates tests limits on validity and reliability. *Arch Clin Neuropsychol*, 17:567–581, 2002.

[51] FR Hampel. The Influence Curve and its Role in Robust Estimation. *J Am Stat Assoc*, 69:383–393,

1974.

[52] C Leys, C Ley, O Klein, P Bernard, and L Licata. Detecting outliers: Do not use standard deviation around the mean, use absolute deviation around the median. *J Exp Soc Psychol*, 49:764–766, 2013.

[53] J Miller. Reaction time analysis with outlier exclusion: bias varies with sample size. *Q J Exp Psychol A*, 43:907–912, 1991.

[54] N Lange, MP Froimowitz, ED Bigler, and JE Lainhart. Associations between IQ, total and regional brain volumes, and demography in a large normative sample of healthy children and adolescents. *Dev Neuropsychol*, 35:296–317, 2010.

[55] J Steiger. Tests for comparing elements of a correlation matrix. *Psychol Bull*, 87:245–251, 1980.

[56] IA Lee and KJ Preacher. Calculation for the test of the difference between two dependent correlations with one variable in common. [Computer software]. Available from http://quantpsy.org, 2013.

[57] MG Packard and BJ Knowlton. Learning and memory functions of the basal ganglia. *Annu Rev Neurosci*, 25:563–593, 2002.

[58] KI Erickson, RS Prakash, MW Voss, L Chaddock, L Hu, KS Morris, SM White, TR Wojcicki, E McAuley, and AF Kramer. Aerobic fitness is associated with hippocampal volume in elderly humans. *Hippocampus*, 19:1030–1039, 2009.

[59] KI Erickson, MW Voss, RS Prakash, Basak, A Szabo, L Chaddock, JS Kim, S Heo, H Alves, SM White, TR Wojcicki, E Mailey, VJ Vieira, SA Martin, BD Pence, JA Woods, E McAuley, and AF Kramer. Exercise training increases size of hippocampus and improves memory. *Proc Natl Acad Sci USA*, 108:3017–3022, 2011.

[60] RC Petersen. Mild cognitive impairment as a diagnostic entity. *J Intern Med*, 256:183–194, 2004.

[61] J Barnes, RI Scahill, RG Boyes, C Frost, EB Lewis, CL Rossor, MN Rossor, and NC Fox. Differentiating ad from aging using semiautomated measurement of hippocampal atrophy rates. *Neuroimage*, 23:574–581, 2004.

[62] SJ Lupien, A Evans, C Lord, J Miles, M Pruessner, B Pike, and JC Pruessner. Hippocampal volume is as variable in young as in older adults: implications for the notion of hippocampal atrophy in humans. *Neuroimage*, 34:479–485, 2007.

[63] AD Baddeley and EK Warrington. Amnesia and the distinction between long- and short-term memory. *J Verbal Learning Verbal Behav*, 9:176–189, 1970.

[64] NJ Cohen and H Eichenbaum. Memory, amnesia, and the hippocampal system. MIT Press, 1993.

[65] JM Monti, GE Cooke, PD Watson, MW Voss, AF Kramer, and NJ Cohen. Relating hippocampus to relational memory processing across domains and delays. *J Cogn Neurosci*, 27:234–245, 2015.

[66] KM Horecka, MR Dulas, H Schwarb, HD Lucas, M Duff, and NJ Cohen. Reconstructing relational information. *Hippocampus*, 28:164–177, 2018.

[67] DE Hannula, D Tranel, and NJ Cohen. The long and the short of it: relational memory impairments in amnesia, even at short lags. *J Neurosci*, 26:8352–8359, 2006.

[68] OA Shipton, M El-Gaby, J Apergis-Schoute, K Deisseroth, DM Bannerman, O Paulsen, and MM Kohl. Left-right dissociation of hippocampal memory processes in mice. *Proc Natl Acad Sci USA*, 111:15238–15243, 2014.

[69] MJ Muller, D Greverus, PR Dellani, C Weibrich, PR Wille, A Scheurich, P Stoeter, and A Fellgiebel. Functional implications of hippocampal volume and diffusivity in mild cognitive impairment. *NeuroImage*, 28:1033–1042, 2005.

[70] MR Trenerry, CR Jack, RJ Ivnik, FW Sharbrough, GD Cascino, KA Hirschorn, WR Marsh, PJ Kelly, and FB Meyer. MRI hippocampal volumes and memory function before and after temporal lobectomy. *Neurology*, 43:1800–1800, 1993.

[71] B Milner. Interhemispheric differences in the localization of psychological processes in man. *Br Med Bull*, 27:272–277, 1971.

[72] M Seidenberg, B Hermann, AR Wyler, K Davies, FC Dohan Jr, and C Leveroni. Neuropsychological outcome following anterior temporal lobectomy in patients with and without the syndrome of mesial temporal lobe epilepsy. *Neuropsychology*, 12:303–316, 1998.

[73] N Leporé, Y Shi, F Lepore, M Fortin, P Voss, Y-Y Chou, C Lord, M Lassonde, I Dinov, AW Toga, and PM Thompson. Patterns of hippocampal shape and volume differences in blind subjects. *NeuroImage*, 46:949–957, 2009.

[74] U Gleissner, C Helmstaedter, and C Elger. Right hippocampal contribution to visual memory: a presurgical and postsurgical study in patients with temporal lobe epilepsy. *J Neurol Neurosurg Psychiatry*, 65:665–669, 1998.

[75] AC Papanicolaou, PG Simos, EM Castillo, JI Breier, JS Katz, and AA Wright. The hippocampus and memory of verbal and pictorial material. *Learn Mem*, 9:99–104, 2002.

[76] R Fama and EV Sullivan. Methods of association and dissociation for establishing selective brain-behavior relations. *Handb Clin Neurol*, 125:175–181, 2014.

[77] EG Fan, Xand Wheatley and SA Villeda. Mechanisms of hippocampal aging and the potential for rejuvenation. *Annu Rev Neurosci*, 40:251–272, Jul 2017.

[78] T Munder, A Pfeffer, S Schreyer, J Guo, J Braun, I Sack, B Steiner, and C Klein. MR elastography detection of early viscoelastic response of the murine hippocampus to amyloid beta accumulation and neuronal cell loss due to Alzheimer's disease. *J Magn Reson Imaging*, 2017.

[79] SF Sorrells, MF Paredes, A Cebrian-Silla, K Sandoval, D Qi, KW Kelley, D James, S Mayer, J Chang, KI Auguste, EF Chang, AJ Gutierrez, AR Kriegstein, GW Mathern, MC Oldham, EJ Huang, JM Garcia-Verdugo, Z Yang, and A Alvarez-Buylla. Human hippocampal neurogenesis drops sharply in children to undetectable levels in adults. *Nature*, 555:377–381, 2018.

[80] MA Yassa, AT Mattfeld, SM Stark, and CEL Stark. Age-related memory deficits linked to circuit-specific disruptions in the hippocampus. *Proc Natl Acad Sci USA*, 108:8873–8878, 2011.

[81] AGW van Norden, KF de Laat, I Fick, IWM van Uden, LJB van Oudheusden, Rob AR Gons, DG Norris, MP Zwiers, RPC Kessels, and F-E de Leeuw. Diffusion tensor imaging of the hippocampus and verbal memory performance: the RUN DMC study. *Hum Brain Mapp*, 33:542–551, 2012.

[82] LM Gerischer, A Fehlner, T Köbe, K Prehn, D Antonenko, U Grittner, J Braun, I Sack,

and A Flöel. Combining viscoelasticity, diffusivity and volume of the hippocampus for the diagnosis of Alzheimer's disease based on magnetic resonance imaging. *NeuroImage: Clin*, https://doi.org/10.1016/j.nicl.2017.12.023, 2017.

Chapter 9

Discussion and future work

9.1 Overview of results

The primary objective of this thesis was to evaluate the clinical utility of brain magnetic resonance elastography (MRE) for its potential use as a novel imaging biomarker for the early characterisation of neurodegeneration. New biomarkers are urgently required to predict those at risk of developing conditions such as Alzheimer's disease and to assist in the identification of new therapeutic targets.

In Chapter 2, theoretical background information required to understand the source of the MRE contrast was provided. The experimental design of a brain MRE investigation was explained, with prominence given to methods capable of generating images with a high spatial resolution. In Chapter 3, a systematic literature review was performed consistent with the guidelines provided by the Preferred Reporting Items for Systematic Reviews and Meta-Analyses (PRISMA). The review aimed to identify studies that had specifically reported MRE measurements for the human brain, in both healthy participants and patients with neurological disorders. The review had two aims: (1) to determine whether brain MRE could provide a quantitative threshold of healthy tissue mechanical properties, and (2) to evaluate the success for MRE to differentiate between healthy control participants and neurological patients. Considering the first aim, studies were identified and published values were converted to common mathematical parameters of shear stiffness, μ and loss tangent, ϕ to provide a valid summary of results. Despite this, there was large variations in reported brain stiffness for healthy participants, attributed to the chosen methodological approach. In general, cerebral stiffness may be determined to be approximately 2.5 kPa, white matter to be stiffer than grey matter, and for the deep grey matter structures to be stiffer than any of the four main lobar regions. The second aim of the review showed that brain MRE was sensitive at detecting differences between controls and patients over a wide range of neurological conditions, including diffuse diseases such as multiple sclerosis, and Parkinson's disease, in addition to patients with focal intracranial tumours of varying malignancy.

Chapter 4 identified three main research centres that contributed the majority of the brain MRE research output, namely: Mayo Clinic, USA, University of Urbana-Champaign, USA, and Charité – Universtätsmedizin, Berlin, Germany. As a result, I visited each of the centres to perform a phantom validation and obtain exemplar brain MRE elastograms. Phantom data revealed superior spatial performance for one protocol, termed *single-frequency non-linear inversion (SF-NLI)*, whereas another termed *multi-frequency MDEV (MF-MDEV)* provided the most accurate measurements for the target most resembling the stiffness of the human brain. Importantly, both approaches provided high-resolution images and could therefore be used to study specific neuroanatomical regions of interest. As a result, I consolidated collaborations with the two associated research centres to refine an experimental protocol for installation at the Edinburgh Imaging Facility, QMRI (EIF-QMRI).

In Chapter 5, the two high-resolution - yet fundamentally different - MRE protocols were installed, optimised and validated at the EIF-QMRI. Comparison of images obtained in Edinburgh, with images from the relevant research centre, showed similar quality raw MRE images and reconstructed elastograms. I also introduced a novel signal-to-noise (SNR) measurement to MRE that could assist in assessing image quality across research sites. However, this SNR measure will need to be widely used before suitable thresholds can be established to define “unusable” data from data determined to be of sufficiently high quality. In this chapter, I also developed a novel Graphical User Interface (GUI), that can perform the automatic, and optimised coregistration of MRE elastograms to T_1-weighted anatomical images. The GUI can also automatically generate values for a range of brain structures for four different MRE derived parameters. This advance will accelerate the process of obtaining MRE results thereby increasing the clinical applicability for the analysis of smaller brain structures.

Chapter 6 focused on the test re-test agreement of both the SF-NLI and MF-MDEV protocols in 6 young and 6 healthy older adults. Results for global cerebrum stiffness found similar agreement for SF-NLI (ICC: 0.89; CI: 0.67-0.97) and limited frequency range MDEV (ICC: 0.90; CI: 0.71-0.97), whereas SF-NLI was clearly superior for the viscosity parameter (ICC: 0.61; CI: 0.06-0.87) when compared to MDEV (ICC: 0.37; CI: -0.28-0.77). Bland Altman difference plots and between coefficient of variation were also better for the NLI-based protocols. All repeatability measures related to the hippocampus were also greater using NLI compared with MDEV methods. Additionally, the NLI protocols were shown to exhibit increased sensitivity to biological variation explained by the wide age range of participants. Collectively, these results supported the use of NLI in a larger study of ageing which was expected to be both highly reliable and biological sensitive.

As a result, Chapter 7 utilised the SF-NLI protocol, with soft prior regularisation (SF-NLI-SPR) to investigate differences in brain mechanical properties between 12 young (mean age: 25 years), and 12 cognitively healthy older adults (mean age: 69 years). To my knowledge, this was the first brain MRE study to ensure cognitive health in older adults as determined through neuropsychological assessment. The administration of a MRE questionnaire shortly after the imaging procedure found that the MRE vibration was well tolerated regardless of subject age, quantitatively suggesting that the actuation component is clinically viable. Novel findings included significantly softer brains in older adults compared to younger adults, with decreases in stiffness evident for the global cerebrum

(-8%), caudate (-24%), pallidum (-15%), putamen (-13%), and thalamus (-18%), when compared to measurements obtained in younger subjects. Interestingly, significant differences were not found between age groups for the stiffness of either the amygdala or hippocampus once each ROI was corrected for volume. As for the measure of relative viscosity, no significant differences between age-groups were reported for either the brain globally or any ROI. The data suggest, however, that with more statistical power, hippocampal relative viscosity may be higher in the older adult group and thus will be subject to future investigation. A further advantage of this study was establishing, for the first time, MRE base-line values for specific brain structures in both young and healthy older adults, to assist in power calculations for future studies. In addition, the clinical usefulness of MRE as an imaging biomarker for disease detection requires that thresholds of healthy tissue are clearly defined to enhance sensitivity and diagnostic potential.

Concurrently, Chapter 8 sought to expand on the hippocampus findings reported in Chapter 7. Recently published studies have linked hippocampal relative viscosity with performance on sensitive tests of memory in young adults. Due to well-known cognitive decline in older age, I investigated whether the higher relative viscosity (i.e. damping ratio, ξ), apparent in older adults was related to performance in a task of episodic memory. Results found that hippocampal ξ was indeed associated with performance on verbal-paired recall, ($p = 0.008$**), whereas hippocampal volume, ($p = 0.65$), or hippocampal stiffness, ($p = 0.98$) was not. No association was found in the control brain regions of the global cerebrum, or caudate. Delving into this further, I found a stronger association involving the left hippocampus, ($r =$ -.93, $p =$ .0.002**), as opposed to the right hippocampus, ($r =$ -.72, $p=$ 0.066). This is a particularly interesting finding due to the well-known role of the left hippocampus in verbal memory, suggesting that MRE could be utilised within the field of psychology to assist with assessments into the unique contribution from each hemisphere for cognitive functioning (i.e. hemispheric lateralisation). In addition, a statistically significant stronger correlation was found between hippocampal ξ and memory performance when voxels containing cerebrospinal fluid (CSF) were removed from the analysis. Removal of CSF from the hippocampal masks prior to inversion is likely to minimise the occurrence of quantitative errors due to data-model mismatch. In support of this procedure, the study demonstrated that removal of CSF voxels influence HC ξ measures in the expected direction (i.e. lower ξ - indicating a more elastic solid due to the removal of fluid), and remains highly correlated to the standard procedure.

Collectively, results presented throughout this thesis support the transition of MRE into a clinical viable, reliable and sensitive imaging modality. Future studies will need to replicate these initial promising findings in a larger number of subjects. There is also a significant need to disentangle separate forms of neurodegeneration, that could be related to either one of changes to neuronal density, inflammation or demyelination. The only viable way to achieve this will be to utilise additional animal models of neurodegeneration to more specifically relate the mechanical signature to a microstructural profile.

9.2 Future work

9.2.1 *Strategies for Improving Imaging Acquisitions*

Multiband excitation and nonlinear motion-induced phase error correction

Work is already underway to further improve the acquisition design of the multi-shot multi-slab sequence used throughout this thesis. A new version for brain MRE has been proposed to include novel features such as multiband excitation and 3D encoding of the distributed slab with multishot spirals [1]. Multiband strategies excite multiple imaging volumes separated in the slice direction and sample both with the same readout. This sequence allows high SNR efficiency and reduced distortions from field inhomogeneity, in addition to parallel imaging acceleration. Parallel imaging is achieved by undersampling both in-plane and through-plane (i.e. also in the slice direction), and has shown to allow higher acceleration factors without the associated artefacts. In addition, correction for nonlinear motion-induced phase errors is also incorporated to allow for the correction of phase errors not handled by linear correction, such as from cardiac pulsation. The use of a navigator before readout also reduces acquisition time by removing a second refocusing pulse. Figure 9.1 demonstrates the performance of the nonlinear motion-induced phase error correction on MRE magnitude images. Compared with the uncorrected dataset, the corrected results exhibit clear improvement to phase inconsistencies, and was also shown to increase OSS-SNR and provide elastograms with improved anatomical agreement. To date, this sequence has been shown to capture whole-brain MRE data at 2 x 2 x 2 mm^3 resolution in just 3 minutes. The reduction in acquisition time indicates a major advance in the possible clinical adoption of MRE. On the other hand, the high SNR efficiency afforded by this design may allow for a higher achievable resolution, although of course, at a cost of an increase in acquisition time.

SLIM-MRE

There exists a complementary need for MRE sequences to reduce scan time to improve patient acceptance or to enable the acquisition of additional displacement data. Sample Interval Modulation (SLIM)-MRE is a recently developed multidirectional motion encoding scheme, [2], that has been

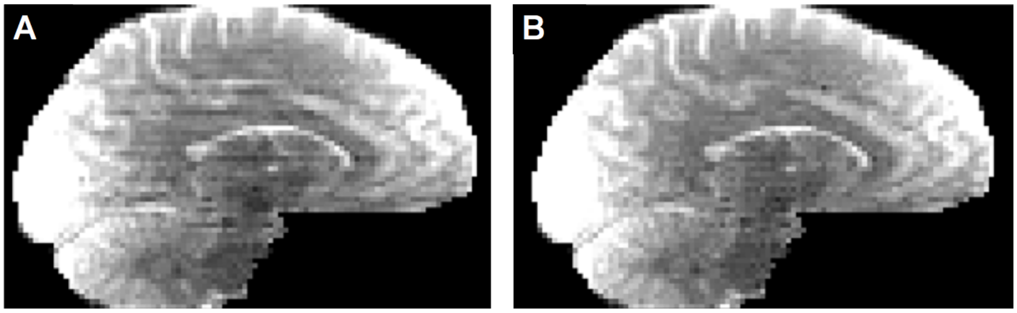

Figure 9.1: Comparison of results without (a) and with (b) nonlinear motion correction. Corrected phase inconsistencies in the slice direction are clearly visible. Image adapted from Johnson et al., 2017 [1], and used with permission.

implemented in a multishot, variable density spiral sequence for use within brain MRE [3]. SLIM-MRE allows for the simultaneous acquisition of the full vector displacement field, by modifying the sequence timings relative to the conventional encoding scheme. By switching the polarity of flow-compensated MEGs, the TE is only marginally greater than the TE used within the conventional sequence. SLIM-MRE and conventional MRE acquisitions were shown to produce nearly identical deformation fields and similar quantitative property estimates. The SLIM acquisition is, however, 2.5 times faster, which may improve the clinical adoption of MRE or provide an opportunity to capture additional displacement data.

9.2.2 *Strategies for Improving Inversion Algorithms*

Higher-resolution reconstruction

Throughout this thesis, I have used the same parameters in the nonlinear inversion (NLI) process for both phantom and *in vivo* studies in the interests of maintaining a standardised protocol to allow for results to be compared with those previously published. These parameters had been chosen previously for stability and repeatability for estimations of larger brain regions with 2.0 mm isotropic data and did not necessarily emphasise spatial resolution in recovered properties [4]. Recently, there has been renewed interest into the achievable resolution of NLI mechanical property reconstruction, which is determined by data resolution and quality, finite element mesh resolutions, regularisation parameters, and optimisation approach. As a result, McGarry *et al.* 2017 have investigated the achievable resolution of brain MRE NLI using high resolution motion data by tuning the existing regularisation weightings and optimisation parameters [4]. The most influential inversion parameters are: (1) the number of conjugate gradient (CG) iterations per subzone iteration; (2) spatial filter (SF) width; and (3) total variation minimisation (TV) weighting. By combining various forms of these parameters, resolution was improved by increasing the number of CG iterations per subzone, decreasing the width of the SF kernel, and decreasing TV weighting. Images were inspected visually, and resolution was assessed by the presence of artefacts, instability, and correspondence to neuro-anatomy.

As a result of this recent work, the NLI parameters were retuned and applied to brain data previously provided in *Chapters 4 and 5*. Comparison of the default inversion, with the new high-resolution inversion, is provided in Figure 9.2. Visual inspection of high-resolution images in all three orientations show excellent anatomical agreement. The sagittal view provides a clear delineation between the gyri and sulci, however, it is acknowledged that softer sulci might be a sliding artefact. This relates to the process of NLI in which all tissue inside the finite-element mesh (i.e. boundary mask) is assumed to be an elastic continuum. As the sulci are actually discontinuous, higher apparent shear strains might be reported due to sliding in the motion data. One possible way to fix this issue woud be to obtain very high-resolution data and build a custom finite-element mesh that follows the boundaries of the sulci so that discontinuities are built into the model. Nevertheless, regions of higher stiffness appear to be maintained across the default inversion and the higher-resolution version. Future studies will need to assess the reproducibility of this approach for generating mechanical property measurements of small brain structures. Importantly, this thesis has provided the necessary framework for such future validation assessments.

Integration of more advanced mechanical models

Identifying specific aspects of neurodegeneration, including neuronal cell death, demyelination, and inflammation, may ultimately require the use of more advanced mechanical models. Despite the brain being a biphasic, fluid-saturated tissue, the viscoelastic model used throughout this thesis is unable to characterise the extracellular fluid exchange of tissue deformation created by actuation. As a result, researchers have extended MRE inversions to include mechanical models of poroelasticity, as an alternative to single-phase MRE methods, by the development of a poroelastic formulation of the equations of motion [5, 6]. So-called magnetic resonance poroelastography (MRPE) can characterise the material response of deformation by describing the brain as both a porous elastic solid and penetrating fluid within two distinct phases. The benefits of such a model have been shown to be more representative of tissue structure and physiology, enabling a more accurate description of tissue deformation [6]. Furthermore, the ability to exploit variations in the fluid distribution, known as *hydraulic conductivity*, could be used as an additional diagnostic measure. However, it has been shown that only low frequency actuation (i.e. 1 Hz) allows for sufficient fluid exchange representative

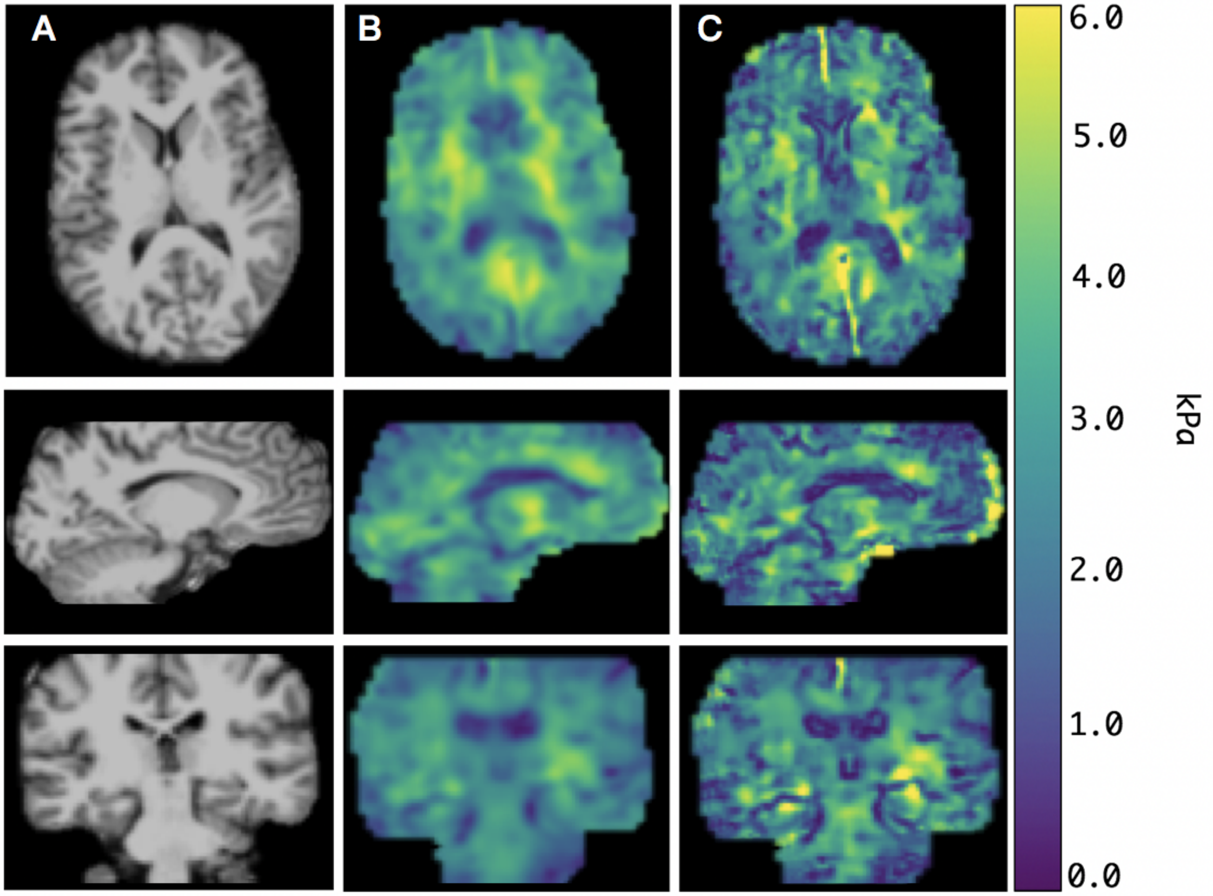

Figure 9.2: (a) T_1-weighted structural image transformed into MRE space to show anatomical structures in all three orthogonal orientations; (b) the default inversion used throughout this thesis, and (c) improved resolution with more conjugate gradient (CG) iterations per subzone iteration, lower total variation minimisation (TV) weight, and smaller spatial filter (SF) width. Note: the softer sulci might be the result of a sliding artefact. In future work, the NLI algorithm could build a custom finite-element mesh to follow the boundaries of the sulci so that discontinuities are built into the model.

of a poroelastic material, whereas frequencies typically used within MRE (i.e. 50 Hz) are more accurately described by viscoelasticity [7]. As a result, MRPE may only be suitable for studies that utilise *intrinsic actuation* [8].

All work throughout this thesis has utilised an isotropic material model, whereas the brain displays anisotropic properties, with highly organised myelinated white matter tracts showing directionally dependent characteristics. As mentioned in *Chapter 3*, a technique known as waveguide elastography (WGE) has been proposed to model the corticospinal tracts (CTS) within the brain as a transversely isotropic material [9]. WGE uses diffusion tensor maging (DTI) to locate the direction of fibre pathways, before the application of spatial-spectral filtering to identify and analyse shear waves that are propagating parallel to the principal direction of the nerve fibres. The applicability of this technique to other brain structures is questionable, however, as WGE analysis is reliant on knowledge of the pathways along which the propagating waves will travel; most brain structures do not possess anisotropic properties on the same scale as the CTS. Nevertheless, the development of an appropriate anisotropic inversion could stabilise results and improve accuracy and will surely be the subject of future work.

9.2.3 *Improving the precision of MRE measurements*

Throughout this thesis, emphasise has been placed on high-resolution MRE to enable the study of specific brain structures of interest. Further improvements in the achievable spatial resolution, as through the strategies mentioned within this section, will enable measurement of even smaller brain regions. Recent years have seen increased interest in measuring the subfields of the human hippocampal formation (HF). The HF is composed of several intricate and packed subregions that include the cornu ammonis fields (CA1, CA2, CA3, and CA4), the dentate gyrus (DG) and the subiculum [10], which are known to be involved selectively, non-uniformly and in the complex progression of different neurological disorders [11–13]. Measuring the mechanical properties and changes of each hippocampal subfield, therefore, will be highly desirable to further elucidate early microstructural changes in conditions such as preclinical Alzheimer's disease.

9.3 Conclusions

The work presented throughout this thesis has shown brain MRE to be a clinically acceptable, reliable, and biologically sensitive neuroimaging modality. The success and continuing interest in brain MRE has seen, and will see, further developments to push boundaries of achievable image resolution and the integration of more physiologically accurate mechanical models, with an acquisition and analysis time that will be clinically viable. These new methods, however, will need to follow a similar validation process to the work presented here, for which this thesis provides an appropriate framework. The possible applications of brain MRE to study health, normal ageing, disease, and cognition are wide-ranging and far-reaching and will provide future researchers with endless fields of enquiry. In view of the findings presented here, brain MRE can be expected to contribute to both basic research and diagnostic neuroimaging in the future.

References

[1] CL Johnson, JL Holtrop, AT Anderson, and BP Sutton. Brain MR elastography with multiband excitation and nonlinear motion-induced phase error correction. *Proc Intl Soc Magn Reson Med*, (242016), 2017.

[2] D Klatt, CL Johnson, and RL Magin. Simultaneous, multidirectional acquisition of displacement fields in magnetic resonance elastography of the in vivo human brain. *J Magn Reson Imaging*, 42:297–304, 2015.

[3] CL Johnson, MDJ McGarry, EEW Van Houten, JB Weaver, KD Paulsen, BP Sutton, and JG Georgiadis. Magnetic resonance elastography of the brain using multishot spiral readouts with self-navigated motion correction. *Magn Reson Med*, 70:404–412, 2013a.

[4] MDJ McGarry, JB Weaver, KD Paulsen, and CL Johnson. Reconstruction of high-resolution MR elastography motion data using nonlinear inversion. *1st International MRE workshop, Berlin*, 2017.

[5] PR Perrinez, FE Kennedy, EEW van Houten, JB Weaver, and KD Paulsen. Modeling of soft poroelastic tissue in time-harmonic MR elastography. *IEEE Trans Biomed Eng*, 56:598–608, 2009.

[6] PR Perrinez, FE Kennedy, EEW Van Houten, JB Weaver, and KD Paulsen. Magnetic resonance poroelastography: an algorithm for estimating the mechanical properties of fluid-saturated soft tissues. *IEEE Trans Med Imag*, 29:746–755, 2010.

[7] MDJ McGarry, CL Johnson, BP Sutton, JG Georgiadis, EEW Van Houten, AJ Pattison, JB Weaver, and KD Paulsen. Suitability of poroelastic and viscoelastic mechanical models for high and low frequency MR elastography. *Med Phys*, 42:947–957, 2015.

[8] JB Weaver, AJ Pattison, MD McGarry, IM Perreard, JG Swienckowski, CJ Eskey, SS Lollis, and KD Paulsen. Brain mechanical property measurement using MRE with intrinsic activation. *Phys Med Biol*, 57:7275–7287, 2012.

[9] A Romano, M Scheel, S Hirsch, J Braun, and I Sack. In vivo waveguide elastography of white matter tracts in the human brain. *Magn Reson Med*, 68:1410–1422, 2012.

[10] A Giuliano, G Donatelli, M Cosottini, M Tosetti, A Retico, and ME Fantacci. Hippocampal subfields at ultra high field MRI: An overview of segmentation and measurement methods. *Hippocampus*, 27:481–494, 2017.

[11] H Braak and E Braak. Staging of Alzheimer's disease-related neurofibrillary changes. *Neurobiol Aging*, 16:271–278, 1995.

[12] MJ West, CH Kawas, WF Stewart, GL Rudow, and JC Troncoso. Hippocampal neurons in pre-clinical Alzheimer's disease. *Neurobiol Aging*, 25:1205–1212, 2004.

[13] SA Small, SA Schobel, RB Buxton, MP Witter, and CA Barnes. A pathophysiological framework of hippocampal dysfunction in ageing and disease. *Nat Rev Neurosci*, 12:585–601, 2011.

Publications

HISCOX LV, Johnson CL, McGarry MDJ, Schwarb H, van Beek EJR, Roberts N, Starr JM 2018. Hippocampal viscoelasticity and episodic memory performance in healthy older adults examined with magnetic resonance elastography. *Brain Imaging Behav, in sub.*

HISCOX LV, Johnson CL, McGarry MDJ, Perrins M, Littlejohn A, van Beek EJR, Roberts N, Starr JM 2018. High-resolution magnetic resonance elastography reveals differences in subcortical gray matter viscoelasticity between young and healthy older adults. *Neurobiol Aging,* **65**, 158-167.

HISCOX LV, Johnson CL, Barnhill E, McGarry MDJ, Huston III J, van Beek EJR, Starr JM, Roberts N 2016. Magnetic Resonance Elastography (MRE) of the Human Brain: Technique, Findings, and Clinical Applications. *Phys Med Biol,* **61**, 401-437.

Rzechorzek N, HISCOX LV, Barnhill E, Hirsch S, Kennedy P, Huston III J, Schwarz T, Sack I, Semple S, Marioni-Henry K, Roberts N 2016. Magnetic resonance elastography – towards a stiffness atlas of the canine brain for translational neurology. *J Vet Intern Med*, **30**, 1935.

HISCOX LV, Leonavičiūtė E, Humby T 2014. The effects of automatic spelling correction software on understanding and comprehension in compensated dyslexia: improved recall following dictation. *Dyslexia*, **20**, 208-224.

Walsh ND, Dalgleish T, Dunn VJ, Abbott R, St Clair MC, Owens M, Fairchild G, Kerslake WS, HISCOX LV, Passamonti L, Ewbank M, Ban M, Calder AJ, Goodyer IM 2012. 5-HTTLPR–environment interplay and its effects on neural reactivity in adolescents. *NeuroImage*, **63**, 1670-80.

FeldmanHall O, Mobbs D, Evans D, HISCOX LV, Navrady L, Dalgleish T 2012. What we say and what we do: the relationship between real and hypothetical moral choices. *Cognition*, **123**, 434-41.

Conference Proceedings

HISCOX LV, Johnson CL, McGarry MDJ, Schwarb H, van Beek, EJR, Roberts N, Starr JM. Hemispheric specialisation of hippocampal viscoelasticity for memory performance in healthy older adults. *International Society for Magnetic Resonance in Medicine (ISMRM).* (June 2018, Paris France). Oral presentation.

HISCOX LV, Johnson CL, Schwarb H, McGarry MDJ, van Beek, EJR, Roberts N, Starr JM. Hippocampal viscoelasticity and episodic memory performance in older adults. *1st International MRE workshop.* (September 2017, Berlin, Germany). Oral presentation.

Marshall H, HISCOX LV, Perrins M, Barnhill E, Sack I, Braun J, Herrmann T, Bernarding J, van Beek EJR, Roberts N. The effect of field strength on brain stiffness estimates using multi-frequency MR Elastography (MRE). *1st International MRE workshop.* (September 2017, Berlin, Germany). Oral presentation.

HISCOX LV, Johnson CL, McGarry MDJ, van Beek, EJR, Roberts N, Starr JM. Hippocampal Viscoelasticity in Young and Cognitively Healthy Older Adults. *2017 Dementia MRI conference.* (May 2017, Cardiff, UK). Oral and poster presentation.

HISCOX LV, Perrins M, Johnson CL, McGarry MDJ, Barnhill E, Huston III J, Sack I, Braun J, van Beek, EJR, Starr JM, Roberts N. Reproducibility Study of Direct and Non-Linear Inversion High-Resolution Magnetic Resonance Elastography (MRE) of the Hippocampus. *International Society for Magnetic Resonance in Medicine (ISMRM).* (April 2017, Hawaii, USA). Poster presentation.

Perrins M, HISCOX LV, Gray C, Semple S, Barclay L, Kirkbride R, Salisbury L, Brown C, Walsh T, van Beek EJR, Roberts N, Griffith D. Muscle Change Associated with Time in Intensive Care Unit (ICU). *International Society for Magnetic Resonance in Medicine (ISMRM).* (April 2017, Hawaii, USA). Poster presentation.

HISCOX LV, Johnson CL, McGarry MDJ, van Beek, EJR, Roberts N, Starr JM. Viscoelasticity of Subcortical Grey Matter Structures in Young and Cognitively Healthy Older Adults. *British Geriatric Society.* (March 2017, Glasgow, UK). Oral presentation.

HISCOX LV, Johnson CL, Hirsch S, Barnhill E, Sack I, McGarry M, Huston J, van Beek, EJR, Starr JM, Roberts N. Comparison of Direct and Non-Linear inversion for measurement of Mechanical Properties of the Hippocampus using Magnetic Resonance Elastography (MRE). *International Tissue Elasticity Conference.* (October 2016, Vermont, New England, USA). Oral presentation.

HISCOX LV, Perrins M, Puertollano M, Johnson CL, McGarry MDJ, Brown C, van Been JR, Starr JM, Roberts N. Magnetic Resonance Elastography (MRE) and Diffusion Tensor Imaging (DTI) in a Multimodal Brain Tissue Integrity Characterisation Pipeline. *CCACE 9th Annual Research Day.* (September 2016, Edinburgh, UK). Poster presentation.

HISCOX LV, Barnhill E, Guo J, Dittmann F, Hirsch S, Perrins M, Herrmann T, Bernarding J, Roberts N, Braun J, Sack I. Impact of Field Strength and Image Resolution on MRE Stiffness

Estimation. *International Society for Magnetic Resonance in Medicine (ISMRM).* (May 2016, Singapore). Oral presentation.

HISCOX LV, Barnhill E, Kennedy P, van Beek EJR, Starr JM, Roberts N. Comparison of Two Image Analysis Pipelines for MR Elastography (MRE). *Annual Scientific Meeting of the European Society for Magnetic Resonance in Medicine and Biology (ESMRMB).* (October 2015, Edinburgh, UK). Oral presentation.

Kennedy P, MacGregor L, Barnhill E, Cooper A, HISCOX LV, Brown C, Braun J, Sack I, van Beek E, Hunter A, Johnson CL, Roberts N. Mechanical properties and force output of quadriceps muscle following eccentric exercise. *International Society for Magnetic Resonance in Medicine (ISMRM).* (May 2015, Toronto, Canada). Poster presentation.

Awards and Grants

December 2017
CCACE development award - £9600

March 2017
Taylor Brown Prize - Best Platform Presentation at the British Geriatric Society Scientific Spring Meeting - £300

September 2016
SINAPSE Image of the Month

May 2015
CCACE pilot study award - £8354

May 2015
Alzheimer Scotland Travel Bursary Award - £1300

May 2014
NeuroResearcher's award - £1300

Appendix I

Appendix II

Search Strategy

Medline

1. Brain (explode)
2. Brain disorder
3. Brain diseases (explode)
4. Cerebral
5. Cereb*
6. 1 or 2 or 3 or 4 or 5
7. Magnetic Resonance Elastography
8. *Elasticity Imaging Techniques /mt
9. (Viscosity/ OR elasticity/) AND (imaging OR MRI).
10. 7 or 8 or 9
11. 6 and 10
11. 11 not (animals/ not humans/)

Total = 399

Embase

1. Brain (explode)
2. Brain disorder
3. Brain diseases (explode)
4. Cerebral
5. Cereb*
6. 1 or 2 or 3 or 4 or 5
7. Magnetic Resonance Elastography
8. Elasticity Imaging Techniques
9. (Viscosity/ OR elasticity/) AND (imaging OR MRI).
10. 7 or 8 or 9
11. 6 and 10
11. 11 not (animals/ not humans/)

Total = 390

Web of science

Brain OR cereb*
Magnetic Resonance Elastography OR Elasticity Imaging Technique
Total= 312

Appendix III